DOCTOR OF PHILOSOPHY

Development of optical fibre devices for distributed monitoring and point-sensing applications

Marsh, Dan H.

Award date:
2003

Awarding institution:
University of Wales, Bangor

Development of Optical Fibre Devices for Distributed Monitoring and Point-Sensing Applications.

Dan H. Marsh

Department of Chemistry,
University of Wales, Bangor

August 2003

A dissertation submitted to the University of Wales, Bangor in accordance with the requirements of candidature for the degree of Doctor of Philosophy.

Abstract

This thesis describes the development of novel optical fibre devices and coatings for sensing and catalysis. The production of a sensor cable able to detect leaks in petrochemical pipelines is described. The cable consisted of a glass-reinforced central rod that was coated in a thin polymer layer designed to expand in the presence of the target fluids. Swelling of the polymer film induced light loss in an adjacent optical fibre by the production of microbends. These microbending losses were detected by optical time domain reflectometry over kilometre lengths of cable, with response times of less than a minute. The development of point sensors using optical fibre is also described. The possibility of coating optical fibres in photoactive semiconductor thin films for sensing or photocatalysis is discussed and a microemulsion technique for the production of nanoscale, mesoporous thin films of titania is detailed. The sol-gel system consisted of water-containing, inverse micelles of Triton X-100, (a well characterised non-ionic surfactant) in a dry cyclohexane environment. Titanium (IV) isopropoxide was used as a precursor and was hydrolysed within the aqueous micelle cores. After thermal treatment of the resultant gels, titania materials were obtained as powders and thin films on conducting glass slides and optical fibres. Powders and thin films on slides were well crystallised, mesoporous anatase. BET surface areas were, in some cases, shown to be in excess of 600 m^2g^{-1}. Calcining of thin films on optical fibre substrates was shown to be detrimental to fibre integrity and thus, alternative methods for the crystallisation of films and the removal of organic residues were explored. Ultraviolet irradiation, hydrothermal treatment and supercritical fluid extraction were investigated. Supercritical fluid extraction and hydrothermal methods were shown to be effective in removing organic residues and steam treatment was successful in the development of an anatase structure at temperatures more than 200 ° cooler than in conventional thermal treatments.

Felix qui potuit rerum cognoscere causas

Virgil Georgica II, AD 490

Acknowledgements

First and foremost I must thank my supervisor, Dr. Maher Kalaji, for his support, encouragement, advice, and importantly, his patience. Thanks also to Drs. John Macdonald and Peter Holliman.

Secondly, grateful acknowledgement is due to Dr. Petr Kluson at the Chemical Institute in Prague, Czech Republic. Petr performed all the supercritical fluid extractions and gas adsorption measurements (together with some other analyses of samples) all of which are explicitly credited to him in the relevant sections.

Thanks also to the technical staff at the Department of Chemistry, in particular Kevin Spencer, John Charles and Denis Williams.

Grateful acknowledgement must also go to Geoff Andrews, Vince Watson, and Dave Walker at Pinacl Communications Systems Ltd. for their assistance in all matters relating to the manufacture of fibre optic cables; to Drs. Walter Johnstone and Dave Moodie at Optosci Ltd., Glasgow, for assistance and advice relating to the operation of the OTDR unit; to Dr. Chris Moran at the University of Strathclyde for advice about the swelling properties of elastomers, and to Vic Rogers and Paul Parker of the Security Design Associates group for advice and assistance in the operation of the custom interface software.

Special mention must go to Dr. Alistair MacLean of Optosci Ltd. and the University of Strathclyde, whose cooperative assistance during the field trials and OTDR testing of the DISH prototypes was greatly appreciated.

Thanks also to Ross Finlay of Light Networking Inc. for training me in the engineering aspects of optical fibre use.

Finally, thanks must go to my parents and especially to Heidi, whose patience and support have made the writing of this little document somewhat more bearable.

List of Abbreviations

° C	degrees celsius
CCI	core – cladding interface
dB	decibels, unit of attenuation
D_h	hydrodynamic diameter
DISH	Distributed Industrial Sensor for Hydrocarbons
DTI	Department of Trade and Industry
EDX	energy dispersive X-ray
EP4412	name of Dow Corning silicone elastomer
EPSRC	Engineering and Physical Sciences Research Council
FTIR	Fourier transform infra-red
FTO	fluorine-doped tin oxide
ğ	grams force (equivalent to 0.00981 N)
GRP	glass reinforced plastic, glass fibres embedded within an epoxy matrix
h	water:alkoxide ratio
HPLC	high pressure liquid chromatography
iPr	isopropyl
ITO	indium-doped tin oxide
K	1000 times, (magnification)
K	degrees kelvin
LED	light emitting diode
LRP	lead replacement petrol
m	alkoxide concentration
MEK	methyl ethyl ketone
MMI	man-machine interface
MORE	microoptical ring electrode
n	water:surfactant ratio, (sometimes referred to as R in literature)
NA	numerical aperture, defined as the sin of the acceptance angle
NIR / IR	near infrared / infrared
OFS	optical fibre sensor
OTDR	optical time domain reflectometer
PC	personal computer
PCS	plastic clad silica
PDMS	polydimethyl siloxane
PFE	pressurised fluid extraction
PMMA	polymethylmethacrylate
ppm	parts per million
PSD	pore size diameter

PVDF	polyvinylidenefluoride
RTP	room temperature and pressure
s	surfactant concentration (in $mol.kg^{-1}$)
SDA	Security Design Associates
SEM	scanning electron microscopy
SFE	supercritical fluid extraction
SM	singlemode
t_g	gelation time
TGA	thermogravimetric analysis
TIR / MTIR	total internal reflection / multiple total internal reflection
TT	thermal treatment
TTB	titanium tetrabutoxide
TTP	titanium tetrapropoxide
TX100	Triton X-100, octylphenylpolyoxytheylene ether surfactants
UHQ	ultra high quality water, >18 MΩ
ULS	ultra low sulfur (diesel)
UV	ultraviolet
UV-vis	ultraviolet visible (spectroscopy)
XPS	X-ray photoelectron spectroscopy
XRD	X-ray diffractometry
Φ	diameter

Contents

	Title	*i*
	Abstract	*ii*
	Acknowledgements	*iv*
	Declarations	*v*
	List of Abbreviations	*vi*
Chapter 1	**An introduction to optical fibre theory**	**1**
1.1	Principles of optical fibres	2
1.2	References	10
Chapter 2	**Development of an optical fibre sensor system for the distributed industrial sensing of hydrocarbon fluids**	**11**
2.1	Introduction	12
	2.1.1 DISH project history & collaborators	12
	2.1.2 Target hydrocarbons and applications	13
	2.1.3 Distributed microbend sensors	15
	2.1.4 The DISH sensor	18
2.2	Experimental	28
	2.2.1 Manufacture of sensor cable & selection of components	28
	2.2.2 First generation prototypes – bare fibre sensors	31
	2.2.3 Second generation – buffered fibre sensors	35
	2.2.4 Third generation – petrol tuned sensors	36
	2.2.5 Field trials	38
2.3	Results and discussion	41
	2.3.1 Assessment of sensor components	41
	2.3.2 First generation prototypes – bare fibre sensors	51
	2.3.3 Second generation – buffered fibre sensors	56
	2.3.4 Third generation – petrol tuned sensors	59
	2.3.5 Field trials	70
2.4	Conclusions	77
2.5	Further work	79
2.6	References	80

Chapter 3	**A reverse micelle, sol-gel method for the production of nanocrystalline titania.**	**83**
3.1	Introduction	84
	3.1.1 Nanocrystalline titania	84
	3.1.2 Sol assembly & reverse micelles	86
	3.1.3 Structure, appearance, calcination & crystallisation	93
3.2	Experimental	97
	3.2.1 Production of sols & viscosity measurement	97
	3.2.2 Post production treatment & aging of gels	98
	3.2.3 Calcining & crystallisation of gels	98
	3.2.4 Characterisation of monolithic gels & titania powders	99
3.3	Results and discussion	100
	3.3.1 Production of sols & viscosity measurement	100
	3.3.2 Post production treatment & aging of gels	102
	3.3.3 Calcining & crystallisation of gels	105
3.4	Conclusions	110
3.5	References and bibliography	111
Chapter 4	**Development of a sol-gel, dip-coating procedure for the deposition of mesoporous, nanocrystalline pure titania and doped titania thin film coatings on both conducting glass slides and optical fibre substrates.**	**114**
4.1	Introduction	115
	4.1.1 Non-distributed optical fibre sensing	115
	4.1.2 Possible applications of titania thin films in point sensing	131
	4.1.3 Coating methods and substrates: slides and fibres	136
4.2	Experimental	140
	4.2.1 Substrate preparation	140
	4.2.2 Deposition of titania thin films on slides and fibres	141
	4.2.3 Characterisation of thin films	143
4.3	Results and discussion	146
	4.3.1 Undoped titania coated slides	146
	4.3.2 Doped titania thin films on slides	153
	4.3.3 Undoped titania coated optical fibres	162
4.4	Conclusions	168
4.5	References and bibliography	171
Chapter 5	**Investigation into the development of alternative methods for the post-coating treatment of titania gel-coated optical fibres.**	**176**
5.1	Introduction	177
	5.1.1 SFE treatment of sol-gel coatings	177
	5.1.2 Hydrothermal treatment	178
	5.1.3 Ultraviolet irradiation	180
5.2	Experimental	182
	5.2.1 Supercritical fluid extraction	182
	5.2.2 Hydrothermal treatment of gels	183
	5.2.3 Ultraviolet irradiation	183

	5.2.4 Direct particle deposition	184
	5.2.5 Substrate preparation – fibre coiling	185
5.3	Results and discussion	186
	5.3.1 Supercritical fluid extraction	186
	5.3.2 Hydrothermal treatment of gels	193
	5.3.3 Ultraviolet irradiation	202
	5.3.4 Direct particle deposition	207
5.4	Conclusions	218
5.5	References	221
Chapter 6	**Conclusions and final comments**	**223**

CHAPTER 1

An introduction to optical fibre theory.

1.1 Principles of Optical Fibres [1]

Modern telecommunications fibres are usually made of high purity silica doped with germanium to produce a desired refractive index. The basic structure (figure 1.0.1) consists of a high purity core surrounded by a cladding layer which is in turn coated with a protective acrylate layer involved in mode stripping (discussed later in this section). Several "standard" classifications of fibre are found. Broadly speaking, fibres are either designated as "singlemode" or "multimode". Singlemode fibres have a small core size, usually 9 μm and hence, only one mode of light can propagate along the fibre. Multimode fibres have larger cores, usually 50, 62.5 or 85 μm and multiple modes will propagate. Core sizes of up to 1000 μm are available although these are restricted to military use and other specialist areas and may use other materials than silica for the core and cladding. These larger core fibres offer a distinct advantage to sensing applications by virtue of their higher power capacity and stronger evanescent field. The use of two such fibres for sensing are discussed in later chapters.

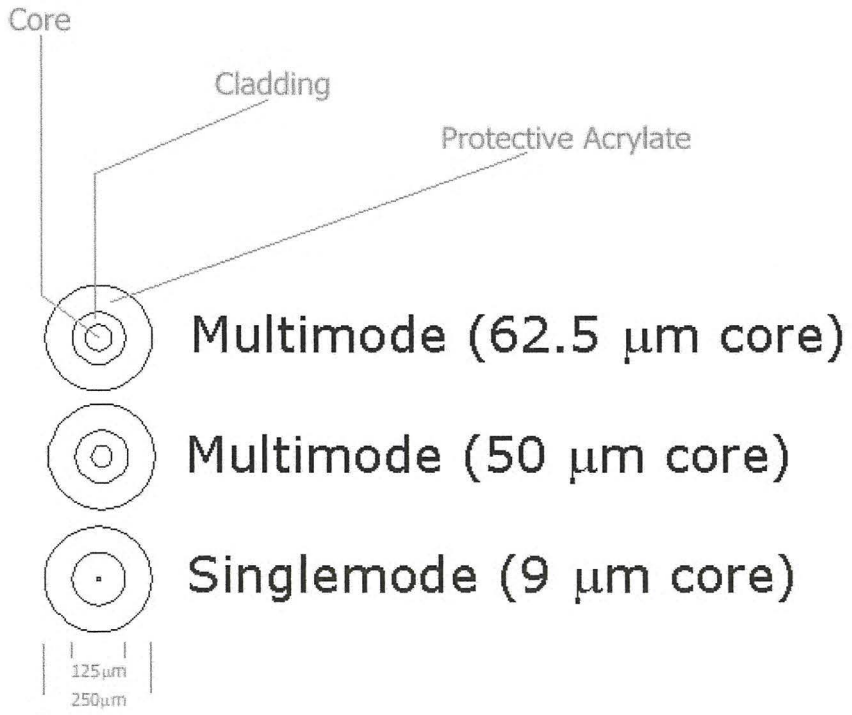

Figure 1.0.1: Diagram to illustrate the cross-sectional structure of optical fibres [1].

Although fibres differ by the relative core and cladding dimensions they are more often described according to a function called Numerical Aperture. This is a measure of the amount of light that can enter (or "launch") into the fibre end and is related to the size of the so-called "cone of acceptance" (figure 1.0.2). Photons which hit the core face with a trajectory from outside this cone will not internally reflect and will be lost into the cladding and subsequently into the acrylate layer.

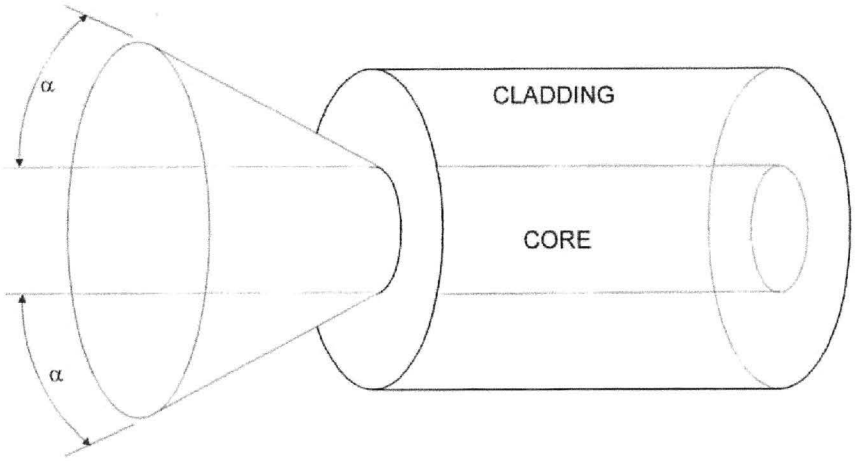

Figure 1.0.2: Diagram to illustrate the concept of the cone of acceptance at a fibre end.

The cone of acceptance is determined by calculation of the angle of acceptance, which is a function of the critical angle determined by Snell's Law of refraction. The numerical aperture is the sine of the acceptance angle (figure 1.0.3).

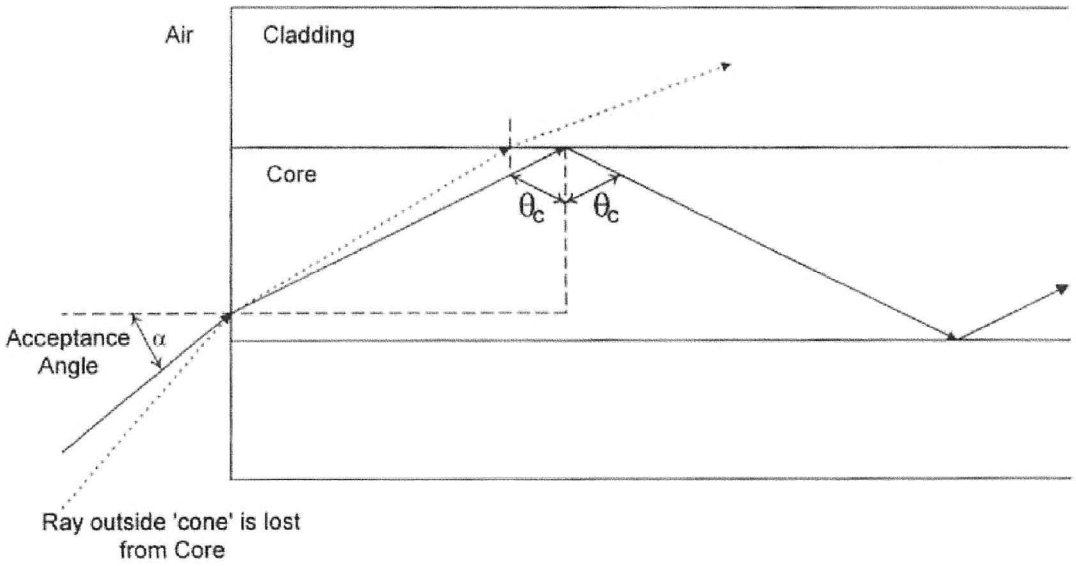

Figure 1.0.3: Diagram showing the angle of acceptance and its relationship to Snell's Law.

There are two types of light source used to launch into fibres. As a general rule LASERs are used with singlemode fibres and either LASERs or LEDs with multimode fibres. This is due to the light gathering efficiency of the two types of fibre – again related to the numerical aperture and cone of acceptance. Multimode fibres have large numerical aperture by virtue of their large core faces and as such can efficiently gather light from relatively low power sources such as LEDs. Due to their small numerical aperture, singlemode fibres require a more intense source, hence the use of LASERs. Typically singlemode fibres have a higher data carrying capacity than multimode fibres for two reasons. Firstly, modern LASER sources can be pulsed on femtosecond scales. The high frequency of the pulses allows Gigabits of data to be transmitted down single fibres. LED sources will pulse at lower frequencies. Secondly, as only one mode (path) of light propagates along a singlemode fibre the transmitted signal suffers less distortion per unit distance travelled and per unit time hence faster data rates can be used.

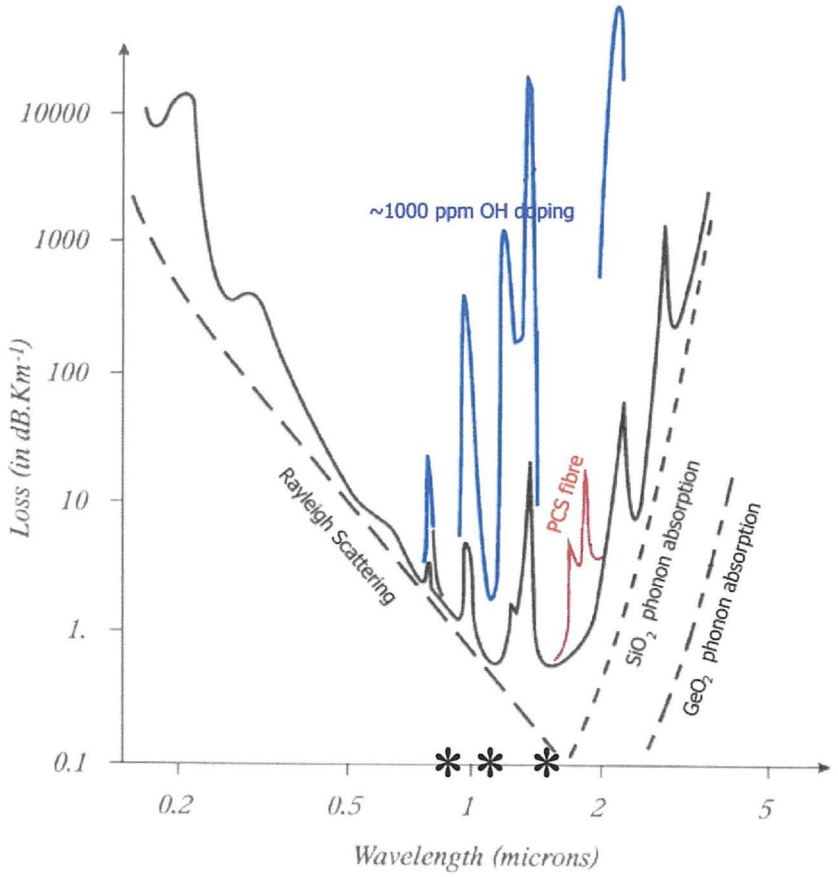

Figure 1.0.4: Absorption spectrum of fused silica cores in standard silica fibre, hydroxide-doped glass fibres and plastic-clad silica (PCS) fibres. [2]

Modern fibres operate in the near infra-red (NIR) region at wavelengths of 850, 1300, 1310, 1550 and 1625 nm. These are chosen due to "windows" in the absorption spectrum of silica and by consideration of Rayleigh Scattering effects. This is illustrated in figure 1.0.4 (previous page). Combination of the wavelength dependent Rayleigh scattering effect and the onset of Si-O absorptions leaves a window of transmission centred between 1 and 2 μm. Superimposition of the silica absorption trace with its characteristic Si-OH absorption peaks onto this window leaves three distinct transmission windows at the wavelengths marked with an asterix (*) on the figure. The black line on the figure shows the trace seen for a standard silica fibre. That for a specially hydroxide doped glass fibre is shown in blue and for a plastic clad silica (PCS) fibre in red.

For sensing purposes the wavelength chosen depends on the operating principles of the transduction mechanism and in some specific types of sensor, on the species of interest. The mechanisms of light propagation along fibres are quite complex, and an in depth analysis is beyond the scope of this report. The simplest case is seen for singlemode fibres. In this situation, light propagates as a wavefront along the fibre (figure 1.0.5)

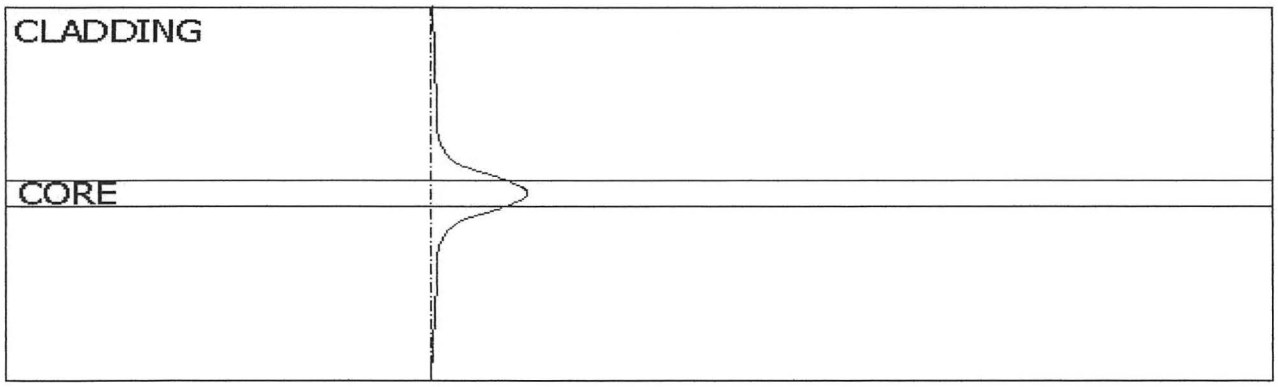

Figure 1.0.5: Diagram of the wavefront and evanescent field.

Due to the narrow core only this "fundamental" mode, the so-called zero order mode is found and can be diagrammatically represented as a single line travelling along the centre of the fibre core. This mode is the fastest mode (path) being the shortest path along the fibre.

A portion of the wave travels within the cladding, and in theory the field extends to infinity. This portion of the wave that travels in the cladding medium is termed the evanescent wave or field [1]. The evanescent field will be lost as the radius of any bend decreases below a critical size. This will be discussed further in the next section. The situation is more complex for multimode fibres. In this case the core of the fibre is sufficiently large in relation to the wavelength of light used that multiple paths or modes are available to the launched light. As shown in figure 1.0.6, the paths are named according to the number of reflections that will occur and hence the length of the path.

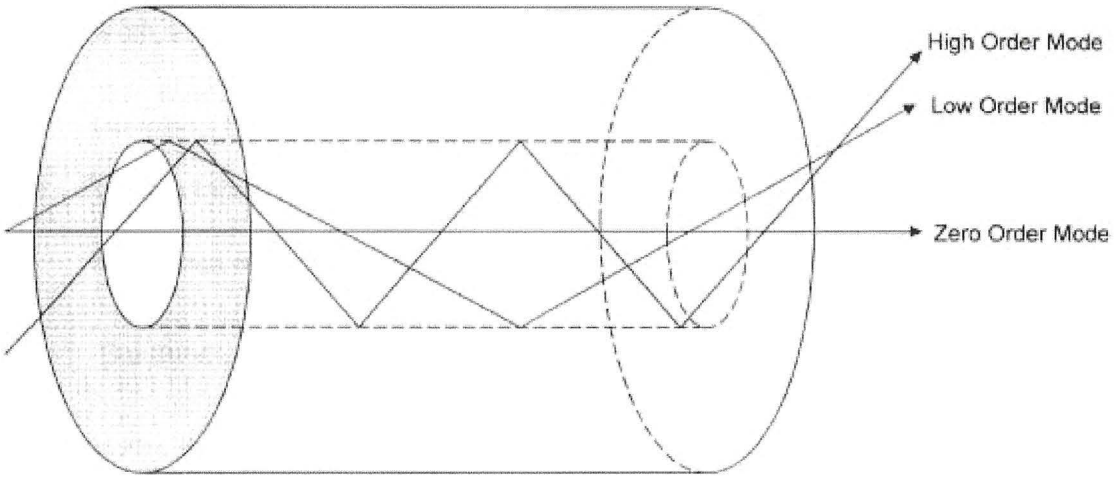

Figure 1.0.6: Diagram to illustrate the paths (modes) within a multimode fibre.

As a result of the differing travel times of the different modes, a single pulse launched into the fibre will spread out. This effect is known as pulse broadening or "mode dispersion". This will limit the data capacity of a fibre and hence, in order to minimise this effect the core of the fibre is modified by the controlled doping of germanium ions. The refractive indices of the cores of modern multimode fibres are graded across the core rather than stepped (figure 1.0.7 overleaf), and such fibres are hence termed graded index multimode fibres. By grading the core of the fibre the numerical aperture is reduced to a value approximately half that of an equivalent stepped index fibre.

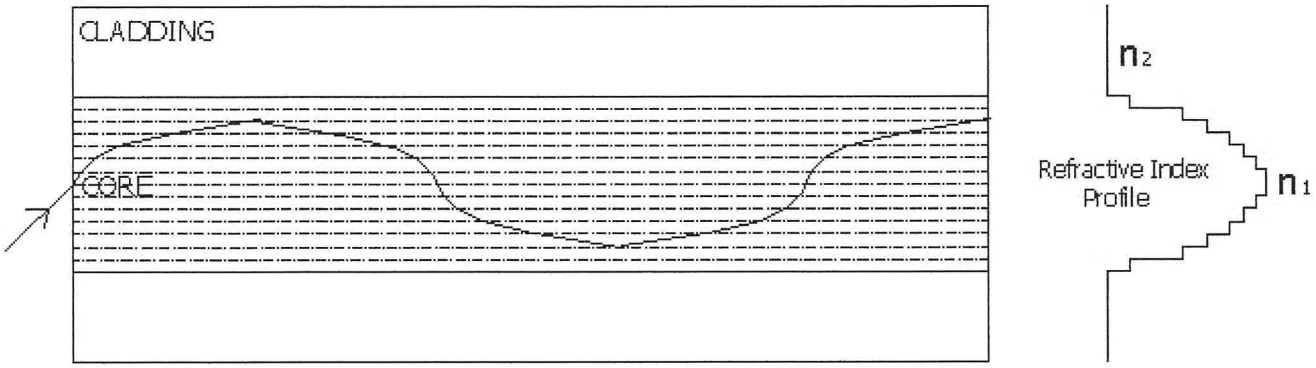

Figure 1.0.7: Graded index fibre illustrating the modified path of the refracted ray.

As a result of this grading the photons travel in spiral paths along the fibre and spend a greater amount of their time in the central, higher index (hence faster) region thus reducing the time delay experienced by the higher order modes.

For a given source of monochromatic light, there are a finite number of modes that can exist in any one fibre [3]. This number is related to the area of the core face, the numerical aperture of the fibre (hence its refractive index profile) and the wavelength of light launched:

$$\text{Number of modes} = \frac{0.5\,(\pi\, d\, (NA))^2}{\lambda^2}$$

Where **NA** is the numerical aperture of the fibre, **d** is the core diameter and **λ** is the wavelength of light launched into the fibre. Hence, to increase the number of modes propagating in a fibre it is necessary to increase the diameter of the core, increase the numerical aperture (by increasing the difference between the core and cladding refractive indices) or decrease the wavelength of light used. Modal distortion is of less importance when using fibres for sensing purposes, however when considering non-point or distributed sensors this effect can be significant. In addition, it should be realised that in solving the modal distortion problem by steering the propagating wave inwards, the evanescent field is

diminished, which although good for telecommunications purposes is generally a bad thing in sensing applications.

It is often, as will be seen in later sections, the interactions or loss of this field that is the crucial step in the transduction mechanism. Thus, for most sensing applications a non-graded or "stepped index" fibre will be a better option.

It is important to note that the primary coating of acrylate serves a dual purpose. Firstly, it protects the fibre from water ingress and minor scratching. Secondly, it serves to remove very high order modes from the fibre system, thus further diminishing the modal distortion. As the acrylate has higher refractive index than the cladding, any high order modes propagating through the cladding and reaching the interface between the cladding and acrylate will be refracted out of the cladding rather than reflecting back towards the core. By thus removing very high order modes the signal distortion is improved. This is known as mode stripping. Logically, this process contributes towards power loss in a fibre system.

Losses in fibre systems originate from two sources, intrinsic losses and extrinsic losses. Intrinsic losses are those caused by interactions of the light with the material of the fibre. These are the absorption of energy by the medium through which the light is passing and the scattering of light. Both these processes are wavelength dependant. Absorption losses are a function of the specific elemental composition of the silica glasses and are minimised by the careful selection of wavelengths where maximum transmittance is observed. Scattering losses consist predominantly of Rayleigh scattering, i.e. scattering in all directions, of light of the same wavelength as that of the incident light. Some small proportion of the light is scattered as Raman and Brillouin scattering at wavelengths shifted above and below that of the incident light. These are both weak effects and do not contribute much to the loss calculations. They are however of substantial importance in the sensing fields as will be seen later. Scattering increases exponentially with decreasing wavelength and thus operating wavelengths are chosen by careful inspection of both absorption data and scattering loss data.

Extrinsic losses are those caused by damage to or bending of the fibre. Two types of bending loss can occur. Microbending is caused by minute imperfections in the core-cladding interface (CCI) and is accentuated at certain bend radii. Microbending losses can be advantageous in sensing as they are easily detected by methods that will be described later. The DISH sensor is an example of a microbend sensor. Macrobending is caused by bending the fibre to such an extent that the conditions which lead to total internal reflection (TIR) fail and light is refracted into the cladding rather than reflecting into the core. This effect can be easily seen if a fibre carrying visible light is bent in a darkened room. The escaping light is clearly visible. It is interesting to note that if a fibre is working correctly no light or glow should be visible along the fibre length except at either end – it is impossible to see the light travelling through the core where no imperfections exist.

Some loss in a system is inevitable but is allowed for by creating a power budget. This power budget takes into account the minimum power requirements at the detector and the launch power of the LASER or LED and thus an allowable proportion of the light can be lost in a system without detriment to signal transmission. As the power of high frequency LASERs and LEDs grows, and the sensitivity of detectors increases, the power budget increases proportionally. This allows telecommunications scientists to design systems that will travel further and carry more data. For sensing purposes, it allows greater scope for the development of devices that rely upon the weak effects of Raman and Brillouin scattering, Rayleigh backscatter in optical time domain reflectometry (OTDR) techniques (further discussed in Chapter 2) and evanescent field transduction mechanisms.

This chapter only provides a brief summary of relevant theory. A more comprehensive treatment of optical fibre theory may be found in any of the texts by Wolfbeis [4], Cattral [5], Culshaw and Dakin [6], Senior [7] or Corish [8].

1.2 References

1 C.M. Davis *(1986) Fiberoptic Sensor Technology Handbook* Optech, Virginia.

2 G. Boisdé, and A. Harmer, (199236) *Chemical and Biochemical Sensing with Optical Fibres and Waveguides* Artech House, London 389pp

3 B. Culshaw, and J. Dakin, Eds.(1996) *Optical Fibre Sensors – Components and Subsystems* vol. 3 Artech House, London 237pp

4 O.S. Wolfbeis, Ed. (1991) *Fibre Optic Chemical Sensors & Biosensors* Volume 1 CRC Press New York

5 R.W. Cattral, (1997) *Chemical Sensors*, Oxford University Press, Oxford, 74pp

6 B. Culshaw, & J. Dakin, Eds. (1997) *Optical Fibre Sensors – Applications, Analysis and Future Trends* vol. 4 Artech House, London 478pp

7 J.M. Senior, (1992) *Optical Fibre Communications: principles and practice.* Prentice Hall, New Jersey.

8 P.J. Corish, Ed. (1992) *Concise Encyclopaedia of Polymer Processing and Applications* Pergamon, Oxford. 771pp

CHAPTER 2

Development of an optical fibre sensor system for the distributed industrial sensing of hydrocarbon fluids

2.1 Introduction

2.1.1 DISH project history & collaborators

The DISH acronym is an abbreviation of Distributed Industrial Sensors for Hydrocarbons. The project was established through the LINK SENSORS scheme run by the Department of Trade and Industry and jointly funded by the DTI and EPSRC. The DISH sensor is based on the design of a distributed water sensor published by Michie *et al.* [1-3]. The water, pH and humidity sensor incorporates a water swellable polymer, a so-called "hydrogel". The DISH scheme aimed to adapt this technology for hydrocarbon detection by replacing the hydrogel with an elastomer that would respond to hydrocarbons liquids. The aims of the DISH project as prescribed in the LINK Scheme application documentation were to "focus on the research and development of a low cost distributed fibre optic sensing system for the detection and location of leaked or spilled hydrocarbons such as fuels, light oils and solvents". "The system comprises a proprietary fibre optic cable which experiences local microbend loss in the presence of hydrocarbons. Interrogation of the cable with an Optical Time Domain Reflectometer (OTDR), enables hydrocarbon spills to be detected and located over a range of several kilometres with a resolution of a few metres." The DISH consortium consisted of several collaborators from both the academic and industrial sectors. **Security Design Associates, SDA** (Swindon) were the project coordinators and in addition to liasing with the DTI and ensuring that key milestones were met it was their responsibility to develop software for the man-machine interface (MMI) and to conduct market research. **University of Strathclyde** (Glasgow) were involved in developing and testing the elastomer materials used. It was their responsibility to evaluate the swelling response of samples. They are the patent holders for the water sensor, *Hydrofast*, which was the precursor to the DISH sensor. **Optosci Ltd.** (Glasgow) were responsible for the development of the optoelectronic hardware which includes the light source, detector, controlling software and data processing. **Pinacl CSL**

(Rhyl) were responsible for the manufacture and development of the sensing element itself, the sensing cable. Manufacturing machinery was purchased from Roblon of Denmark and installed in the factory solely for development of the DISH sensor. Evaluation and testing of the sensor element as manufactured at Pinacl was carried out both in house (at Pinacl) and at the chemistry department of the **University of Wales, Bangor.**

2.1.2 Target hydrocarbons and applications

The DISH sensor is targeted at the petrochemical processing, storage and distribution industries including those which use hydrocarbon fuels in the automotive, aviation and shipping industries. The sensor could be used to monitor the integrity of storage tanks and their interconnecting pipe networks both on terrestrial and marine installations as well as in double-skinned tankers around the world's oceans. Continuous monitoring of fuel lines in aircraft, both commercial and military, would allow the development and installation of comprehensive bypass systems to isolate damaged sections before ignition or explosion could occur. The sensor could be adapted to monitor different feedstock pipelines in a chemical plant so providing a complete leakage detection system for all the fluids used. Pipeline and fuel-line integrity monitoring systems currently in use are generally based on a network of pressure monitors which detect changes in hydraulic pressure within the pumped systems and thus infer where leaks must be occurring. The DISH sensor aims to eliminate the time delay involved in locating damaged sections by identifying leaks to within a metre, in real time, thus allowing a more rapid response to potentially hazardous leaks. Hydrocarbon liquids from across a broad spectrum of activities were used to evaluate the sensor and its responses. Table 2.1 (overleaf) describes the fluids used, their respective compositions and their origins and applications.

Fluid	Fraction & source	Boiling point range	Typical constituents / additives	Uses	Ref
Unleaded motor spirit	Light gasoline & naptha fractions; blended fluid	30 – 220 °C	C4 – C10 hydrocarbons; detergents, dyes & antiknock compounds (<0.1 %); 'oxygenates' *e.g.* EtOH (5 %), MeOH (3 %), methyl t-butyl ether (15 %).	Fuel for spark ignition internal combustion engines.	4
Lead replacement petrol	(as above)	(as above)	C4 – C10 hydrocarbons; detergents, dyes & alkyl lead compounds (0.03 – 0.19 %)	(as above)	4
Supergreen	(as above)	(as above)	As for LRP; octane-rating improving additives	Pre-1986, high octane rating internal combustion engines	5
ULS Diesel	Gas oil fraction (heavy middle distillates)	163 – 357 °C	Crude mix of C9 – C20 hydrocarbons; obtained by 'straight run' distillation of gas oil	Automotive diesel fuel.	6
Gas oil	Gas oil fraction (heavy middle distillates)	150 – 450 °C	Highly complex mixture of C11 – C25 hydrocarbons including paraffins, cycloalkanes, polycyclic aromatics, mixed aromatic cycloalkanes and olefins	Agricultural, railroad and marine diesel fuels. 68 possible gas oil products.	6
Aviation kerosene	Kerosene fraction (light middle distillates)	145 – 300 °C	C9 – C16 hydrocarbons including alkanes, cycloalkanes, alkylbenzenes, alkylnaphthalenes.	Commercial (non-military) Jet fuel.	7
Condensate	Gas oil fraction (vacuum distillation condensate)	205 – 400 °C	Complex mixture of C11 – C25 hydrocarbons;	Chemical feedstock and for blending with heavy fuel oils.	7
Fuel oils	Blended from heavy distillation residues and gas oils	350 – 650 °C	C20 – C50, density > 1000 kgm^{-3}, complex heterocyclics, high MW asphaltenes and organometallics, upto 20 % 3 to 7 ring polycyclics	Fuel for industrial plants, ships, power stations in boilers, furnaces and engines.	8

Table 2.1: Description of the hydrocarbon fluids used together with their respective compositions, origins and applications.

2.1.3 Distributed microbend sensors

Sensors based on the principle of induced microbending losses operate by encasing an optical fibre within a device or stucture that will provide a periodic mechanical stress to the fibre at either single, multiple or continuous regions along its length. The applied periodic stress induces the formation of multiple small bends (microbends) in the fibre which in turn cause a periodic perturbation at the core-cladding interface. This perturbation causes guided modes within the core to be coupled to radiative modes in the cladding which are subsequently lost from the fibre.This power loss can be monitored in one of two ways. Simple measurement of the throughput power, *i.e.* the ratio between the launched and received powers requires access to both ends of the fibre and will involve calibration procedures to reference the detector to the source. Figure 2.0.1 illustrates this set-up.

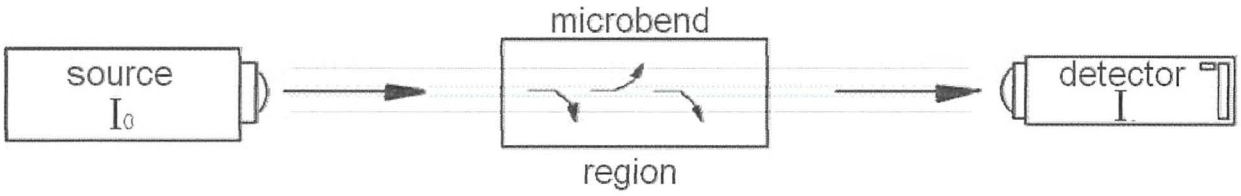

Figure 2.0.1: Microbending loss measurement.

This first type of microbend sensor will enable a point loss to be calculated, that is, there is no way of knowing where along the fibre the losses are occuring and therefore will prevent identification of the precise location of the chemical species. This does not present any problem when designing point sensors where short lengths of fibre are used in a handheld or probe form. When wishing to gain information on the spacial distribution of an analyte it is necessary to use the second type of microbend system, a distributed system. In this situation, optical time domain reflectometry (OTDR) is the detection mechanism. In OTDR both the source and detector are at the same end of the fibre. The basic principle of this technique is that pulses (typically between 20 and 200 ns) of light are launched into the fibre, and the time taken for the backscattered light from that pulse to return to the detector is calculated.

As Rayleigh scattering occurs at every point along the fibre core, the returning pulse is considerably longer than the initial pulse. As the speed of light in the fibre and the time since the pulse was sent are known, it is a simple matter to calculate the distance along the fibre from where the received light was scattered. This calculation combined with the measurement of the intensity of the returning light enables the plotting of a graph of received power *vs* length. The trace should be linear if the fibre core is homogenous along its length, and has a negative slope as can be seen in figure 2.0.2.

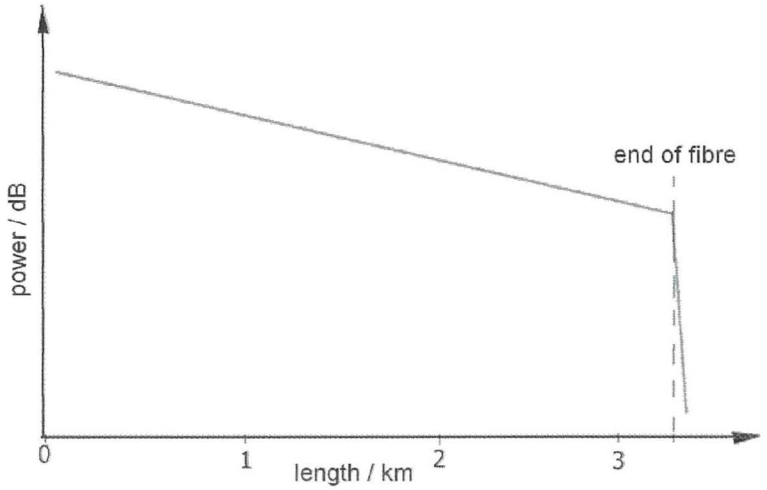

Figure 2.0.2: OTDR trace showing end of fibre as sharp drop-off of backscattered light.

The negative slope is due to the continuous loss of power along the fibre by scattering and absorption which causes the travelling pulse to gradually diminish in power and thus the Rayleigh scattering from further along the fibre has lower intensities. The end of the fibre is clearly seen by a sharp drop in power. Any losses in the system will be visible as steps in the trace. The slope before and after the step will have the same gradient as the fibre is unchanged. Multiple steps are possible and will show where loss is occuring along the fibre length. OTDR techniques are routinely used in the telecommunications industry to check whether cables have been installed correctly and to identify breaks or damage to the fibre system.

Figure 2.0.3 shows the trace that would be observed for losses occuring at 1 km, 2 km and 3 km lengths along the fibre.

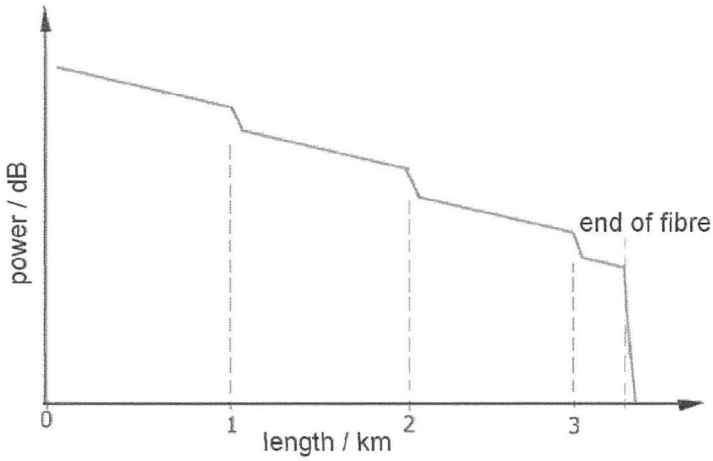

Figure 2.0.3: OTDR trace showing loss events at 1, 2 and 3 km.

The mechanisms by which a chemical or physical change can induce these losses into a fibre are many and varied [9-19]. The simplest mechanism involves crushing the fibre between plates which contain ridges at a period that will induce microbends to form when the plates are squeezed together. A coil of fibre placed between two such plates would form the basis of a pressure sensitive sensor. In figure 2.0.1 (above) the central section of the diagram was simply marked "microbending region". The reason for this is that the mechanism by which microbending is induced into the fibre by a measurand of interest varies greatly [9-21]. The closest that is possible to a generic design was discussed by Lagakos *et al* [22]. They describe the "microbender" as a fibre sandwiched between two plates. The plates are covered on their inner faces by ridges of a certain amplitude and separation such that when the two plates are squeezed by an external force the fibre is bent periodically. This design has been integrated into numerous pressure sensors in such devices as burglar alarms and slippage sensors. A variety of other structures can be used. The simplest of which is a variation of the "generic" structure. Patented by Grossman [23], this sensor was designed for vehicle monitoring. A simple cable structure containing ridged tapes transferred a periodic force to the central fibre each time a vehicle compressed the cable structure.

Capable of "distributed" (*i.e.* over a length rather than at a point) measurement, a precursor to the DISH sensor was designed [1-3] to detect water and monitor pH in an aqueous environment. This sensor, named Hydrofast, has a structure similar in design to the DISH construction, the principle difference being a water swellable hydrogel material in place of the hydrocarbon sensitive elastomers used in the DISH sensor. Thus the DISH structure has promise of application to many analytes. The only requirement being a polymer that will swell in the presence of the required analyte. A 1991 patent filed by Bergqvist [24] describes a microbend temperature sensor that involved a central structure which expanded with temperature, an axially laid fibre optic and a helical wire bound at a critical periodicity. Donlagic and Culshaw, have published results [25,26] that suggest another possible modification to the microbending sensor. It is reported that by splicing a length of singlemode fibre between the launch optics and the microbend sensor it is possible to launch only the fundamental mode into the multimode core, *i.e.* only the zero order mode is present. It is reported that this brings down the dry attenuations to less than 1 dB km^{-1}. The "dry attenuation", usually quoted in dB per km, is defined as the loss per unit length of a fibre in its dry state (*i.e.* not wetted with an analyte hydrocarbon liquid). "Wet loss" is thus the loss induced when the sensor is exposed to an analyte. It is also reported that as the zero order mode is more microbend sensitive than the other modes the loss induced by a given applied periodic force may be up to six times the loss induced if the multimode fibre is fully filled.

2.1.4 The DISH sensor

For distributed sensing, a cable that incorporates a ridged structure or similar and some means of applying pressure to the ridges and fibre in the presence of an analyte such as a swellable polymer will form the basis of a chemical sensor. The DISH sensor is an example of this.

One of the components of the DISH sensor is a fibreglass reinforced plastic (GRP [27]) rod. This rod is present to provide mechanical strength to the sensor cable both under strain and under compression. It also provides a solid substrate against which the expanding elastomer can exert a force thus ensuring that the forces associated with the swelling polymer are transferred to the optical fibre.

The rod itself contains large numbers of fine glass fibres embedded in a thermosetting resin. It is these fine glass fibres that take any strain in the cable and the resin which gives compressive strength. A diagram of the structure of the coated GRP rod is shown below in figure 2.0.4.

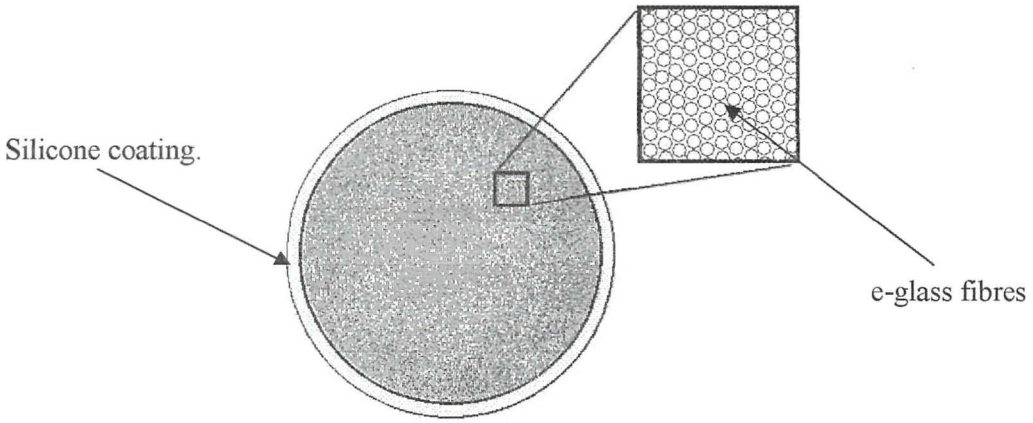

Figure 2.0.4: Diagram of a cross-section of a silicone coated GRP rod. The inset box represents a 100 μm x 100 μm area containing glass fibres with a diameter of 10 - 15 μm.

The GRP rod is coated with a thin layer of a polysiloxane elastomeric material that is designed to swell in the target liquid. Polysiloxanes (silicones) have the general structure [27-30] shown in figure 2.0.5.

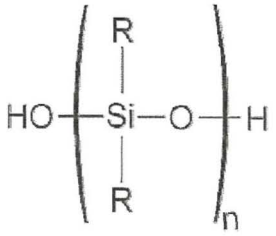

Figure 2.0.5: General structure of silicone elastomers [27-30].

The simplest silicone is polydimethylsiloxane (PDMS) where the siloxane chain has the general structure shown [28,29] in figure 2.0.6 where n typically lies in the range 3000 to 5000.

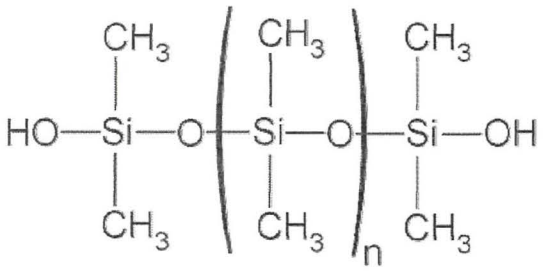

Figure 2.0.6: General structure of polydimethylsiloxane [28,29].

Early syntheses were carried out by the hydrolysis of dichlorodimethylsilanes as shown [28-30] in figure 2.0.7.

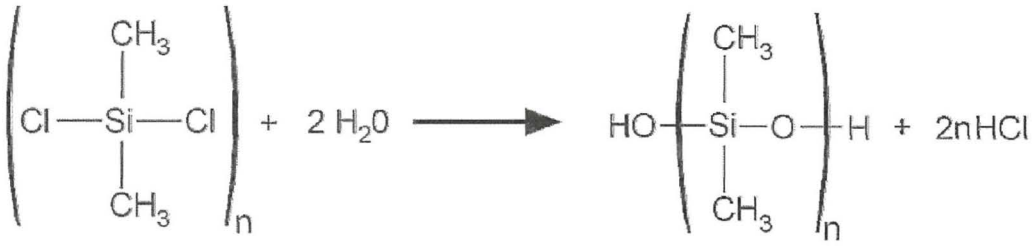

Figure 2.0.7: Production of PDMS by hydrolysis of dichlorodimethylsilane [28-30].

Modern syntheses are carried out by ring opening and subsequent polymerisation of cyclic polysiloxanes.

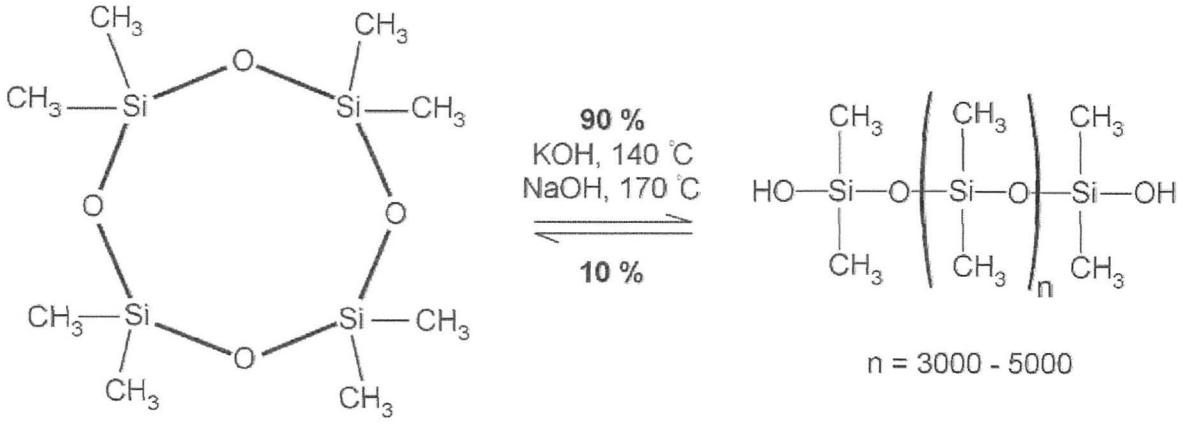

Figure 2.0.8 Base catalysed ring opening and polymerisation of octamethylcyclictetrasiloxane [29,30].

The base catalysed ring opening of octamethylcyclictetrasiloxane (figure 2.0.8) is reversible and at curing temperatures up to 200 °C the equilibrium lies 90 % towards the polymerised chains [29,30]. At temperatures in excess of 200 °C the polymer chains are broken as the equilibrium moves towards the cyclic species. In the case of the Dow Corning elastomer used in the DISH sensor (designated 'EP4412') the equilibrium lies such that less than 5 % of the cyclic species are present. Silicones are by definition [27] relatively weak compared to more dense and higher modulus organic polymers. In order to improve the elastomer's modulus and tensile strength the polysiloxane chains are bound to each other, or crosslinked, using either chemical or physical interconnections, such that irreversible sliding of chains past each other is prevented [27]. This is achieved either by periodically attaching large, bulky groups to the chain which inhibit free movement of the chains, or by chemically binding chains to each other. Chemical binding can be achieved in a variety of ways. Hydrosilylation [27,31] involves attaching pendant vinyl groups to one in every 50 to 100 silicon atoms on half of the chains and inserting silicon hydrides at the same frequency on other chains. In the presence of Pt catalysts at temperatures in excess of 60 °C, these react with no loss in mass [31] forming permanent linkages between neighbouring chains and establishing a network with greater tensile strength and modulus than the equivalent uncrosslinked elastomer. Alternatively [27], it is possible to react pendant alkoxy groups with neighbouring silanol groups in the presence of organo-tin catalysts. The strength of crosslinked silicones can be further improved by the addition of other materials to the elastomer mix. It is common to find a large suite of additives and fillers present in any silicone product [5,27-29]. Fillers are used to increase the batch viscosity and artificially increase the density and modulus (strength) of the material. The addition of calcium carbonate or precipitated silica to polysiloxane rubbers is a common practice and may account for 20 % or more of the volume of some elastomer products [27-29].

The addition of silica fillers can increase the tensile strength of silicones by a factor of 40, from 0.34 MPa for an amorphous, uncrosslinked elastomer up to 13.8 MPa [29] in cases where strong filler-polymer bonding exists. Bonding between fillers and polymer chains can be both physical or chemical in nature. For silica filling materials, Van de Waals bonds exist together with hydrogen-bonding of silica silanol groups with polymer silanol groups and chain oxygen atoms [29]. Fillers increase the viscosity of the uncrosslinked elastomer such that plasticising additives are required to improve 'processability'. These plasticisers vary in nature. Hydrocarbon oils, mostly mixtures of paraffins, napthenes and aromatics may be used. In addition vegetable oils, coal-tar and pine oil products may be found. Paraffins (mixed alkanes) have a tendency to bleed out and so are used in only small amounts. Napthenic process oils are compatible with most elastomers as are aromatic oils which due to their excellent compatibility are the most widely used product [27].

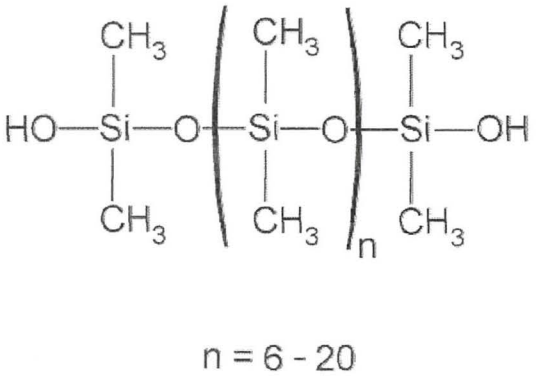

Figure 2.0.9: Structure of a short chain, low molecular weight silicone liquid plasticiser [29].

In silicone elastomers where high surface area siliceous particles are added, a low molecular weight silicone with chain length of less than 25 (figure 2.0.9) may be used as a plasticising liquid which exists as a free liquid within the elastomer's network [29,32]. In the DISH sensor an optical fibre is laid alongside the elastomer coated rod. The fibre and the coated rod are bound to each other such that they are held together firmly but not crushed. Figure 2.1.0 illustrates the basic structure of the sensor.

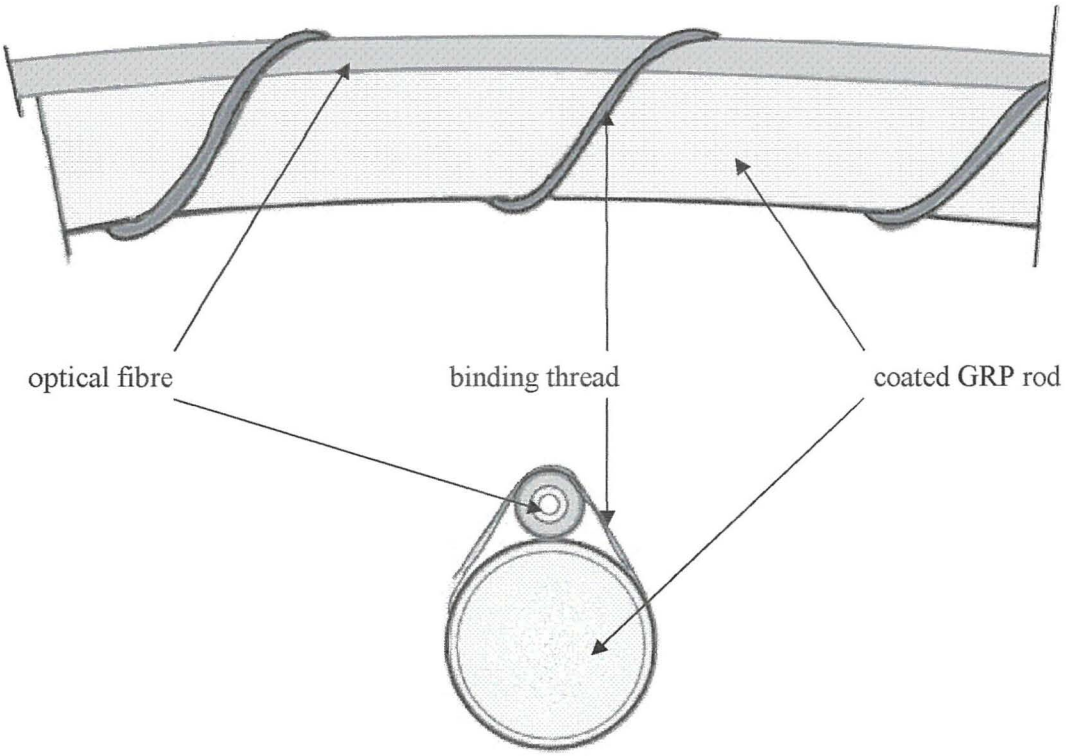

Figure 2.1.0: Structure of the DISH sensor showing longitudinal (top) and cross-section (bottom) views of the coated GRP rod, optical fibre and binding thread.

The fibre lies alongside the coated rod and is held in place by a binder thread. This binding is set at a critical deformation period which will cause maximum microbending losses by coupling guided modes to radiation modes which are subsequently lost from the cladding. This will be further discussed in subsection 2.2. The operating principle of the DISH sensor is relatively simple. When the sensor comes into contact with a hydrocarbon liquid the hydrocarbon is absorbed into the elastomeric coating. This is illustrated in figure 2.1.1.

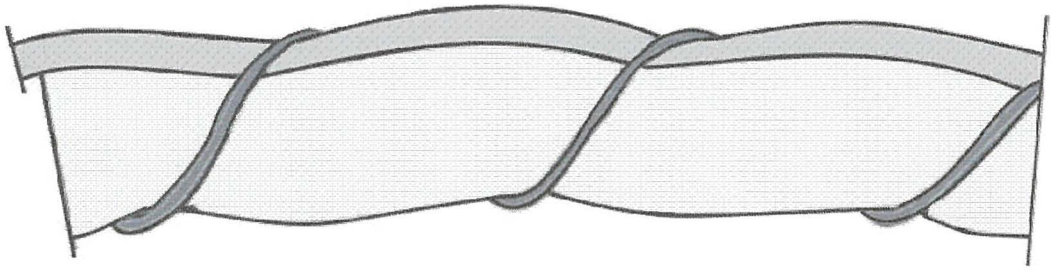

Figure 2.1.1: Structure of the DISH sensor in its swollen state after wetting with a hydrocarbon liquid.

The elastomer swells as a result of the absorption of liquid and this volumetric expansion deforms the fibre. Only that portion of the fibre which is unbound can move with the expanding rubber, thus the fibre experiences a periodic deformation along its length such that the guided modes within the fibre are coupled out of the core and into the cladding where they are attenuated. This microbending loss is detected by OTDR monitoring as described previously. The step which is induced in the OTDR trace can be difficult to distinguish from the noise in the signal and so as to facilitate easy identification of the step two traces are used. A background or reference trace is recorded and subsequent traces are compared with the reference by superimposing the two traces. Additional features will be seen on any OTDR trace. Spikes will be seen in the trace at the beginning and end of the sensors where strong reflections from the face of the sensor core and the distal tip cause higher than average backscatter. These features are shown in figure 2.1.2.

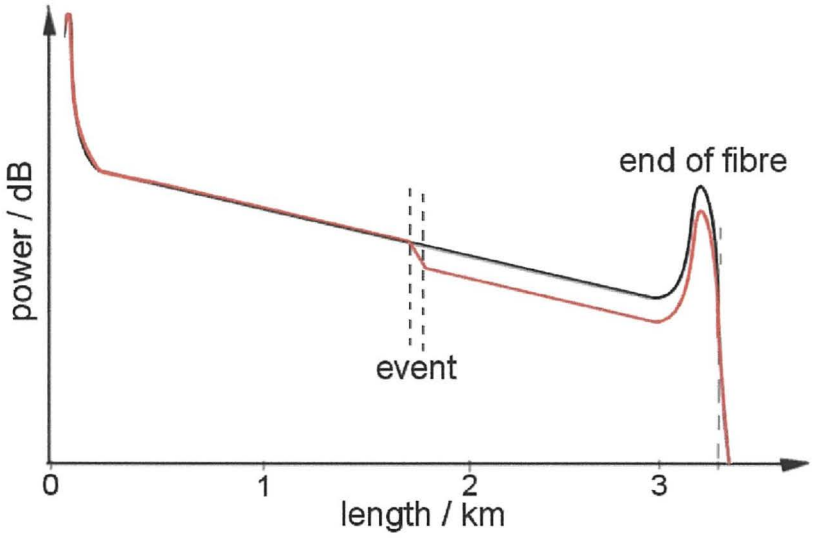

Figure 2.1.2: Illustration of a typical OTDR trace showing the appearance before (black) and after (red) an event has been detected.

The detection of events in this way is illustrative of the way in which manual testing of the assembled sensors is carried out. Detection of events in the integrated system works by software manipulation of raw data obtained from the custom OTDR unit and is displayed as a simple alarm readout on a laptop computer (figure 2.1.3 overleaf).

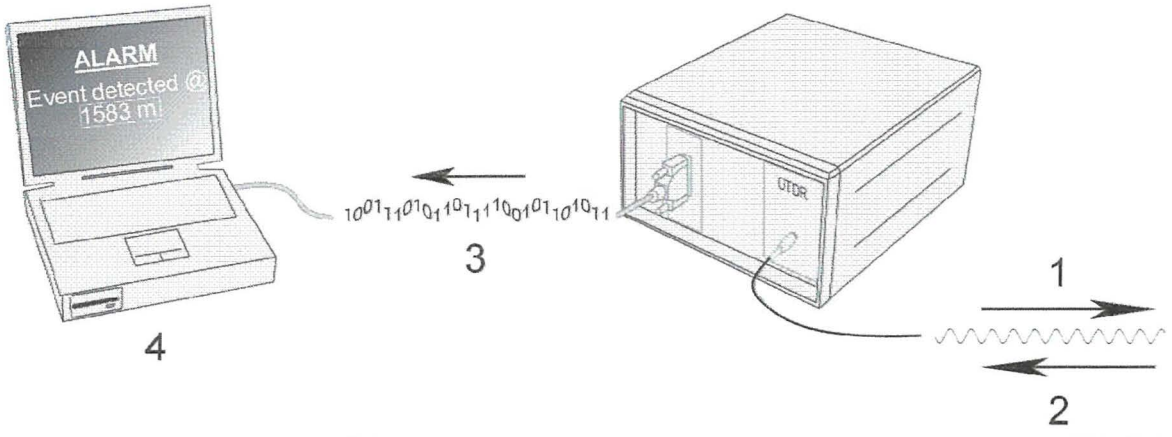

1:	OTDR launches a pulse of near-infrared light along the sensor fibre.
2:	Backscattered light returns from fibre and is detected in the OTDR unit.
3:	Power and time data is transmitted in its raw form to the analysis software.
4:	Custom software inspects data for events by identifying differences between new data and a stored reference trace. Any differences are further distinguished by differential analysis. Events with amplitude exceeding a preset trigger level are reported as detected events and the location, in metres, is displayed on screen.

Figure 2.1.3: Order of operation of integrated sensor system, by which events are detected.

Silicones have a characteristically poor resistance to hydrocarbon solvents [27,29] due to this swelling response. The swelling of silicones and elastomers is a well-known phenomenon [5,29,31-34]. The expansion results from passive diffusion of solvent molecules across a diffusion gradient into the matrix of the silicone where they become associated with the polymer chains [34] *via* loose interactions. The swelling response may be thought of as partial dissolution of a polymer by a solvent. The long chain molecules of linear or branched polymers will interact with solvent molecules, causing coil expansion from an unperturbed state. In the case of un-crosslinked polymers the chains may become completely disentangled and a homogeneous solution would result. However, in the case of crosslinked materials this is not possible and swollen states are obtained. In general, the dissolution (swelling) of polymers is energetically favourable as typical polymer solutions show large positive deviations from ideal behaviour,

thus ensuring that the free energy of mixing is large and negative. Deviations in entropy are attributed [35,36] to size differences between solvent and polymer molecules, *i.e.* the movement of individual polymer chains is severely impeded by neighbouring chains in the solid state. In the solution state the restrictions are removed and thus the chain is in continual motion and able to adopt a vastly increased number of equi-energetic conformations hence an increased entropy contribution. Deviations in the enthalpy term are caused by solvent-polymer interactions and may be estimated by consideration of solubility parameters. Solubility parameter is related to the cohesive energy density (**CED**) which is in turn related to the molar energy of vaporisation, **E**, and the molar volume, **V**:

$$\delta = (E/V)^{1/2} = (CED)^{1/2}$$

The enthalpy term, $\Delta\mathbf{H}$, for a particular solvent/polymer pair may be related to the solubility parameters of solvent and polymer by [35]:

$$\Delta\mathbf{H}_{mixing} = (\delta_{solvent} - \delta_{polymer})^2 (\mathbf{V}_{solvent})(\Phi_{polymer})$$

where $\Phi_{polymer}$ is the volume fraction of the polymer. Compatible mixtures will have similar solubility parameters and thus small $\Delta\mathbf{H}_{mixing}$. Thus with a small positive enthalpy contribution and a large positive entropy term, the free energy of mixing is large and negative. The solubility parameters of liquids are readily calculable from vaporisation energies as explained above, however those of polymers must be obtained by comparative techniques. It is generally agreed [29,32-34] that the swelling response will continue until the forces arising from the cohesion of the polymer chains balance the osmotic pressure [34] and the extent of swelling depends upon the relative hydrophobicity/hydrophilicity of the solvent and polymer [38-41]. It is also thought that the structure and density of the elastomer must be taken into account by consideration of the effective chain density [32], the 'polymeric free volume' [37]and the void

microstructure [34]. The viscosity of the solvent also affects the rate of expansion [33]. Predictions of the percentage expansion may be performed by consideration of solubility parameters [29,33] or by definition of a polymer-solvent interaction parameter [32]. However, it is emphasised by Doig *et al.* [33] that the relationship is not simple; that significant errors are often found between theoretical calculations and physical measurements. It is further emphasised that if physical measurement allows simple and accurate determination of the degree of expansion for a particular solvent-elastomer pair, then the usefulness of theoretical prediction is questionable [33]. The presence of hydrogen bonding between solvent and polymer will further complicate the system [42,43]. A hydrogen bonding index, γ, aids in the prediction of compatibility. For example, acetone and carbon disulphide have identical high solubility parameters but have very different γ (9.7 and 0.0 respectively). Hydrogen bonds will, in general, result in the enhancement of the solubility of polymer chains in a particular solvent. Flory Huggins theory [35-42] can provide an accurate prediction of swelling but only for a limited number of cases.

2.2 Experimental

2.2.1 Manufacture of sensor cable & selection of components

The central strength member used was a 0.9 mm diameter, commercially produced, fibreglass reinforced rod. A suitable silicone material was identified after exhaustive testing [44]. This elastomeric coating was Dow Corning Silastic EP4412, a one part, addition cure silicone designed specifically for ease of coating. The one part block, as purchased, is a mixture of several components. The curing reagents contained within the block are inactive due to the presence of an inhibiting agent which must be removed before curing will commence. In order to apply a thin coating of EP4412, the silicone precursor may be dissolved in an appropriate solvent (methylethylketone or xylene), to make a 15 – 25% by volume solution. The item to be coated can then be dipped into the solution and withdrawn. The coating thickness is controlled by the speed of withdrawal from the coating solution and by the choice of solution concentration. To cure the applied coating, the dipped item must first be heated to between 50 and 70 °C to drive off the solvent before a second heating stage (up to 170 °C) is employed to drive off the volatile inhibitor and allow the curing agent to act. A second silicone coating, Varflex, reportedly similar to the Dow Corning elastomer was also tested. It is possible that the Varflex silicone contained substantial amounts of silica or calcium carbonate filler as a fine white powder was detected on the surface of the silicone which had an opaque appearance unlike the transparent EP4412 [5]. Telecommunications grade, multimode optical fibres were chosen due to their relatively low cost compared to specialist fibres, their good availability and the lower cost of the optoelectronics required. Fibres from several different manufacturers and of differing quality were chosen to enable identification of the best performing grade and type. Two main classes of multimode fibre exist with core dimensions of 50 and 62.5 μm, and both were used in manufacturing trials to ascertain the most appropriate choice. The two fibre types were labelled as 50/125 or 62.5/125 to denote

the core and cladding diameters. Early sensor prototypes incorporated fibres used straight off the reel from the manufacturer without additional coating. These fibres had a thin coating of acrylate material which brought the final fibre diameter up to 250 μm. The UV cured acrylates provide mechanical protection from compression or abrasion and prevent water ingress into the fibre. It also serves to maintain a degree of flexibility to the fibre which is lost after removal of the acrylate. The generalised structure of an acrylate polymer is shown in figure 2.1.4 below.

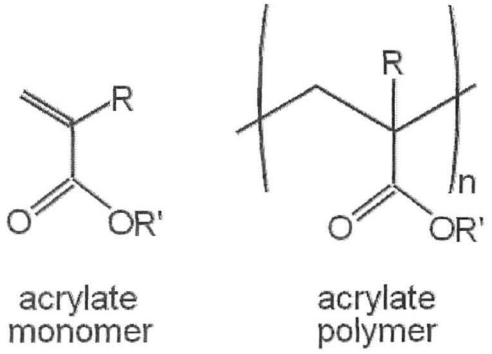

Figure 2.1.4: General structures of acrylate monomer and acrylate polymer.

In addition, the acrylate aids in the removal of very high order modes from the cladding by a process known as mode stripping. This is important in the control of dispersion effects. As the acrylate has a refractive index greater than that of the cladding, any optical modes propagating within the cladding and striking the cladding-acrylate interface will be refracted out of the fibre. Figure 2.1.5 shows the refractive index profiles of multimode fibres.

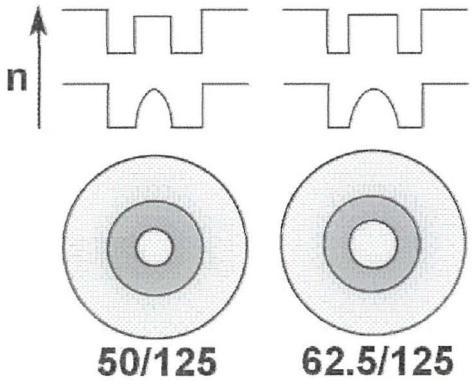

Figure 2.1.5: Illustration of the refractive index profiles of multimode optical fibres. The profiles for stepped index and graded index fibres are given for both 50/125 and 62.5/125 fibres.

Later prototypes incorporated fibres that had been coated with thicker layers of protective polymeric materials used in telecommunications cabling. These coatings were of varying thickness, typically 450, 600 or 900 μm outer diameter. The sensor was bound at a pitch that gave a period equivalent to the calculated fundamental period for microbending. Binding was also carried out at the 1st, 2nd, 3rd and 4th harmonics as it has been shown [47] that multiples of the fundamental period will also result in coupling of guided modes. The calculations for both 50/125 and 62.5/125 optical fibres are shown in box 2.1 below.

$$\text{Critical period, } \Lambda_c = \frac{2\pi\, a\, n_1}{NA}$$

$$\text{Numerical Aperture, } NA = (n_1^2 - n_2^2)^{1/2}$$

50/125	**62.5/125**
n_2 (cladding) = 1.457 n_1 (core) = 1.472 core radius, a = 25 μm	n_2 (cladding) = 1.457 n_1 (core) = 1.487 core radius, a = 31.25 μm
$NA = (1.472^2 - 1.457^2)^{1/2}$ $= 0.210$	$NA = (1.487^2 - 1.457^2)^{1/2}$ $= 0.297$
$\Lambda_c = \frac{2\pi\, a\, n_1}{NA} = 1101$ μm	$\Lambda_c = \frac{2\pi\, a\, n_1}{NA} = 983$ μm
$\therefore \Lambda_c = \mathbf{1.1\ mm}$	$\therefore \Lambda_c = \mathbf{0.98\ mm}$

Box 2.1: Calculation of critical microbending periodicity for 50/125 and 62.5/125 fibres.

The thread used to bind the sensor together was a lightweight aramid yarn manufactured by Roblon of Denmark. The thread was applied helically to the sensor under controlled tension and lay length.

Binder tensions are quoted in units of grams-force, ğ, defined as the tension produced in a thread when a mass of 1 g is suspended vertically under the influence of gravity and equivalent to 0.00981 N. The binding was carried out at Pinacl Ltd, Rhyl.

To assess the rate of swelling of the silicone coated rods, samples (50 mm) were cut and their initial diameters were measured to sub-micron accuracy using a laser micrometer (Anritsu, Japan). Each sample was immersed in a flask of a particular hydrocarbon liquid and removed at time intervals of 1 minute to observe increases in diameter. The data was tabulated for each liquid and curves were plotted of total diameter *vs.* time. Samples of coated rod were placed in vials (25 ml) containing samples of hydrocarbon liquids in order to investigate the resistance of the silicone coatings to petrochemicals. The rods were left for 7 days and then removed and scanning electron micrographs were recorded.

Sensors incorporating an acrylate covered (bare) fibre were developed and tested and were referred to as 'first generation' prototypes. Fibres which were sheathed with a protective polymeric coating (buffering) were then assembled into sensors which were developed and tested under the designation 'second generation' sensors. Subsequent to the successful development of buffered sensors, these were then further developed to optimise response to petrols and were referred to as 'third generation' sensors. Third generation sensors were installed in a series of field trials to test, demonstrate and integrate the combined monitoring system.

2.2.2 First generation prototypes – bare fibre sensors

Upon production of each prototype during the course of the development, the sensors were subjected to analysis by optical time domain reflectometry (OTDR). OTDR allowed a quick check of whether or not a fibre was undamaged along its length and allowed a length measurement to be made. The OTDR software allowed measurement of power losses at

marked events. For sensing applications, the OTDR could operate in real time, continually updating the trace. Alternatively, it could be operated in time-averaging mode over a prescribed time which considerably improved the signal to noise ratio. This was often used when only small differences were under scrutiny. In the case of the DISH sensor, changes in optical power of only 0.1 dB for a one metre event were expected. This represented a power loss of less than 2.5 % of the signal. Superimposition of a reference trace and a live trace allowed these small variations to be seen.

Immediately after manufacture, sensors were checked to ensure that no defects were caused during manufacture such as kinking or breaking of the fibre. An estimate of the dry attenuation of the fibre was made. The dry attenuation gave an indication of the condition of the fibre after assembly compared to that of the fibre before binding. A slight increase was expected dependent on the tension applied. The response of sensors was assessed on a test bench, designed so that the sensors could be left on their reels during testing. A one metre section of sensor cable was reeled off and fixed to the bench top. In all cases, a standard length of 1 metre was wetted with liquid. Figure 2.1.6 shows the setup of the test rig.

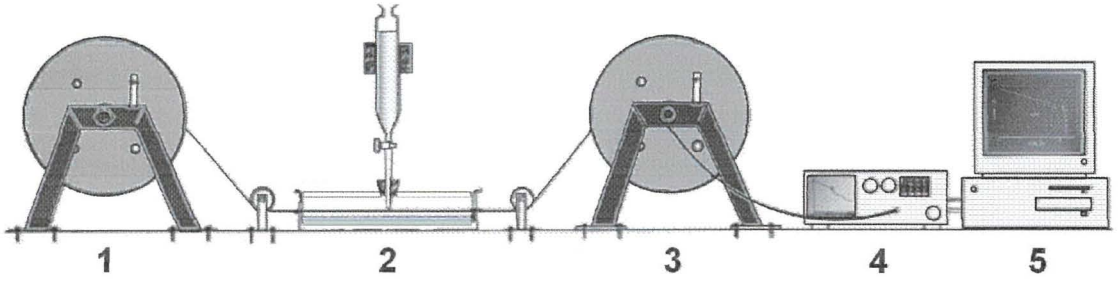

1: PAYOFF REEL – drum wound with assembled sensor cable.
2: EXPOSURE ZONE – region where 1 m of sensor was wetted with analyte.
3: TAKEUP REEL – reel to wind tested sensor onto.
4: OPTICAL TESTING HARDWARE – OTDR or power meter.
5: COMPUTER – for data recording and output.

Figure 2.1.6: Diagram of the test bench used to perform wetting tests and response analysis of manufactured sensor cables.

The test bench was used with either an OTDR unit or a data logging power meter. Throughput measurements gave more accurate assessment of sensor response time and the magnitude of the loss induced by wetting. When used with OTDR techniques, access to only one end of the optical fibre was required whereas with throughput power measurement methods it was necessary to connect to both ends of the sensor. For OTDR measurements the fibre was connected to a commercial OTDR unit (Antel, dual band, modular OTDR) and a reference trace taken. A 1 metre test length of sensor was wetted with a hydrocarbon liquid (typically unleaded petrol or lead replacement petrol) whilst a live trace was taken.

As the liquid was added, a time averaged trace was taken for between 30 seconds and 3 minutes. The presence of any loss events on the trace was recorded and an estimate of the size of the loss together with its location (in m) along the fibre was recorded for comparison with the known exposed position. Throughput measurements were performed on an EXFO IQ data logging power meter with two sources, a dual band LED source operating at 850 or 1300 nm for multimode measurements and a dual band LASER source operating at 1310 an 1550 nm for singlemode applications. The IQ unit had an InGaAs detector. Measurements could be taken in 3 formats: relative power measured in decibels (dB), absolute power measured in microwatts (μW) or absolute power in relative units called dBm, (defined as dB above 1 mW). The most commonly used systems were the relative methods (dB and dBm) due to their easy interconversion. Referencing to the power source, without the test fibre, *via* a standard fibre of known attenuation, allowed measurement of the loss induced in the fibre by external influences and gave an accurate measure of the attenuation of the fibre system under test. This in turn allowed precise measurement of the loss per unit length by combination with OTDR results; these values were quoted as $dBkm^{-1}$. Although the OTDR generated loss measurements they were approximations based on the gradients of the traces obtained.

Alternatively, the fibre was connected to the source and detector and a reference was taken with the fibre undisturbed and dry. Experiments were then carried out, monitoring the loss in the fibre whilst changes in temperature, pressure and humidity were applied or the sensor was exposed to physical deformations such as twisting, bending and straining or exposed to chemicals. Thus, with the use of data logging software, response curves were generated for a sensor fibre. Using the exposure testing rig shown above in figure 2.1.6, a 1 metre section of each sensor was exposed to petrochemicals whilst connected to a power meter, source and data logger. Readings were taken 10 times per second and a response curve plotted. Similar tests were also carried out using a hand held source and power meter.

Two sensors were assembled using bare multimode fibre of two grades in order to assess whether the quality of the optical fibre affected the response characteristics of the sensor. The recorded grade refers to the bandwidth at 850 and 1300 nm respectively. The two fibres used were Fibrecore 160/200 (lower grade) and Fibrecore 200/600 (higher grade). The assembled sensors were manufactured with a binder tension of 18 ğ and with a 4 mm lay length to minimise dry attenuation. A 50 μm EP4412 coated rod was used as the central strength member. Both sensors were exposed to unleaded petrol and their responses in each case were monitored by OTDR.

Because of concerns about the durability of the acrylate coating in the environment (with particular emphasis on water penetration) a bare fibre sensor was immersed in water whilst connected to the OTDR unit and the resulting trace monitored for signs of degradation. In addition, the acrylate coatings of the optical fibres used were assessed by immersion tests. Samples of multimode optical fibre were cut (50 mm) and immersed in vials (25 ml) containing assorted solvents and reagents. These were left for 24 hours before removal of the fibres. The appearance of the acrylate was recorded. A qualitative assessment of how easily the acrylate could be removed from the fibre was performed.

2.2.3 Second generation – buffered fibre sensors

As before, all response tests were performed using a standard length (1 metre) of sensor. As a result of concerns about the physical strength and chemical resilience of the bare acrylate fibres it was decided to investigate the use of buffered optical fibres. Buffering or coating of optical fibre with plastic materials is used in the telecommunications industry to protect fibres from mechanical damage. The acrylate had been shown to deteriorate in under 24 hours in the presence of petrol. Multimode fibres were extrusion coated with Hytrel, a DuPont block copolymer of short-chain diol erephthalate and long-chain polyether diol terephthalate [45]. Hytrel is designed specifically to resist chemical attack and has no extractable plasticiser. A 325 μm coat of Hytrel was applied over the acrylate layer to give a total external diameter of 900 μm. A thinner coat of 175 μm was also used which gave a total outer diameter of 600 μm.

An experimental layer, 100 μm thick was attempted giving a total outer diameter of 450 μm. Figure 2.1.7 compares the appearance of the coated fibre sensors with that of the bare fibre sensors.

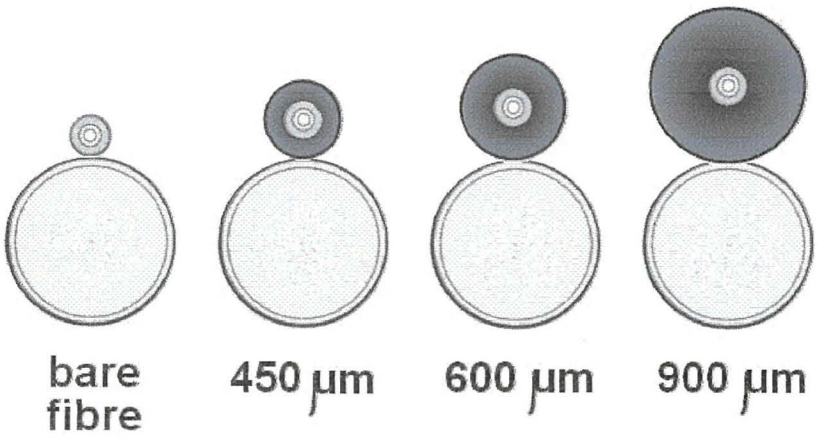

Figure 2.1.7: Relative dimensions (seen in cross-section) of a bare fibre sensor and buffered fibre sensors.

The response of buffered fibre sensors was assessed using both OTDR and throughput measurement methods. Dry attenuations were recorded before and after manufacture.

2.2.4 Third generation – petrol tuned sensors

Once a working design incorporating a buffered (and therefore protected) fibre had been established it was then necessary to tune the design to optimise its sensitivity to each analyte. Sensors for petrol detection were manufactured with varying tensions, lay lengths (binding periods), silicone type and coating thicknesses. These were assessed for dry attenuation, response to petrol, recovery after exposure and response to repeated exposure. Response testing of final tuned designs to other analytes such as solvents and other fuels was carried out. In order to determine the optimum operating conditions of the sensor and whether or not significant problems would be encountered in hot or cold environments the sensor was subjected to a program of environmental testing. This involved the live monitoring of a sensor whilst inside an environmental test chamber programmed to cycle temperature and humidity. The sensor was monitored using the power meter. A reading was taken every 10 minutes. Measurements using a broad spectrum, high intensity light source (Xe arc lamp, Oriel) and photodiode array detector were made of the absorbance characteristics of an assembled sensor from the near UV to near-infrared region. The detector was calibrated against a Hg emission source for the range 250 – 700 nm and a Ne emission source for the range 650 – 1100 nm. As shown in figure 2.1.8, a coil of optical fibre was placed into an oven and connected to the light source and detector. The detector was in turn connected to a personal computer with the controlling software (Instaspec Basic).

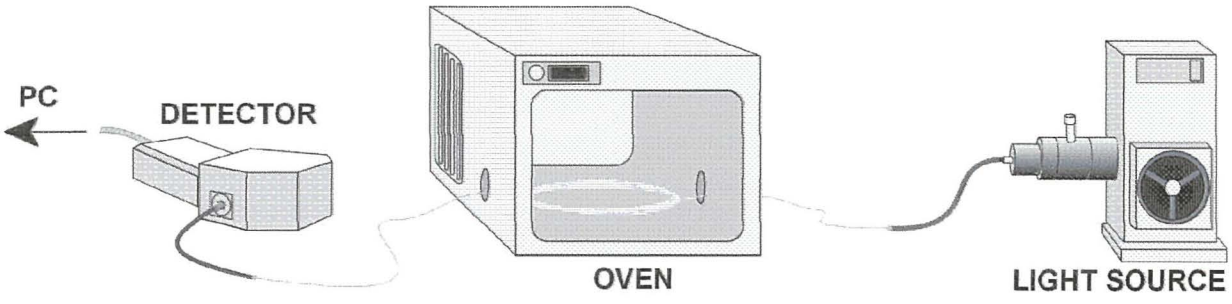

Figure 2.1.8: Bench setup for the UV-visible spectrophotometer analysis of optical fibre under an applied temperature regime.

Background traces were taken with the oven at room temperature and the light source off. A reference trace was taken at room temperature with the light source on. A continuous time series of traces was taken. 2000 accumulations were taken and combined additively to give each trace, every 35 seconds for 90 minutes. The oven temperature was ramped up to 85 °C over 30 minutes, kept constant for a further 30 minutes and then allowed to cool slowly for a further 30 minutes. The attenuation at 850 nm, relative to the reference was recorded from each trace. Further similar experiments were performed on other fibre samples and on lengths of assembled sensor.

Response tests were performed using an alternate setup which allowed the standard 1 metre length of sensor to be fully immersed in the analyte liquid. Previous tests had been limited to wetting and then covering a length of sensor. The new tests were performed with separate, handheld source (EXFO, FOS-124A, dual band LED 850/1300nm) and power meter units (EXFO, FOT-22A, Ge detector). These were connected to a sensor which was inserted into a coiled glass tube of total length 1 m. Figure 2.1.9 illustrates the setup used. The liquid under test was then poured into the tube and the response of the sensor with time was monitored.

A final, long term test was initiated whereby a Hytrel sensor of 50 m in length was coiled in a winchester bottle. The sensor was connected to the data-logging power meter (EXFO, IQ unit) and tap water was added.

Figure 2.1.9: Apparatus used to test the response of sensors that were fully immersed in analyte liquids. A handheld light source and power meter were connected to either end of a sensor cable. A 1 m length of sensor was contained in a glass coil which was filled with the liquid under test.

The power levels were recorded over 24 hours and the data trace plotted to observe fluctuations in the transmitted power. The sensor remained in the bottle for a further 18 months. Power readings were taken every 2 months for six months and then every 6 months thereafter.

2.2.5 Field trials

A field trial was setup in Tewkesbury, UK. A sensor system with a total length of 1.4 km was established by alternating 100 m lengths of third generation buffered petrol sensor with 100 m lengths of optical fibre cable (Meteor™, Pinacl). The sensor lengths were placed into 2 m troughs as shown in figure 2.2.0.

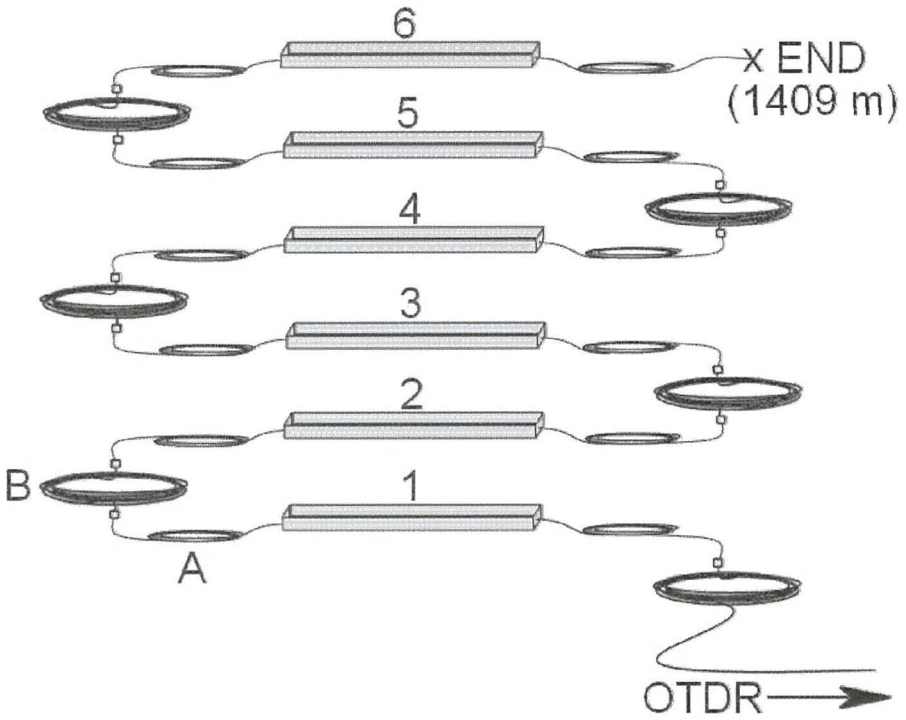

Figure 2.2.0: Diagram showing layout of Tewkesbury field trial. System comprised of six 100 m lengths of sensor cable with their central sections within a 2 m trough (numbered 1 to 6). Each length of sensor (A) was spliced to the next with 100 m lengths of outdoor optical fiber cable (B). A 250 m lead-in was attached at the front-end of the system. Total system length was 1.4 km.

Testing was performed with the commercial OTDR (Antel). Systematic testing of each trough in turn was performed by exposing the sensor within the trough to petrol. The magnitude of

the loss and the location in metres along the sensor was recorded. Blind tests were then performed. Troughs were selected at random and exposed, the response of the OTDR was monitored to see whether it was possible to determine which trough had been wetted.

A second field trial was established three months later in the grounds of Pinacl, Rhyl, Wales. A 400 m sensor was laid out across the ground and then left for 2 weeks exposed to the weather and to disturbance by animals. The sensor was tested in a different way to that performed at Tewkesbury. Portable troughs, 1.5 m in length and covered with a lid were used. The troughs were filled with dry, fine sand and the section of sensor to be wetted was buried to a depth of 1 cm. After wetting of the sand with petrol (250 ml) along the trough's length, the lid was fixed and sealed to prevent evaporation and the response of the sensor was monitored by OTDR.

This trial was the first time that the prototype custom OTDR and software was successfully used with a finished sensor design. The layout of the second trial is illustrated in figure 2.2.1 below.

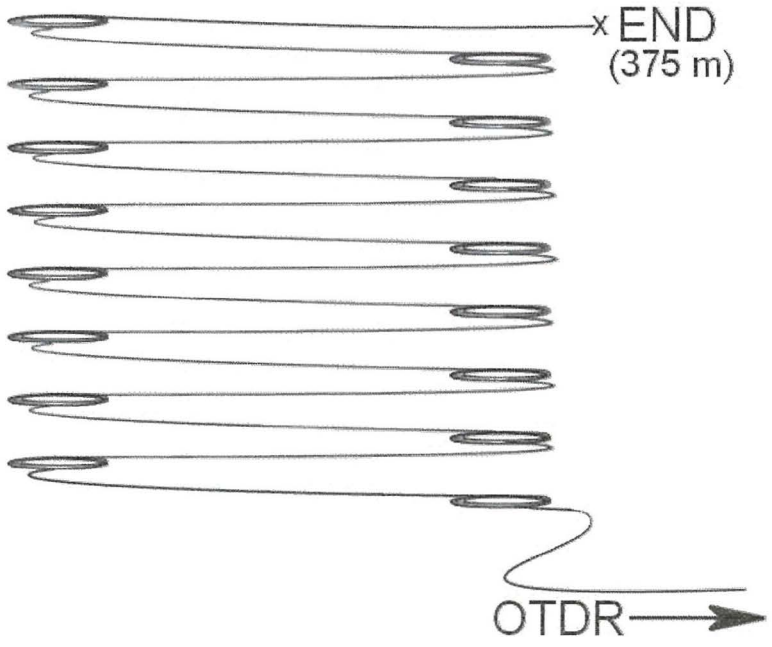

Figure 2.2.1: Diagram showing layout of first Pinacl field trial. System comprised a single 375 m sensor. The sensor was laid out in a field as shown with small coils inserted between 10 m straight lengths. A 1.5 m, portable, sand filled trough was moved to any point for response testing. The sensor was interrogated with both the Antel OTDR and the custom built unit.

A third field trial was set up at Pinacl using the same layout as in figure 2.2.1 above except that a longer sensor length was used. An optimised third generation petrol sensor of over 2 km in length was used, giving a total system length of 2500 m. The sensor was tested with petrol at varying distances along its length to determine the maximum operational range of the integrated system. The custom OTDR unit was used together with the custom-designed event detection software.

A final field trial was performed at Pinacl to test the combined system with a finished sensor design, the custom OTDR and the final user interface software. A single 400 m length of third generation petrol sensor was laid out so as to imitate a petrochemical storage depot. The layout of the depot was installed into the custom user interface and testing was performed at one of several locations along the sensor. Testing was performed within portable sand filled troughs. The display of the user interface was monitored to determine whether a correct alarm would be generated and whether the location would be calculated accurately. The system was also tested to see whether multiple events could be detected by simultaneously exposing more than one section of sensor. Figure 2.2.2 shows the layout used and the schematic installed in the analysis software.

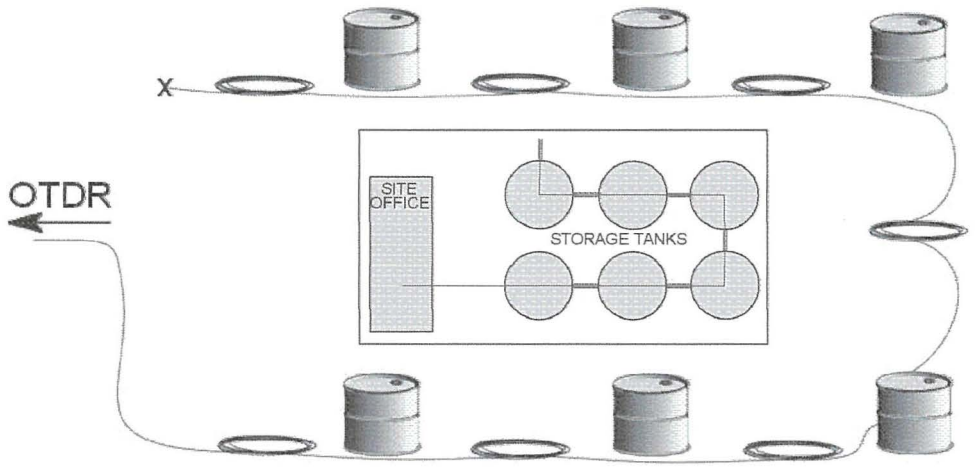

Figure 2.2.2: Diagram showing layout of second Pinacl field trial. System comprised a single 400 m sensor. The sensor was laid out to represent a petrochemical storage depot with six tanks. This layout was installed in the custom OTDR software as shown in the inset.

2.3 Results and discussion

2.3.1 Assessment of sensor components

The results of the swelling assessment for a rod with a 100 μm thick coating of Varflex rubber are displayed in figure 2.2.3. The rod had an initial total diameter of 1050 μm. The micrometer had a maximum measurable diameter of 1310 μm. Thus, it is not possible to infer to what degree the expansion continued after reaching 1310 μm.

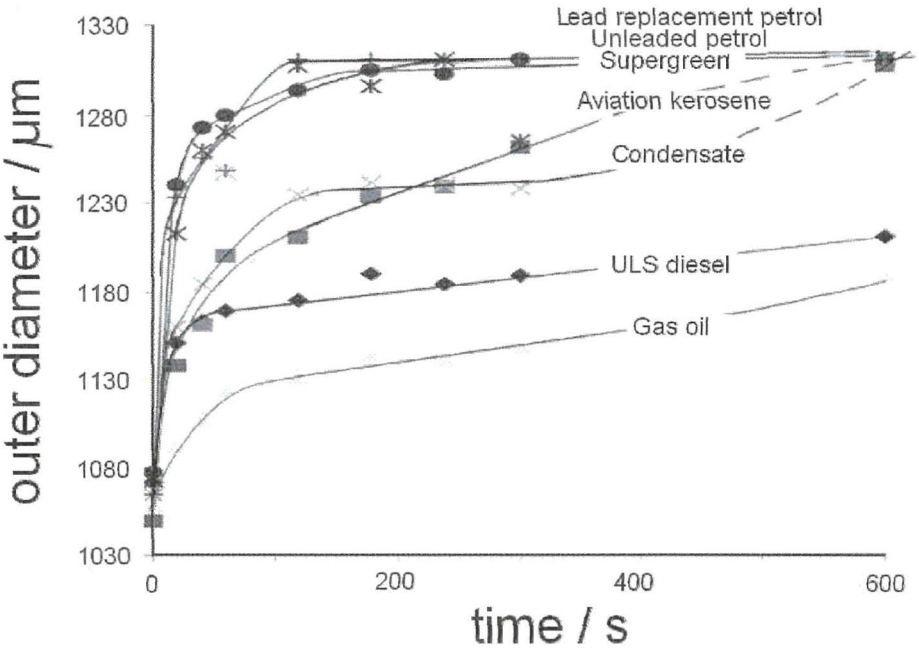

Figure 2.2.3: Results of swelling tests on a 100 μm thick coating of Varflex silicone.
NB: The y-axis shows total outer diameter of the coated rods. Percentage swellings quoted in the text refer to the increase in thickness of the elastomer coating itself.

The data suggest the Varflex rubber responds quickly to volatile liquids. The liquids can be divided on the basis of their responses into four categories. The petrols (unleaded, lead-replacement and supergreen) responded most quickly, achieving 50 % swell in 30 seconds and an increase in coating thickness relative to the original thickness of at least 120 %. Aviation kerosene and the condensate responded less quickly taking twice as long to reach 50 % swell but achieved a percentage increase equivalent to that of the first group, (120 %) within the same time frame. The third group consisted of only the ULS diesel, which achieved 50 % swell very quickly in under 30 seconds but only reached a percentage increase of 70 %.

Gas oil took considerably longer, in the region of 1 – 2 minutes, to reach 50 % swell and achieved only a 65 % increase in thickness.

The recovery of the Varflex coated rod (in still air at room temperature) was assessed to determine if the trend observed for the expansion held true for the recovery during drying. Figure 2.2.4 shows the recovery data obtained. Samples were left immersed in each fluid for at least 30 minutes to ensure maximum swell had been reached. It is important to note that all the samples have a starting swollen diameter of 1310 μm. This demonstrates that although the expansion data given in figure 2.2.3 previously show slow expansion for ULS diesel and gas oil, maximum swell is eventually achieved, within 30 minutes, in excess of 1310 μm outer diameter for ULS diesel and in excess of 1200 μm in the case of gas oil.

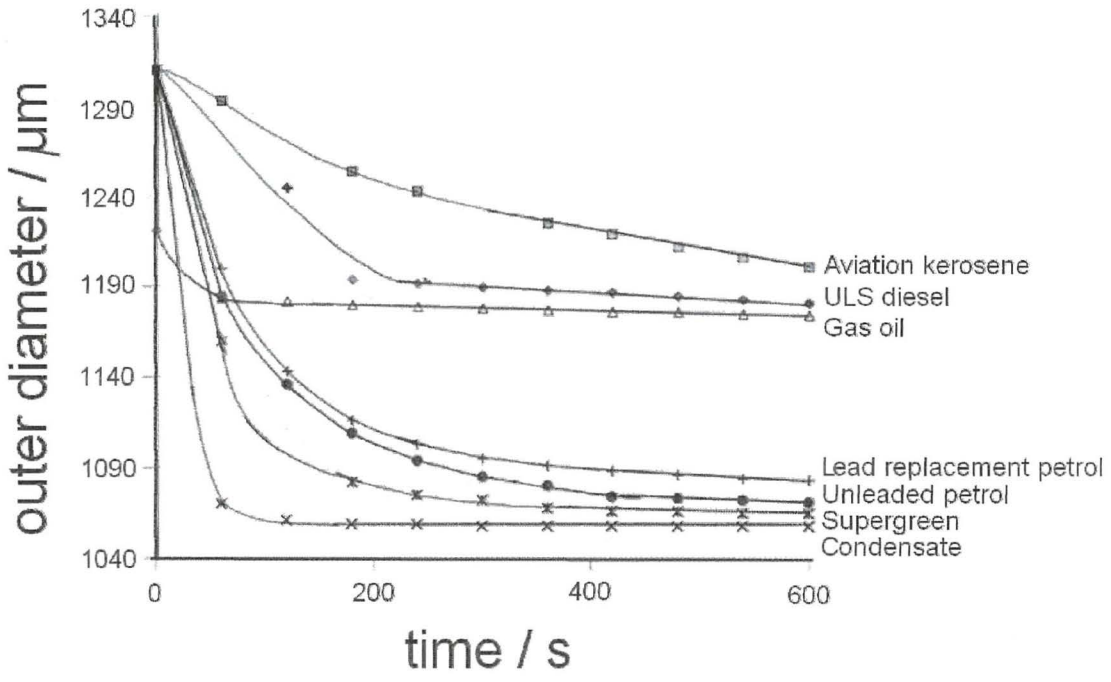

Figure 2.2.4: Recovery data for 100 μm thick coatings of Varflex silicone.

At first glance the recovery data fall into two distinct groupings with the petrols being the fastest to recover. Condensate was the quickest to return to its original dimensions, in under two minutes. A broad division into two groups based on whether or not the sample returned to its original dimensions results in two clear groups. ULS diesel, gas oil and aviation kerosene

did not recover completely and may require intervention to drive off all absorbed material. Washing with a lighter solvent such as petrol could aid the recovery by diluting the heavier material.

The results of the swelling assessment for rods with 50 μm thick coatings of EP4412 rubber are displayed in figure 2.2.5. Initial rod dimensions were between 1000 and 1010 μm.

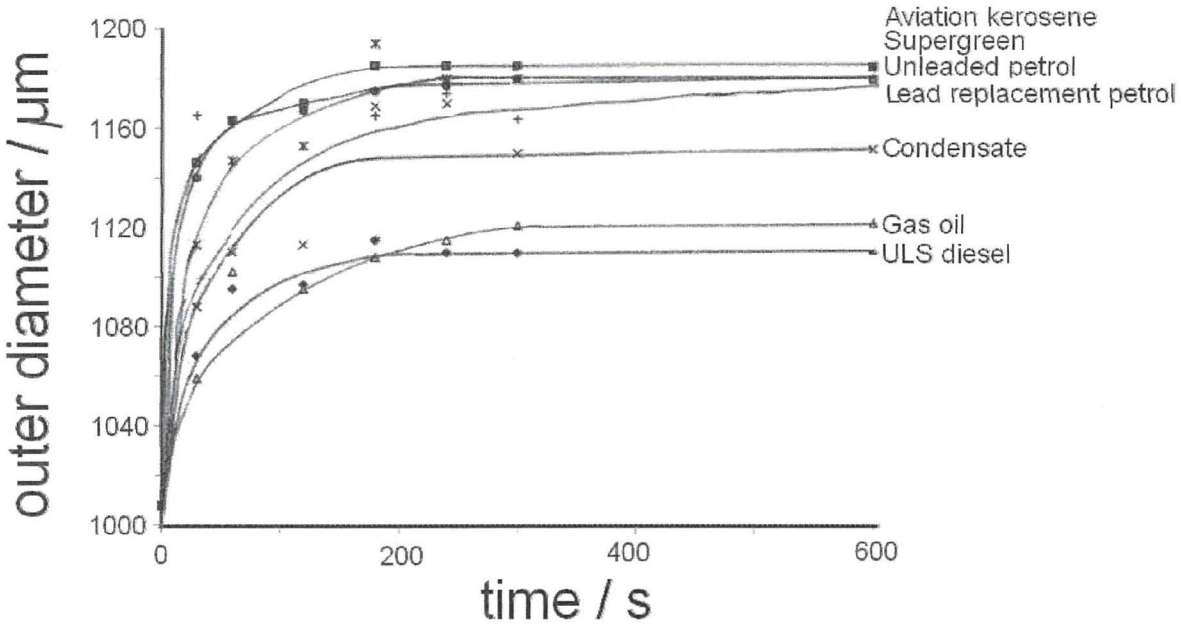

Figure 2.2.5: Expansion data for rods coated with 50 μm of EP4412.

The expansion data for EP4412 reflect the results seen for Varflex except for the aviation kerosene, which was the quickest to respond in this case. Aviation kerosene, and the petrols showed a percentage increase in coating thickness of at least 170 % and achieved 50 % swell in substantially less than a minute. The condensate achieved a 50 % swell between 30 and 60 seconds after immersion and reached a 145 % increase in coating thickness. Gas oil and ULS diesel also reached their 50 % swell in under a minute but reached a maximum coating swell of less than 115 %. It is worthy of note that the EP4412 coating thickness increased by a factor of at least two and by as much as 2.7 in the cases of unleaded petrol, aviation kerosene and supergreen.

Recovery data, as shown in figure 2.2.6, are similar to those seen in figure 2.2.4 for Varflex.

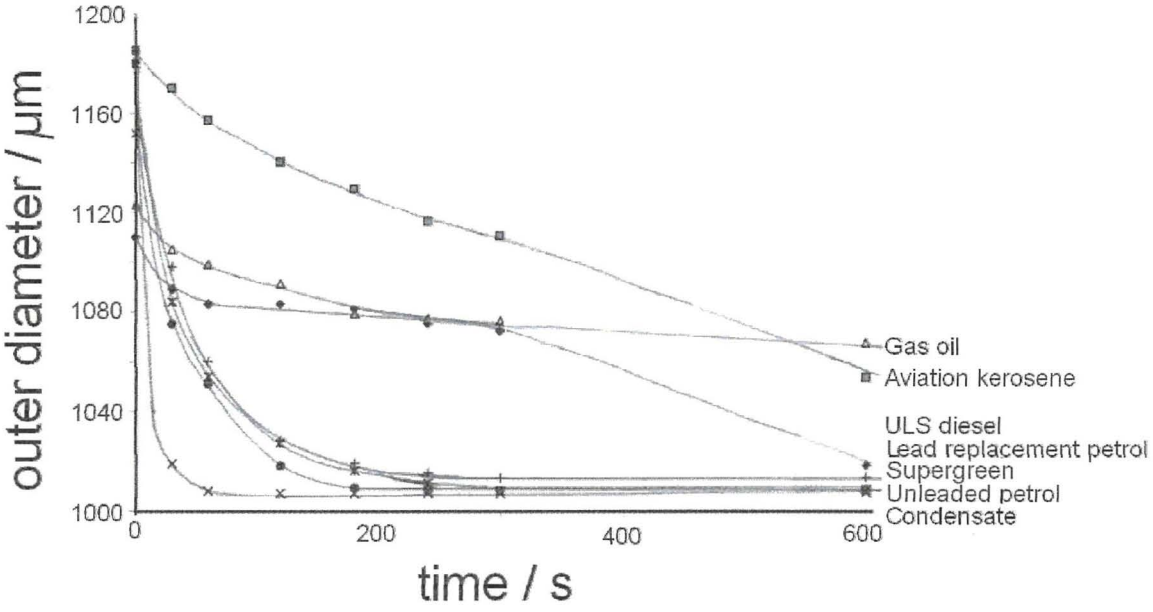

Figure 2.2.6: Recovery of 50 µm thick coatings of EP4412.

Again, gas oil and aviation kerosene failed to recover completely within 10 minutes. ULS diesel showed an improved recovery in the EP4412 compared to the Varflex material, almost recovering completely to the original dimension within the 10 minute timeframe. As previously for the Varflex silicone, the condensate showed a very rapid recovery rate, recovering to its dry dimensions in 1 minute. Although the two sets of data cannot be directly compared due to the difference in coating thickness it appears that the EP4412 was the better of the two materials as the coating thicknesses increased by at least 100 %, even for the less responsive fluids. Maximum swell increases of up to 170 % were seen for EP4412 as opposed to 120 % for the Varflex material. The elastomers responded fastest to the lower molecular weight and more volatile fluids. This is consistent with the mechanism of swelling described in the introduction and in the literature [35-42]. As reported by Favre and co-workers in a number of papers [39-42] pdms films and membranes typically demonstrate an affinity for low molecular weight, non-hydrogen bonding organic solvents and show large degrees of swelling. Here, both silicones responded fastest to the petrols, which are characterised by low average molecular weight and high volatility (low boiling point). Both sensors also showed slow

swelling rates in response to the heavier, less volatile liquids, such as diesel and gas oil. These trends were mirrored in the rates of recovery. The elastomers recovered fastest after exposure to the petrols than after exposure to diesel and gas oil. Rates of swelling and recovery after exposure to the intermediate fluids, the aviation kerosene and condensate were more unusual. Despite both silicones showing a relatively fast response to aviation kerosene, the rate of recovery was the slowest of all the fluids. It would be consistent with previous work [34] to infer that the hydrocarbon components of the aviation kerosene form strong associations with the elastomer chains after absorption and are therefore desorbed slowly upon recovery. The opposite behaviour is seen for the condensate. In the case of both elastomers the condensate causes an expansion rate intermediate between that of petrol and diesel. The rate of recovery is greatest for the condensate in the case of both silicones, characterised by rapid and complete recovery to the starting dimensions. It is likely that only very weak interactions are formed between the hydrocarbon components within the condensate and the elastomer chains and thus the desorption and accompanied contraction is rapid. The errors in the swelling data in this experiment were high and difficult to quantify. The method involved the removal of the sample from the liquid in which it was immersed in order to take a reading of diameter. The length of time taken to remove each sample and transfer it into the measuring aperture of the laser micrometer differed from sample to sample. It was inevitable that as soon as the sample was removed from the liquid, evaporation began and the degree to which this proceeded was not possible to determine. It is concluded that the results above gave a good qualitative "feel" for the performances of the two rubbers, but to produce reliable quantitative results, the method would require considerable modification. A means of monitoring the diameter accurately whilst the rod is still immersed in the liquid would remove the innate errors incurred by the removal of the sample and the possible complications due to the presence of a liquid film.

Electron micrographs of the coating surfaces yielded clues as to their structure, their composition and their resistance to damage from exposure to the petrochemical fluids under investigation. The EP4412 samples all appeared to suffer no significant damage or change to their surfaces. Figure 2.2.7 is a series of scanning electron micrographs of the EP4412 surface as produced without any petrochemical exposure.

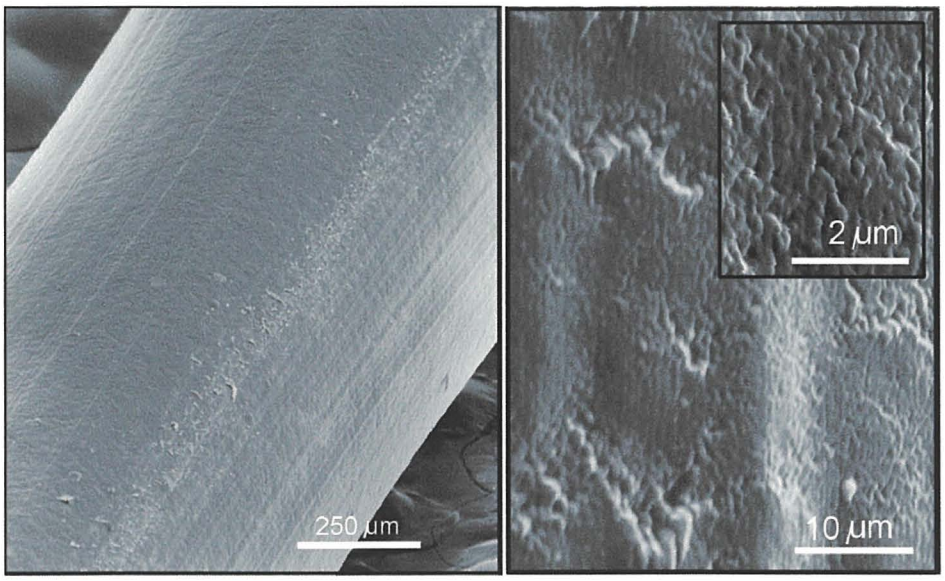

Figure 2.2.7: Scanning electron micrographs of an unexposed EP4412 coated rod (50 µm) at three different levels of magnification. The bars in each image give the appropriate scale.

The striations running along the length of the sensor are a manufacturing defect caused by the extrusion of the silicone through a heated diehead. The obvious scar running from bottom-left to top-right is a scratch also formed during the manufacturing process and can be observed on all EP4412 samples. There is a pronounced surface texture apparent from the micrographs, exhibiting a rough, spongelike appearance. After exposure to petrochemical fluids the EP4412 surface appeared to remain unchanged. For the heavier fuel oil, which did not evaporate after exposure, deposits were left on the EP4412 surface which, when observed under high magnification (figure 2.2.8 overleaf), were suggestive of dried deposits formed from oil droplets. It can be inferred that the high molecular weight tar residues within the fuel oil were too viscous and too large (typically in the range C20 – C50) to be absorbed into the silicone but remained on the surface in droplet form.

The degree to which the lower molecular weight gas oil components penetrated the silicone matrix could not be determined.

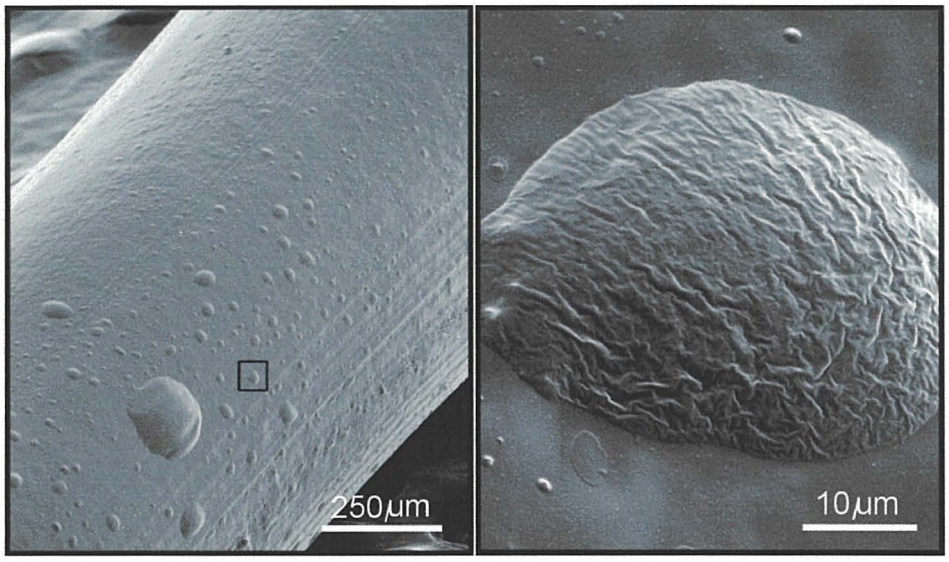

Figure 2.2.8: Scanning electron micrographs of tar residues on surface of EP4412 after exposure to fuel oil.

The Varflex rubber samples have a different surface altogether. This is due to the different coating method used to deposit the Varflex silicone onto the rods. The solution-based method leads to a smoother coating which conforms to the non-circular morphology of the substrate. No striations can be seen along the surface, as can be seen from the micrograph in figure 2.2.9.

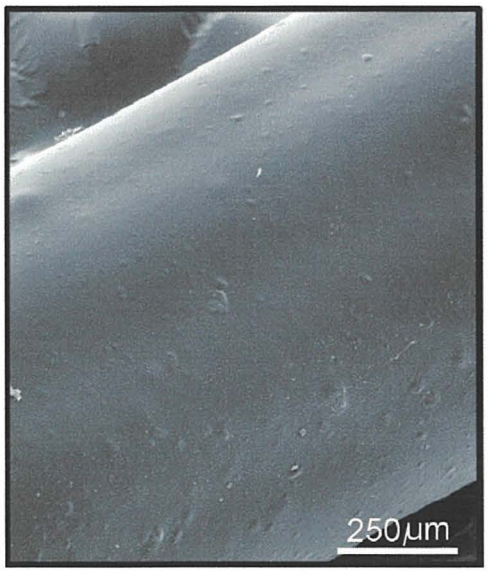

Figure 2.2.9: Scanning electron micrograph of the appearance of rod coated with the Varflex silicone. A smooth surface is apparent together with inclusion defects.

The solution coating method did however lead to the formation of considerable numbers of defects, characteristic of dust and bubble inclusion during the coating and curing processes. Varflex samples exhibited shrinkage of the films after exposure. A characteristic wrinkling was observed in all the micrographs for the Varflex material. Figure 2.3.0 illustrates this phenomenon for a Varflex coated rod exposed to lead replacement petrol.

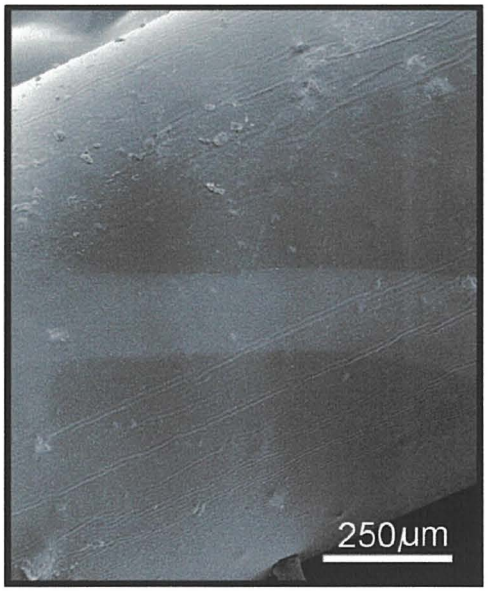

Figure 2.3.0: Scanning electron micrograph of Varflex coated rod after exposure to lead replacement petrol.

The effect was considerably more pronounced for certain fluids. Gas oil and ULS diesel produce the effect clearly as shown in figures 2.3.1 and 2.3.2 (overleaf) respectively.

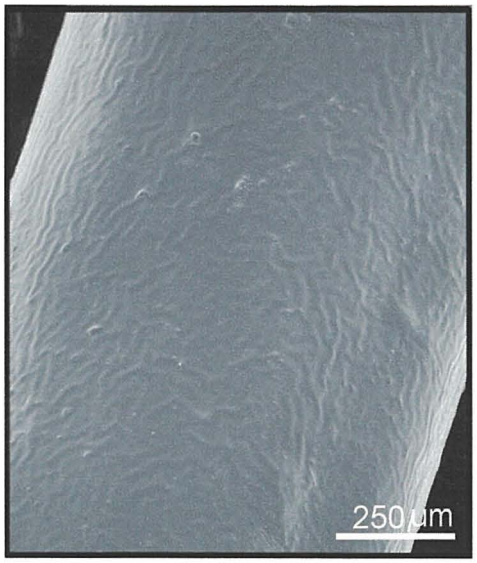

Figure 2.3.1: Scanning electron micrograph of Varflex coated rod after exposure to gas oil.

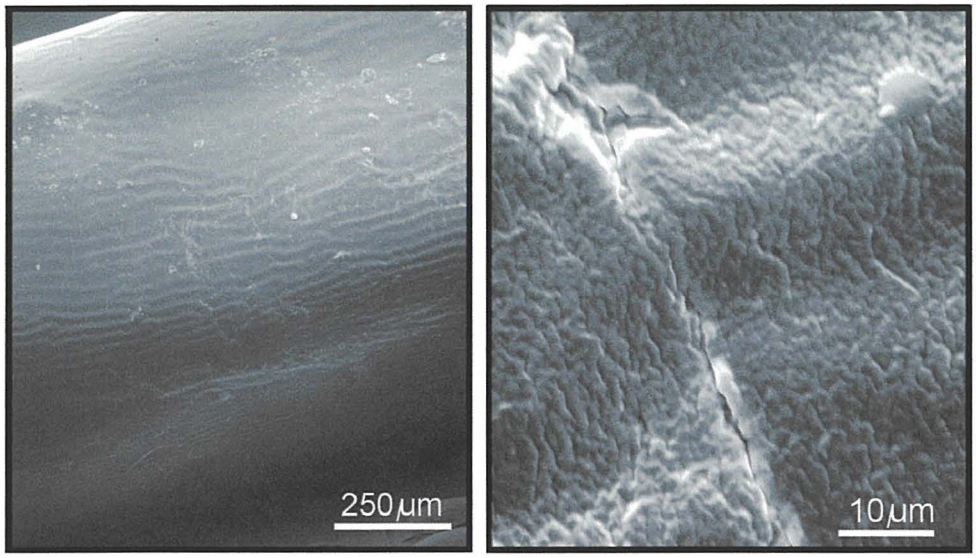

Figure 2.3.2: Scanning electron micrographs of Varflex coated rod after exposure to ULS diesel. The micrograph at right shows the fine structure visible under higher magnifications.

The most pronounced shrinkage was seen after exposure to condensate. Figure 2.3.3 shows a micrograph obtained of a Varflex sample exposed to the condensate.

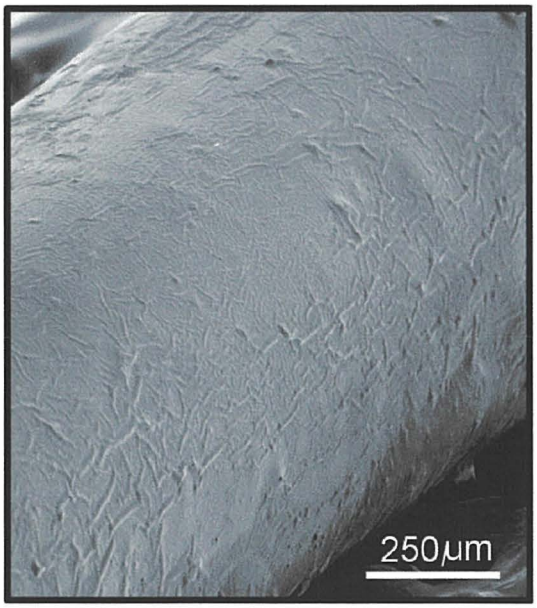

Figure 2.3.3: Scanning electron micrograph of a Varflex coating exposed to condensate.

It is possible that the Varflex silicone contained a filler compound, a common practice in cabling, although this was neither confirmed or denied by Varflex Corporation. The Varflex silicone was opaque and a fine white powder was reported on its surface [44] which suggests that a silica or calcium carbonate filler was present. The presence of a filler would also imply the presence of a plasticiser to counteract the hardening effect of the filling material.

Common plasticisers are petroleum distillates such as paraffins, napthenes and aromatic oils [27] or non-reactive, short chain length polysiloxanes [29,32]. These plasticisers, due to their mobile nature, are easily leached out [27,32,33]. A silicone weight loss of 25 % was reported [32] after extraction of a mobile polysiloxane from an elastomer in toluene. In addition, the presence of fillers can affect the recovery of elastomers. It is reported [27] that the inclusion of a rigid phase incapable of elastic recovery may cause a decrease in recoverable strain and a loss of elasticity by the formation of vacuoles around filler particles during extension. Repetitive swelling and recovery may then cause fracture of the elastomer. The phenomenon of wrinkling and shrinkage seen here supports the hypothesis that a filler compound is present after manufacture and that a plasticiser is leached out after exposure to petrochemical fluids leading to a pronounced decrease in volume.

As seen for the EP4412 samples, after exposure to fuel oil the Varflex material showed tar residues on the silicone surface. Figure 2.3.4 shows micrographs of the surface features observed.

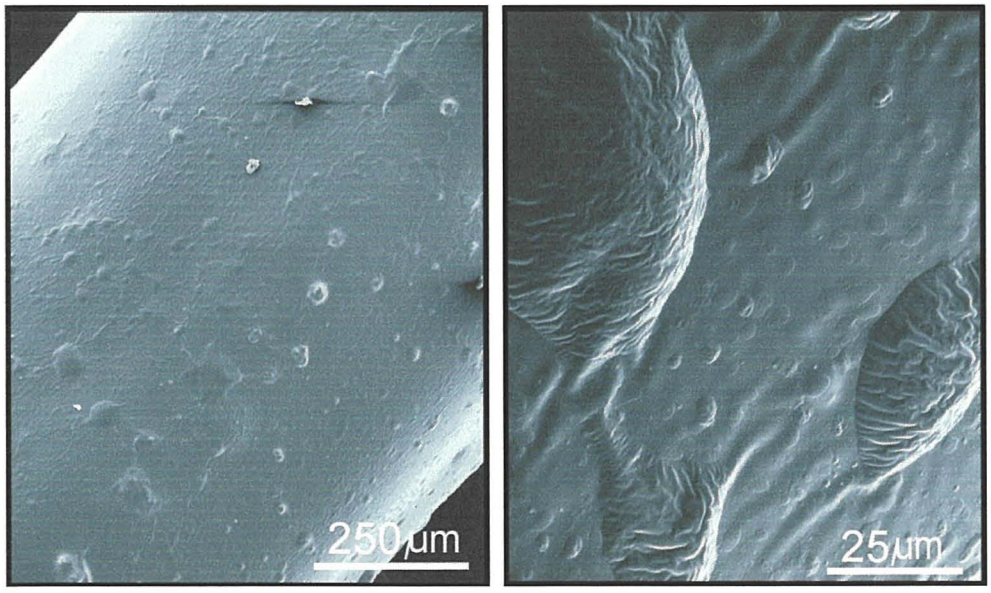

Figure 2.3.4: Micrographs showing droplet residues observed on a Varflex coating after exposure to fuel oil.

The associated shrinkage and wrinkling in the Varflex silicone, favoured the use of EP4412 in the sensor design as it did not exhibit these phenomena and appeared more stable.

The EP4412 had substantially fewer inclusion defects and it was plausible that the striation and associated surface texture may improve the absorption of the petrochemical liquids. The EP4412 was shown to have a greater expansion performance for all the fluids assessed and showed faster rates of recovery for the petrols, diesels, condensate and aviation fuel. Both coatings were subsequently used in the development of sensors to compare their relative performances before a decision was made as to which silicone to use.

2.3.2 First generation prototypes – bare fibre sensors

The first sensors manufactured used a "bare" fibre. Unlike the buffered fibres used in later sensors which were coated in Hytrel®, these early prototypes used the fibre with only an acrylate coating for protection. Development of the manufacturing process to enable this prototype to be made continued until early March 2000 when the first operational prototype, 960 metres in length was produced. This sensor used the Varflex silicone at 50 μm coating thickness, a bare multimode fibre and the fundamental periodicity. The binder tension was set at 18 ğ. A 100 m section of this sensor was cut and a reference OTDR trace taken.

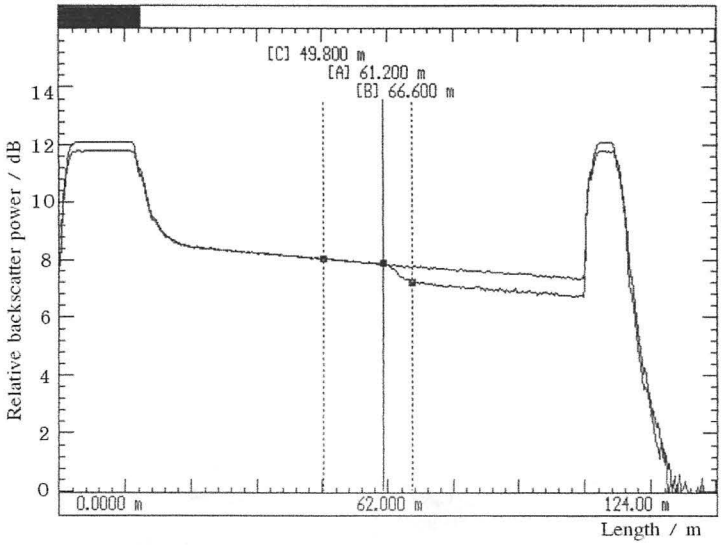

Figure 2.3.5: OTDR response of a bare fibre sensor: varflex rubber, 18 ğ tension, fundamental periodicity, response to petrol.

The sensor was then exposed to unleaded petrol and a second trace was taken and superimposed against the reference (figure 2.3.5 above).

A sensor using EP4412 was made with identical settings and parameters. It too was exposed under the same conditions as the Varflex sensor; figure 2.3.6 shows the trace obtained for the EP4412 sensor with a bare fibre.

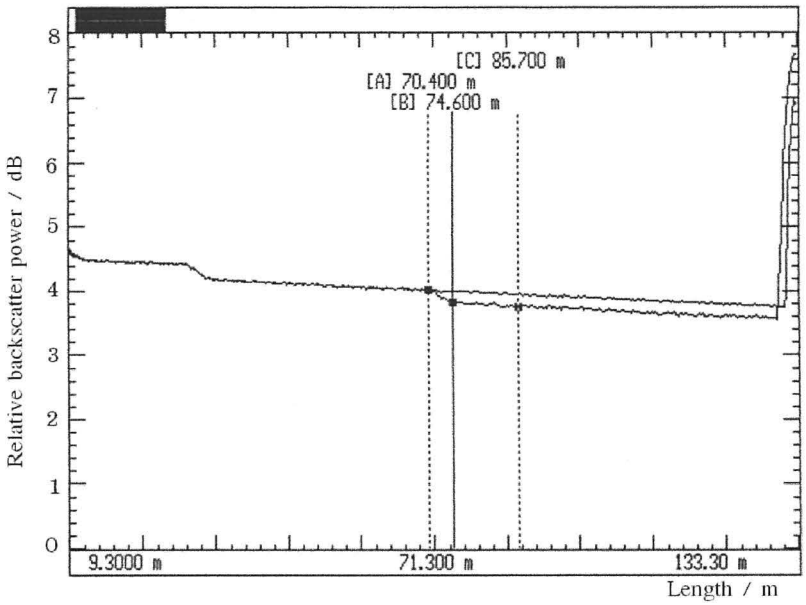

Figure 2.3.6: OTDR response of a bare fibre sensor: EP4412 rubber, 18 ğ tension, fundamental periodicity, response to petrol.

The loss event was seen clearly in both cases; the wetted length (1 m) induced losses of 0.7 dB and 0.4 dB for the Varflex and EP4412 respectively. However, the dry attenuations were high and would not be practical for a final sensor. Testing of the EP4412 sensor with diesel yielded a large response as is seen in figure 2.3.7 below.

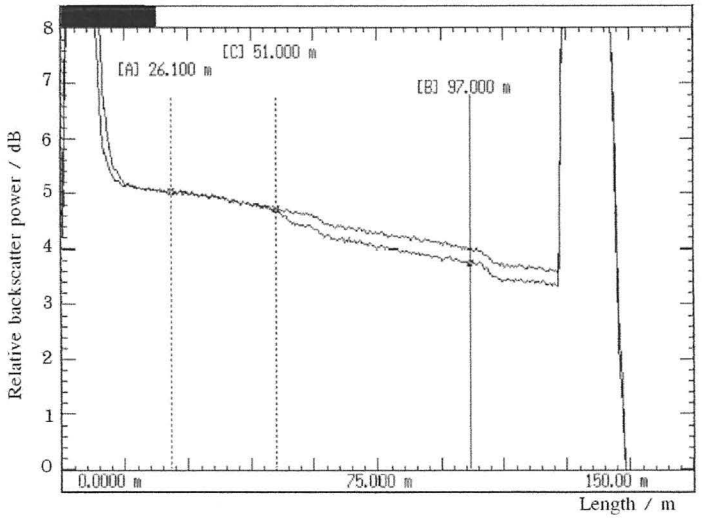

Figure 2.3.7: OTDR response of a bare fibre sensor: EP4412 rubber, 18 ğ tension, fundamental periodicity, response to diesel.

Results by Johnstone *et al.*[46] showed that the same bare fibre EP4412 sensor was able to detect the presence of crude oil. The OTDR trace they obtained is shown in figure 2.3.8.

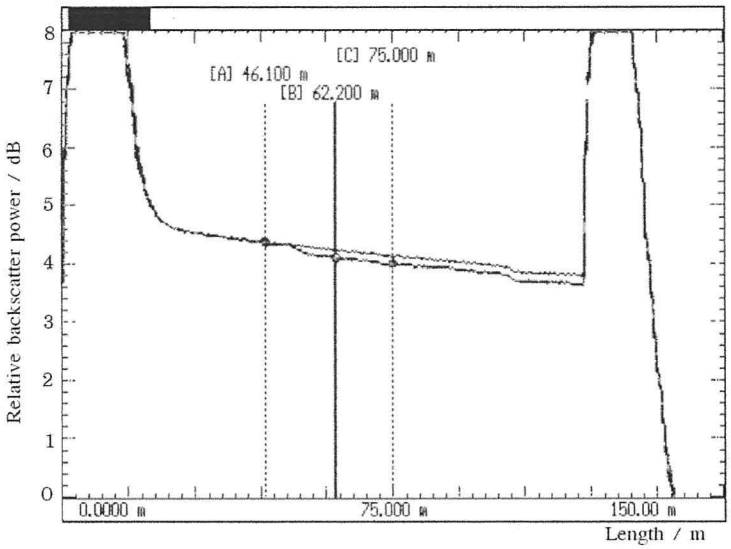

Figure 2.3.8: Bare fibre, EP4412 rubber, 18 ğ tension, fundamental periodicity, response to crude oil. (Reproduced with permission from Johnstone *et al.*[46])

Two further sensors made to identical manufacturing processes but with differing grades of optical fibre were exposed to unleaded petrol. The responses observed varied significantly. Figures 2.3.9 and 2.4.0 (overleaf) show the OTDR traces obtained for the low grade (Fibrecore 160/200) and high grade (Fibrecore 200/600) fibres respectively.

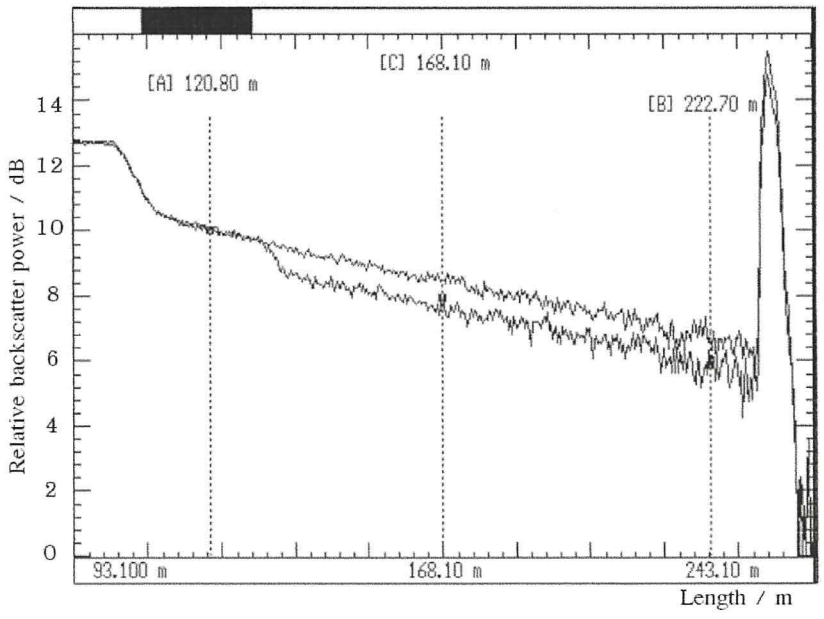

Figure 2.3.9: OTDR response of lower grade, 160/200 fibre to unleaded petrol. (1.0 dB loss)

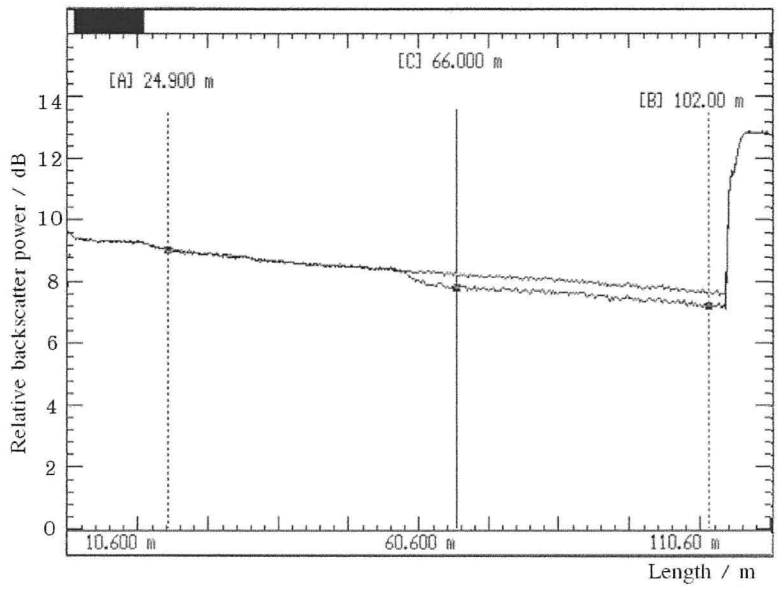

Figure 2.4.0: OTDR response of high grade, 200/600 fibre to unleaded petrol. (0.5 dB loss)

The lower grade fibre showed a loss twice that of the higher grade fibre. This implied that the lower grade, more responsive fibre would be suitable for use in sensors for hydrocarbon liquids that produced poor expansion in the silicone such as crude oil. The less responsive, higher grade fibre could be used in sensors for petrols which did not require the additional sensitivity.

Investigation into the chemical resistance of the acrylate layer was carried out. The results of the test are shown in table 2.2 which lists the chemicals tested, whether the acrylate layer passed or failed and a reason for failure where appropriate.

Fluid	Pass / Fail	Reason for failure
Water	pass	
Soil water	pass	
Methanol	fail	Acrylate wiped off with fingers.
$HCl_{(aq)}$ (2 M)	pass	
$NH_4OH_{(aq)}$ (2 M)	fail	Acrylate became opaque and easily scratched off.
Unleaded petrol	fail	Acrylate became yellow-brown, easily scraped off.

Table 2.2: Results of qualitative chemical resistance testing of bare fibre acrylate.

The results appeared to show that the acrylate was resistant to water, ground water and acidic solutions. However, the poor resistance to petrol and methanol indicated that the bare fibre sensors would not be sufficiently rugged to survive multiple exposures to petrochemicals but would be suitable for single use, disposable systems in clean environments such as within double skinned pipes or tanks. One of the first bare fibre prototypes was placed into a large volume of water whilst connected to an OTDR. The attenuation was seen to decrease slightly as can be seen from the slight decrease in slope in figure 2.4.1.

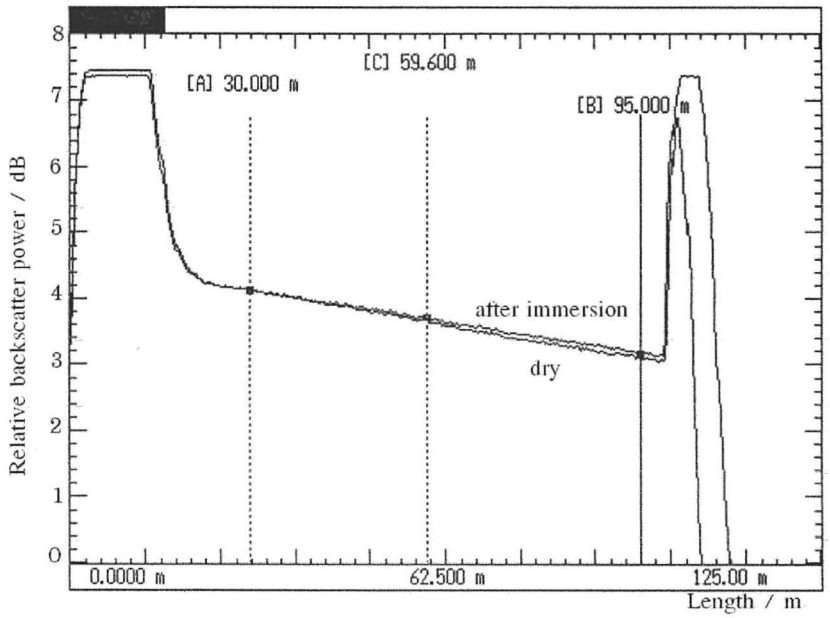

Figure 2.4.1: OTDR trace showing slight decrease in attenuation after bare fibre sensor was fully immersed in cold water. Difference manifests as a change in slope along entire length of sensor.

As the attenuation decrease occurred along the entire fibre length, manifested as a decrease in the negative gradient, it was surmised that the change was not due to water ingress at a single point along the fibre as this would appear as a step, or localised loss at the point where the acrylate has failed. It is likely that the change was the result of the change between room temperature and the cold water. The aramid material used for binding has a negative coefficient of expansion and as such when the sensor was cooled the binder would have expanded and thus the tension of the binding thread over the underlying fibre would have decreased. This would have decreased the attenuation of the fibre.

It was quickly realised that these sensors were only practical in a laboratory situation where the sensors were protected from the rigours of survival in a less than perfect installation environment. Although the fibres were covered in a protective acrylate layer, this coating was thin and easily damaged. Water ingress into a fibre would result in the propagation of microscopic fissures in the cladding surface and would eventually lead to the fibre being unusable and exceedingly fragile. Coating the fibres with a second protective layer was necessary.

2.3.3 Second generation – buffered fibre sensors

As the key to the operation of the sensor was to allow liquids unimpeded access to the silicone coating it would be to the detriment of sensor response to attempt to protect the fibre from water ingress after the sensor had been assembled. The solution to this problem lay in coating the fibre with an additional protective layer before it was bound into the sensor. Fortunately, it is standard practice to coat fibres in polymeric materials before cabling. During the early stages of the manufacture of data communication cables each fibre is "buffered" (coated) up to a total diameter of 600 or 900 μm. Materials used vary depending on the application of the cable. One material, DuPont's Hytrel™, is designed primarily to be resistant to chemical attack from non-polar materials such as oils and hydraulic fluids, even at elevated temperature and is resistant to most polar fluids such as acids, bases, amines and glycols at room temperature and up to 70 °C [45]. Tabulated data included in the guide state that benzene, cyclohexane, ethanol, jet fuel, lacquer solvents, toluene, mineral oil, silicone grease and sea water will have "minor, little or no effect" [45].

Sensors were manufactured incorporating both a 900 μm and a 600 μm buffering. The sensor with a 900 μm buffering had low dry attenuation (approximately 6 $dB.km^{-1}$) comparable to that of uncabled fibre, this represents a 75% drop in power over each kilometre.

Figure 2.4.2 shows the dry trace obtained for the 900 μm outer diameter sensor. Although the dry loss was good, no response could be seen when the sensor was exposed to petrols.

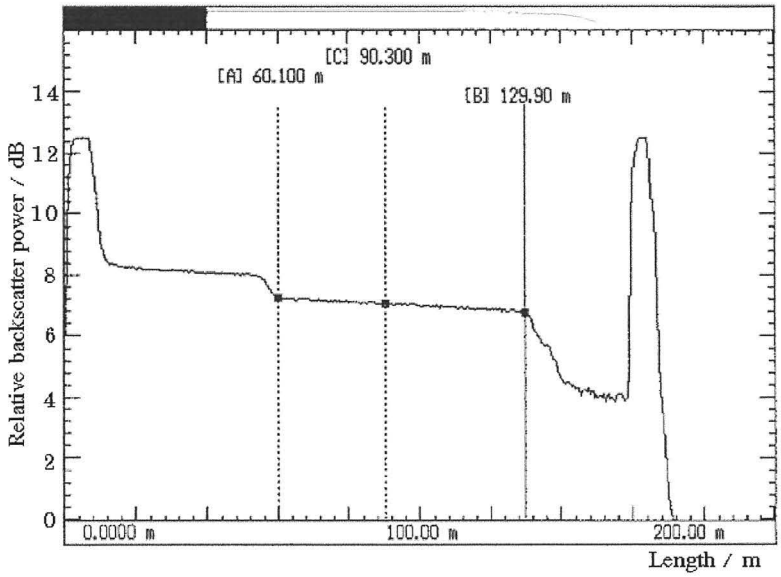

Figure 2.4.2: Dry attenuation trace of 900 μm buffered fibre sensor. (*N.B.* The sensor was made with sections of the sensor having different periodicity, thus the step marked by cursor [A] at 60m is a transitional zone between sections and not a petrol induced loss)

It appeared that the fibre buffering was too thick and the force produced by the swelling rubber was not effectively transferred to the fibre within the buffering. Figure 2.4.3 is an electron micrograph of a section through an assembled 900 μm buffered sensor. The core, cladding and acrylate coating can be clearly distinguished as can the glass-fibre reinforced rod to the right of the buffered fibre. The 900 μm buffered sensors were discarded.

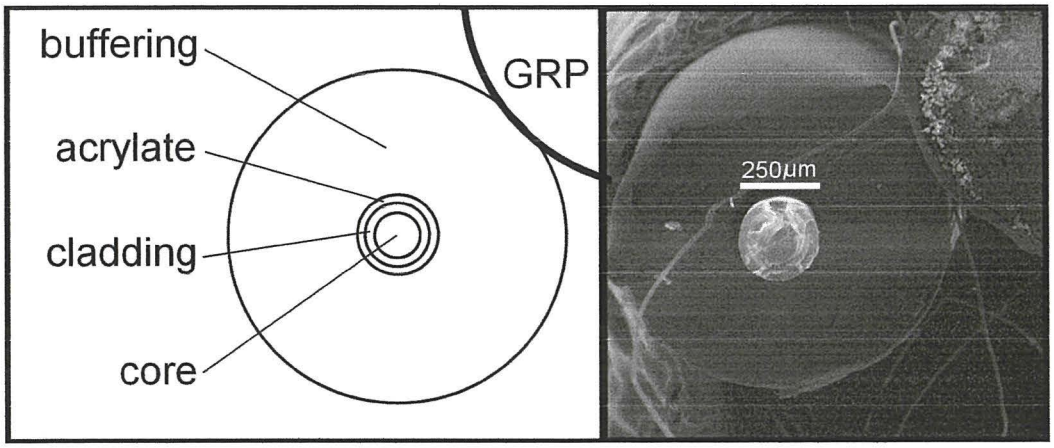

Figure 2.4.3: Electron micrograph of a section through an assembled 900 μm buffered sensor.

The 600 μm sensor showed a clear but poor response on wetting with petrol. (figure 2.4.4)

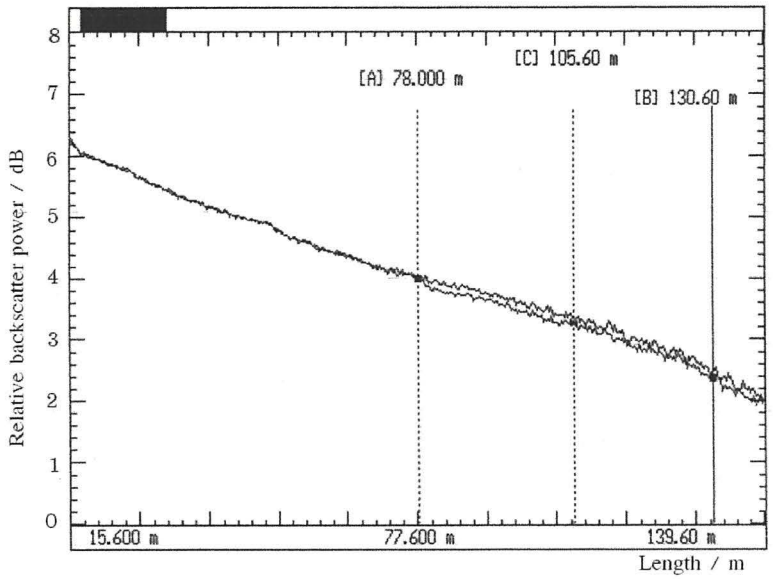

Figure 2.4.4: OTDR trace of a 600 μm Hytrel buffered fibre sensor exposed to unleaded petrol.

An additional sensor was made to the same design as both the 600 and 900 μm sensors but with an experimental 450 μm buffering. The 450 μm buffering was produced by extrusion of a thin layer of Hytrel only 100 μm thick over the acrylate layer. This is only marginally thicker than the acrylate itself which is 62.5 μm thick. Figure 2.4.5 shows the OTDR trace obtained after exposure to unleaded petrol.

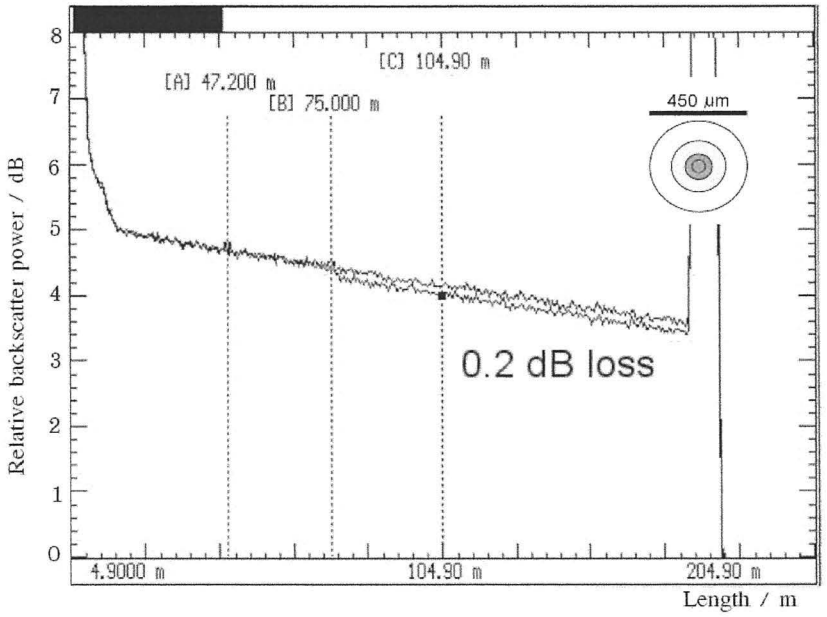

Figure 2.4.5: OTDR trace of 450 μm Hytrel buffered fibre sensor after exposure to petrol.

The result obtained was ideal for the sensor system's requirements, as the exposed length (1 m) induced a loss of 0.2 dB in the sensor when wetted with petrol which was in the range required (0.1 – 0.2 dB) for optimum detection by the custom OTDR unit. The 450 μm fibre buffering was a good compromise between the sensitivity of the bare fibre sensors and the resilience of the buffered sensors. Unfortunately, the 450 μm buffering was not a standard cabling product and the manufacturing process whereby the buffering was applied was deemed to be too unstable, unpredictable and costly. The 450 μm buffered fibre sensors were scrapped despite their excellent character.

2.3.4 Third generation – petrol tuned sensors

The second generation design for petrol detection incorporated a 62.5/125 multimode fibre with a 600 μm Hytrel buffering and a 50 μm silicone coating. It has been shown [47] that microbending losses may be induced not only at the fundamental period but also at multiples of the critical spacing. Sensors with multiple periodicity were assessed for their response to petrol so as to determine how variation of the binding periodicity affects sensor response. The dry attenuation of each section remained constant. Thus, it can be inferred that variation of the binder periodicity in a Hytrel buffered sensor had no effect, detrimental or advantageous, on the dry attenuation of the sensor and thus on the maximum effective range of the sensor. A length (1 m) in each section was wetted with unleaded petrol and the magnitude of the loss at each section estimated. Figure 2.4.6 overleaf, shows the OTDR traces obtained and an estimate of the losses achieved. The desired optimum loss induced by a 1 metre wetted section was 0.1 dB. This value was stated by the designers of the signal processing and detection system. The results in figure 2.4.6 (overleaf) indicate that the sensor operated with equal sensitivity at the first, second or third harmonics.

The magnitude of the sensor response at the fundamental period was significantly lower than the responses obtained at the harmonics, and it is hypothesised that the close proximity of adjacent binding wraps did not allow the buffered fibre sufficient freedom to bend.

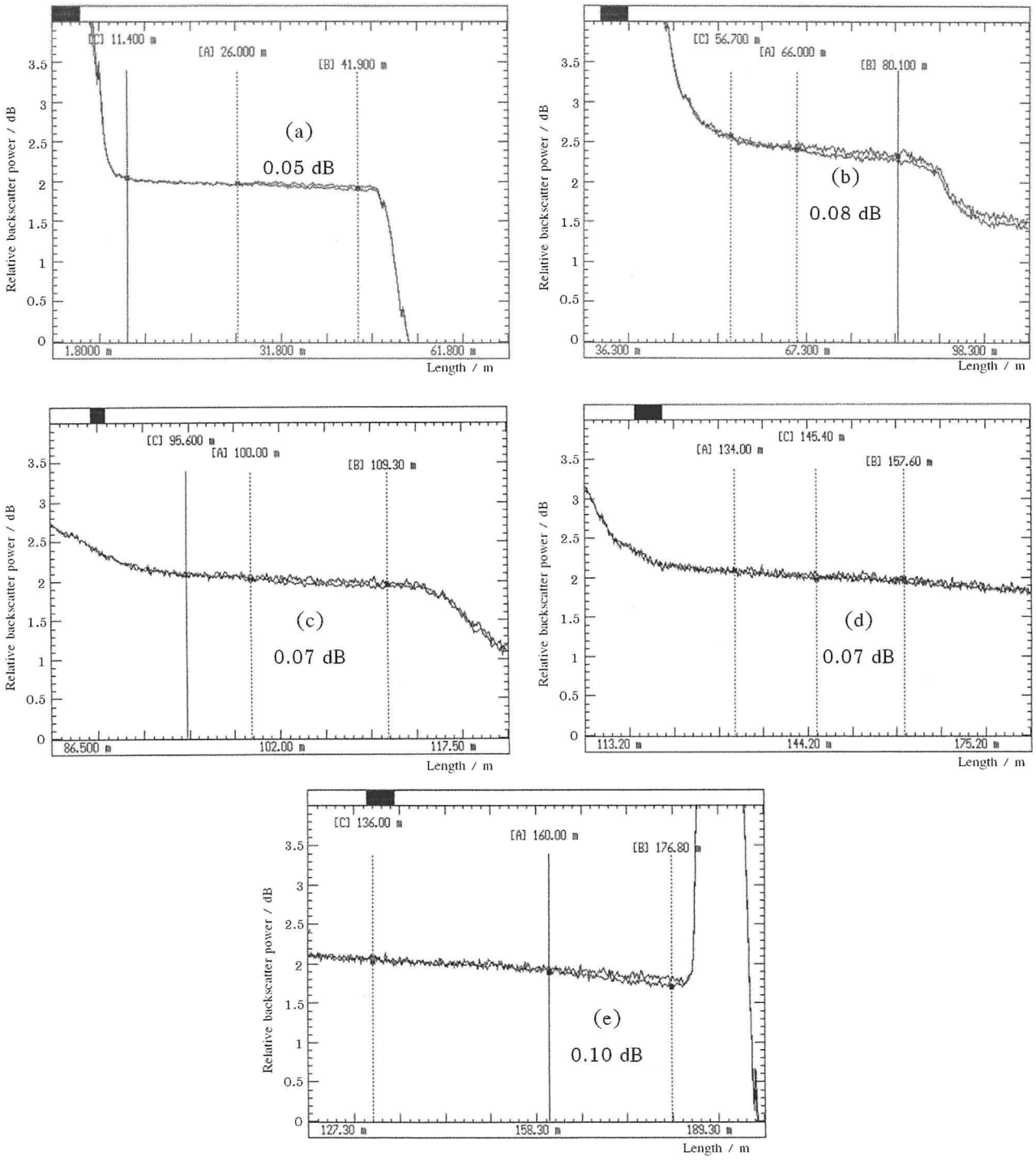

Figure 2.4.6: OTDR response traces of (a) fundamental period, (b) 1st harmonic, (c) 2nd harmonic, (d) 3rd harmonic and (e) 4th harmonic.

Use of the harmonics yielded better responses overall and the section set at the second harmonic gave the most reproducible results. A lay length of 3 mm (the 2nd harmonic) was chosen for the design.

Given the structure of the DISH sensor, it can be expected that the tension of the binder thread will have a significant effect on the magnitude of the response and on the overall attenuation and range of the sensor. A length (1 m) of sensor with an applied tension of 100 ğ was wetted with unleaded petrol and the OTDR response recorded. Figure 2.4.7 shows the traces obtained.

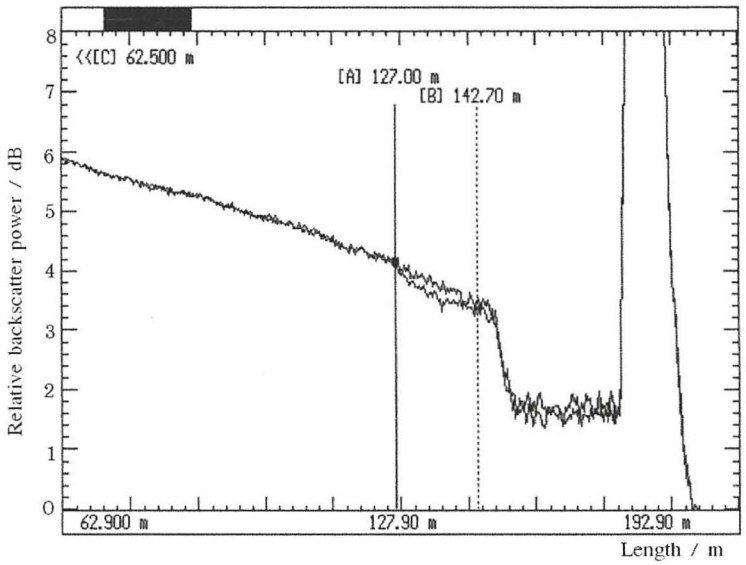

Figure 2.4.7: OTDR trace of sensor with tension of 100 ğ. Loss of 0.2 to 0.3 dB was seen.

The response to petrol was good, showing a greater than 0.2 dB loss for a wetted length of 1 m. The attenuation was high (approximately 35 $dBkm^{-1}$) which would limit the effective range of the sensor to less than 500 m. A second sensor with the applied tension reduced by 20 % to 80 ğ was tested under the same conditions as previously. The traces obtained are shown in figure 2.4.8 (overleaf).

The response shown by the reduced tension sensor was again above the optimum value for detection by the custom system but was accompanied by high attenuation (in excess of 20 $dBkm^{-1}$) which would severely limit the sensor's range.

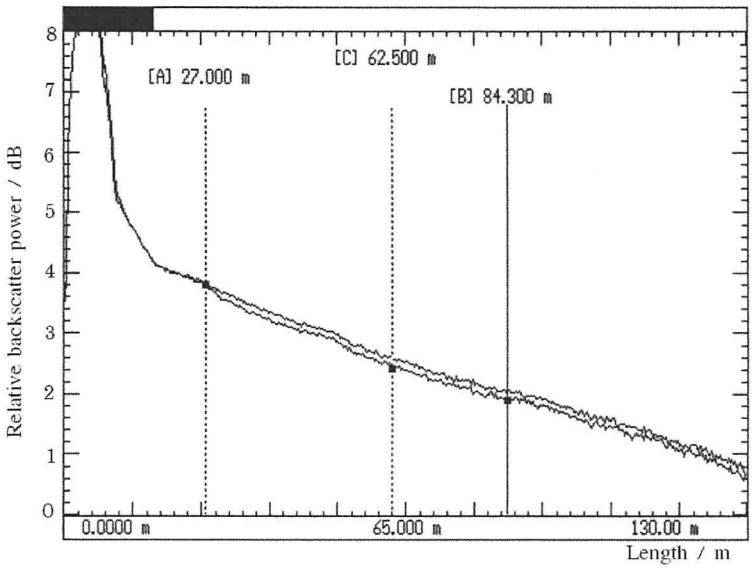

Figure 2.4.8: OTDR traces showing the response to petrol of a sensor with a binder tension of 80 ğ.

It was hypothesised that the high attenuations observed may be symptomatic of crushing of the fibre, *i.e.* the induction of microbends in the fibre by periodic crushing, thus increasing the overall attenuation. This was confirmed by visual inspection of the fibre which showed permanent deformation even after the removal of the binder thread. It was necessary to find a trade-off between response and induced attenuation. A sensor with a tension of 15 ğ was tested (with petrol) under the same conditions as previously and its OTDR response was recorded so as to determine if a significant reduction in tension would reduce the dry attenuation to values substantially lower than 10 $dBkm^{-1}$ whilst achieving the desired response of around 0.1 dB per wetted metre.

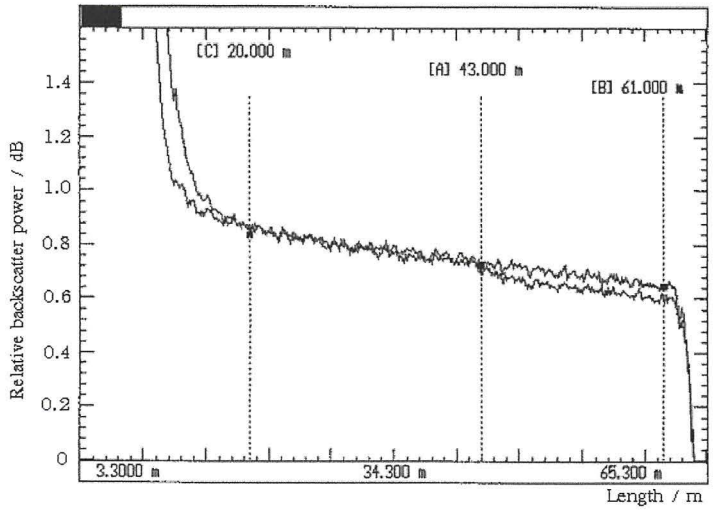

Figure 2.4.9: OTDR trace obtained from a short length of sensor with a binder tension of 15 ğ. An induced loss of approximately 0.1 dB was seen.

The first sensor at this tension (15 ğ) produced excellent attenuation (4.5 $dBkm^{-1}$). A second sensor made with a different batch of fibre to the same specification showed that reproducible attenuations of around 5 $dBkm^{-1}$ were possible. The OTDR response obtained for one of these two sensors which is typical of the responses seen, is shown in figure 2.4.9 above.

Sensors with applied tensions of less than 15 ğ gave unpredictable responses. It is probable that lower tensions did not allow sufficient transfer of stress from the swelling elastomer to the fibre and did not show reliable responses as a result. The optimised design for the petrols was therefore a 600 μm Hytrel buffered fibre, second harmonic binding (3 mm), 50 μm coating of silicone and a binder tension of 15 ğ.

To aid in the decision of which silicone material gave the most reproducible results, more sensitive assessments of response were made using a power meter and data logger. Two sensors were made to the optimised design above; one made with the Varflex elastomer, the other with EP4412. They were exposed to petrol whilst connected to the power meter. Readings were taken 10 times per second for 800 seconds. After referencing of the power meter to the dry attenuation, a length (1 m) of the EP4412 sensor was exposed to lead replacement petrol, and the response with time recorded. The results are shown in figure 2.5.0.

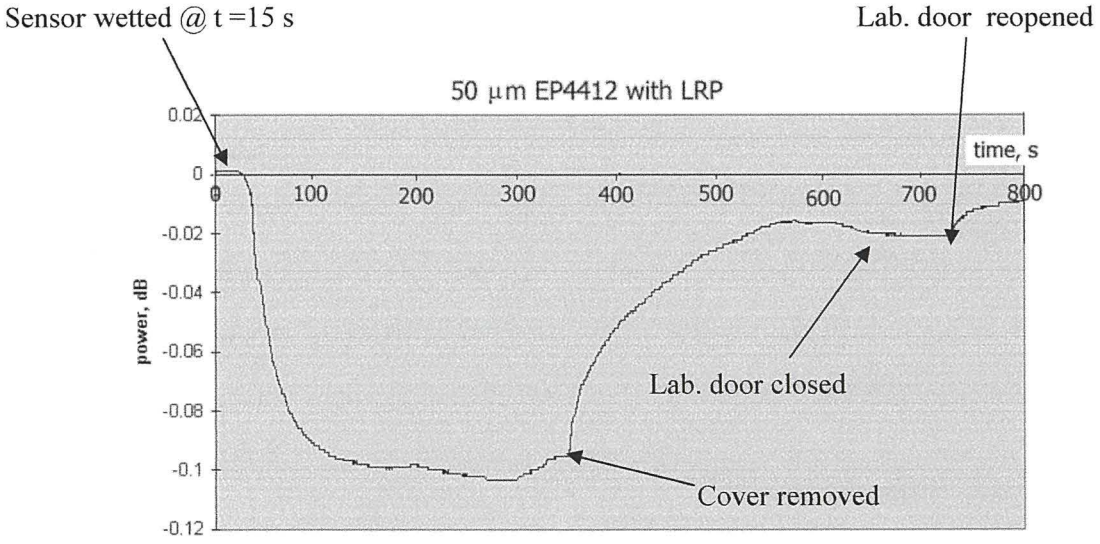

Figure 2.5.0: Response curve of EP4412 sensor wetted with lead replacement petrol.

The results showed that 10 seconds after application of the petrol, the transmitted power dropped off, steadying at - 0.1 dB. After several minutes the cover was removed and the petrol allowed to evaporate. This can be seen clearly. The door of the laboratory was closed and then opened again and this was also clearly visible from the trace. It is likely that closing the door stopped a slight breeze and so the rate of evaporation of the petrol was slowed. When the door was opened again the flow of air was restored and the sensor went on to recover completely and return to a steady 0.000 dB.

The second sensor, made with Varflex rubber was subjected to exactly the same regime. The sensor was exposed twice, with both exposures recorded for comparison. Figures 2.5.1 and 2.5.2 show the traces obtained from the first and second exposures respectively.

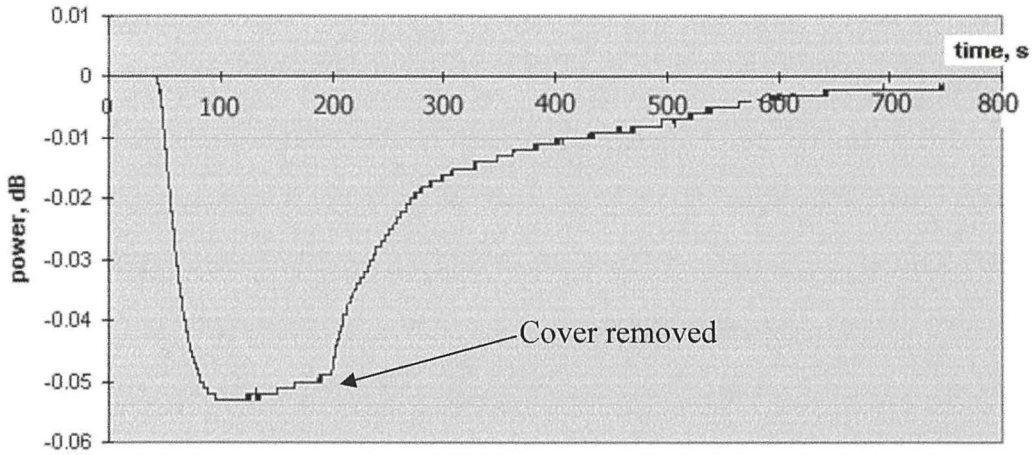

Figure 2.5.1: Response curve for the Varflex sensor – first exposure.

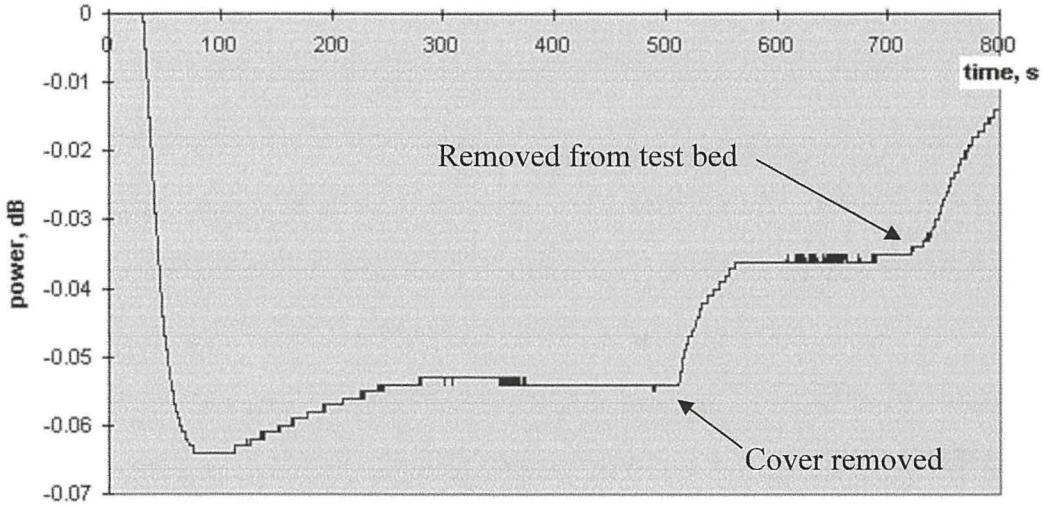

Figure 2.5.2: Response curve for the Varflex sensor – second exposure.

It was noted that the maximum power loss was approximately 20 % greater upon the second exposure (– 0.065 dB as opposed to – 0.055 dB). After the first wetting the sensor recovered smoothly back to 0.000 dB. After the second exposure the sensor only recovered partly after removal of the cover, then levelled off at – 0.035 dB. It is hypothesised that the presence of a dense vapour layer immediately above the sensor minimised the rate of evaporation. The sensor rapidly recovered when removed completely from the test bed. A similar phenomenon was seen in all three traces at the base of their initial troughs. The power reached a minimum, and then recovered slightly before steadying. It is again hypothesised that the establishment of a vapour layer around and above the sensor prevented recovery unless dissipated by external manipulation.

Comparison of the response curves for the two elastomers led to the conclusion that the EP4412 has slightly better all round performance yielding on average greater losses, faster response rates and more thorough recovery. Further tests assessing the environmental performance of the two elastomers were performed, however the results showed that any differences in environmental performance between the two elastomers were negligible compared to the magnitude of the effects on sensor performance of other sensor components. In order to be able to predict better the behaviour of the sensor in extreme environments a sensor was exposed to a programme of varying temperature and humidity over 4 hours. The temperature was ramped from room temperature down to - 40 °C, (0 % relative humidity) where it was kept constant for 30 minutes before ramping back up to + 80 °C; the cycle was then repeated at 90 % relative humidity. The results obtained from the power meter data log together with the temperature regime followed are shown overleaf in figure 2.5.3. As the temperature decreased to – 40 °C the transmitted power increased to + 0.25 dB then fell to – 0.97 dB as the temperature increased to + 80 °C. On the second cycle as temperature again was ramped to – 40 °C and + 80 °C with relative humidity greater than 90 %, the power

followed a similar trend to the first cycle but with the peak powers being + 0.1 dB and – 1.03 dB. It appeared as though the presence of high humidity caused higher attenuation in the cable, which accounted for the shifts in the peak power levels. Power was seen to increase at cold temperatures and decrease at high temperatures implying that the tension on the fibre increased at cold temperature and decreased at high temperatures.

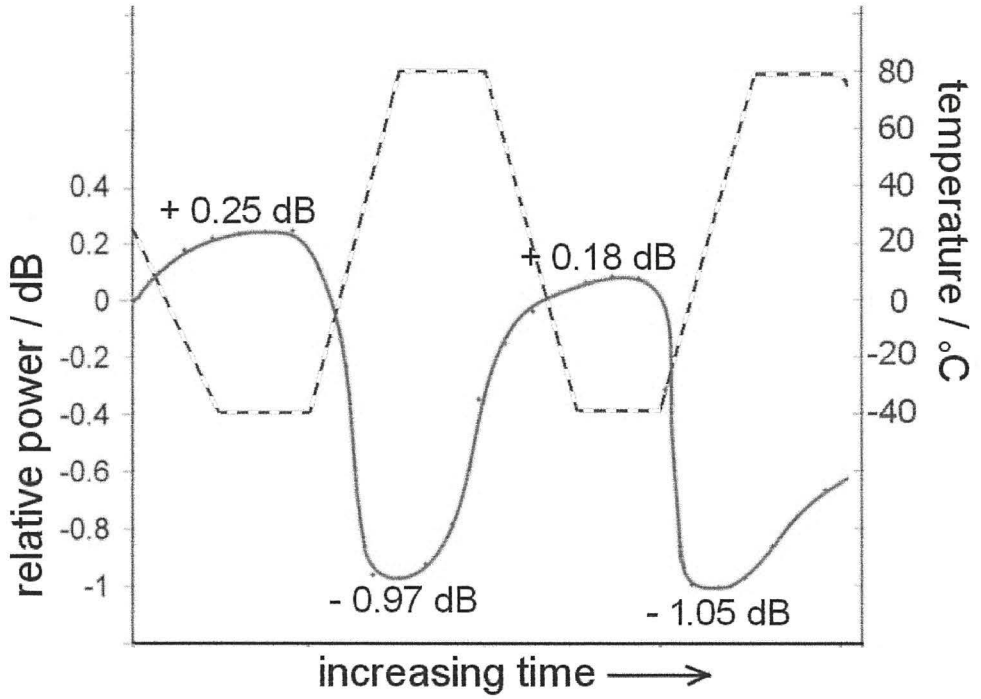

Figure 2.5.3: Results of environmental test: Power loss/gain of the sensor, relative to the start of testing is shown together with peak power values. The temperature program, consisting of eight 30 minute sections is shown by a broken line.

It is probable that this was an effect due to expansion and contraction of the aramid, the material used in the binder thread, which has a negative coefficient of thermal expansion. This meant that as temperatures dropped, the aramid material expanded and hence slackened the binder thread. This in turn led to an increase in transmitted power. The opposite case held true for high temperatures. This effect was exaggerated as the other components behave "normally", *i.e.* they contract at cold temperatures and expand at high temperatures. It was thus shown that the sensor will respond to changing temperature and that this may lead to misleading data were localised temperature changes to occur in an installed sensor system.

The attenuations seen in this test were large. A loss of 1 dB over a 50 m length of sensor translates to a loss of 20 $dBkm^{-1}$. The sensor used in these environmental tests was connected to the power meter and exposed to a suite of hydrocarbons to see how it responded after the rigorous environmental programme.

Example traces are shown in figure 2.5.4. Each trace shows the results for two consecutive wettings, hence the double wells seen. Response times and general shapes were similar to those seen before the environmental test, however the magnitude of the response decreased dramatically, only reaching 10 to 20 % of the response seen prior to the environmental cycle.

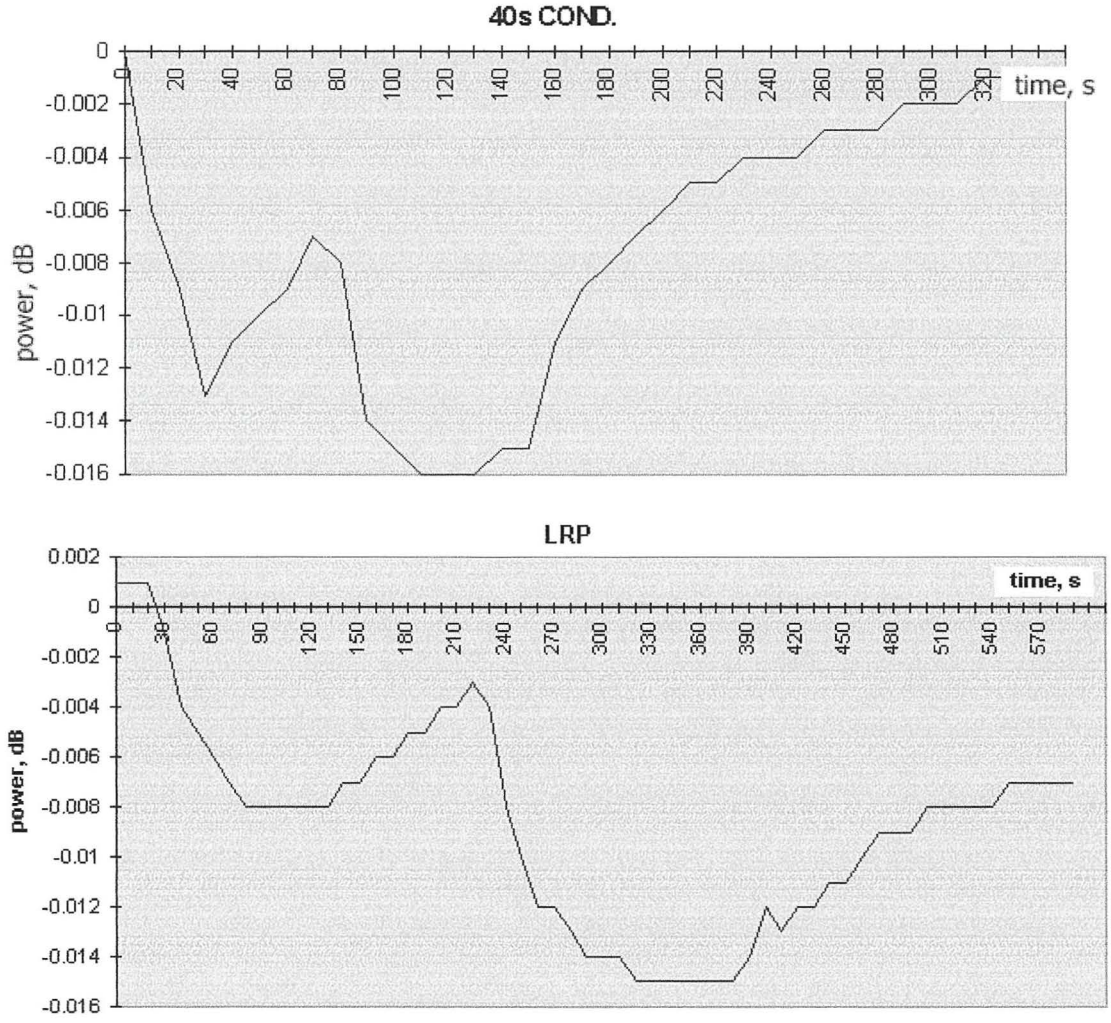

Figure 2.5.4: Response curves obtained for sensor previously exposed to extremes of heat and cold. The upper and lower traces were obtained after exposure to condensate and petrol respectively.

It can be inferred from the diminished responses seen above, that one or more of the components of the sensor were permanently affected or damaged by the environmental program. Hytrel has good resistance to polar fluids at room temperature, but its resistance at temperatures in excess of 70 °C is poor [45]. It is therefore possible that exposure to high humidity and temperatures of 80 °C may have weakened the protective coating and allowed the aramid binder to cut into the surface. Cutting of the silicone elastomer by the aramid thread was seen and was attributed to contraction of the binder whilst the sensor core expanded with rising temperature. Figure 2.5.5 shows an electron micrograph of the sensor after the environmental program.

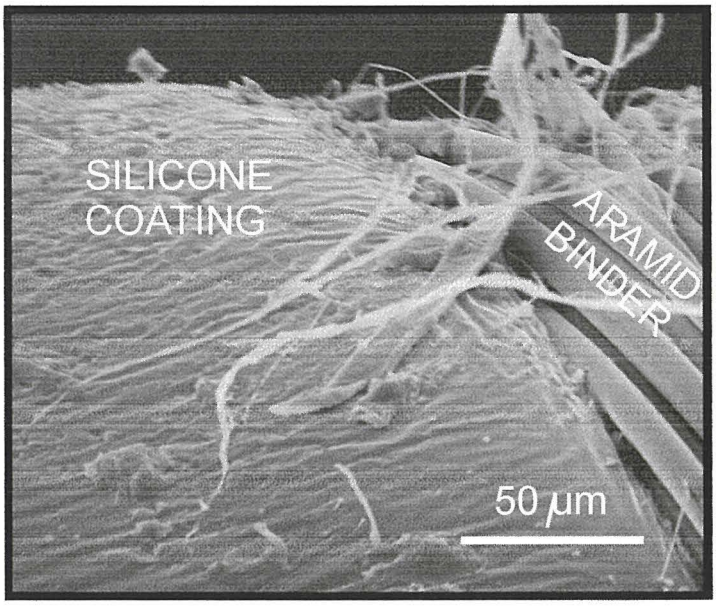

Figure 2.5.5: Scanning electron micrograph showing cutting damage to the silicone elastomer by contraction of the aramid binder during exposure to high temperatures.

A Hytrel sensor of 50 m in length, was completely coiled in a winchester bottle, the sensor was connected to the power meter and cold tap water was added to the bottle and the sensor's response recorded. Figure 2.5.6 (overleaf) shows the results for the first 11 hours of this test. Upon addition of the water the relative power throughput increased over 15 to 20 minutes to a maximum value of + 0.16 dB.

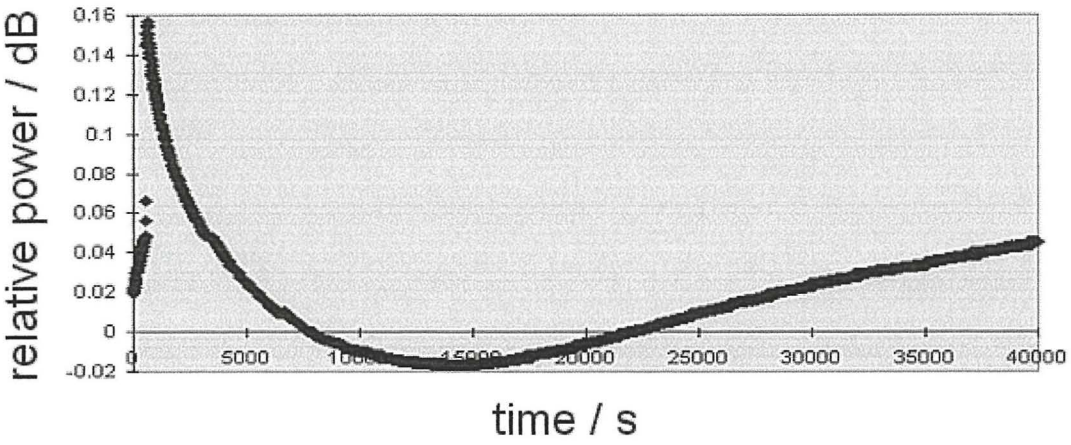

Figure 2.5.6: Results of first 11 hours of water immersion test.

The relative power then fell gradually back towards zero over the following 2 hours, before oscillating around the zero line overnight. It is thought that this was simply a temperature effect. It has been shown in figure 2.5.3 above that as temperature falls, transmitted power increases. Thus, as the water added to the flask was some 10 °C cooler than room temperature, the initial 15 minute rise in power was due to the sensor cooling to match the temperature of the water that had been added. The fall in power over the next two hours was demonstrative of the flask of water equilibrating with the surrounding room temperature air. It fell below zero due to the fact that over the two hours since the test had begun (and the reference value taken) the room temperature had increased during the warm afternoon. Power levels then began to rise when the laboratory cooled as evening and night fell. The data for the following morning concurred with this hypothesis as power again dropped during the morning and early afternoon as temperatures rose. The test was begun in June, 2000. A power reading taken in August, 2000 showed that the power had still not fallen. The power continued to fluctuate and further readings did not fall below – 0.05 dB. It can therefore be concluded that the sensor was sufficiently protected from water (over the range of room temperatures experienced).

2.3.5 Field trials

The first field trial at Tewkesbury demonstrated that the sensor cable could be spliced into a network with existing fibre cable to produce a total system length of well over kilometre. Figure 2.5.7 shows a typical OTDR trace obtained. The locations of each trough are labelled for comparison with the layout diagram included. The small steps observed in the trace are due to splicing losses at the joins between the sensor cable and standard fibre cable sections.

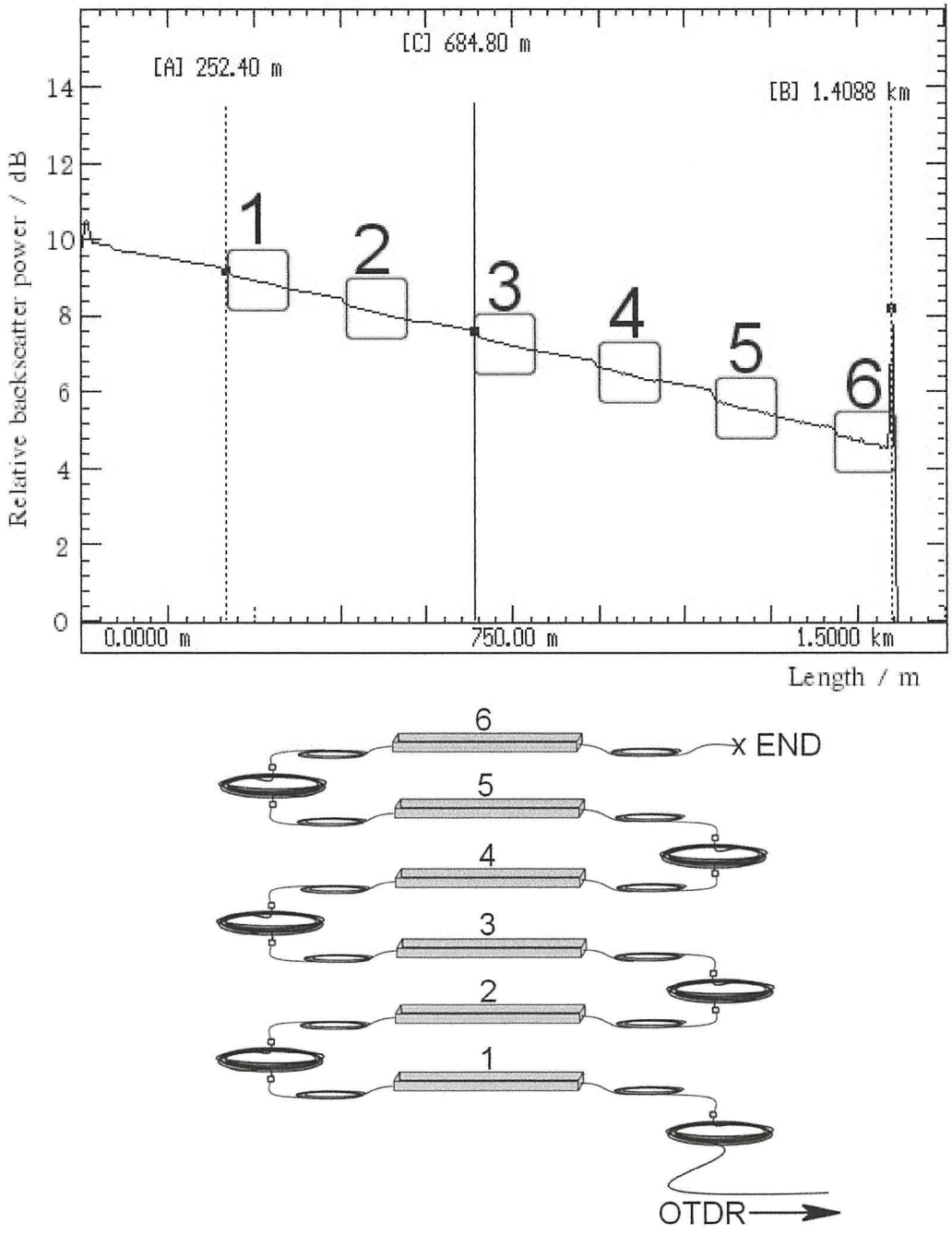

Figure 2.5.7: OTDR trace obtained for Tewkesbury field trial site. Location of sensor lengths are numbered on the OTDR trace for comparison with setup diagram included.

A series of systematic tests showed that each section produced a response to petrol that could be easily detected by eye from an OTDR trace. A series of blind tests were then performed by exposing sections of sensor at random locations to petrol and then inspecting the OTDR trace to attempt to allocate at which point the sensor had been activated (figure 2.5.8). Again, the steps observed in the trace are due to splicing losses at the joins between the sensor cable and standard fibre cable sections. It is the diversion of the two traces that is indicative of an event.

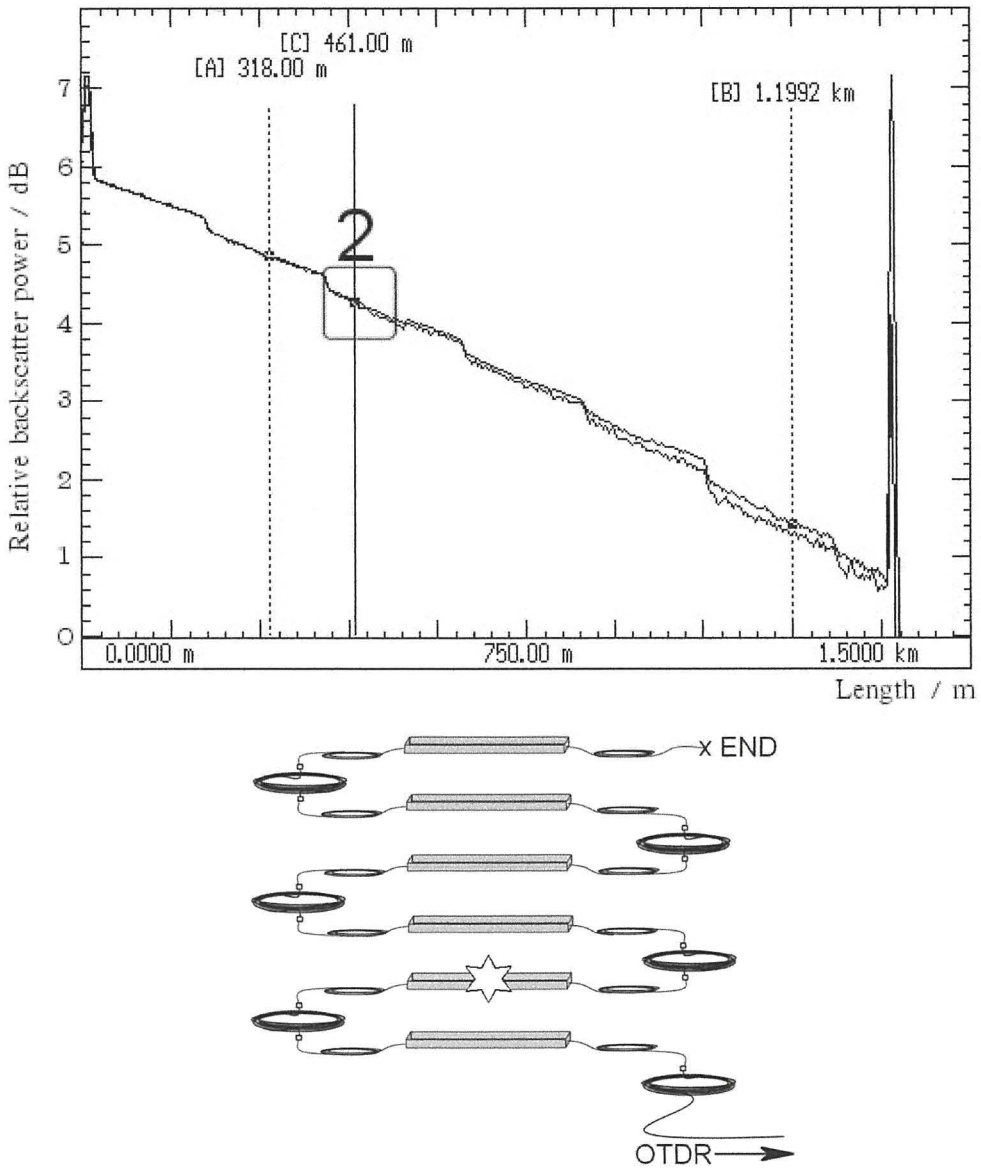

Figure 2.5.8: Results of blind test. When the sensor in trough 2 was exposed to petrol the OTDR trace above was obtained within 2 minutes. The divergence of the sample trace from the reference is clear and is highlighted with a box. This result was obtained in wet and windy conditions showing that the presence of water does not prevent detection.

The second field trial at Pinacl was also a success. Again systematic testing was carried out followed by a series of blind tests. Figure 2.5.9 shows sample results.

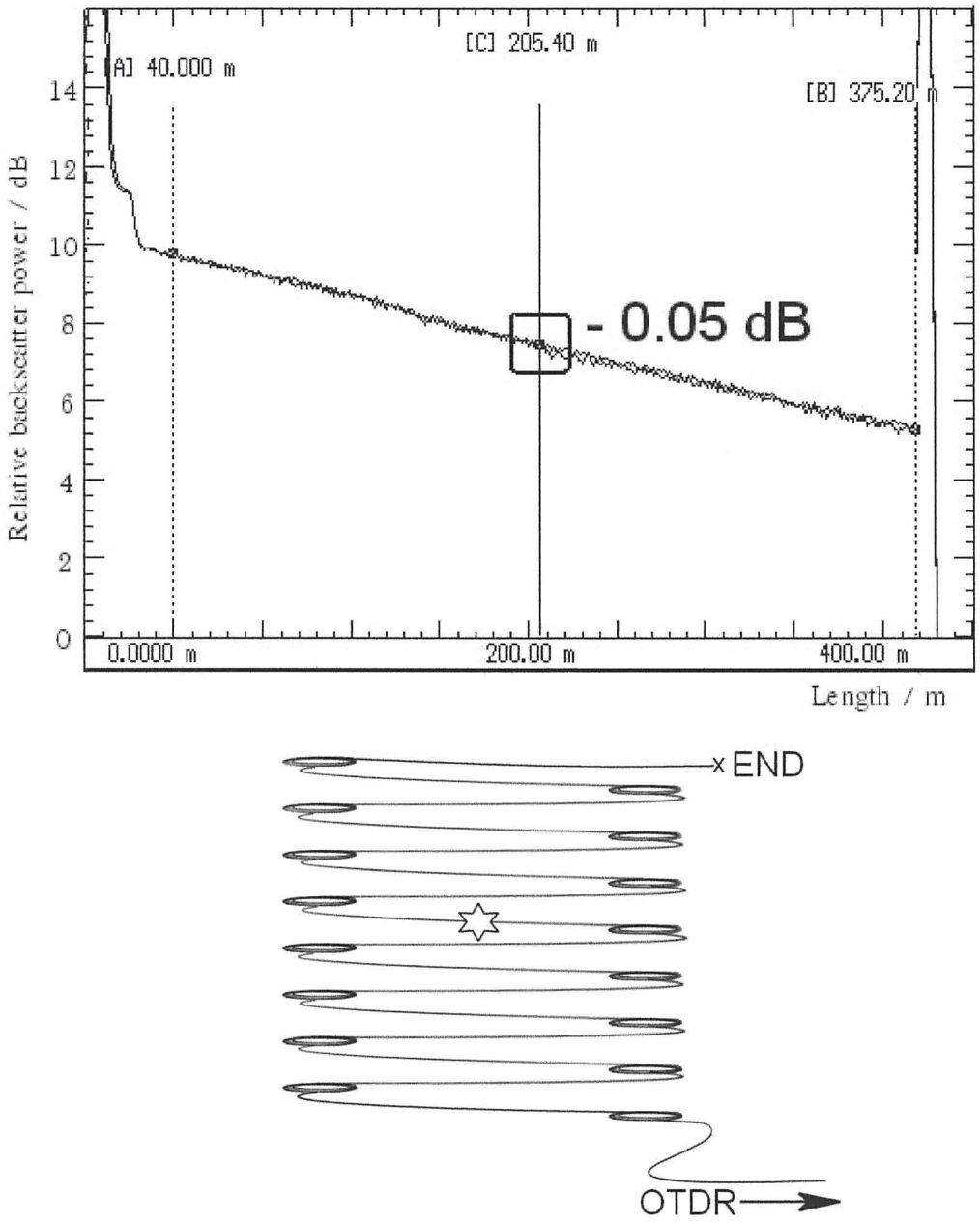

Figure 2.5.9: Result of blind test. When the sensor was exposed to petrol at the position shown, the OTDR trace above was obtained. The divergence of the sample trace from the reference is clear and is highlighted with a box.

The divergence of the two traces was sufficiently clear to be seen with the y-axis sensitivity reduced to a minimum as shown in the figure above. The custom designed OTDR unit was connected to the sensor cable at the second field trial and was capable of detecting events.

At the third field trial, testing of a long length of sensor was performed. Responses to petrol were shown at sections along the length of the sensor and were detected with the custom unit. A final test, at the end of the sensor demonstrated that the detection of events over 2000 m from the OTDR unit was possible. Figure 2.6.0 below shows OTDR traces obtained from 2 separate tests showing that results are reproducible even at ranges greater than 2000 m.

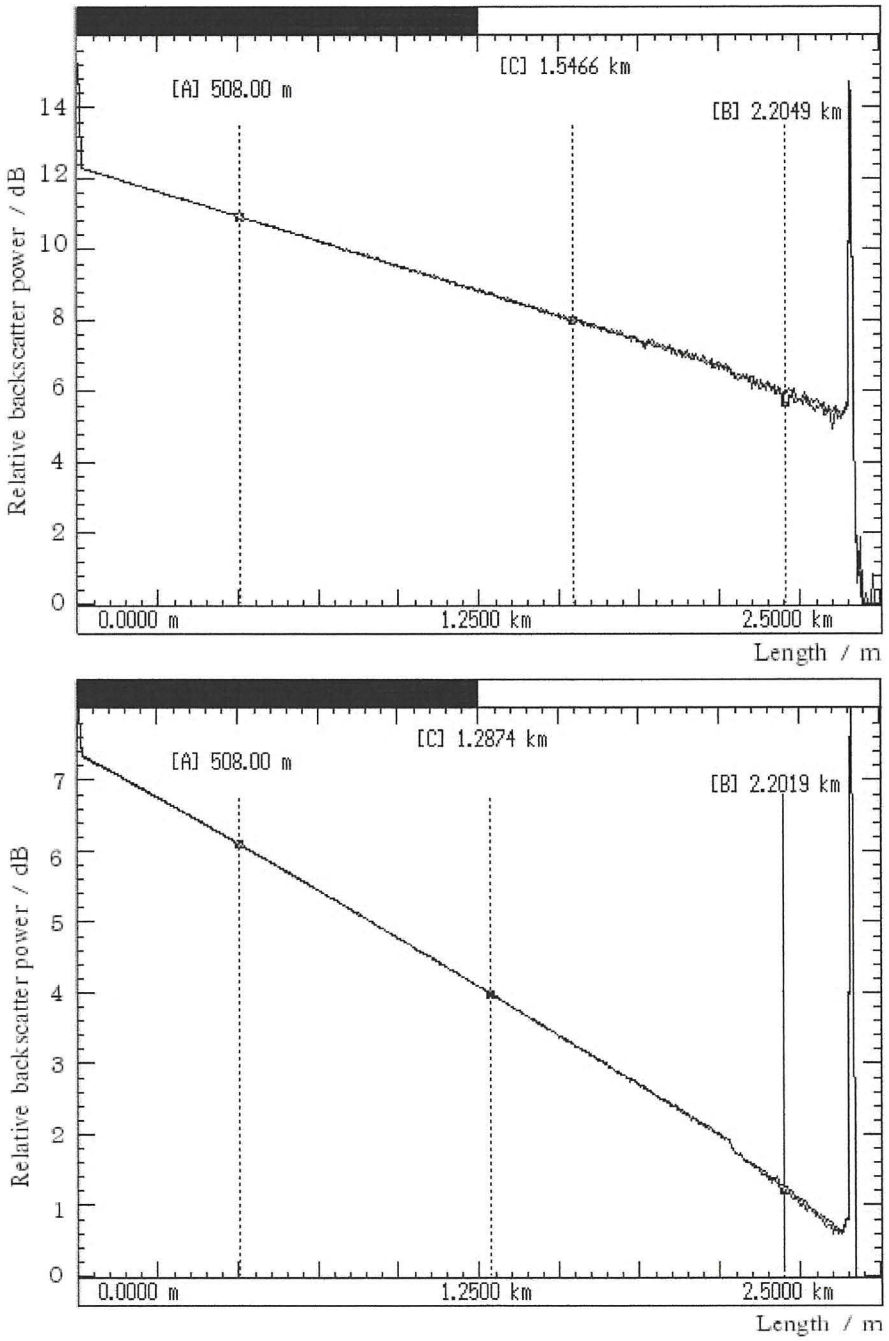

Figure 2.6.0: OTDR responses of a sensor with 1.5 m lengths exposed to petrol at 2.2 km from the OTDR. The divergences of the reference and signal traces are not clear to the naked eye but were detected by the system.

The user interface and detection algorithms required additional modifications to facilitate a clear event display and to improve sensitivity. These changes were completed by the manufacturer before the final field trial. At the trial, the system was set up to mimic a 'real' installation. A petrochemical storage depot was simulated and input into the user interface. Figure 2.6.1 shows the user interface display screen as captured after a double blind test had been performed.

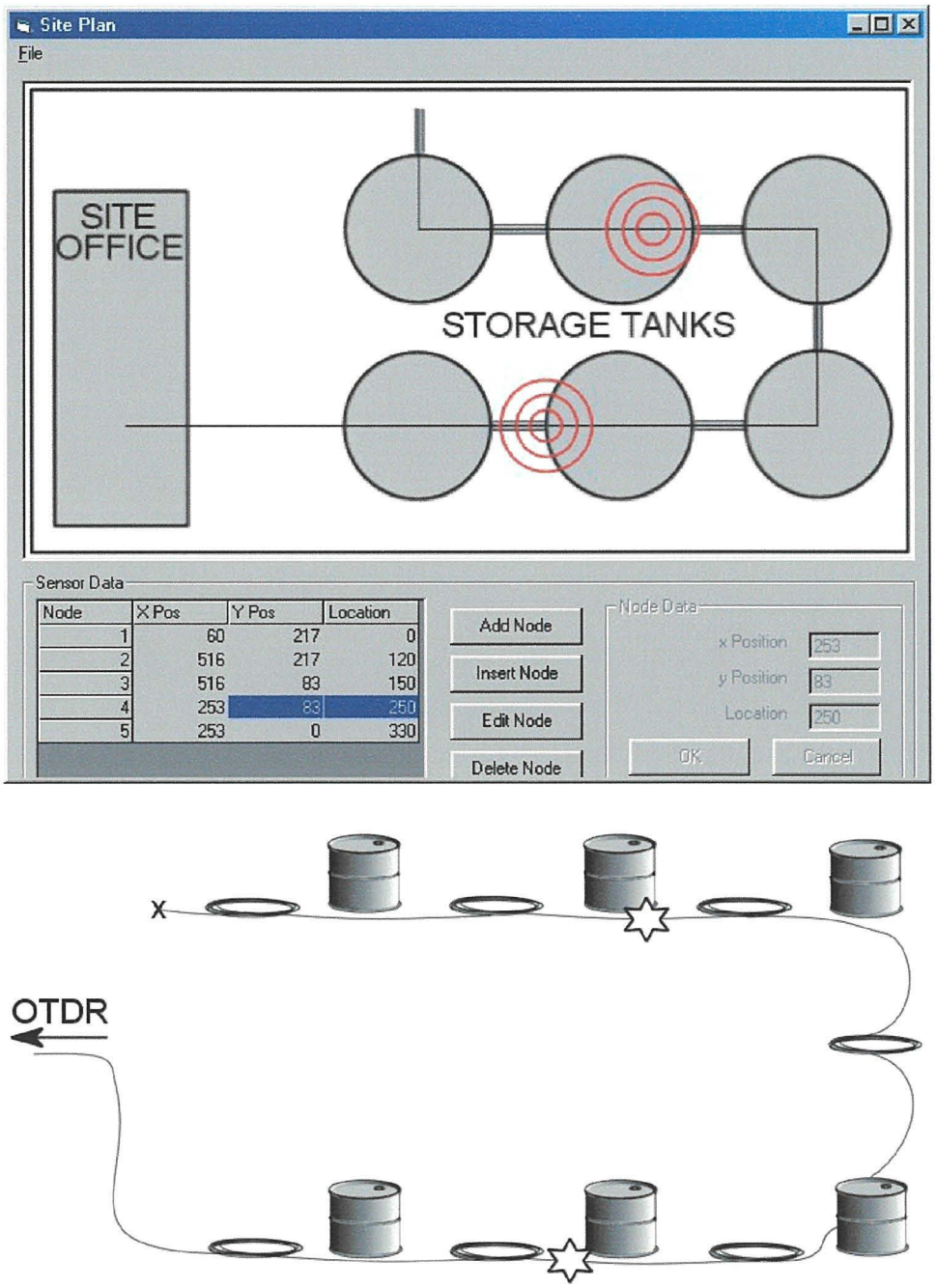

Figure 2.6.1: Results of double blind test. When the sensor was exposed to petrol at the two positions shown, the custom system identified the two locations on its output display as shown.

The OTDR traces obtained are shown in figure 2.6.2.

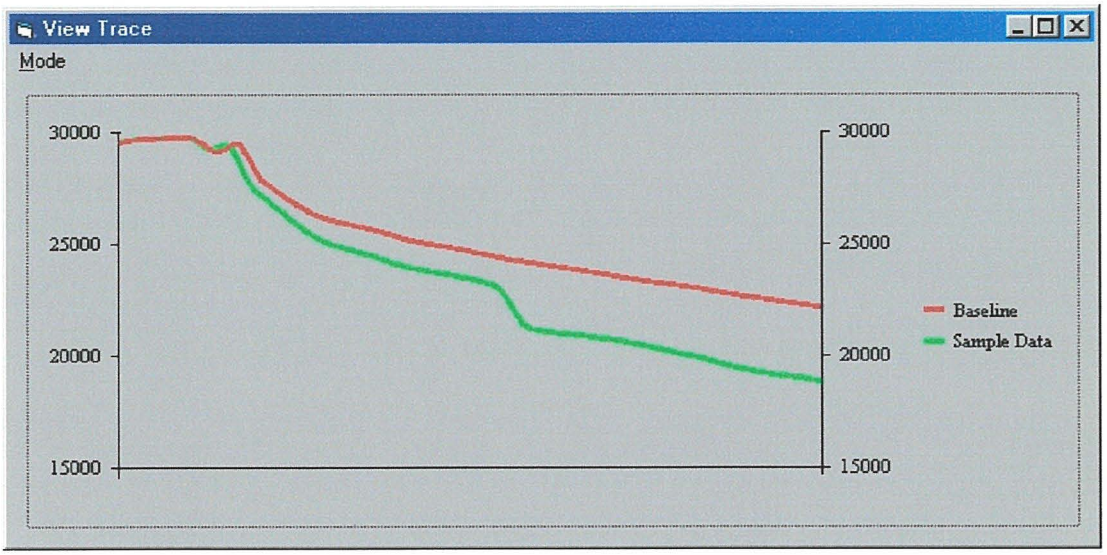

Figure 2.6.2: Baseline (upper) and sample (lower) traces acquired by the custom OTDR. Two concurrent events are observed in the sample data as steps.

The lower sample data diverged from the upper reference trace at two points. These two events were identified by subtraction and differential analysis of the two OTDR traces. The trace that resulted exhibited spikes where events had occurred. These led to alarm triggers if a preset threshold was exceeded as shown in figure 2.6.3.

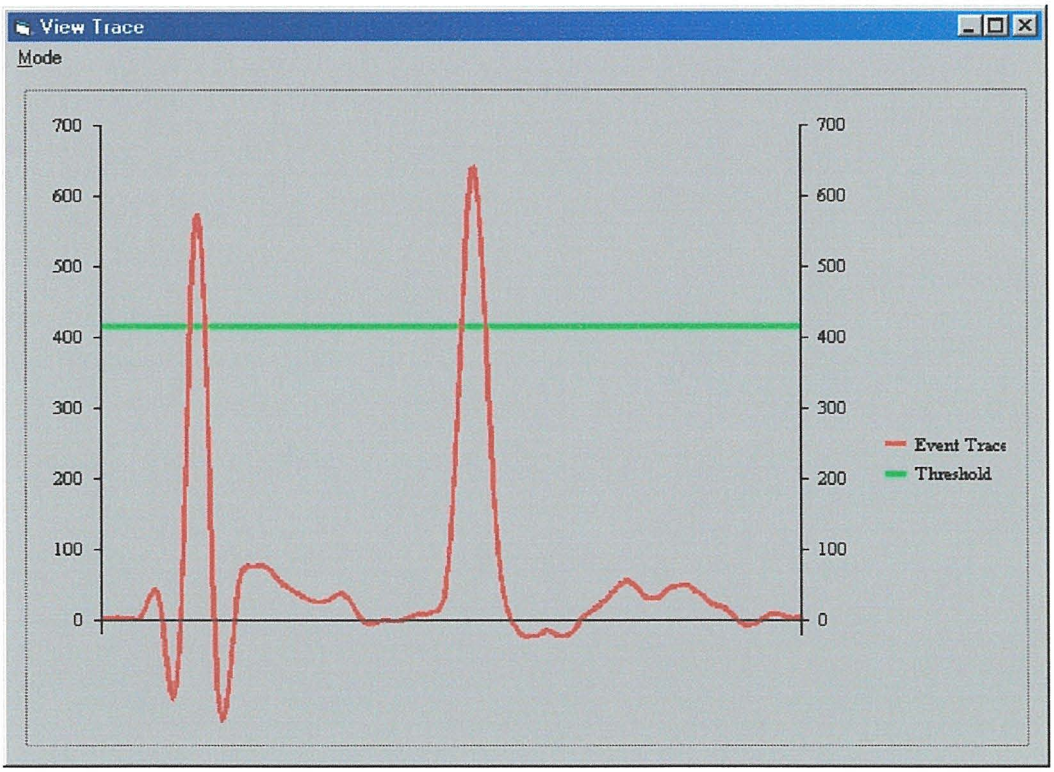

Figure 2.6.3: Result obtained after differential algorithm was applied. Two clear peaks rise above the preset threshold intensity triggering an alarm for the two concurrent events.

The signal processing software developed by SDA for the sensor took 2^{10} averages then stored the trace in a buffer before taking another 2^{10} traces and subtracting the two to spot any changes that had occurred. The software was able to spot differences of less than 0.005 dB. The sensors were tuned to give a response of 0.1 dB per metre wetted, equivalent to 20 times the detection limit of the unit.

The mechanism of operation of the detection system is such that it should minimise false readings due to temperature fluctuations as the signal processing algorithms are designed to detect changes in backscattered power that are localised. As environmental temperature fluctuations will cause either an increase or decrease of the power gradient along the entire sensor length, this should not cause any false alarms. However, it is important to note the system would not be able to distinguish between 'events' triggered by petrochemical exposure and those that may be triggered by localised temperature fluctuations caused by overheating at some point along the cable. Such overheating may be caused by only a small length of sensor exposed to the sun, by exposure to spilled hot fluids or to heating from some other extraneous source such as electrical or mechanical equipment.

2.4 Conclusions

An operating sensor cable has been produced which showed response to petrols in less than 30 seconds and achieved the target response of 0.1 dB per metre wetted. Successful operation of the sensor system at a range of over 2 km was demonstrated. Further development of the sensor to tune it for other analytes must be completed to ensure its competitive edge in the marketplace and to underpin the groundwork that has been carried out during the course of this project.

It was eventually decided that the sensor would use the EP4412 elastomer after consideration of its performance advantages, the likelihood of filler materials and the leaching of plasticisers from the Varflex material and issues relating to the supply and cost of materials. The final sensor design was thus confirmed as a 600 μm Hytrel buffered fibre, overlying a 50 μm, EP4412 coated 0.9 mm GRP rod. The binder tension was set at 15 ğ and a lay length equivalent to the second harmonic at 3 mm was used. One unresolved issue remained to be addressed by the manufacturing parties involved. The use of aramid for the binder led to problems with attenuation and tension damage at elevated or lowered temperatures. This effect may in turn lead to misleading signals in those instances where temperature fluctuation is confined to limited length of sensor. This could be solved by using an alternative binder, such as e-glass yarn, which, in common with the other sensor components has a positive coefficient of expansion, and would minimise the temperature response seen thus far.

It has been observed that occasionally a higher response was seen than was expected. It is thought that this was due to the construction of the sensor binding. The main transduction mechanism of the DISH sensor was an induced microbending effect which will occur wherever numerous small, periodic bends are applied to the fibre and will be accentuated where the bending is applied to the core-cladding interface at a critical spacing dictated by the refractive indices of the core and cladding. Theory states that the periodicity of the binder

thread must be equal to either the fundamental period or one of its harmonics for the microbending effect to be sufficiently large to be observed. The machinery used to manufacture the sensor does not allow sufficiently precise control to guarantee that the applied period is exactly on the required frequency. In addition the binding thread has a finite width of 0.5 mm and can not be said to act at a point but rather to act over a short length (0.5mm) of the fibre. However, the sensors will work almost irrespective of the applied period and it was seen that responses were around 0.07 dB per metre wetted for all the harmonics of the binding. On occasions where the periodicity and the lie of the binder matches a multiple of the critical spacing an enhanced response was observed.

2.5 Further Work

There is considerable scope for the further development of the DISH sensor. Tuning of the sensor for aviation fuel would open up a huge potential range of applications, on the ground and in the air. Development of a sensor for crude oil and common petrochemical or other industrial feedstocks, products and wastes would be similarly rewarded. The DISH sensor could be adapted to monitor for other analytes of interest, particularly noxious or flammable fluids, either gaseous or liquid. Distributed sensing of methane, carbon monoxide or formaldehyde would be highly advantageous and further work could be geared in this direction. Talks between the DISH group, Sensa Ltd. and British Petroleum have yielded a possible pilot scheme. Pipeline simulation tests are ongoing in cooperative arrangement with Sensa Ltd., who are developing a leak detection system. Sensa have developed a series of distributed optical fibre sensors for production and integrity monitoring in downhole applications in the oil and gas production industries. Their systems use Raman backscatter to monitor temperature along fibres up to 15 km in length. They are currently trialling a system for pipeline leak detection which works by detecting localised cooling caused by rapid expansion of high pressure and liquefied gases through faults or leaks. Their system will not work for liquids and thus they are interested in marketing the DISH sensor alongside their own technology.

2.6 References

1 W.C. Michie, B. Culshaw, A. Maclean, M. Konstantaki, S. Hadjiloucas, *Cem. Conc. Compos.*, **19** (1997) 35 - 44

2 W.C. Michie, B. Culshaw, M. Konstantaki, I. McKenzie, S. Kelly, N.B. Graham, C. Moran, *J. Lightwave Technol.*, **13** (1995) 1415 -1420

3 W.C. Michie, B. Culshaw, I. McKenzie, M. Konstantaki, N.B. Graham, C. Moran, F. Santos, E. Bergqvist, B. Carlstrom, *Optics Lett.*, **20** (1995) 103 - 105

4 CONCAWE Product Dossier 92/103 *Gasolines*, CONCAWE, Brussels, (1992)

5 BP-AMOCO, private communication, (2002)

6 CONCAWE Product Dossier 95/107 *Gas oils*, CONCAWE, Brussels, (1996)

7 CONCAWE Product Dossier 99/52 *Kerosenes / Jet fuels*, CONCAWE, Brussels, (1999)

8 CONCAWE Product Dossier 98/109 *Heavy fuel oils*, CONCAWE, Brussels, (1998)

9 C.M. Davis, *Fiberoptic Sensor Technology Handbook,* Optech, Virginia (1986)

10 Boisdé, G. and Harmer, A. (1996) *Chemical and Biochemical Sensing with Optical Fibres and Waveguides*, Artech House, London 389pp

11 B. Culshaw, and J. Dakin, Eds. (1996) *Optical Fibre Sensors – Components and Subsystems vol. 3,* Artech House, London 237pp

12 B. Culshaw, and J. Dakin, Eds.(1997) *Optical Fibre Sensors – Applications, Analysis and Future Trends vol. 4,* Artech House, London 478pp

13 J.W. Berthold, *J. Lightwave tech.*, **13** (1995) 1139 -1199

14 B.L. Anderson, J.A. Brosig, *Optical Engineering*, **34** (1995) 208 - 213

15 J.N. Fields, *Appl. Phys. Lett.*, **36** (1980) 799 - 801

16 F. Luo, J.Y. Liu, N.B. Ma, T.F. Morse, *Sensors & Actuators A*, **75** (1999) 41- 44

17 T.Yoshino, K. Inoue, Y. Kobayashi, *IEEE Proc. Optoelectronics,* **144** (1997) 145 -150

18 D. Donlagic, M. Zavrsnik, *Optics Letters*, **22** (1997) 837 - 839

19 S. Kumar, H.K. Dixit, *Ins. Elect. Telecomm. Eng.*, **40** (1994)197 - 201

20 O.S Wolfbeis, Ed. (1991) *Fibre Optic Chemical Sensors & Biosensors vol. 1.* CRC Press New York

21 A.D. Kersey, *Optical Fibre Tech.*, **2** (1996) 291-317

22 N.Lagakos, J.H. Cole, J.A. Bucaro, *Applied Optics*, **26** (1987) 2171-2180

23 B.G.Grossman, *Canadian Patent* 2242435-A (1999)

24 E.A.Bergqvist, *European Patent* 0490849-A1 (1991)

25 D. Donlagic, B. Culshaw, *J. Lightwave Technol.*, **17** (1999) 1856-1868

26 D.Donlagic, B. Culshaw, *J. Lightwave Technol.*, **18** (2000) 334-342

27 *Concise Encyclopaedia of Polymer Processing and Applications*, P.J. Corish (Editor), Pegamon Press, Oxford, (1992).

28 D.C. Edwards, Chapter 4 in *Handbook of Elastomers*, A.K. Bhowmick and H.L. Stephens (Editors) Marcell Dekker Inc., New York, (1998)

29 K.E. Polmanteer, Chapter 17 in *Handbook of Elastomers*, A.K. Bhowmick and H.L. Stephens (Editors) Marcell Dekker Inc., New York, (1998)

30 S.R. Sandler and W. Karo, *Polymer Syntheses*, volume 2, Academic Press Inc., Orlando, (1977)

31 E.M. Barral, M.A. Flandera, J.A.Logan, *Thermochimica acta*, **5** (1973) 415 – 432

32 J. Comyn, F. de Buyl, N.E. Shephard, C. Subramaniam, *International journal of adhesion and adhesives*, **22** (2002) 385 - 393

33 S.D. Doig, A.T. Boam, A.G. Livingston, D.C. Stuckey, *Journal of membrane science*, **154** (1999) 127 – 140

34 D. Fink, A. Petrov, T. Asmus, V. Hnatowicz, J. Vacik, J. Cervena, *Surface coatings and technology*, **158-159** (2002) 228 – 233

35 A. Vetere, *Fluid Phase Equilibria*, **97** (1994) 43-52

36 T.C. Merkel, V.I Bondar, K. Nagai, B.D. Freeman, I. Pinnau, *J. Polymer Science B: Polymer Physics*, **38** (2000) 415-434

37 B.K. Sharma, *J. Physique IV*, **4** (1994) 713-716

38 E. Favre, *European Polymer Journal*, **32** (1996) 1183-1188

39 E. Favre, Q.T. Nguyen, D. Sacco, A. Moncuy, R. Clement, *Chemical Engineering Communications,* **140** (1996) 193-205

40 E. Favre, P. Schaetzel, Q.T. Nguygen, R. Clement, J. Neel, *J. Membrane Science*, **92** (1994) 169-184

41 E. Favre, Q.T. Nguygen, P. Schaetzel, R. Clement, J. Neel, *J. Chemical Society: Faraday Transactions*, **89** (1993) 4339-4346

42 E. Favre, R. Clement, Q.T. Nguygen, P. Schaetzel, J. Neel, *J. Chemical Society: Faraday Transactions*, **89** (1993) 4347-4353

43 S.E.Cross, W.J. Pugh, J. Hadgraft, M.S.Roberts, *Pharmaceutical Research*, **18** (2001) 999-1005

44 A. Maclean and C.R. Moran, *Summary Of Swelling Comparison Tests For EP4412 and Varflex Silicones*, University of Strathclyde, private communication, 1999.

45 *Fluid and Chemical Resistance Guide*, DuPont Technical Report HYT-504

46 W Johnstone, A. MacLean, C.R. Moran, B. Culshaw, University of Strathclyde, private communication, July 2001

47 J.N. Fields, *App. Phys. Lett.,* **36** (1979) 779 - 801

CHAPTER 3

A reverse micelle, sol-gel method for the production of nanocrystalline titania.

3.1 Introduction

3.1.1 Nanocrystalline titania

Metal oxide materials are the subject of intense research efforts globally and are much reported in the literature [1-31]. These have diverse applications in photocatalysis, environmental technology, chemical synthesis, photovoltaics, sensing, semiconductor devices and protective coatings [1,11,15,32,33,34]. Titania exists in eight possible crystal structures [3,7,13,18,35] : brookite, anatase, rutile, bronze, *columbite, baddeleyite, hollandite and ramsdellite.* The first four occur naturally whereas those listed in italics are synthetic allotropes prepared by high-pressure treatment of either anatase or rutile. Rutile is the only truly stable form whereas all the others are metastable [3], although below a particle size of 14 nm [3] and at lower temperatures [6] anatase is the more stable phase. Calcining of amorphous films at temperatures up to 700 K will generally yield anatase [1,3,18]. The conversion to rutile is then observed as temperatures climb to, and exceed, 900 K [1,3,18]. The melting point of rutile is reached at 2128 K [22]. Only anatase, rutile and amorphous phases are suitable for thin films [5]. It is the semiconductor nature and the associated photoactivity of titania that makes it so interesting for research. Anatase has an indirect bandgap of 3.2 eV [18] whereas rutile possesses an indirect bandgap of 2.92 eV and a direct bandgap transition of 3.13 eV [13]. The bandgap of anatase corresponds with the near-UV region (180 – 350 nm) [36]. Although rutile has a bandgap slightly lower in energy than anatase and would therefore seem a better candidate for photocatalysis, it does not exhibit the extensive surface hydroxylation of the anatase form, which is beneficial to catalytic processes. Absorption of a photon with energy equal to or greater than 365 nm (3.2 eV) will generate an electron-hole pair as an electron is transferred from an oxygen atom to a titanium atom within the titania matrix. Immediate recombination may occur, however if the electron migrates to the surface via a random walk then it may encounter oxygen, which acting as an electron scavenger can prevent the recombination from occurring. The resulting oxygen anion will

react with water producing a highly reactive perhydroxyl radical. The slower moving hole will also migrate to the surface where it will abstract an electron from an adsorbed hydroxide ion generating a hydroxyl radical which will proceed to oxidise any organic material present at the surface. This process is illustrated schematically in figure 3.0.1.

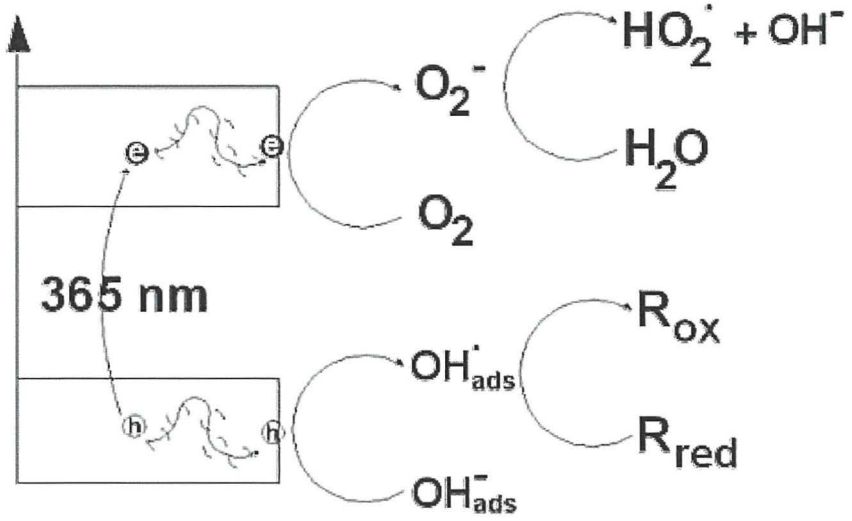

Figure 3.0.1: Photogeneration of electron-hole pairs and subsequent surface reactions.

At the surface the structure is terminated with hydrogen atoms rather than titanium atoms, such that the surface is hydroxylated. This causes the electric potential of the surface to be more negative than that of the bulk. This change in electric potential repels electrons and retards their migration to the surface. However, in the presence of oxygen at the surface the electron can lower its energy by transferring to the oxygen molecule. Figure 3.0.2 illustrates the electron transfer steps taking place as charge separation and migration occurs.

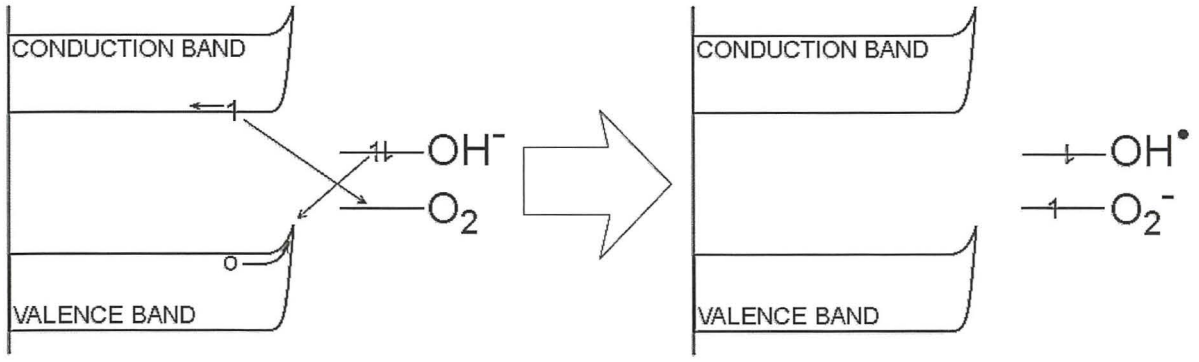

Figure 3.0.2: Electron transfer steps after charge separation (1 = electron, o = hole) showing generation of reactive radical species.

The same property of the surface aids in prevention of recombination as holes will migrate to the higher energy surface. This is due to the readiness of surface electrons to drop into the lower energy holes. Once at the surface a hole is unlikely to migrate towards the bulk as this would require an energy input. Charge separation in this way increases the probability of oxidation at the surface for each photon absorption, and hence improves the quantum efficiency of the device as a whole. By virtue of the fact that the hole will reach the surface before an electron, the oxidising hole tends to react first. This prevents recombination and thus the reductive reaction of an electron with oxygen or another electrophile is inevitable. Anatase has a higher adsorptive activity for oxygen and water than rutile due to extensive surface hydroxylation [18]. It follows from this that removal of the surface hydroxylation will significantly reduce the photocatalytic activity of the surface by aiding recombination of electron-hole pairs.

3.1.2 Sol assembly & reverse micelles

There are several common methods for the manufacture of metallic oxide thin films. Choice of reagent varies substantially but two main classes of precursor [15] are found. These are metal alkoxides [3,6,8,9,11-14,17-23,35,38-43] and metal salts such as tetrahalides [6,28,37,43] and tetranitrates [45]. For the generation of titanium dioxide (titania) films, the prevalent method is the hydrolysis of titanium (IV) alkoxides, with the butoxide (TTB) and propoxide (TTP) forms being most common. Alkoxides are highly reactive compounds [15]; TTP is no exception and is readily hydrolysed in air by ambient moisture. Figure 3.0.3 illustrates the hydrolysis mechanism.

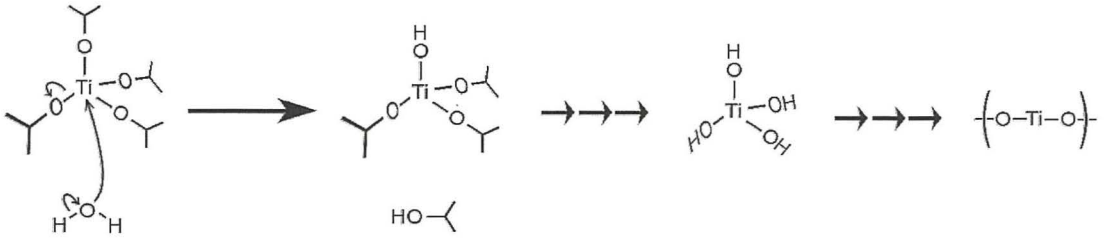

Figure 3.0.3: Hydrolysis of TTP showing condensation of isopropanol, production of the hydroxide after further hydrolysis and the final titania matrix after polycondensation.

Because of this, when endeavouring to generate nanocrystalline materials the kinetics of a procedure are critical as uncontrolled hydrolysis leads to precipitation and subsequent flocculation of larger particles. These large particles are generally opaque with relatively low specific surface area and are used primarily as a white pigment [46]. In order to maintain tight control over the hydrolysis it is necessary to manage the quantity of hydrolysing agent present. The use of a surfactant solution above its critical micelle concentration [40,47] controls hydrolysis rates by limiting the amount of water present and its location. Each individual micelle of surfactant molecules can be likened to a microscopic reaction vessel, which will contain a known amount of reactant material. Sol-gel methods are popular as they allow precise control over the kinetics of the reactions and thus give good control over the final form of the crystalline product. By careful choice of the components of the sol system and the experimental conditions it is possible to dictate the rate of hydrolysis and crystal growth. There are two essentially different approaches to the system; "direct micelles" in an aqueous or hydrophilic environment or "reverse micelles" in a hydrophobic environment. Success in the generation of nanoparticulate materials has been widely reported by both methods. Systems consist of several key components and it is the way that the solvent, surfactant and reactants interact that influence the structure of the sol and therefore of the final product. For example, it is reported [13] that by changing the composition of the solvent the applied coats will differ in thickness. Similarly, changing the length of the hydrophilic chain will alter the structure of the micelles. Auvray *et al* [38] compared TX100 and TX50, two octylphenyl polyether alcohol surfactants that differ only by 4.5 oxyethylene units. They reported that TX100 gave a lamellar liquid crystal phase system where TX50 gave inverse micelles of an oblate-spherical form.

Brown *et al.*[15] reported that the presence of an organic shell around the growing clusters ensures small particle size and has a profound impact on pore connectivity in the final film.

Dabadie *et al.*[21] stressed this, stating that pore size is directly related to the alkyl chain length of the surfactant. Flocculation of any precipitated particles is inhibited by electrostatic repulsion [22], varying the solvent will affect this.

The work described in this chapter relies on the use of an inverse micelle system consisting of a dry cyclohexane solvent with dispersed surfactant molecules of Triton X100™, a well characterised [1,8,14,39,43,47-49] non-ionic surfactant. Other surfactants used in the literature are tetramethyl ammonium hydroxide [11], polyoxyethylene nonylephenol ethers [50], AOT [14], TX50 [40], TX35 [41], acetylacetone [19], alkyltrimethyl ammonium bromides [20,21] and polyethyleneglycol [30,45]. TX100, p-(1,1,3,3-tetramethylbutyl)phenoxypoly(oxyethylene)glycol, is composed of an octyl-phenyl hydrophobic group with a hydrophilic hydroxy-terminated polyoxyethylene chain. Figure 3.0.4 shows the structure of the surfactant used in this work (Triton X-100).

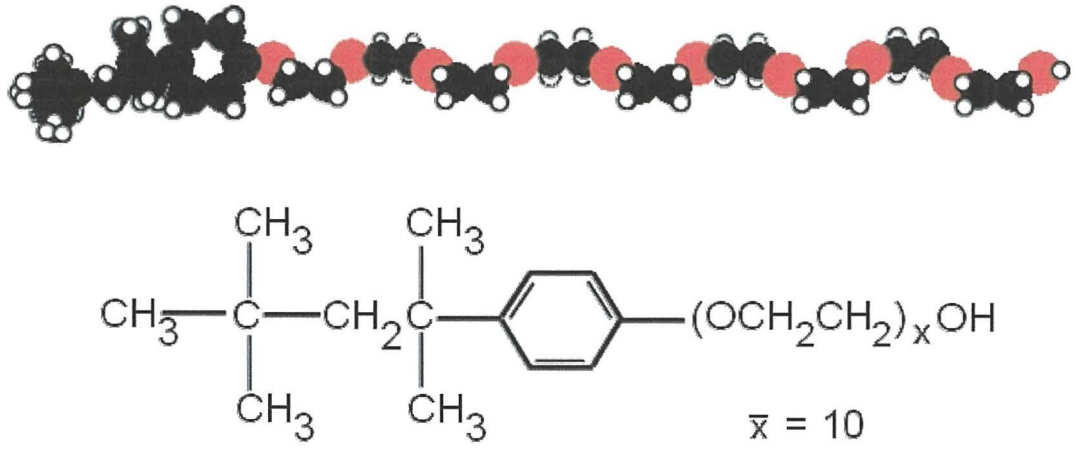

Figure 3.0.4: TX100, p-(1,1,3,3-tetramethylbutyl)phenoxypoly(oxyethylene)glycol

Micelles formed by TX100 are non-spherical and are best described as oblate ellipsoids in form [1,14,47,48]. The apparent hydrodynamic diameter of the micelles in cyclohexane as calculated by the Stokes-Einstein [49] equation varies between 21 nm and 61 nm in the dry (absence of water) and wet (presence of water) states respectively [1,48].

It is important to note that this figure is only a guide to the particle size as the particles do not take up a spherical orientation. It is further noted by Brown *et al.*[49] that the degree of chain extension of the polyoxyethylene moiety is open to question as is the extent of hydration of the micelle. Aggregation number (at 303 K and with a water:surfactant ratio ~ 1) is around 40 [1,48]. The aggregation number is a measure of the average number of surfactant molecules making up each micelle and in the literature is often quoted as a non-integer, mean value. The system is controlled primarily by three experimental parameters [14,37,38,39,48,]:

n- the water:surfactant ratio or the "hydration ratio" (typically in the range 1 - 4)

h- the water:alkoxide ratio or the "hydrolysis ratio" (typically 1 - 2)

m- the concentration of alkoxide solution (as a molality rather than molarity)

An additional quantity, s, can be introduced which is defined as the concentration of surfactant solution in mol kg^{-1}. A value of s = 0.85 mol kg^{-1} was used by Kluson *et al.* [1]. Some confusion can occur with quoted values for m and s, as the units are mol kg^{-1}. Commonly, in surfactant work this is *the number of moles of alkoxide per kilogram of solution* whereas a molality is defined as *the number of moles of solute per kilogram of solvent*. In situations where the solute has a large molar mass, the potential errors caused by this confusion are significant. It is therefore recommended that due care is shown when attempting to reproduce work quoted in the literature where this is left unclear. The hydration ratio, n, is sometimes [1,48] referred to as "R".

It has been shown [14, 38,39,48] that a micelle's structure changes as water is added to the system, *i.e.* as n increases. In the dry state (n = 0) the surfactant molecules are completely solvated by cyclohexane and take up the structure as shown in figure 3.0.5 with the hydrophobic octylphenyl groups facing outwards and the terminal hydroxy groups grouped together in the centre of the micelle [48].

The polar interior of the micelle contains non-polar solvent molecules [55], whereby the ratio of cyclohexane to TX100 can be as high as 4.5 in the dry state, decreasing to 3 at a hydration ratio of 2.5. This is due [55] to solvation of the polyoxyethylene chains by cyclohexane molecules and was confirmed by Zhu and Schelly [55] by UV-vis studies using methyl orange as a probe.

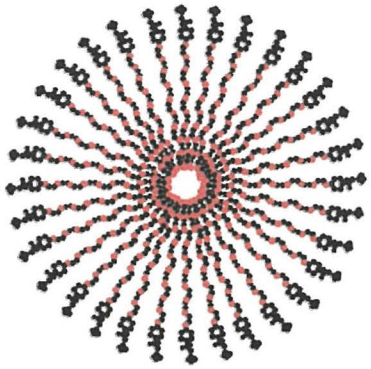

Figure 3.0.5: 2D representation of the orientation of surfactant monomers within the structure of a micelle formed from TX100 in the presence of dry cyclohexane. Note actual shape is non-spherical and best described as an oblate spheroid.

It is this unusual behaviour that determines the aggregation behaviour of TX100 in cyclohexane and it has been shown that TX100 does not form reverse micelles in either benzene (TX100 to soluble) or n-hexane (TX100 solubility too low) [48,55]. In addition to the displacement of solvent, the overall size of the micelle changes with water content, n, and with temperature. Zhu *et al.*[48] report that a maximum micelle size is obtained with mean aggregation number = 40.4 at n = 1.0, T = 303 K. This is illustrated in the graph in figure 3.0.6.

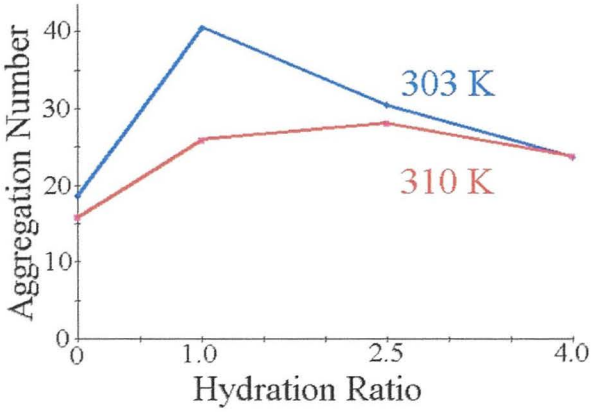

Figure 3.0.6: Effect of Hydration ratio, n, on micelles. (Data from Zhu *et al.*[48])

When the temperature is increased to 310 K the maximum moves higher than n = 1 up towards 2.5, with mean aggregation number equal to only 28.1. Figure 3.0.7 shows the variation of surfactant monomer concentration with changing values of n for the same two temperature regimes of 303 and 310 K.

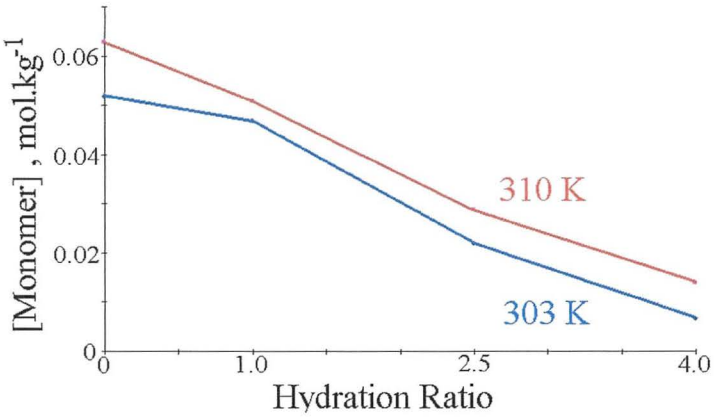

Figure 3.0.7: Effect of Hydration ratio, n, on monomer concentration. (Data from Zhu *et al.*[48])

As can be seen from the above graphs, although there are maxima of aggregation number for both temperatures, the monomer concentration continues to decrease with increasing hydration ratio. It can be thus deduced that as the hydration ratio increases the proportion of surfactant molecules in the micellar state as opposed to the monomer state increases and that at high values of n, micelles contain fewer surfactant molecules but are greater in number. It can also be deduced that as temperature is decreased aggregation is promoted.

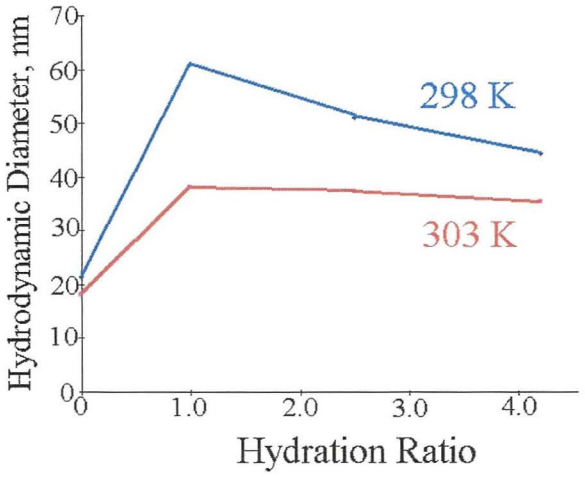

Figure 3.0.8: Change in apparent hydrodynamic diameter with Hydration ratio. (Data from Zhu *et al.* [48]) S = 0.824 mol kg^{-1}

Figure 3.0.8 (above) which shows a plot of apparent hydrodynamic diameter, D_h , against hydration ratio, n, illustrates that apparent micelle size increases as water content increases up to n = 1.0. As can be seen by comparison of figures 3.0.6, 3.0.7 and 3.0.8, the addition of water to the system results in a decrease in free monomer and a corresponding increase in the size of micelles up to a maximum hydrodynamic diameter (around n = 1) of 61 nm and 38.3 nm (at 298 K and 303 K respectively). As further water is added the free monomer concentration continues to fall but micelle size now appears to decrease steadily. It is important to note that as the particles are not spherical, these figures for hydrodynamic diameter are only a guide.

It is a distinct possibility that the steady decrease in micelle size and aggregation number may indicate that the micelle is changing shape as further water is added. It is also worthy of note that for a given hydration ratio the apparent hydrodynamic diameter decreases with increasing temperature, *i.e.* for just a 5° C increase in temperature the apparent hydrodynamic diameter, D_h, decreased by more than a third.

For values of n>1, further solvent is displaced from the micelle core [48] up to a maximum value of n = 4.2 at which phase separation occurs [39], leading to uncontrolled precipitation [38]. Typically, n lies between 1.0 and 2.0 with hydrolysis rate increasing with n.

Peres-Durand *et al.*[39] reported a logarithmic decrease in gelation time, $\mathbf{t_g}$, with increasing hydration ratio:

$$t_g = A\, e^{-kn}$$

Where **A** is a constant characteristic of the surfactant/alkoxide pair and **k** is a constant characteristic of the surfactant only. It has been further noted [38] that to completely hydrolyse the starting material to the divalent oxide, the hydrolysis ratio, h, should be equivalent to the stoichiometric ratio for alkoxide hydrolysis. Papoutsi *et al.*[8] used the combination n = 2, h = 2, as did Stathatos *et al.* [14].

In an early paper, Guizard *et al.* [37] used a value of h = 2.2 whilst assessing the effect of varying hydration ratio on gelation time. Their results indicated that n is a key parameter regulating gelation time and affecting sol evolution and gel structure by affecting micelle size. For n = 1.1, small, slow growing, monodisperse aggregates are formed. For larger values of n (1.3 & 1.5) gelation times halved, producing larger interpenetrated clusters. In a later paper [39] investigating the effects of varying each of the three separate parameters, it is reported that for values of h = 1.7, the amount of water per alkoxide molecule is too low and hence acts as a rate limiting factor. In addition, the paper goes on to conclude that transparent gels can be obtained over only a narrow range of n values and that this range decreases as the hydrolysis ratio or the alkoxide molality increases.

The alkoxide molality, m, is typically [37,39] between 0.8 and 1 mol kg^{-1}. In a recent paper Kluson *et al.* [1] described the generation of nanocrystalline thin films from a sol containing less than 0.7 mol kg^{-1} of alkoxide.

3.1.3 Structure, appearance, calcination & crystallisation

Gel formation proceeds via two processes. This scheme is illustrated in figure 3.0.9 below. Firstly, hydrolysis, by water, of the titanium-alkoxy bonds in the TTP leads to cleavage and the liberation of isopropanol.

$$\text{H-OH} + \text{iPrO-Ti-(OiPr)}_3 \xrightarrow{\text{- iPrOH}} \text{HO-Ti-(OiPr)}_3$$

$$\text{H-OH} + \text{HO-Ti-(OiPr)}_3 \xrightarrow{\text{- iPrOH}} \text{Ti(OH)}_2\text{(OiPr)}_2$$

$$\text{H-OH} + \text{Ti(OH)}_2\text{(OiPr)}_2 \xrightarrow{\text{- iPrOH}} \text{Ti(OH)}_3\text{(OiPr)}_1$$

$$\text{H-OH} + \text{Ti(OH)}_3\text{(OiPr)}_1 \xrightarrow{\text{- iPrOH}} \text{Ti(OH)}_4$$

Figure 3.0.9: The hydrolysis of TTP with sufficient water to allow complete hydrolysis. (iPr = isopropyl)

This results in the formation of intermediate compounds with 1,2,3 or 4 hydroxy groups around the central titanium atom. In the presence of an excess of water this reaction will rapidly go to completion with the rapid precipitation and subsequent flocculation of titanium hydroxide out of the solution.

In a dry micellar environment where water, the hydrolysing agent, is limited and contained within the micelle core, the rate of hydrolysis is slow and due to lack of water will not go to completion. This means that only the monohydroxylated intermediate is likely to be formed (for a hydrolysis ratio of 1) and it is at this point that the second process becomes significant. Polycondensation reactions, where two titanium intermediates react together to form Ti-O-Ti linkages are responsible for the beginnings of the gel network. Where two monohydroxylated titanium intermediates come together (illustrated in figure 3.1.0) they can polymerise with an associated condensation of water which can then lead to further hydrolysis of alkoxide groups on the same or nearby molecules.

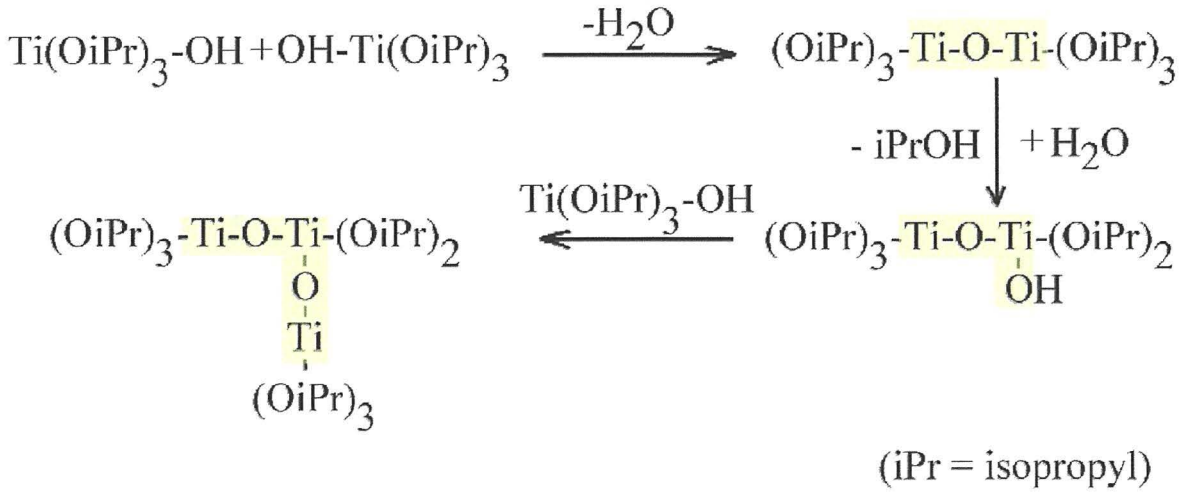

Figure 3.1.0: An illustration of one of many possible polycondensation routes resulting in the development of Ti-O-Ti linkages (highlighted), leading to the formation of a titania network.

This slow process of polycondensation will continue until all isopropoxide groups have been cleaved and the titania network is completed. This mechanism leads to an amorphous network of crosslinked Ti-O-Ti-O-Ti chains. The presence and distribution of surfactant residues form

an integral part of the final gel structure. Also present in the interstices of the growing titania network are the reaction products (water and isopropanol), together with unreacted starting material, namely titanium isopropoxide, and cyclohexane solvent.

Of the structure of the raw gels, organic residues [1] account for some 55 – 60 wt % of the gel. In order to obtain a pure titania film these residues need to be removed by application of a high temperature (> 523 K) calcining routine. The thermal treatment has several purposes. The high temperatures vaporise volatile organic carbon (VOC) compounds from within the gel matrix, which are subsequently thermolysed. This removes the surfactant residues which contribute a large proportion of the set gels and any remaining solvent or reaction products. The thermal treatment also aids in the densification of films and the development of the anatase [3,5,7] crystal structure. The crystallisation of anatase occurs around 573 K together with associated morphological changes such as sintering of the titania nanoparticulates and continued grain growth.

Figure 3.1.1, adapted from Peres-Durand *et al.*[39], shows typical differential thermal analysis results of the transition of amorphous titania to the anatase form. The initial exotherm at around 573 K is the region in which the anatase formation occurs.

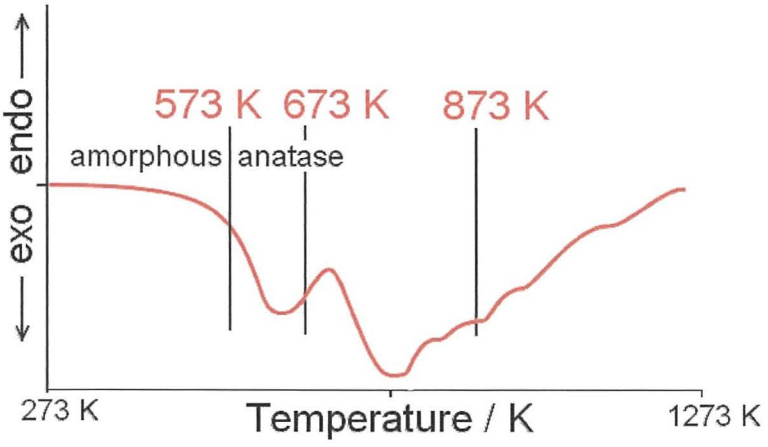

Figure 3.1.1: Typical DTA trace showing amorphous to anatase transition [39].

Further exotherms are seen after 673 K, but these have no associated allotropic transitions. These further exotherms are the result of the elimination of organic residues within the matrix.

It is interesting to note therefore, that the transition to the photoactive form of titania occurs before the destruction of organics. This has profound implications for possible autophotocatalytic destruction of the surfactant residues. The additional change in mass above 673 K, associated with the organic destruction is confirmed with thermogravimetric analysis (TGA), as shown in figure 3.1.2 below.

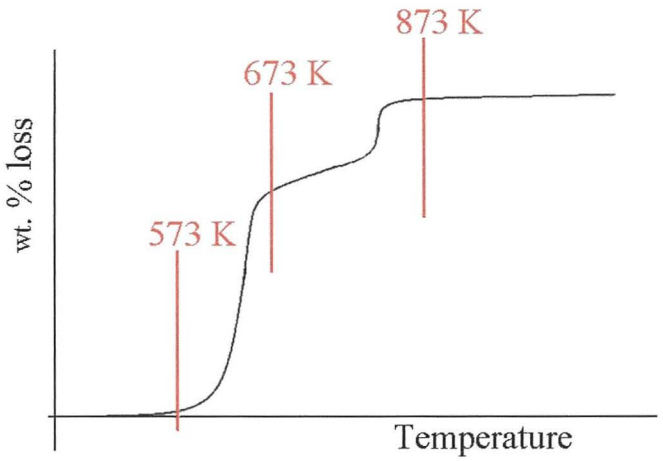

Figure 3.1.2: TGA results illustrating organic destruction from films [40].

Development of crystal structure may also be observed with X-ray powder diffraction methods. Figure 3.1.3 illustrates the spectra for the main crystallographic phases of anatase obtained at low temperatures. The peaks for rutile are also shown.

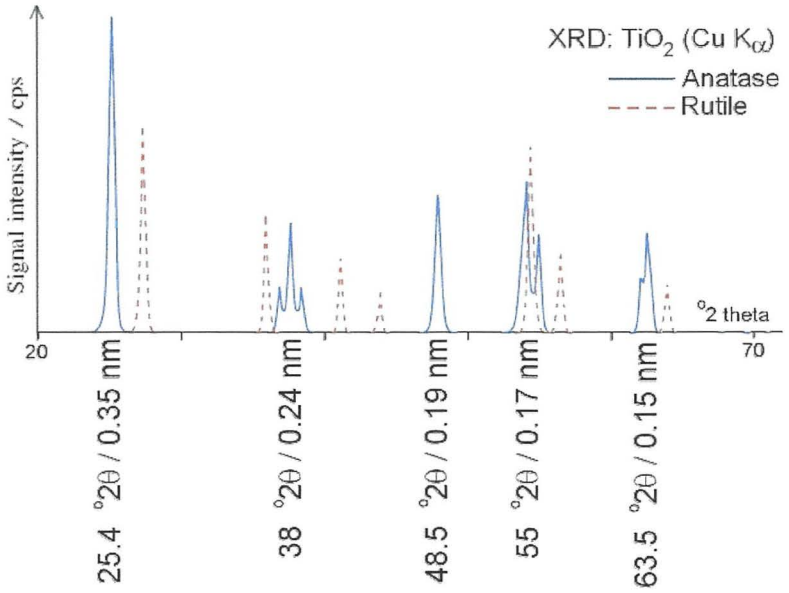

Figure 3.1.3: Illustration of the main diffraction peaks for anatase (and rutile) titania.

3.2 Experimental

3.2.1 Production of sols and viscosity measurement.

Sols of Triton X-100, a non-ionic surfactant, were assembled in dry cyclohexane at concentrations in excess of the critical micelle concentration. Ultra-high quality water was added, followed by the addition of a liquid titanium alkoxide, after stirring. The composition as recommended by Kluson *et al.*[1] was used with the following stoichiometries: n = 1, h = 1, S = 0.85 mol kg^{-1}. Triton X100 (Sigma-Aldrich, 99.99%) was added to dry cyclohexane (Sigma-Aldrich, HPLC grade, water content <0.01 %) to give a surfactant concentration of 0.85 mol kg^{-1}. Water (UHQ millipore water, >18 MΩ.cm) was added, at a hydration ratio of 1.0, and the sol stirred for 1 hour in a waterbath at 303 K, under a nitrogen atmosphere in a closed vessel. Liquid titanium (IV) isopropoxide (TTP, Sigma-Aldrich, 99.999 %) was then added at a constant molar ratio of 1.0 and the solution stirred briefly before transferral to a water-jacketed vessel at 303 K for viscosity measurement. This produced a sol with final alkoxide concentration, m = 0.68 mol kg^{-1}. Viscosity measurements were made on sols to determine the gelation time. A Brookfield rotary viscometer was used for all measurements, figure 3.1.4.

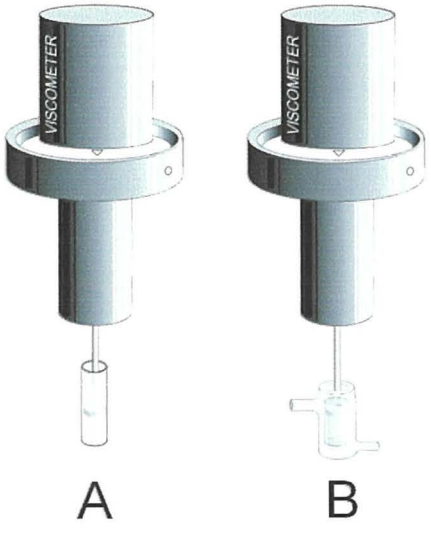

Figure 3.1.4: Rotary viscometer setups used for viscosity measurements of sols.
A: without temperature control; B: with temperature controlling water jacket

Viscosity measurements were converted to a relative scale from 0 – 1, with 0 being the initial viscosity of the sol before addition of the alkoxide and 1 being the observed viscosity maximum. After viscosity measurements were completed the gels were poured onto watch glasses to allow gelation and evaporation to come to completion.

3.2.2 Post-production treatment and aging of gels

As-produced, 'raw' gels were either stored immediately or left for further tests. Some gels were poured onto watch glasses to allow evaporation of solvents and reaction by-products before storage. Others were covered and sealed immediately to prevent evaporation. Some samples were stored in the light, others in the dark. Some samples were washed to remove the oily exudate that covered gel surfaces. Washing was performed in dry cyclohexane (Sigma-Aldrich, HPLC grade) and washed samples were dried open to the air (at room temperature or at 343 K) on filter papers and the resulting 'xerogels' were then stored in dry sample tubes. Heating of raw gels to accelerate solvent evaporation was performed in a laboratory oven open to the air at 343 K for between 2 and 24 hours. The resulting monolithic, 'whole' gels from this process were either broken up and stored in dry sample tubes or left in the dish for further testing. The aging characteristics of these whole gels were monitored and their evolution recorded. Selected raw gel, xerogel and whole gel samples were pulverised and stored in a powderlike form for further analysis.

3.2.3 Calcining & crystallisation of gels

Raw, whole and xerogel samples and powders were subjected to thermal treatment in the presence of air in a bench-top muffle furnace. Samples were placed on a heat-resistant watch glass and exposed to elevated temperature regimes in the range 15 – 850 °C (288 – 1123 K). Temperature was monitored with a handheld meter connected to a thermocouple probe.

Exhaust gases were pumped to waste providing an artificial airflow through the heating chamber. Samples were treated for time periods ranging from 10 minutes up to several hours. After thermal treatment, calcined powders were stored in dry sample tubes.

3.2.4 Characterisation of monolithic gels & titania powders

Digital photographs of gels were taken for comparison of gel colour and appearance. Infrared spectroscopy was performed on a Perkin Elmer 1600 series FTIR spectrometer. Elemental analysis to determine total residual carbon content of gels and calcined powders was performed on a Carlo Erba 1108 analyser. Crystallinity of raw, calcined and xerogels was determined by X-ray powder diffraction analysis on pulverised samples. A Philips X-Pert diffractometer using a Ni filtered Cu Kα source operating at 40 kV and 45 mA was used for all measurements. Fast scans of 30 minutes duration, and long scans of 10 hours duration were performed over a range of 5 – 75 °2θ.

3.3 Results and discussion

3.3.1 Production of sols & viscosity measurement

Surfactant solutions of TX100 in cyclohexane (0.85 mol kg^{-1}), prepared to the prescribed, literature composition, were clear and colourless after thorough mixing. Upon the addition of water, a slight turbidity was observed which was attributed to the formation of complex surfactant assemblies containing relatively large pools of water. After vigorous mixing for 1 hour, the micellar solutions became clear and colourless as water was efficiently dispersed amongst small micelles. Upon addition of the alkoxide the solution attained a pale straw colour that remained unchanged throughout the gelation process. After addition of the alkoxide to the sol there was an initial induction period where no change in viscosity was observed and it is thought [1,37] that this corresponds to the diffusion of the alkoxide to the centre of the micelles and to the initial hydrolysis within the micelle. Figure 3.1.5 shows the induction period and the characteristic gelling curve obtained.

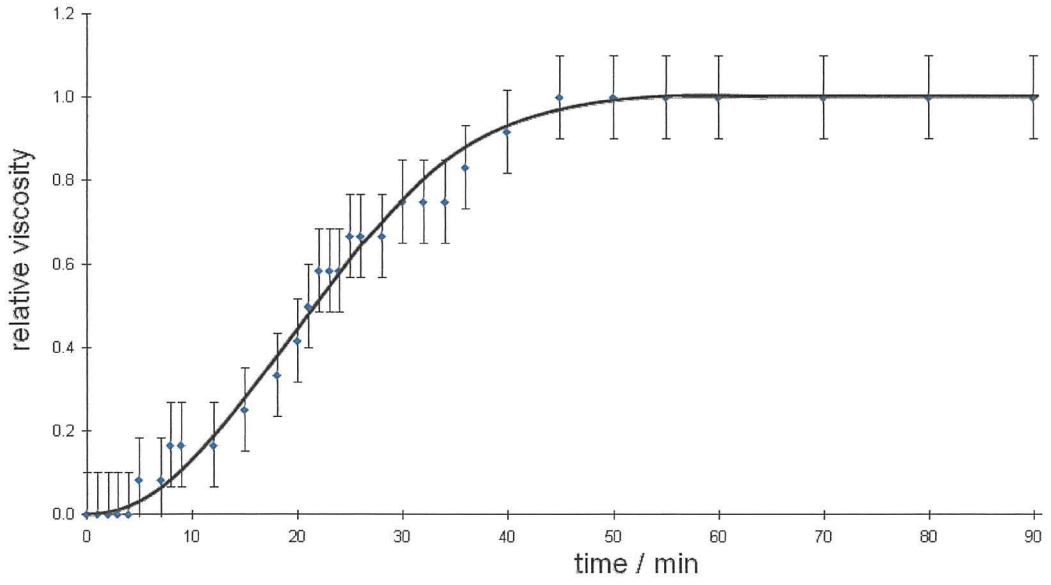

Figure 3.1.5: Viscosity curve showing progression of gelling. (Alkoxide was added at t=0)

The initial region of the curve is flat, corresponding to an induction period where the alkoxide migrates to the micelle core and hydrolysis products begin to be generated. (Others, notably Guizard et al. [37] have reported a similar induction period.) These intermediate compounds

then begin the polycondensation step in tandem with further hydrolysis. This is mirrored by an increase in viscosity of the sol. As the polymeric amorphous networks continue to grow and hydrolysis and polycondensation slow down a decrease in gradient is observed leading to the point of gelation completion where the curve flattens off. It is worth noting that although the viscosity of the sol does not appear to increase after this point, the sol still appears as a viscous liquid and not as a solid gel. It is likely that as hydrolysis has not gone to completion, that insufficient structure exists for a solid consistency. In addition, the presence of substantial quantities of solvent, namely cyclohexane, acts to inhibit densification of the gel. As solvent evaporation occurs the viscosity continues to rise. This effect was clearly seen if sol viscosities were measured after 24 and 36 hours, as illustrated by the example trace shown in figure 3.1.6.

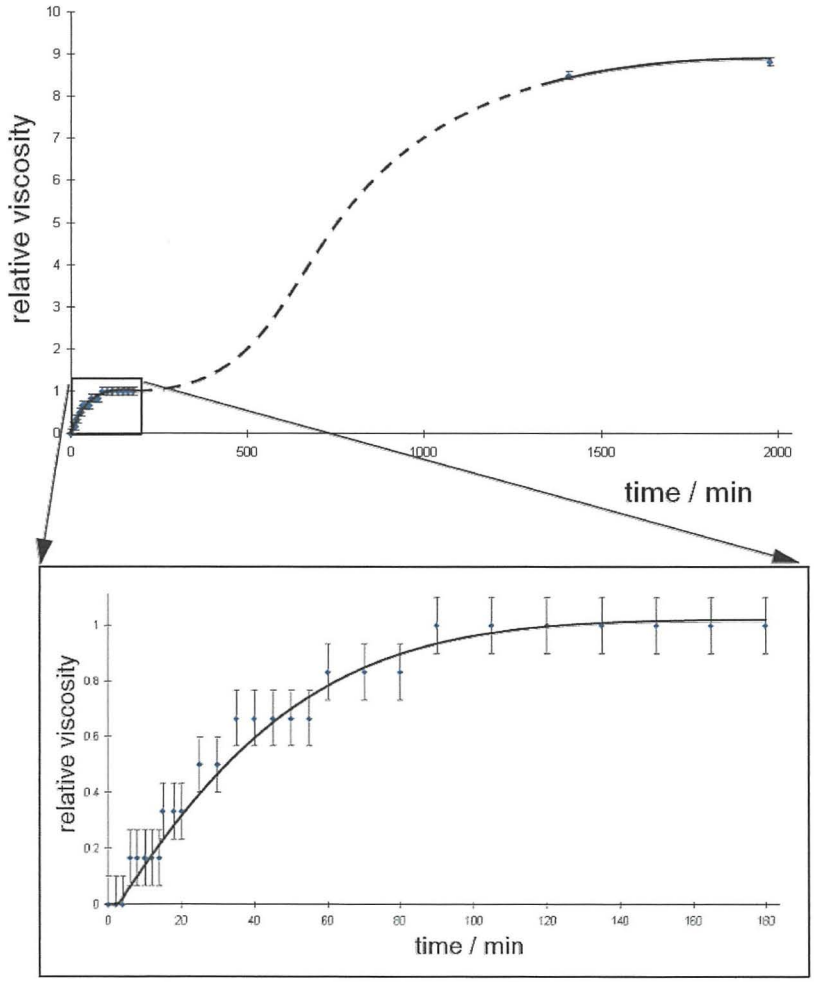

Figure 3.1.6: Gelling curves obtained over a 36 hour period illustrating the effects of evaporation upon viscosity after gelling completion.

3.3.2 Post production treatment and aging of gels (washing, drying and storage)

Figure 3.1.7, A, shows the consistency of the completed gel without exposure to ambient air. The dish remained covered after the completed sol was poured and it remained smooth and intact. Figure 3.1.7, B, illustrates the effect on the gel of evaporation and atmospheric moisture, where extensive cracking of the gel has occurred as solvent and reaction products such as isopropanol were liberated. The colour of both gels A & B is representative of the pale straw colouring of the coating sol. After several hours exposed to air and light in the laboratory the colour of gels changed markedly to an intense yellow colour, figure 3.1.7, C, which fluoresces under white light from a xenon arc lamp. After uncovering, the gel in A cracked and took on the appearance of B. It is interesting to note that where evaporation and contact with ambient moisture is totally prevented (by sealing sols in airtight jars with no headspace) sols do not gel and remain in a liquid state indefinitely.

Figure 3.1.7: Bulk gels in the covered raw state, A, the uncovered raw state, B and the final aged state, C showing changes in colour and texture.

Titania sols and the resulting gels obtained are characteristically clear, often with a pronounced yellow colouration. This yellow colouration is reported with both Ti (IV) isopropoxide [8] and Ti (IV) butoxide [51-54] precursors in the production of titania sols. The yellow glacé gel that was reported by Papoutsi *et al.* [8] for a similar coating sol was attributed to high alkoxide content of the gel although the same phenomenon was observed here for a sol with an alkoxide molality less than that recommended in the literature. As discussed earlier, the recommended [37,39] range of alkoxide molality lies between 0.8 and 1.0 mol kg^{-1}.

In these experiments the system used a molality of 0.67 mol kg^{-1}, a hydration ratio of 1 and a hydrolysis ratio also equal to 1. The ratios recommended as optimum by Papoutsi *et al.*[8] were n = 2, h = 2 and equimolar amounts of alkoxide to surfactant. It has been further reported [39] that hydrolysis ratios of 1.7 or less will act as a rate limiting factor due to the amount of water per alkoxide molecule being too low. The fact that sols did not gel in the absence of atmospheric moisture confirms that there was insufficient water in the initial sol for complete hydrolysis to occur.

After aging at room temperature for several days the gels began to liberate an oily exudate. The exudate was soluble in cyclohexane and after rinsing yielded a glass-like gel of a more brittle nature. After rinsing with cyclohexane no further sweating was observed. Following failed attempts with mass spectrometry, the exudate was identified by infrared absorption analysis. Comparison of the spectra obtained for the exudate with those of the pure surfactant, TX100, showed a clear correlation (figure 3.1.8).

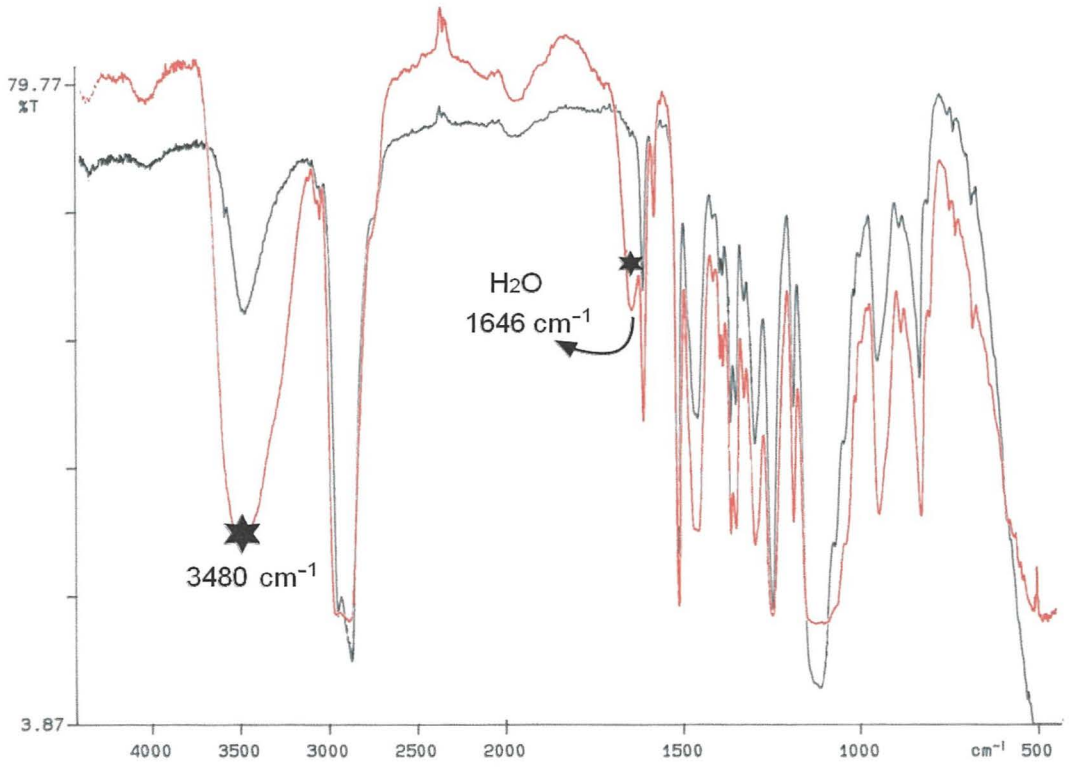

Figure 3.1.8: Comparison between FTIR spectra of gel exudate (red) and Triton X-100 (black). Key differences due to water inclusion at 1646 and 3480 cm^{-1} are highlighted.

This indicates that a large proportion of the residual surfactant was exuded from within the gel interstices as solvent evaporation proceeded. The two traces overlay fairly well, but two clear differences may be observed at 1646 and 3480 cm^{-1}. These indicated the presence of water in the exudate. As water was a product of the polycondensation reactions within the gel, it is only to be expected that it would be present within the gel interstices after gelling completion. Confirmation of the identification of the exudate was obtained by comparison of the FTIR absorption spectra for the exudate and a sample of TX100 that had been hydrothermally treated in a steambath for 20 minutes at 100 °C. The two over-laid spectra are shown below in figure 3.1.9.

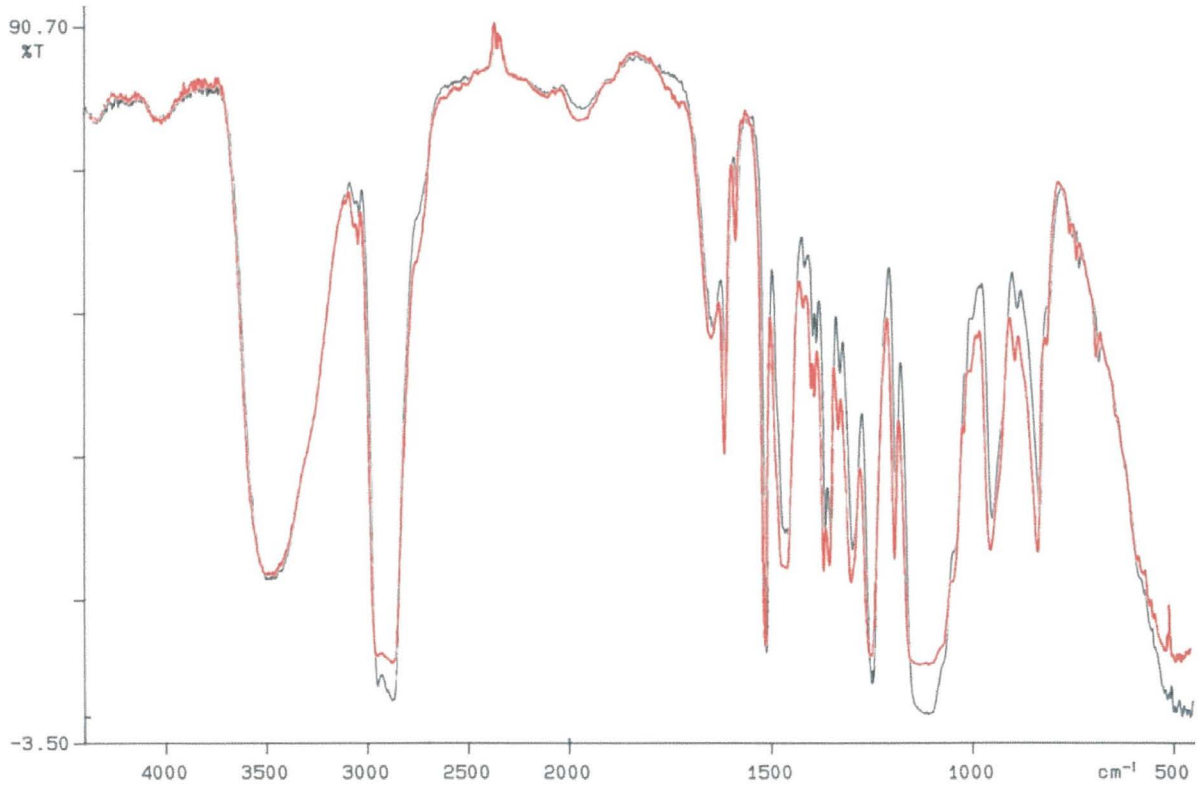

Figure 3.1.9: Comparison between FTIR spectra of gel exudate (red) and steamed Triton X-100 (black).

A near-perfect fit was obtained indicating that the exudate was primarily surfactant with added water that may or may not be bound to the Triton X-100.

3.3.3 Calcining and crystallisation of gels

During thermal treatment, raw gels underwent a characteristic sequence of changes in appearance as temperatures were ramped. Blackening of the yellow gel with accompanied smoke evolution was seen at temperatures greater than 473 K, sometimes followed by spontaneous ignition of the evolving gases at around 523 K or greater. The volume and density of smoke decreased with increasing temperature until a point was reached where no further change was observed, at which point, at 700 K and above, a pale yellow, crystalline powder was obtained. Upon cooling to room temperature the powder lost its pale yellow colour and became white. Figure 3.2.0 is a graph of residual carbon content (as measured by elemental analysis) against maximum treatment temperature.

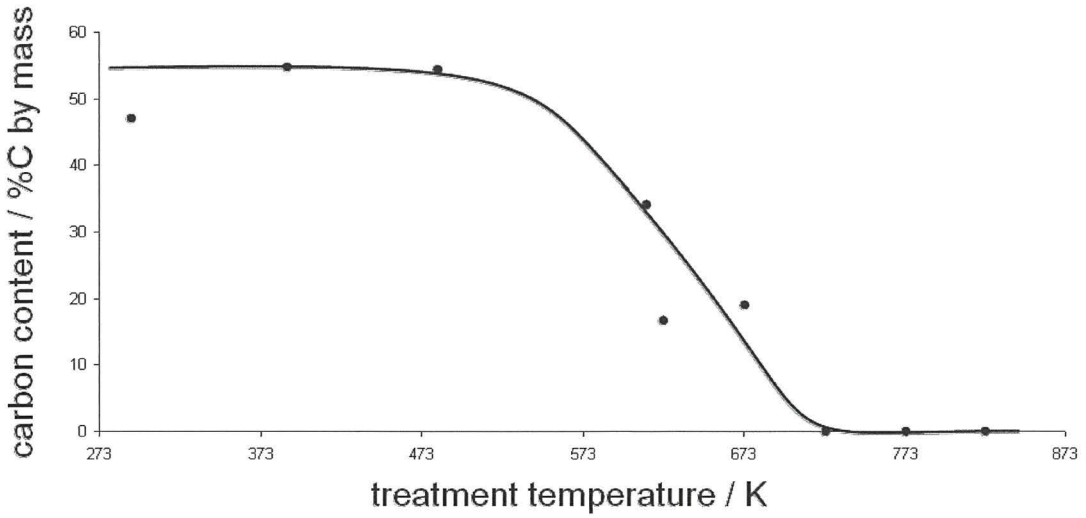

Figure 3.2.0: Results of elemental analysis of gels after thermal treatment. Graph shows residual carbon content as %C by mass *vs.* maximum treatment temperature in degrees Kelvin.

Electron micrographs of gels treated at different temperatures indicate that the degree of crystallinity increases with treatment temperature. Figure 3.2.1 (overleaf) shows the morphology of a pulverised raw gel sample. Figure 3.2.2 (also overleaf) shows a series of electron micrographs of a gel that had been thermally treated at 673 K. The raw gel (figure 3.2.1) has a gelatinous appearance although under high magnification it is possible to discern a measure of structure in a layered morphology.

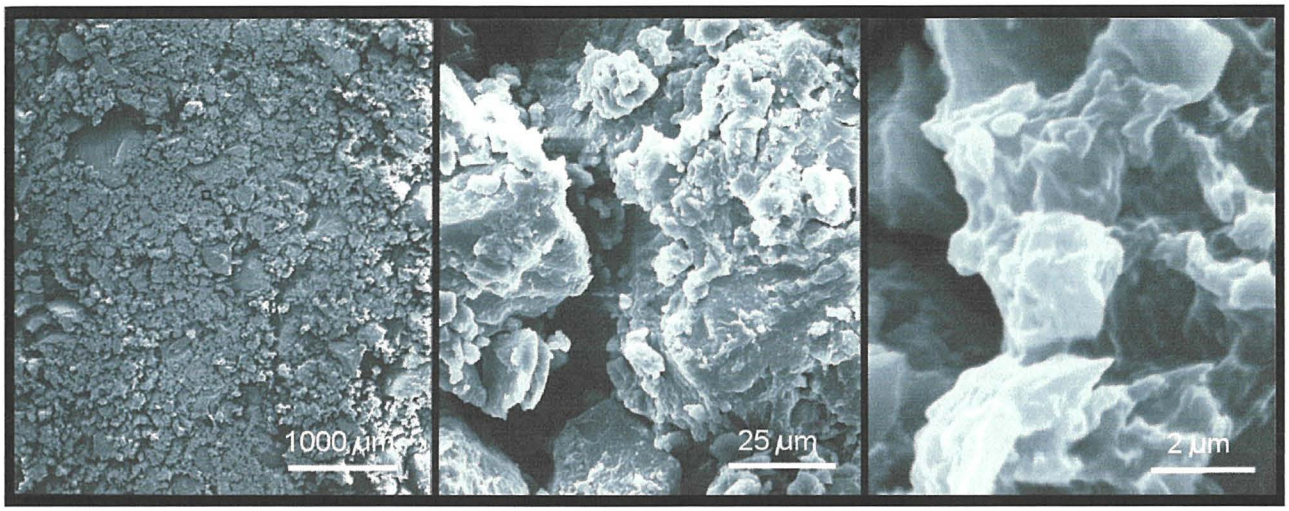

Figure 3.2.1: Electron micrographs of pulverised raw gel without any thermal treatment.

The gel calcined at 673 K (figure 3.2.2) shows a more crystalline nature under high magnification although the grain size of the individual particles is too small to be observed. It is only after treatment at high temperatures in excess of 750 K that the grain size has become sufficiently large to be observed directly.

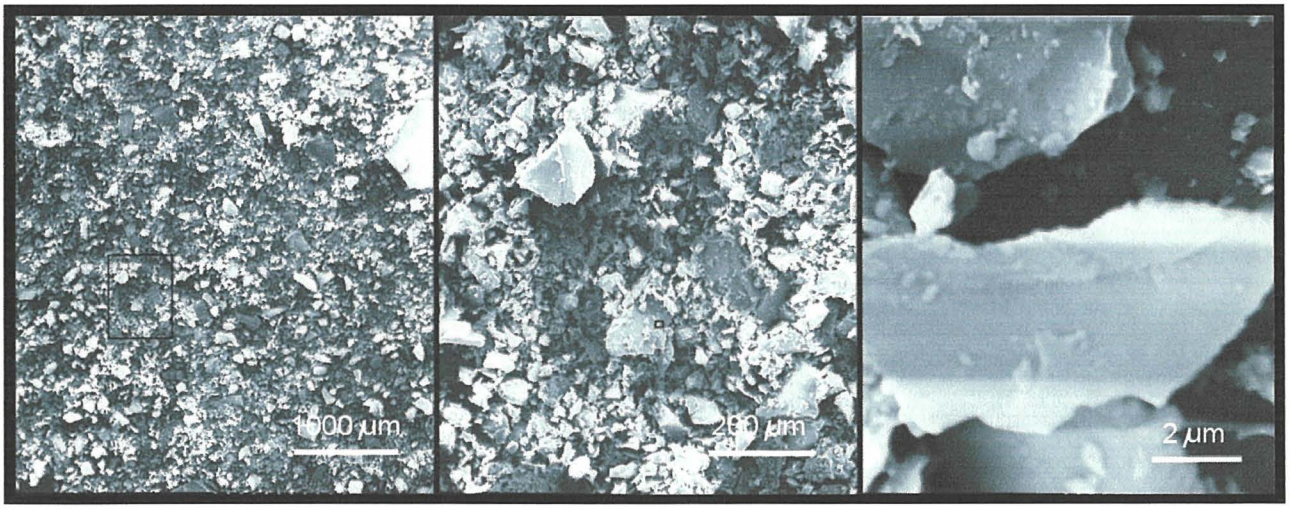

Figure 3.2.2: Electron micrographs of pulverised gel thermally treated at 673 K.

Figure 3.2.3 (overleaf) shows a series of electron micrographs obtained of a gel that had been calcined at 923 K. Comparison of figures 3.2.1 through 3.2.3 clearly shows the developing crystallinity with the grain size of the gel calcined at 923 K measurable as approximately 50 to 100 nm, in the fourth micrograph of figure 3.2.3.

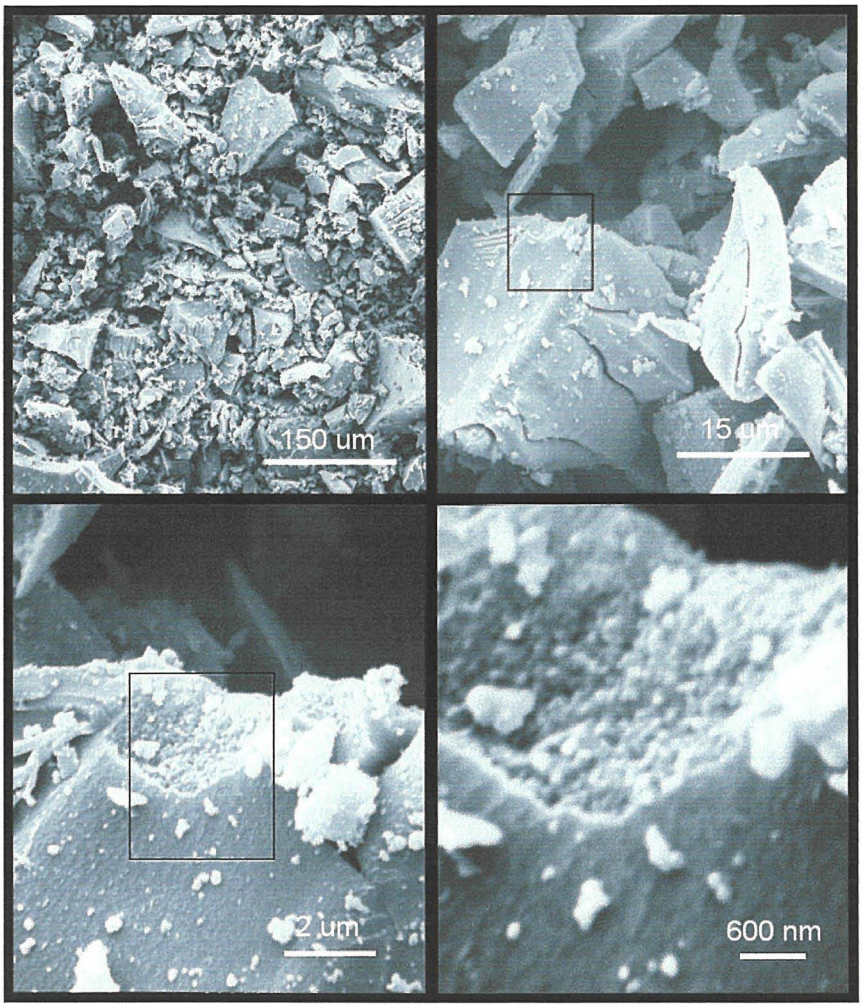

Figure 3.2.3: Series of electron micrographs of a pulverised gel thermally treated at 923 K.

The development of crystallinity was also observed using X-ray powder diffraction measurements and the results are shown below. Figure 3.2.4 shows the diffraction pattern obtained for a raw gel sample, and is clearly amorphous.

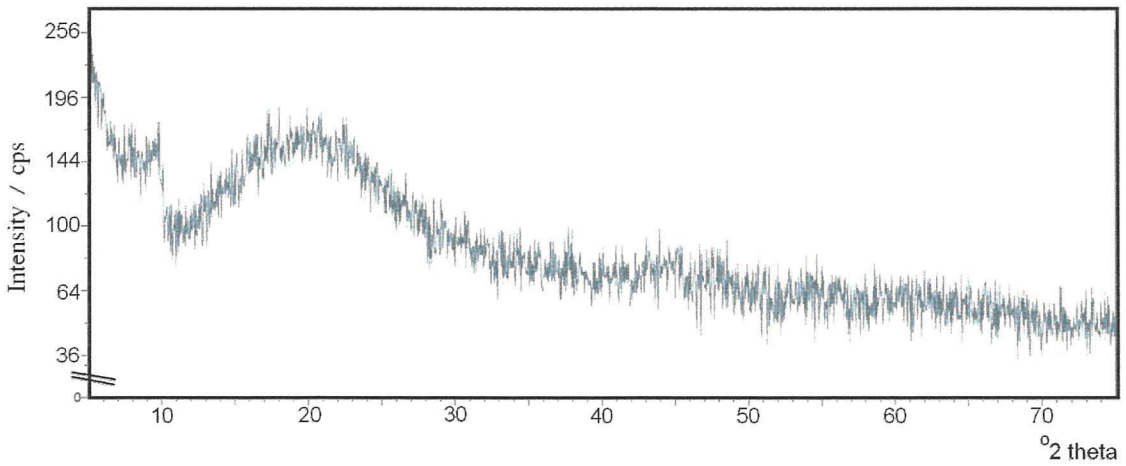

Figure 3.2.4: X-ray diffraction results for raw gel showing an amorphous structure.

Thermal treatment led to the development of the anatase crystal structure at temperatures in excess of 623 K in reasonable agreement with the literature data shown in figures 3.1.1 and 3.1.2 in earlier sections. The observed peaks on the X-ray diffraction results are broad for those gels calcined at temperatures around 600 to 700 K indicating fine particle size. Figure 3.2.5 shows a typical result for gels calcined at 623 K.

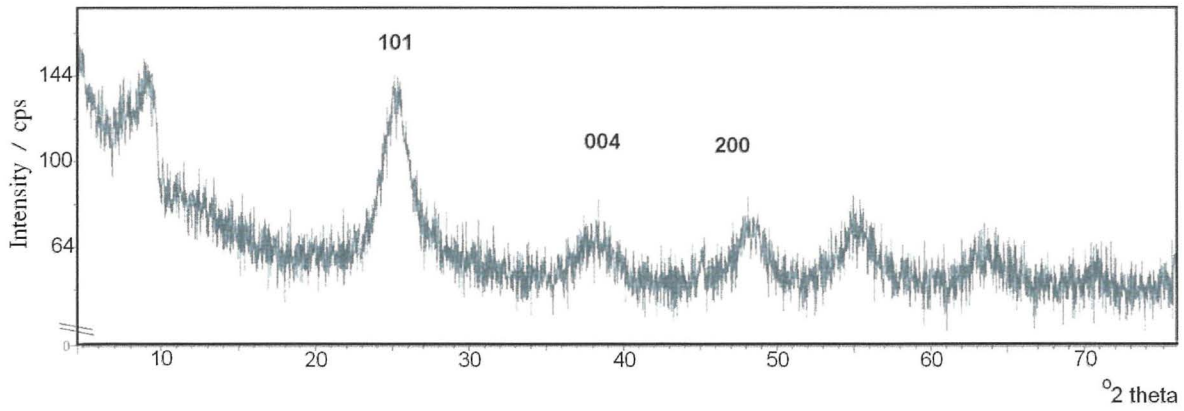

Figure 3.2.5: X-ray diffraction results for gel treated at 623 K, showing broad peaks, indicative of an anatase structure.

Figure 3.2.6 (overleaf) illustrates the temperature dependence of the traces obtained for gels calcined at temperatures of between 623 and 823 K. As the treatment temperature increased, the intensity of the peaks increased and the breadth (width at half maximum height) decreases by a factor of between 2 and 5. The anatase structure was observed for all gels calcined above 623 K and rutile phase was detected for samples calcined above 800 K. An estimate of crystallite size was calculated from the Scherrer formula [54], shown below.

$$L_{\text{(particle size)}} = \frac{k\lambda}{\beta \cos\theta}$$

where **L** = particle size, **k** = 0.89, λ = wavelength of Cu K_α X-ray (0.15424 nm), β = line width at half maximum height and θ = diffraction angle (θ = 25.4 / 2 for **101** peak).

Approximate grain sizes of 5 nm and 23 nm were obtained for gels treated at 623 K and 823 K respectively. It is possible that a combination of grain growth processes led to an approximately five-fold increase in particle size during thermal treatment. The coarsening of grain size in the solid-state is driven by a reduction in the total grain and interface boundary energy and involves two distinct but simultaneous processes; grain boundary diffusion and Ostwald ripening by long-range diffusion [56,57]. This, in solids, is governed by atomic diffusion due to the enhanced diffusivity of atoms at the grain boundaries [58] and proceeds primarily by evaporation and condensation [59,60].

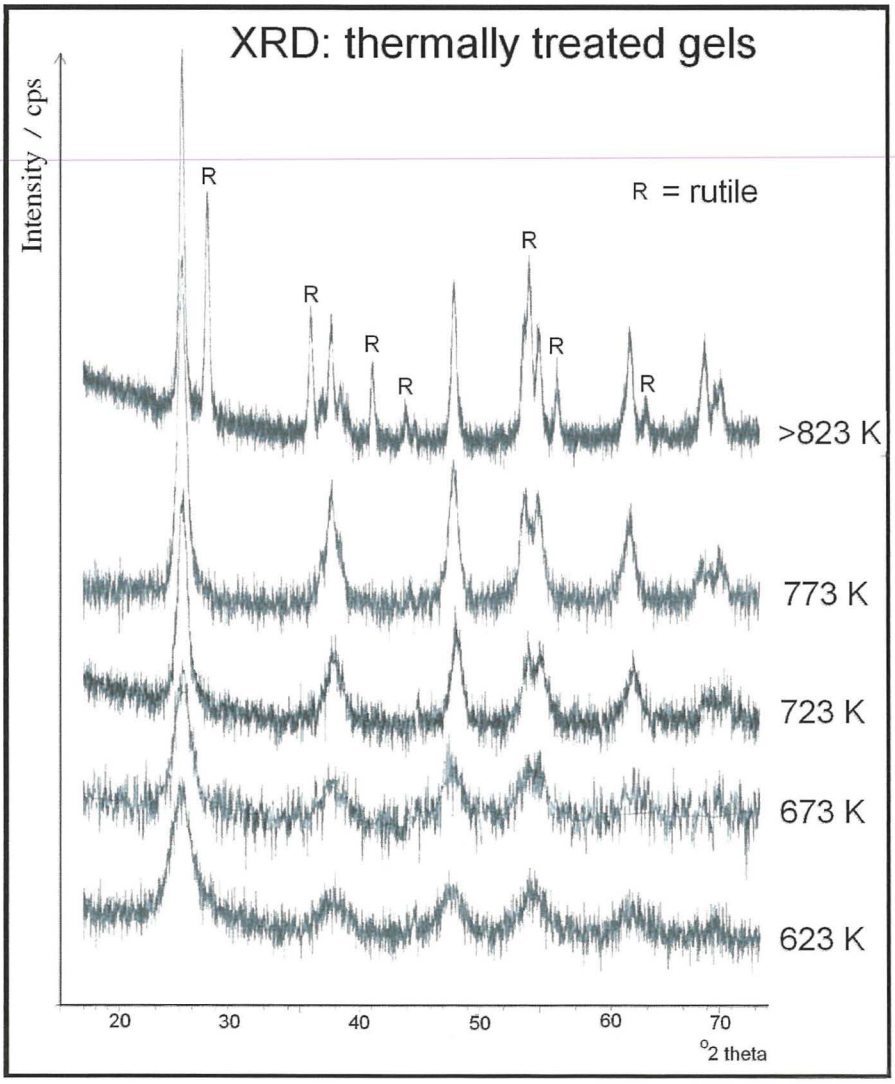

Figure 3.2.6: X-ray diffraction results showing the temperature dependance of crystallinity in calcined gels.

3.4 Conclusions

Stable sols were prepared from Triton X-100, a well-characterised non-ionic surfactant, in cyclohexane and remained stable and transparent after the addition of water and liquid alkoxide. Viscometry confirmed the presence of a short induction period and a repeatable gelling curve with a gelling rate that would be ideal for use in dip-coating methodology. Viscometry and aging behaviour showed that the sols would remain stable for an indefinite period, in excess of several months, where solvent evaporation and water ingress was prevented. Where evaporation was unrestricted, densification and extensive polymerisation occurred leading to the formation of solid monolithic gels after 24 to 48 hours. Further aging led to gel fracture and the development of a characteristic, intense yellow colouration that gradually became more amber as aging continued over several days. Aging also led to the liberation of surfactant residues (together with a small quantity of excess water from polycondensation reactions) in the form of a viscous, oily exudate. X-ray diffractometry confirmed that the as-produced gels were amorphous and retained their amorphous state until thermal treatment induced crystallisation of the anatase phase. Thermal treatment enabled the consistent production of nanocrystalline titania powders as either single-phase anatase or a mixed-phase (anatase & rutile) dependent upon the temperature regime employed. Crystal grain sizes, calculated from the Scherrer relationship, were shown to vary from approximately 5 nm for anatase phase at 623 K to almost 25 nm for mixed phase at temperatures in excess of 823 K. Carbon content was shown to decrease with increasing temperature of thermal treatment, requiring a temperature of greater than 723 K to remove all residual organic content.

3.5 References & bibliography

1: P. Kluson, P. Kacer, T. Cajthaml, M. Kalaji, *J. Mat. Chem.* **11** (2001) 644-651

2: P. Kluson, P. Kacer, *Chemicke Listy*, **94** (2000) 432 - 436

3: P.I. Gouma, P.K. Dutta, M.J. Mills, *Nanostructured Materials*, **11** (1999) 1231-1237

4: J.M. Herrmann, H. Tahiri, Y. Ait-Achou, G. Lassaletta, A.R. Gonzalez-Elipe, A. Fernandez, *Applied Catalysis B: Environmental.*, **13** (1997) 219-228

5: D. Mergel, D. Busechendorf, S. Eggert, R. Grammes, B. Samset, *Thin Solid Films,* **371** (2000) 218-224

6: M. Gratzel, *Current Opinion in Colloid and Interface Science,* **4** (1999) 314-321

7: L. Kavan, M. Gratzel, S.E. Gilbert, C. Klemenz, H.J. Scheel, *J. Am. Chem. Soc.,* **118** (1996) 6716-6723

8: D. Papoutsis, P. Lianos, P. Yianoulis, P. Koutsoukos, *Langmuir*, **10** (1994) 1684-1689

9: A. Fernandez, G. Lassaletta, V.M. Jimenez, A. Justo, A.R. Gonzalez-Elipe, J.M. Herrmann, H. Tahiri, Y. Ait-Achou, *Applied Catalysis B: Environmental* **7** (1995) 49-63

10: M. Kubeckova, M. Sedlar, V. Matejec, *J.Non Cryst. Solids,* **147&148** (1992) 404-408

11: S.D. Burnside, V.Shklover, C. Barbe, P. Comte, F. Arendse, K. Brooks, M. Gratzel, *Chem. Mater.,* **10** (1998) 2419-2425

12: P.P. Ahonen, U. Tapper, E.I. Kauppinen, J.C. Joubert, J.L. Deschanvres, *Materials Science and Engineering*, **A315** (2001) 113-121

13: T. Yoko, L. Hu, H. Kozuka, S. Sakka, *Thin Solid Films,* **283** (1996) 188-195

14: E. Stathatos, P. Lianos, F.del Monte, D. Levy, D. Tsiousrvas, *Langmuir*, **13** (1997) 4295-4300

15: C. Guizard, A.C. Julke, A. Ayral, *J. Mat Chem*, **9** (1999) 55-65

16: A. Ayral, C. Guizard, L.Cot, *J. Mat Sci Lett*, **13** (1994) 1538-1539

17: A. Ayral, A.El Mansouri, M.P. Vieira, C. Pilon, *J. Mat. Sci Lett,* **17** (1998) 883-885

18: G. Zhao, S. Utsumi, H. Kozuka, T. Yoko, *J. Mat Sci*, **33** (1998) 3655-3659

19: H. Tada, M. Tanaka, *Langmuir*, **13** (1997) 360-364

20: M. Klotz, A. Ayral, C. Guizard, L. Cot, *J. Mat Chem,* **10** (2000) 663-669

21: T. Dabadie, A. Ayral, C. Guizard, L. Cot, P. Lacan, *J. Mat Chem*, **6** (1996) 1789-1794

22: A. Larbot, J.P. Fabre, C. Guizard, L. Cot, J. Gillot, *J. Am Ceram Soc,* **72** (1989) 257-261

23: H. Imai, H. Hirashima, K. Awazu, *Thin Solid Films,* **351** (1999) 91-94

24: J. L. Keddie, P.V. Braun, E.P. Giannelis, *J. Am Ceram Soc,* **77** (1994) 1592-1596

25: D.J. Taylor, B.D.Fabes, *J. Non Cryst Solids*, **147** (1992) 457-462

26: M. Burgos, M.Langlet, *J. Sol-Gel Sci Tech,* **16** (1999) 267-276

27: N.Asakuma, T. Fukui, M. Aizawa, M. Toki, H. Imai, H. Hirashima, *J. Sol-Gel Sci Tech,* **19** (2000) 333-336

28: K. Shimizu, H. Imai, H. Hirashima, K. Tsukuma, *Thin Solid Films,* **351** (1999) 220-224

29: H. Imai, H. Morimoto, A. Tominaga, H. Hirashima, *J. Sol-Gel Sci Tech,* **10** (1997) 45-54

30: Y. Kotani, A. Matsuda, M. Tatsumisago, T. Minami, T. Umezawa, T. Kogure, *J. Sol-Gel Sci Tech,* **19** (2000) 585-588

31: G.W.Scherer, *J. Sol-Gel Sci Tech,* **8** (1997) 353-363

32: N.J. Piell, M.R. Hoffmann, *J. Solar Energy Engineering – Transactions of the ASME,* **119** (1997) 229-236

33: R.D. Sun, A. Nakajuma, I. Watanabe, T. Watanabe, K. Hashimoto, *J. Photochem & Photobiol A: Chem,* **136** (2000) 111-116

34: W. Choi, J.Y. Ko, H. Park, J.S. Chung, *App Cat B – env,* **31** (2001) 209-220

35: W.W. So, S.B. Park, S.J. Moon, *J. Mat. Sci. Lett.,* **17** (1998) 1219-1222

36: R.A. Potyrailo, S.E. Hobbs, G.m. Hieftje, *Anal Chem*, **70** (1988) 1639-1645

37: C. Guizard, J.C. Achddou, A. Larbot, L. Cot, *J. Non Cryst. Solids*, **147 & 148** (1992) 681-685

38: L. Auvray, A. Ayral, T. Dabadie, L. Cot, C. Guizard, J.D.F. Ramsay, *Faraday Discussions*, **101** (1995) 235-247

39: S. Peres-Durand, J. Rouviere, C. Guizard, *Colloids & Surfaces A: Physicochemical & Engineering Aspects*, **98** (1998) 251-270

40: A. Ayral, J. Phalippou, T. Woignier, *J. Mat Sci,* **27** (1992) 1166-1170

41: A.M. Seco, M.C. Goncalves, R.M. Almeida, *Mater Sci Eng-B: Solid State Materials for Advanced Technologies,* **76** (2000) 193-199

42: K.M.S. Khalil, M.I. Zaki, *Powder Technology*, **120** (2001) 256-263

43: J.M. Herrmann, H. Tahiri, Y. Aitichou, G. Lasssaletta, A.R. GonzalezElipe, A. Fernandez, *Applied Cat. B: Env.,* **13**, (1997), 219-228

44: H. Fujii, M. Ohtaki, K. Eguchi, *J. Am. Chem. Soc.,* **120** (1998) 6832-6833

45: X. Liu, J. Wang, L. Wang, X. Yang, L. Lu, X. Wang, *J. Mat Sci Eng,* **A289** (2000) 241-245

46: F. Cotton, G. Wilkinson, *Advanced Inorganic Chemistry*, Wiley & Sons, New York, 1988, 5th Ed.

47: B. Andersson, G. Olofsson, *J. Chem. Soc. – Faraday Transactions,* **84** (1988) 4087-4095

48: D.M. Zhu, K.I.Feng, Z.A. Schelly, *J. Phys Chem,* **96** (1992) 2382-2385

49: W. Brown, R. Rymden, J. Van Stam, M. Algrem, G. Svensk, *J. Phys Chem*, **93** (1989) 2512-2519

50: G.L. Li, G.H. Wang, *Nanostructured Materials*, **11** (1999) 663-668

51: Z. Wang, X. Hu, *Electrochimica Acta*, **46** (2001) 1951-1956

52: P.P. Ahonen, U. Tapper, E.I. Kauppinen, J.C. Joubert, J.-L. Deschanvres, *Materials Science & Engineering,* **A315** (2001) 113-121

53: G. San Vicente, A. Morales, M.T. Gutierrez, *Thin Solid Films,* **391** (2001) 133-137

54: H.P. Klug, L.E. Alexander, *X-ray Diffraction Procedures*, Wiley & Sons, New York, 1954

55: D.-M. Zhu, Z.A. Schelly, *Langmuir*, **8** (1992) 48-50

56: D. Fan, L.Q. Chen, *J. Am. Ceram. Soc.,* **80** (1997) 1773-1780

57: J. Zhu, L.Q. Chen, J. Shen, V. Tikare, *Computational Materials Science,* **20** (2001) 37-47

58: P.Heitjans, S. Indris, *J. Phys. Condens. Matter.,* **15** (2003) R1257-R1289

59: A. Martino, A.G. Sault, J.S. Kawola, E. Boespflug, M.L.F. Phillips, *J. Catalysis,* **187** (1999) 30-38

60: V.P. Zhdanov, B.Kasemo, *Surface Science,* **437** (1999) 307-316

CHAPTER 4

Development of a sol-gel, dip-coating procedure for the deposition of mesoporous, nanocrystalline pure titania and doped titania thin film coatings on both conducting glass slides and optical fibre substrates.

4.1 Introduction

The development of a distributed optical fibre sensing system was described in Chapter 2. This chapter describes the application of thin films of the titania material discussed in Chapter 3 onto conducting glass slides and optical fibres. Immobilisation of porous, photoactive thin films onto optical fibres should enable the development of interesting and novel non-distributed, 'point-sensors'.

4.1.1 Non-distributed optical fibre sensing

Spectroscopic sensors

There are many possible means of incorporating optical fibre into sensing configurations. The simplest system uses the fibre to carry light to and from the active sensing mechanism. This is effectively remote spectrophotometry rather than a true optical fibre sensor. Incident light is guided to a photochemical cell or fluorescent interface at the distal end of a fibre. The presence of a species of interest interacts to produce a chromophore or change the absorption and/or emission characteristics of a dye molecule [1-5]. This change is detected by monitoring the returning light and comparing it with the incident light. Measurement of the absorbance at a particular absorbance band of the returning light allows quick quantification of the "strength" of the colour and hence by calibration, the concentration of the analyte of interest. A simple example would be to immobilise a pH sensitive indicator within a membrane permeable to hydrogen ions [2,6]. Monitoring the absorbance at appropriate wavelengths will sense a transition through a particular pH range.

The means of carrying the light can vary. A single fibre with a reflective coating at the end combined with optics at the near end to separate out the bands of interest from the backscatter will work well, however if stronger illumination is required then fibre bundles can be used. These fibre bundles may be split into two or more bunches at each end to allow easy separation of incident and returned light. Other methods include absorbance set-ups such that one fibre or bundle leads to one side of a small absorbance cell [7], a second receives light that

has passed through the solution under investigation and returns to a detector. The simplest of remote spectroscopic sensors must be that patented by Johnson [8]. It involves a cell consisting of two fibre ends separated by a short gap. No light will be transmitted across the gap unless liquid is present due to reflections at the incident fibre endface. Most sensors found in the literature are considerably more complex. A remote spectroscopic method for the monitoring of methane gas in air developed by Culshaw *et al.*[9] operates by measurement of characteristic absorption bands of methane in the near infrared region. A multiplexed network of these sensors is currently undergoing field trials at a landfill site in Fife, Scotland. A plethora of papers describe fibre optic probes incorporating a wide variety of immobilised dyes and encapsulated compounds. Cattrall [2], described an optrode for *in vivo* glucose monitoring which utilises a cell surrounded by a dialysis membrane whose inner surface is coated with a reagent that binds sugars. Bound to this coating is a layer of fluorescein labelled dextrose, which is displaced as glucose diffuses into the cell. The freed dextran diffuses into the path of an excitation pulse transmitted along a fibre and the resulting fluorescence is coupled back into the fibre and to a detector. Alderete [6], has patented a sensor for carbon dioxide which uses a pH sensitive dye immobilised within a silicone capsule at the distal tip of a fibre and Fowler *et al* [10], hold a world patent for an *in vivo* monitor probe for blood gases and pH. Many sensors of this type are published each year and the number of publications is increasing as the potential of this sensing mechanism is more fully realised. As a subtle variation on the technique, several authors [11-14] report sensors dependent on the concentration specific swelling of polymer beads or thin films. The swelling film or bead is immobilised such that swelling deforms a reflective surface, either a polished plate or the surface of the bead itself. The movement of this reflective surface alters the path length of a reflected beam. Interferometric techniques allow changes in path length of less than a nanometre to be detected. A novel method patented by Hopenfield [15], involves the replacement of a short section of cladding with a material with a higher index than the core, thus light is lost at that point into the new

cladding due to the breakdown in internal reflection. The coating is designed to react with an analyte of interest and at least partially degrade. The degradation of this material allows an increase in the light passing through the modified section.

Evanescent Field Sensors

The evanescent field is a small portion of the propagating wave that penetrates into the cladding of the fibre and diminishes rapidly with distance from the core-cladding interface (CCI). Higher modes propagate in such a way that they reach the CCI and are internally reflected. However the reflections are not perfectly elastic nor do they occur at a finite point along the CCI as would be expected from ray optics. The electric field amplitude of the light penetrates into the cladding and decays exponentially with distance x into the rarer medium:

$$E = E_0 . e^{(-x/d_p)}$$

Where $\mathbf{E_0}$ is defined as the electric field at the CCI, and $\boldsymbol{d_p}$ is defined as the depth at which the electric field amplitude decays to $1/e$ of E_0 [16]. The depth of penetration, $\boldsymbol{d_p}$, can be further defined as:

$$d_p = \frac{\lambda}{2\pi \left[(n_2)^2 \sin^2\theta - (n_1)^2\right]^{1/2}}$$

Where $\boldsymbol{n_1}$ and $\boldsymbol{n_2}$ are the refractive indices of the core and cladding respectively, and θ is the angle of propagation of the incident light. The evanescent field is continuous along the CCI. Unfortunately, it does not penetrate sufficiently far into the cladding to allow sensing with the cladding layer intact on most modern telecommunications fibres. At wavelengths in the visible region, $\boldsymbol{d_p}$ varies between 50 and 1000 nm [16]. The use of longer wavelengths, typically in the near infrared region, extends the depth of penetration of the evanescent field. Commonly [17,18], plastic-clad silica (PCS) fibres are used. These have a silicone cladding around a silica core. The cladding is easily removed to expose the core and allow interactions with the evanescent field. Other coatings may then be applied to the exposed core such that the analyte will change the optical properties of an absorbance based or fluorescence based

dye. These changes can then be monitored by evanescent spectroscopy. A simplified diagram of a stripped PCS sensor is shown in figure 4.0.1.

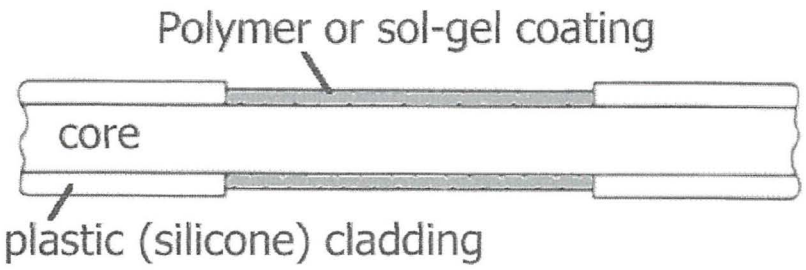

Figure 4.0.1: Use of a stripped PCS fibre for an evanescent field sensor.

It is important to recall that the cladding layer protects the core from damage and prevents fissure propagation due to minute defects in the core surface. When the cladding is removed the fibre becomes fragile and so requires careful handling. Most evanescent field sensors incorporate a fibre immobilised on a protective support, such as a steel frame. There are three basic classifications of evanescent field sensors: absorption sensors, index sensors and fluorescence sensors. Absorption sensors can be envisaged as using the same principles as spectrophotometry, except that the region that surrounds the core and is sampled by the evanescent field has replaced the absorption cell. The process will work equally well for absorbing species of interest or for non-absorbing species in the presence of a suitable dye reagent. For a simple spectrophotometry set-up, the relationship between the incident and transmitted intensities are described by a modified Beer-Lambert's law, with additional factors to correct for the limited fraction of the incident light that exists as the evanescent field. Absorption methodology may operate at single, discrete wavelengths as in spectrophotometry, where it is the absorbance at both a reference frequency and a sample frequency that provide quantification of an analyte. In addition, as a consequence of the good transmittance of certain fibre materials at near-infrared and infrared regions, absorption evanescent field sensors may be used in infrared spectroscopy. Standard Fourier Transform Infrared (FTIR) techniques may be modified [16,19] to integrate the additional signal processing

required and thus produce FTIR spectra that are similar in nature to those obtained by standard methods. The signals obtained are easiest to decipher when obtained using single mode methods as multimode operation can involve several thousand distinct modes, each with subtly different propagation patterns; the traces obtained can be highly complex. This capability offers the possibility of powerful remote spectrometry for FTIR analysis of inaccessible sample sites. The challenges of this sort of sensor are many, of which the development of the sophisticated signal processing is not the least.

Index Sensors [16] operate on the principle that the effective refractive index, n_e , of the evanescent wave will change as the optical density of the medium surrounding the core varies. For example, if heavy metal ions diffuse into the sensing region surrounding the cladding, the refractive index locally will vary. Thus, the path length of the high order modes (those that produce the evanescent field) will alter slightly. The small change, δn, in the refractive index of the sampled region will be translated into a small change in the effective index of the guided modes, δn_e. These small changes in index can be detected by interferometric methods. These sensors can be highly sensitive although their selectivity is poor.

Fluorescence based evanescent field sensors [16] rely upon the excitation of a fluorophore by the evanescent field. This fluorescence may be quenched by, increased by or shifted by the species of interest. The signal processing is relatively simple; the monitoring of a reference and a fluorescence band allows fairly simple quantification of an analyte. The difficulties in this type of sensor are two-fold. Firstly, it is necessary to prevent interference with or quenching of the fluorescence. Quenching by material other than the analyte of interest can occur from species within the sensor itself or from species permeating into the sampling region. Thus, this sensor type often incorporates selective membranes and porous cell technology. Secondly, although fluorescence radiates in all directions, it is important that sufficient fluorescence is coupled into the fibre core by forward propagating modes to enable

the fluorescence to reach the detector. The power coupled into the core, P_c, as a fraction of the total power launched, P_t, can be calculated [20] by:

$$\frac{P_c}{P_t} = \frac{f(V)}{2\, n_2^2\, k_{fl}^2\, a^2}$$

Where **a** is the core radius, n_2 is the core index, k_{fl} is $2\pi / \lambda_{fl}$ where λ_{fl} is the wavelength of the fluorescence and **f(V)** is a complex parabolic function [20] that approximates to 0.23 V^2 for $V < 30$. **V,** the V-number, is a measure of the number of modes propagating within a given fibre and a given light source and can be calculated as:

$$V = k_0\, a\, (n_2^2 - n_1^2)^{1/2}$$

Where **a** is the core radius and $k_0 = 2\pi / \lambda_0$. If $V < 2.4$ then the fibre will operate as single mode. For large values of **V** the fibre will be multimodal. Power efficiencies of a few percent are possible with careful choice of parameter. As a general rule, source and detector cannot be sited at the same side of the sensing region as only the forward propagating modes are of sufficient intensity to couple the fluorescence into the core. The backscatter within the core is much weaker, that is

$P_{t\,(forward)} >> P_{t\,(backwards)}$ and thus, by the equation above, insufficient coupling can occur. Evanescent field sensors have seen explosive growth in the gas sensing and contamination monitoring fields [1,16,18,19,21-24]. Kvasnik and McGrath [18] have patented an evanescent field sensor that operates by evanescent field-induced raman emissions from the core-cladding interfacial region, which is further discussed in a later section. Potyrailo *et al.* [24] reported the development of an evanescent field sensor operating at near-ultraviolet wavelengths (254 nm) using a plastic clad silica (PCS) fibre. The sensor was shown [24] to give a linear response to ozone over the range 0.02 – 0.35 vol%. Malins *et al* [25], published research on the development of personal ammonia sensors for safety monitoring. These sensors have cyanine dyes

immobilised within a thin porous glass film which is sampled by the evanescent field and which, it is claimed, can reversibly detect ammonia at levels between 5 and 100 ppm. Lennie and Kvasnik [26], developed a near-infrared evanescent field sensor to measure the water content of solvents by monitoring the 950 nm hydroxyl stretching overtone band. Heinrich and Rose [27] patented an index based evanescent field sensor in 1999 for the detection of hydrocarbons or carbon dioxide by designing a drawable PCS fibre with a polysiloxane coating into which the analytes of interest will absorb, thus changing the refractive index of the cladding layer. This sensor is capable of quantifying hydrocarbons in an aqueous medium. Bürck *et al* [28], designed a sensor for the monitoring of hydrocarbon compounds in waste and ground water. The probe contains a length of sensing fibre coiled onto a steel support frame. The sensor fibre consists of a silica glass fibre clad with a hydrophobic silicone. Although similar in structure to Heinrich and Rose's sensor [27], this evanescent field sensor is absorption based and by using complex optical filtering and inspection of the C-H overtone bands in the near infra-red, is able to identify and quantify a range of contaminants including aromatic solvents, fuels, mineral oils or chlorinated hydrocarbons from around 200 $\mu g\ L^{-1}$ up to several hundred $mg\ L^{-1}$. Stewart *et al.* [29], report on the possibility of evanescent sensing using D-fibres (a speciality fibre with a "D" shaped cross section) for gas sensing in the near infrared region. Focusing on methane sensing, the difficulties faced due to low sensitivity and high background noise together with the high costs and scarcity of D-fibre were emphasised, but the authors suggest that the use of sol-gel coatings and laser sources may overcome some of these difficulties and yield a viable distributed sensing technique. Jin *et al.* also worked with D-fibre [30] and developed a means of monitoring the surface of a D-fibre sensor for moisture contamination that would affect its operation as a gas sensor. Water on the surface of a fibre will affect the polarisation of plane polarised white light propagating through it. This change can be detected using polarimetry. Another novel, if somewhat vulnerable design, was patented in 1999 by Hamburger *et al.* [31]. The mechanism described involves the removal of the

protective buffering layer to expose the cladding of a silica fibre. The cladding is then scratched and roughened to liberate the evanescent field and allow easy access by analyte gases and liquids. The authors claim that the sensor will monitor "humidity, contaminant levels, pollutant levels, battery solution and composition of the surrounding gaseous or liquid media" [31]. Khijwania and Gupta [32] reported the development of an evanescent field sensor incorporating a U-shaped, bent fibre probe. Decreasing the fibre bend radius and stripping the cladding from a PCS fibre increases the evanescent field penetration depth. The cladding is removed and the fibre is bent to a radius of less than 1 cm before being recoated with a thin film (130 nm) of polyvinylidenefluoride (PVDF).

The PVDF film prevents the surface reactivity of the silica core, which could cause a non-linearity in response. The sensor, illustrated in figure 4.0.2 below, showed a linear response with concentration of a methylene blue dye solution over the concentration range 0 to 25 μM.

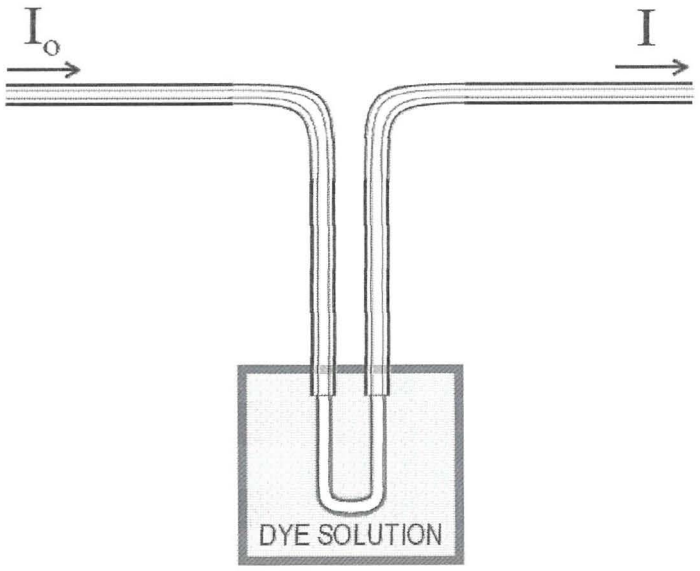

Figure 4.0.2: Illustration of a U-bend evanescent optical fibre sensing system developed by Khijwania and Gupta [32].

In a later paper [33] it was reported that the evanescent absorption coefficient increases with decreasing U-bend radius down to bending radii of less than 1 mm.

It was stressed that in the case of a U-bend sensor the optimum bending radius is affected by cross coupling of higher order modes between the exposed straight arms of the U-bend at small radii as shown in figure 4.0.3.

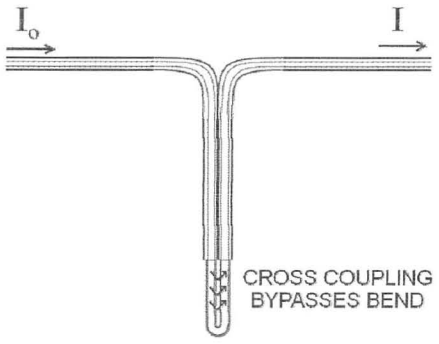

Figure 4.0.3: Diagram of a U-bend evanescent optical fibre illustrating the phenomenon of cross-coupling which can occur at small bend radii causing a significant decrease in the area of interaction between the evanescent field and the sampling region.

Cross-coupling will result in a decrease in the interaction area and thus a corresponding decrease in the sensitivity of the sensor. That is, as bend radius decreases, the penetration depth , d_p, of the evanescent field at the tip increases until a maximum value beyond which further decrease in radius will result in increasing cross-coupling. Despite a continued increase in d_p the net result of increasing cross-coupling is a decrease in evanescent field intensity at the tip. A further adaptation of the U-bend structure was reported by Gupta and Ratnanjali [34] based upon earlier work by Muto *et al.*[35] who found that the absorption (at 530 nm) of a phenol red dye-doped PMMA fibre was dependent upon relative humidity and who subsequently developed a plastic optical fibre sensor for the monitoring of humidity in air and soil samples. Gupta and Ratnanjali adapted the technology for an evanescent field sensor using the U-bend structure and reported the production of a humidity sensor that could detect relative humidity in the range 20 to 80 % with a response time of 5 seconds.

The use of the U-bend configuration has thus been shown to be a feasible adaptation to improve upon the simple evanescent field sensor design shown earlier in figure 4.0.1 allowing a significantly improved interaction between the evanescent field and the sampling region.

Scattering (Raman, Brillouin)

Although scattering sensors could technically fit into the classes above, they can be considered a separate class of optical fibre sensor in themselves. There are three principle types of scattering that can occur in fibre systems: Rayleigh, Raman and Brillouin. Rayleigh scattered light is at the same wavelength as the incident light i.e. elastic scattering. Figure 4.0.4 shows the spectra of Rayleigh, Raman and Brillouin scattered light. Both Raman and Brillouin scattering processes shift the scattered light to higher or lower wavelengths than the incident beam. Although weak effects, these processes are the basis of several distinct sensing mechanisms. On a relatively simple level, Raman sensors can be used to monitor temperature by virtue of the temperature dependence of the Raman shift that occurs.

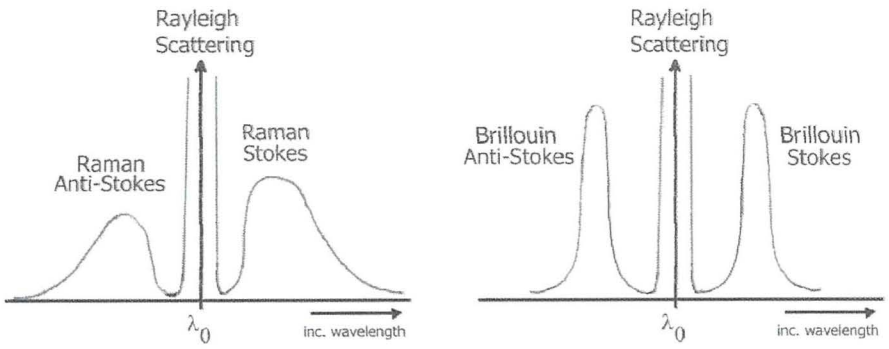

Figure 4.0.4: Illustration of the origin of Raman and Brillouin shifts.

The observed shifts are seen to decrease with increasing temperature [85-87]. Perturbation theory [87] states that shift in phonon frequency is attributed to thermal (volumetric) expansion of the lattice and to phonon-phonon coupling [86,87]. In addition, anharmonicity of the vibrational potential energy may lead to increases in linewidth with increasing temperature [86,87].

This can be done by using a short or a coiled length of fibre with a detector capable of picking out the weak signal. 1000 times (30 dB) weaker than the Rayleigh scattering, which in turn involves only about 1% of the incident photons. To improve sensitivity and detection limits, the magnitude of the Raman effect [16,36] can be increased by the use of high power sources.

As for all Raman work, a laser source is critical due to its narrow spectral width and high launch power. As the Raman effect is independent of incident wavelength, it can be possible to use lasers operating at higher energy (shorter wavelength) regions. There comes a point however, where the incident energy is sufficiently high to induce fluorescence from the core, which, being several orders of magnitude more intense than the Raman effect and exhibiting considerably broader spectral width, will mask the Raman spectrum. This typically occurs in the visible – UV region although this only affects the Stokes lines. A trade off between improved signal to noise ratios and fluorescence is required. The source of the Raman scattering in this "simple" sensor is the core material of the fibre. In order to use this Raman effect in the sensing of chemical species a different approach is required. In Raman chemical sensing, the detector needs to look for shifts of particular magnitude. Although the wavelength of the incident light is not critical, the size of the shift is characteristic of particular compounds. A Raman chemical sensor can be based upon either evanescent field or remote spectroscopic principles. The evanescent field can interact with any species entering the interfacial region, and can, in theory, result in Raman emissions which will couple back into the core and hence back to a detector. Any means of allowing an interaction between the incident light with a medium to be analysed can be adapted to create a Raman sensor as Raman emissions will occur whenever light interacts with a species. Successful Raman sensors for chemical sensing are few and far between, unlike those for temperature. Only one example is given here [18]. Kvasnik and McGrath patented a quasi-distributed Raman sensor array in 1993. A PCS fibre is stripped of its cladding over several cm of its length and a new cladding of unspecified nature is coated over the exposed gap. The stripped sensing sections are created along the length of the fibre spaced several metres apart. An excitation pulse of light in the UV, visible or infrared region is launched through the fibre and the excited Raman scattering is analysed at the detector. When a Raman emission is detected from a species of interest, optical techniques such as optical time domain reflectometry (discussed in Chapter 2)

allow identification of the position along the fibre from which the emission originated and hence the location of the analyte. This is a quasi-distributed sensor, which is better suited to multiplexed monitoring of widely separated points and thus is included in this section on non-distributed sensors.

Fibre grating sensors

The higher refractive index of optical fibre cores is achieved by doping of the silica with metals such as germanium and boron. This Ge-doped silica within the fibre core is photosensitive to wavelengths corresponding to particular absorption bands of the germanium-silica bonds. When exposed to intense ultraviolet radiation (248 nm) some of these bonds are broken and a localised change in refractive index occurs. It is thus possible to write periodic structures (Bragg gratings) into the core of fibres by exposing the core to the interference pattern of two high power UV-LASER sources.

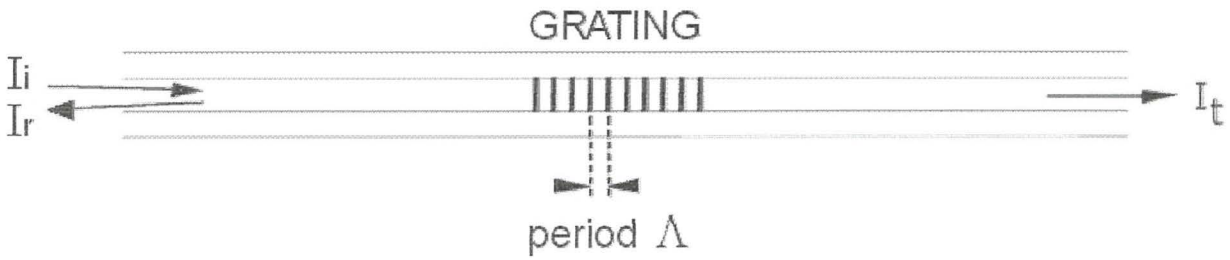

Figure 4.0.5: The Basic Principle of Bragg Grating Sensors.

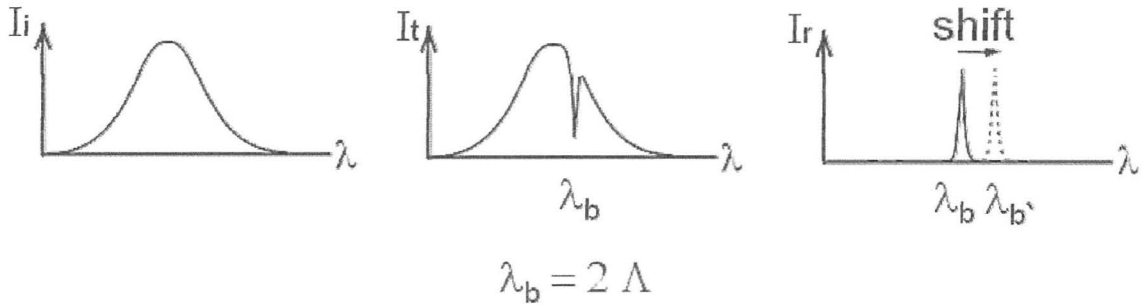

Figure 4.0.6: Typical Spectral Data from a Bragg Fibre Grating.

Figure 4.0.5 illustrates the basic principles of a Bragg Grating sensor and the spectral data for the incident, transmitted and reflected light are shown in figure 4.0.6 [1,16,23].

The grating can be written at a chosen grating dimension so as to reflect only a narrow band of the incident light. With grating pitches of the order of 0.5 μm and total grating lengths of over 5 mm, the grating can comprise more than 10 000 periods creating a highly resonant device [23].

Any change in the periodicity of the grating, Λ, will cause the reflected band to shift. This may be brought about by physical deformation of the fibre by an applied stress or strain or by thermal expansion and contraction of the fibre. Detection and measurement of the shift together with appropriate calibration can provide a sensitive real-time sensor. Bragg grating sensors are rarely used for chemical sensing. Their predominant use is in the sensing of temperature and strain and they are commonly used for detecting changes in these parameters during construction of bridges, dams and high rise buildings. Using a Bragg sensor for chemical species is considerably more difficult. A means of modulating the exchange of heat in exothermic or endothermic reactions to induce a temperature change in a fibre is feasible and worth investigating although notably, there seems to be a distinct lack of literature in this area. Any physical change that leads to deformation of a structure can in theory be adapted to sensing; vibration detection and pressure monitoring are examples of this.

This technique does not allow true distributed sensing and is better described as a quasi-distributed array of individual sensing units, remotely addressed through a fibre link. This is possible by writing multiple gratings along a length of fibre (Figure 4.0.7).

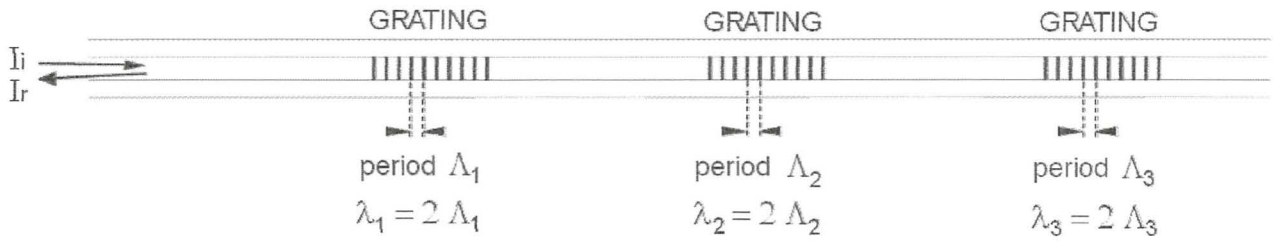

Figure 4.0.7: Quasi-distributed measurements using multiple gratings. [19]

Each grating must have its own unique period and the wavelengths must be sufficiently separated so as to distinguish the signals received from each. Writing narrow band gratings and using a broadband source allows more gratings to be inserted in each fibre, however it is important to ensure that the power received at the detector is sufficient to separate signals from backscatter noise.

Peaks will be detected at wavelengths characteristic of the periods of each grating (figure 4.0.8). The software and opto-electronics at the detector are required to be highly sophisticated to analyse for shifts in each signal. As the grating periods vary with temperature, stress and strain and may also fluctuate slightly if the fibre is disturbed, the calibration procedures and signal processing elements of fibre grating sensors are one of their main drawbacks.

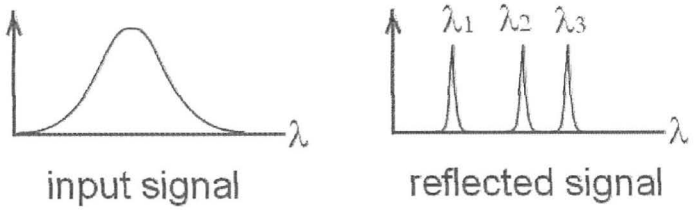

Figure 4.0.8: Signals received from a quasi-distributed fibre grating sensor.

Morey *et al.*[37] have pioneered the development of a series of strain sensors based on this principle. A report on simultaneous monitoring of strain and temperature in structures was published in 1991. The wavelength of the holographic Bragg grating written into the core will vary with both temperature and applied axial strain [23,38-40]. Thus, any grating signal will be due to a combination of both these effects. In order to be able to distinguish one signal from the other, it is necessary to write two gratings near to each other in the fibre core. One of the two gratings is then mechanically isolated from strain and will thus only measure temperature variations. The signals obtained from this sensor can be used to provide a temperature reading and to extract the strain value from the second grating.

Micro-optical ring electrodes (MORE)

Combination of optical and electrochemical techniques allows the production of photoelectrochemical sensor probes. One such sensor is a micro-optical ring electrode (MORE) described by Pennarun *et al.* [41] and consists of a commercial multimode fibre as a light guide and insulating core surrounded by a thin-ring gold electrode deposited by sputter coating. The fibre is a 125 μm multimode fibre; the gold coating was 600 nm thick. A ring electrode is defined [42] as a 'thin ring' if the ratio of internal ring diameter, **a**, to external ring diameter, **b**, is greater than 0.91 as illustrated in figure 4.0.9 below.

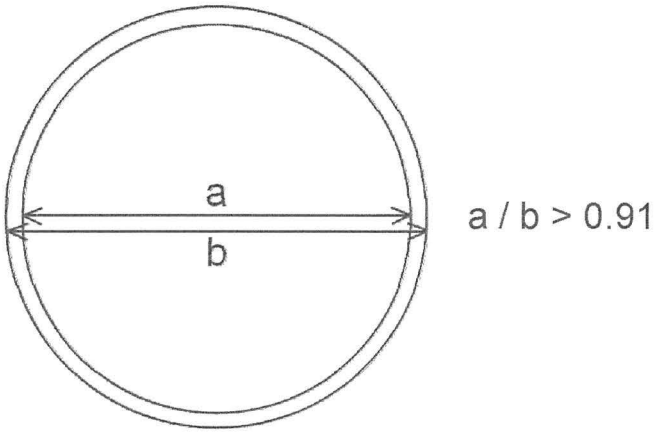

Figure 4.0.9: Illustration of the definition of a thin-ring as defined by Symanski & Bruckenstein [42] whereby the ratio of **a / b** must not be less than 0.91.

The entire assembly is coated with an electrically insulating varnish or polymer. The tip is polished to produce a smooth, unbroken gold ring. This structure forms a highly sensitive sensing device.

When light is transmitted through the optical fibre core, photoexcited species in solution are formed at the core face and may then be oxidised or reduced at the gold ring upon lateral diffusion. Expressions for the steady state diffusion current, $I_{d\,(ss)}$, at thin-ring microelectrodes have been derived and in the absence of convective mass transport, there is a linear dependence obtained between $I_{d\,(ss)}$ and the solution concentration, **C**:

$$I_{d\,(ss)} = nFDCl_o$$

Where l_o is a function of the thin-ring geometry defined by:

$$l_o = \frac{\pi^2 (a+b)}{\ln\left[16\left(\frac{b+a}{b-a}\right)\right]}$$

and **n** = the number of electrons involved in the REDOX step, **F** = Faraday's constant, **D** = diffusion coefficient, and **a** and **b** are the internal and external diameters of the ring as defined previously. Additional expressions for the diffusion limited current, $I_{d\,(t)}$, at thin-ring microelectrodes are also given:

$$I_{d\,(t)} = nFDCl_o\left[1 + \frac{l_o}{(4\pi^3 Dt)^{1/2}}\right]$$

where l_o is redefined as:

$$l_o = \frac{\pi^2 (a+b)}{\ln\left[4e^{3/2}\left(\frac{b+a}{b-a}\right)\right]}$$

Pennerun [41] reported that during investigation of the photoelectrochemistry of the phenothiazine dye methylene blue (MB^+) in aqueous solution using the MORE, the chronoamperometric response obtained by potential step methods was in excellent agreement with the predicted value at all times up to the completion of the experiment after 30 seconds. In addition, the steady state current, both experimental and predicted, agreed with that obtained by cyclic voltammetry at low sweep rates. The MORE sensor was sufficiently sensitive that it was able to detect the presence of short-lived photoexcited states of MB^+. A photoanodic current under illumination was observed on the forward cathodic sweep due to the oxidation of photogenerated triplet state methylene blue ($^3MB^+$) to the 2+ radical cation (MB^{2+}). The subsequent reduction of the MB^{2+} to MB^+ and ultimately to the reduced form of

methylene blue, leucomethylene blue (LMB) was also seen on the forward cathodic sweep by a photocathodic current under illumination at more negative potentials. The MORE sensor was thus shown to be able to elucidate complex photoelectrochemical behaviour such as that of methylene blue and detect the presence of photoexcited triplet species with lifetimes of the order of 90 μs.

Microbend OFS

The transducer in this type of sensor is mechanical in nature enabling the target parameter or chemical to modulate the microbend losses in a fibre. This category of sensors rely on the losses induced when a fibre is deformed at small radius inducing microbends into the fibre. This microbending loss is caused by the coupling of high order modes out of the fibre core which are then lost in the cladding and primary coating. Microbend sensors used in distributed sensing were discussed in Chapter 2.

4.1.2 Possible applications of titania thin films in optical devices

It was an aim of this research work to investigate the design of optical devices for sensing and photocatalysis by the development of porous thin films of the titania material discussed earlier in this chapter and their deposition onto optical fibre substrates. It is important here to define the many possible sensor configurations and transduction mechanisms proposed.

Optical absorption probes.

As described earlier in this chapter, many optical sensors are simply a means of remote absorption spectroscopy. By creating a notch in a fibre such as in the morphology shown in figure 4.1.0 (overleaf), it would be possible to perform optical absorption measurements of a remote solution at the distal tip of a fibre cable by immersion of the probe into the solution under investigation. Application of a porous thin film of photoactive titania on the inner faces

of the notch would allow the simultaneous spectroscopic identification of absorbing species and the monitoring of the photodegradation of those species at the titania surface.

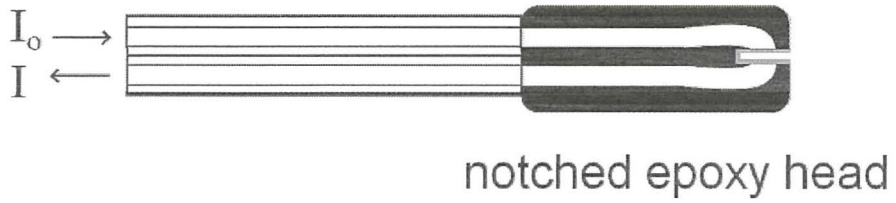

Figure 4.1.0: Representation of a notched fibre sensor for remote spectroscopy.

Coated fibre sensors

Coiling or bending of optical fibres will result in an increased evanescent field penetration depth. This property can be used to produce fibre sensors with a general appearance illustrated in figure 4.1.1 below.

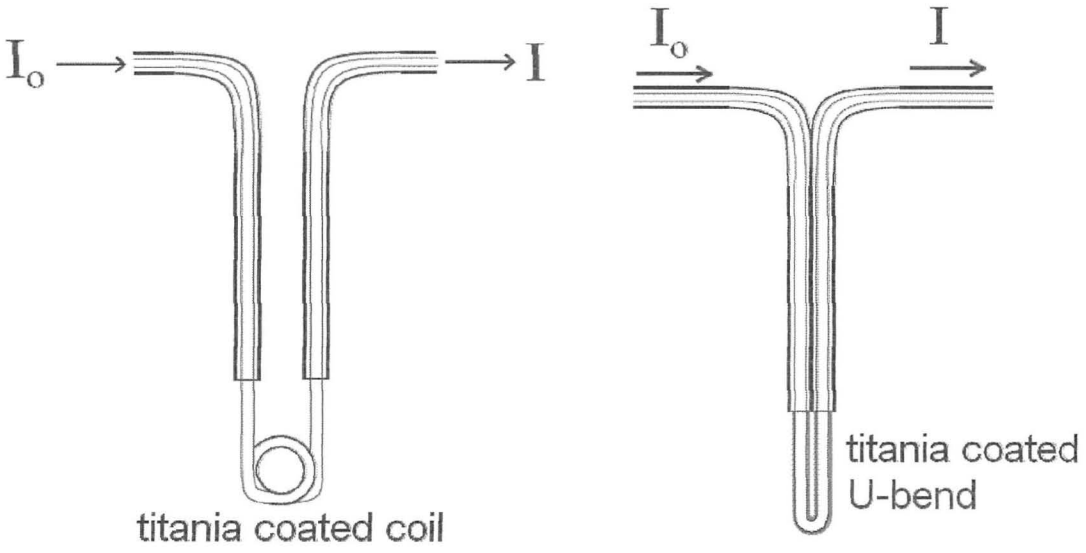

Figure 4.1.1: Representation of 2 possible coiled fibre geometries for evanescent field sensing.

Coating of these coiled geometries with thin films of titania would produce sensitive sensing devices that would operate by evanescent field absorption spectroscopy. Ensuring that sufficient forward propagating light was coupled back into the core would require careful adjustment of the fibre geometry, but should be possible with careful design.

Certainly, devices of this nature should allow photodegradation of species in solution or in the vapour phase by evanescent activation of the supported catalyst. The potential of such a device for monitoring of gaseous contaminants would be worthwhile investigating.

Polished block sensors

An alternative system for evanescent field sensing and/or photocatalysis may be created by use of embedded fibres, polished to expose the core as shown in figure 4.1.2. This geometry may be used for simple evanescent field sensing but may be utilised (as could other evanescent geometries) for fluorescence-based devices.

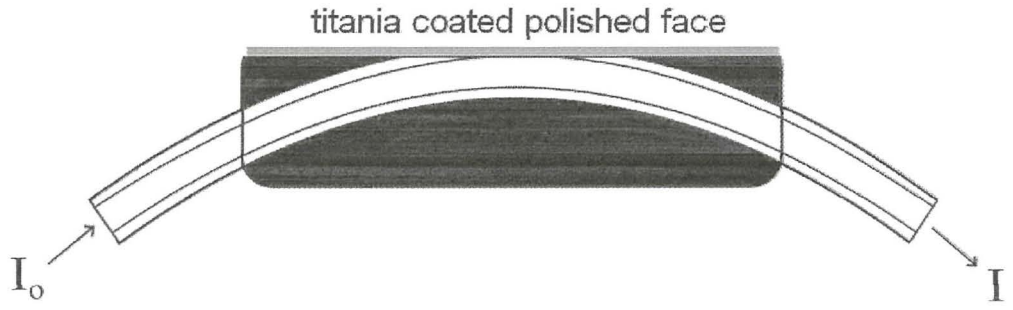

Figure 4.1.2: Illustration of a polished fibre geometry for fluorescence-based evanescent field sensing with doped or undoped thin films. An identical but uncoated structure may be used for simple evanescent field operation.

Application of a titania thin film doped with an element such as europium is possible. Europium (Eu^{3+}) doped titania has been shown [43] to emit a strong red luminescence under near-ultraviolet illumination where titania acts as a sensitiser in the system. The presence of europium does not affect the crystallinity of the titania as the europium atoms occupy voids at grain boundaries rather than titanium or oxygen sites in the lattice [43]. This sort of device could have great application in the gas-sensing field. The concentration of gases that act as quenchers, such as oxygen, could be monitored by measurement of the intensity of the luminescence coupled back into the core. The same operating principles could be applied to stripped fibres and to coiled or bent fibres in addition to the polished block sensor described above. In order to improve on the sensitivity of the polished block system, it would be

relatively easy to combine two such devices to create a device capable of in-line monitoring of pumped gas flows in reaction vessels, atmospheric sensors or portable devices. Such a 'cross-coupling' system is illustrated in figure 4.1.3.

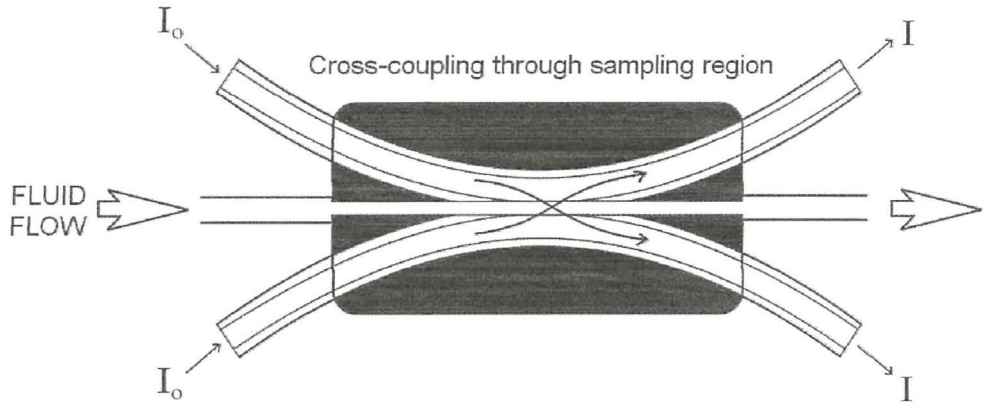

Figure 4.1.3: Illustration of a cross-coupling sensor that could be used for in-line flow monitoring of fluids or gaseous mixtures.

The incorporation of a porous matrix within the void between the two plates would increase the residence time of analytes of interest, particularly if the porous material was tailored for the preferential adsorption of a class of analytes, such as alcohols, aldehydes or halides. The system would be capable of simple optical absorption measurements of a chromophore or by use of a suitably doped film, fluorescence quenching. As an example, immobilisation of phenol red within the porous matrix would allow the system to detect humidity in a fluid flow as the optical absorption of phenol red at 530 nm has been shown to vary with humidity [34,35].

Titania sensitised MORE sensors

Micro-optical ring electrodes (MORE) have been shown [41,42,] to be sensitive probes useful in the investigation of redox systems. When coupled with a disk of oxidised titanium metal, it has been reported [44,45] that MORE are capable of detecting the electroreduction at the ring of oxidised species produced at the illuminated titania surface.

Immobilisation of a porous thin film of photoactive titania directly onto the polished face of the optical fibre core (see figure 4.1.4) of the MORE would produce a sensing probe capable of photooxidation and electroreduction of species at the fibre tip.

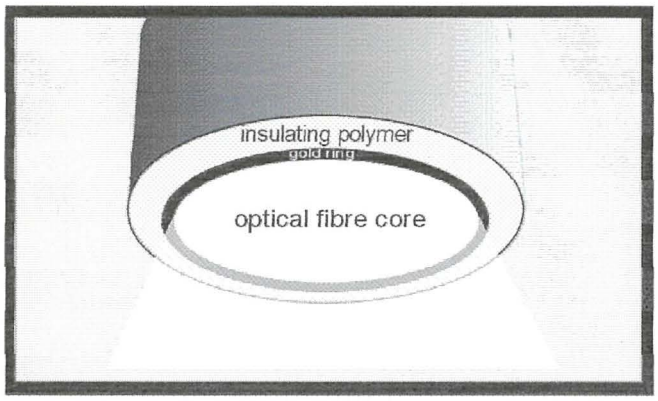

Figure 4.1.4: Illustration of the distal tip of a micro-optical ring electrode (MORE) showing the illuminated optical fibre core face, which would be suitable for the deposition of a titania thin film.

Combination of the above-described arrangements for sensing devices would produce the possible device structure illustrated in figure 4.1.5 that shows that by embedding a gold-coated optical fibre into the resin block prior to polishing, it would be possible to obtain an embedded ring-electrode. It is important to note that the electrode as shown would not have a circular profile and would therefore not operate according to expressions for MORE derived by other authors [41,42] which assume a circular profile.

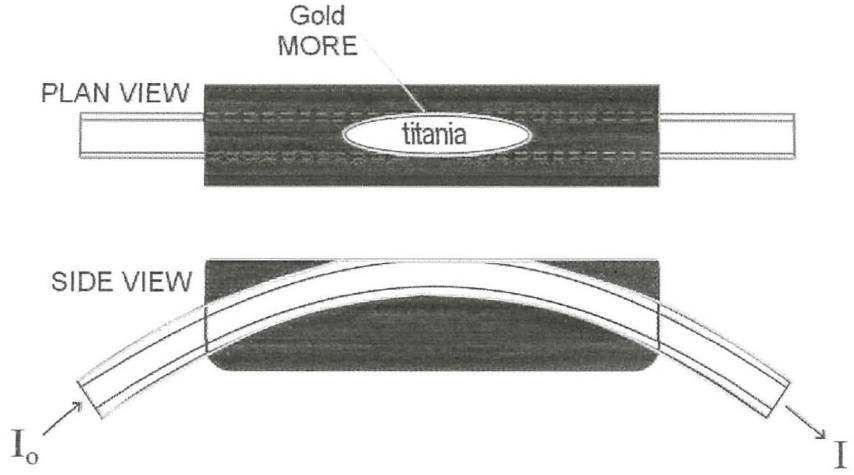

Figure 4.1.5: Illustration of a cross-coupling polished block arrangement incorporating a non-circular micro-optical ring electrode at the boundary of the polished face and a titania coating on the face surface.

4.1.3 Coating methods and substrates: slides and fibres

Standard telecommunications optical fibres are not particularly well suited to sensing applications and to the proposed device arrangements discussed above. This is due primarily to their large cladding thicknesses and poor transmission characteristics outside the telecommunications band of wavelengths. Optical fibre types that would be better suited to sensing would be those with larger numerical aperture, a thinner cladding dimension or an improved transmission in the visible, near-UV and UV regions of the electromagnetic spectrum. Two such types are large core plastic (usually PMMA) fibre and plastic clad silica fibres. These fibres are designed for specialist applications such as indoor or military installations. The relative profiles of these fibres and standard telecommunications fibres are shown in figure 4.1.6.

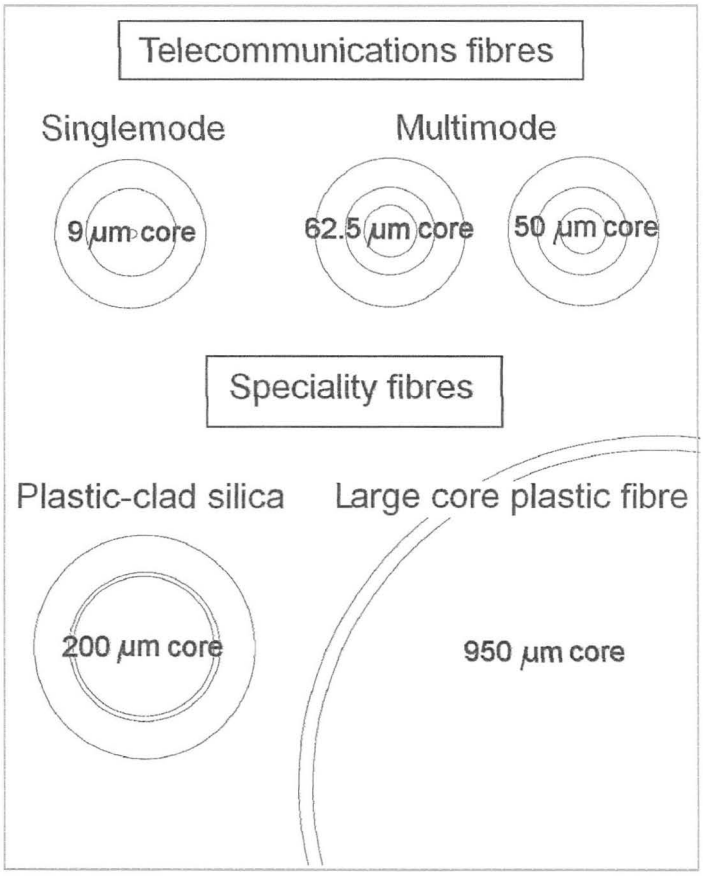

Figure 4.1.6 Relative dimensions of telecommunications and speciality fibres used for sensing.

Kubeckova, Sedlar and Matejec [46] reported the deposition of titania thin layers (500 nm) onto fused silica (quartz) fibres that had been specially manufactured with a large core and, importantly, without any cladding. Their films were deposited by a dip-coating procedure from a titania sol whereby fibres were withdrawn at a controlled rate from a titania containing sol and then calcined at 500 °C for 30 minutes. The fragility of exposed core fibres was demonstrated by Potyrailo [24] where disruption of Si-O-Si linkages at the fibre surface was shown to be the result of nucleophilic attack by water. This led to the formation of micro-cracks in the surface, which after propagation led to premature failure of the fibre. It was also shown that the activation energy of the water attack is a function of stress in the fibre wall. Fibres with exposed cores are thus extremely sensitive to bending forces, have poor lifetimes and are unsuitable for sensing devices unless the core is sufficiently protected.

Khijwania and Gupta [32,33] developed U-shaped probes designed for evanescent field sensing; the surface reactivity of the exposed silica cores was inhibited by deposition of a thin (130 nm) polymeric coating of polyvinylidenefluoride (PVDF) or polymethylmethacrylate [34,35]. It is therefore important to ensure that any sensing fibre arrangement incorporates some means of isolating the fibre from stress or chemical attack. Any chemical protection is best applied at manufacture or by a dip-coating procedure of exposed short lengths later.

Dip-coating [47,48] may also be applied to the coating of planar substrates such as slides or films. In this instance, other techniques are also available. Titania thin films may be laid down by, for example, plasma deposition techniques [49] or chemical vapour deposition [50,51]. Sol-gel methods are popular and commonly used [47,48,52-57] and may incorporate dip-coating, spinning or doctor blade techniques. Spinning of coatings onto slides is reported [53] to give better optical and mechanical properties due to the reduced retention of organic residues that results. An additional advantage of the sol-gel method is that it is relatively simple to produce doped or mixed-oxide thin films by incorporation of appropriate reagents in the starting mixture.

Frindell *et al.* [43] reported on the doping of titania with europium chloride whereby the Eu^{3+} ion is sensitised by the titania leading to a characteristic [43,78-80] red luminescence at 610-630 nm. Due to the large size of the Eu^{3+} ion (0.98 Å) relative to that of titania (0.68 Å), the europium ions are unable to incorporate into the lattice and occupy voids at the grain boundaries rather than titanium vacancies.

Mixed oxides of the type $Eu_xTi_yO_z$ are possible with the sol-gel technique as shown by Ovenstone *et al.*[78] who added an aqueous solution of europium nitrate to a mixture of titanium tetrachloride in water. They report that the amorphous mixed oxide has better luminescence than crystalline samples as the amorphous material can incorporate twice as much europium as the anatase form. The introduction of europium is further reported to delay the onset of crystallisation of anatase to a higher temperature, thus causing an increasing calcination temperature with increasing doping ratio.

Monovalent cationic doping of titania from sol-gel has been demonstrated by Lopez *et al* [56] however it was shown that lithium doping led to the production of the p-type [58] rutile phase of titania. Lithium is known to insert well into the titania lattice but shows distinct differences in insertion behaviour for the three polymorphs, anatase, rutile and brookite [81-83]. Certainly all three structures are based on titanium oxygen octahedra leaving octahedral vacancies which are suitable sites for intercalation. The packing in each case differs as is reflected in their densities (rutile: 4.25 gcm^{-3}, anatase: 3.89 gcm^{-3}, brookite: 3.76 gcm^{-3}) [81]. Given [81] that the ionic radius of the Li^+ ion is the same as that of the Ti^{4+}, *i.e.* around 0.68 Å [43], and the empty octahedral sites in rutile and brookite are 0.4 Å and 0.58 Å respectively, it can be seen that intercalation of lithium into these two polymorphs will be poor relative to that of anatase where the octahedral sites are considerably larger.

It was concluded by Zachau-Christiansen *et al.* that at room temperature (25 °C) rutile did not show insertion of lithium unlike anatase and brookite.

Indeed, calculations from first principles have shown [83] that there should be no intercalation into rutile at room temperature. An interesting phenomena is predicted by these same calculations which suggested that phase separation would occur into a lithium rich phase and a lithium poor phase. Thus, assessment of lithium intercalation at room temperature into a crystalline film should yield an indication of crystalline phase.

4.2 Experimental

4.2.1 Substrate preparation

Conducting glass slides with sputtered fluorine-doped tin oxide (FTO) coatings were cut to size by scoring with a tungsten-carbide knife and snapping. Slides for X-ray diffraction analyses were cut to fit sample holders (15 x 20 mm), otherwise slides were cut into 10 mm x 50 mm strips. After cutting, all substrates were immersed in UHQ distilled water (>18 MΩ) and placed into an ultrasonic bath for 10 minutes and dried under nitrogen flow. Substrates were then stored under vacuum at 80 °C. Prior to use, samples were degreased in hexane, air dried, rinsed in acetone, air dried, then finally rinsed in water and dried under nitrogen flow. Slides were dip-coated in pairs, in a back-to-back configuration to minimise coating of the back face of the glass. Indium-doped tin oxide (ITO) glasses were used to determine any substrate effect upon the final coating morphology. These ITO slides were prepared in exactly the same fashion as the FTO slides.

Optical fibres were cut into 10 to 15 cm lengths. Large-core plastic fibre lengths were cleaned with isopropanol fibre-cleaning wipes (lens-tissue soaked in 2-propanol and sealed in individual sachets) and dried in air. Plastic-clad-silica fibres required additional preparation. The outer protective nylon layer was removed using commercial fibre strippers and the inner thin plastic clad fibre was cleaned using fibre wipes as for the plastic fibre. Many fibres were coated with the cladding layer intact. Others had the cladding layer removed by a variety of methods. Attempts to remove the cladding layer included immersion in concentrated acids at varying temperatures as well as immersion in a range of organic solvents, again at varying temperatures. The cladding was also removed using heat treatment in a furnace and a blue Bunsen flame. After cladding removal fibres were again cleaned with isopropanol wipes and/or water rinses. After cladding removal, the silica cores were highly unstable and fractured within minutes of exposure to air and/or moisture. Thus coating was performed immediately after stripping.

4.2.2. Deposition of titania thin films on slides and fibres

Sols were prepared and characterised as described in Chapter 3. As a general scheme, the solvent, surfactant and hydrolysing agent were combined to generate the micellar sol. After stirring to ensure homogeneity, the alkoxide was added. The optimum time for dip-coating was shortly after addition of the alkoxide (TTP) to the sol. Figure 4.1.7 is a flowchart illustrating the coating process.

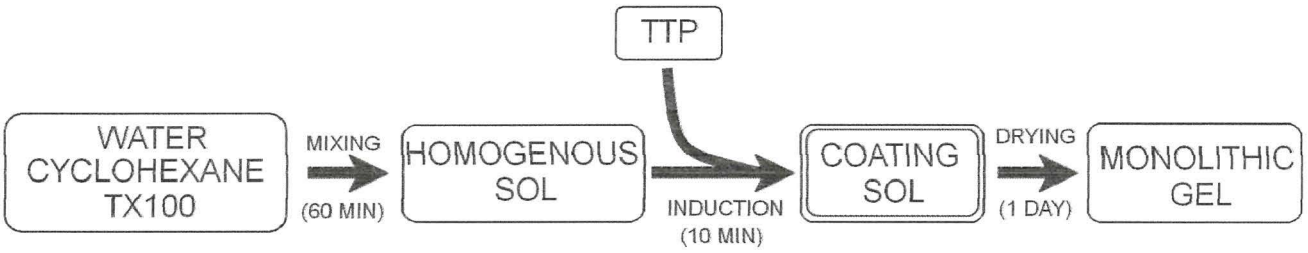

Figure 4.1.7: Flowchart illustrating the stages of sol generation and coating.

Slides were coated in pairs, back-to-back and supported with a crocodile clip attached to a mechanical, home-made, dip-coating device illustrated in figure 4.1.8 below. Slides (10 x 50 mm) of FTO coated glass were coated with between 1 and 5 coats. Raw slides were dried at 353 K for 2 hours before being transferred to a vacuum oven at 343 K for 24 hours to age. Vacuum dried slides were calcined in a muffle furnace at 623 K for between 10 and 20 minutes.

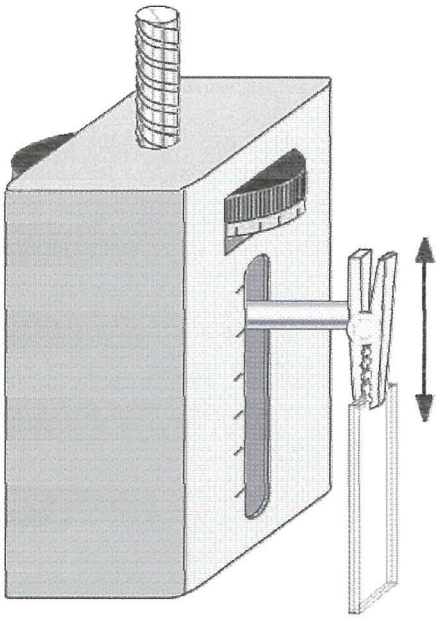

Figure 4.1.8: Illustration of the device used to control the rate of dipping during coating.

Dip coating proceeded according to the following scheme: samples were lowered into the sol at 1 cm per second and left immersed for 30 seconds. The slides were then withdrawn from the sol at a rate of between 1 mm and 5 mm per second. Generally, slower withdrawal rates led to smoother and thinner films. Faster withdrawal does not allow sufficient time for even drainage of excess liquid from the slides and leads to 'runs' and drips on the slide surface. Ideally the withdrawal rate should be comparable with the rate at which excess fluid is drained; this ensures only very thin liquid films are deposited. Rapid evaporation and drying in air would cause rapid drying of thick liquid films before even drainage has occurred thus resulting in thicker films. The wet slides were allowed to rest in air for between 1 and 5 minutes prior to repeat dipping. After final coats were applied, the pairs of coated slides were removed from the crocodile clip, separated using tweezers, and allowed to dry in air for 10 minutes before being transferred into the drying ovens.

An alternative method of multiple-coat application involved the application of single coats of raw gel and thermal treatment at elevated temperature to calcine the film prior to cooling and repeat coating. Lithium and europium doped titania films were deposited from doped sols using the same mechanisms described above. Doping of sols was achieved by addition of appropriate aqueous solutions of the dopant metal ion in the place of the pure water used for undoped titania sols. A 1 $\%_{wt}$ Li^{+} sol was obtained by addition of 610 µl of 4 $moldm^{-3}$ aqueous lithium chloride to the Triton X-100 solution prior to addition of the alkoxide. Likewise, a 1 ‰ atomic ratio Eu^{3+} doped sol was prepared by the addition of 610 µl of 0.028 $moldm^{-3}$ aqueous europium sulphate.

The procedure adopted for the coating of optical fibres was similar to that described above for slides. Cleaned prepared fibres were supported on cardboard sheets or glass tubes which were then held in the crocodile clip shown in figure 4.1.8 earlier. As for slides, coating was performed in an open system (*i.e.* exposed to ambient moisture).

As for the slide coating, samples were rapidly lowered into the sol and withdrawn at a slower rate. The number of coats applied varied between 1 and 20 depending on the nature of the experiment. Typically, a 5 cm length of fibre was coated leaving between 5 and 10 cm of uncoated fibre to allow handling. After coating, "raw" samples (coated fibres) were placed in an oven at 338 K for between 2 and 48 hours. After this preliminary drying stage, the "dried" samples were transferred to a vacuum oven at 343 K for storage prior to further tests. Samples dried under this regime were termed "vacuum-dried" samples. Some samples on optical fibre were exposed to thermal treatment to attempt to calcine the films. This was on the whole unsuccessful and resulted in considerable fibre damage.

4.2.3 Characterisation of thin films

Samples at all stages of production, both in the pre- and post-coated states were prepared for electron microscopy by sputtering with a thin layer of gold, with typical thickness less than 100 Å. Samples were placed in the chamber of the microscope and micrographs recorded to observe the quality of films, to estimate film thickness and to discern any morphological changes in the film surface after testing. Energy dispersive X-ray (EDX) analysis was used where possible to identify the composition of the films. Estimates of film thickness were determined by inspection of the film at fractures, fissures and the film edges. Where no such features were discernible the film was manually scratched with a needle point in a grid pattern and micrograph images were recorded of the edges of the scratches thus induced. In addition to the SEM estimates, a measure of the thickness of applied coatings on fibres was gauged using a Laser Micrometer (Anritsu). This micrometer is capable of measuring wire diameters to within 50 nm. By measuring the mean diameter of the uncoated fibre and repeating the measurements after coating, it was possible to gain an accurate assessment of coating thickness.

In order to determine the elemental composition of the films and to assess to some degree the oxidation state of titanium, the films were subjected to X-ray photoelectron spectroscopy (XPS) using a VG scientific XPS instrument with a water-cooled dual magnesium / aluminium source. Samples were mounted onto polished copper studs using conductive silver paint. Broad survey spectra were recorded over the full possible range of binding energies and fine resolution spectra were obtained of those regions of interest, principally the Ti2p, O1s and, for calibration purposes, the C1s. All spectra were pre-corrected for the spectrometer work function and were further calibrated for surface charging effects by adjustment of the adventitious carbon based adsorption component of the C1s peak to 285.0 eV [84] . Iterative peak fitting with background corrections were performed on high resolution spectra to ascertain individual peak components.

Samples of coated and uncoated slides were analysed by X-ray diffractometry (XRD) to yield information about the extent of crystallinity of the titania in the samples. A Ni filtered Cu Kα source operating at 40 kV and 45 mA was used for all measurements. Samples were scanned between 5 and 75 ° 2θ. Short, 30 minutes scans were used to give a quick indication of the presence or absence of crystallinity and longer scans of between 2 and 18 hours were recorded to improve the signal to noise ratio of spectra. The spectrometer used was a Philips X-Pert diffractometer designed primarily for powder measurements and was thus not particularly well suited to the measurement of thin films on flat samples. Good spectra of the sputtered substrates were obtained but no spectra were seen for the thin films on the slide surfaces. Attempts to determine XRD diffractograms of coated fibres were similarly unsuccessful.

Ultraviolet-visible (UV-vis) spectrometry measurements were performed using an Oriel broad spectrum, high intensity Xe arc lamp. Light from the source was coupled into an optical fibre cable and through a beam collimator. After passing through the sample the light was captured by a second collimating beam probe and transmitted *via* a second optical fibre to the detector.

The Oriel detector consisted of a grating to disperse the beam onto a photodiode array. The detector was calibrated against a Hg emission source for the range 250 – 700 nm and a Ne emission source for the range 650 – 1100 nm. Measurements were performed in a black box to minimise ambient light and were background corrected.

Conducting glass slides have a characteristic absorbance profile and this was accounted for by subtraction of a reference trace obtained from a blank sample. Spectra were recorded as accumulations of multiple scans, typically 1000, so as to minimise noise in the traces. Some difficulties were seen due to changes in surface reflectivity with coating type and thickness due to orientation of the samples in the beam. Very small differences in sample alignment from the beam normal could lead to beam reflection in addition to absorption and transmission.

This occasionally lead to anomalous values for absorption in some spectra. The most common manifestation of this phenomena was as negative absorbances. The software used by the system (Instaspec Basic) gave results as % transmittance or as linear % absorbance. It is important not to confuse the % absorbance values quoted in this text with logarithmic absorbance calculated from the % transmittance, as would be more commonly used.

4.3 Results and discussion

4.3.1 Undoped titania coated slides

Good quality thin films of titania were deposited onto acid-cleaned conducting glass substrates. An electron micrograph of the substrate surface is shown in figure 4.1.9 below. The sputtered tin oxide surface is characteristically rough on a sub-micron scale and has a film thickness of 1 μm.

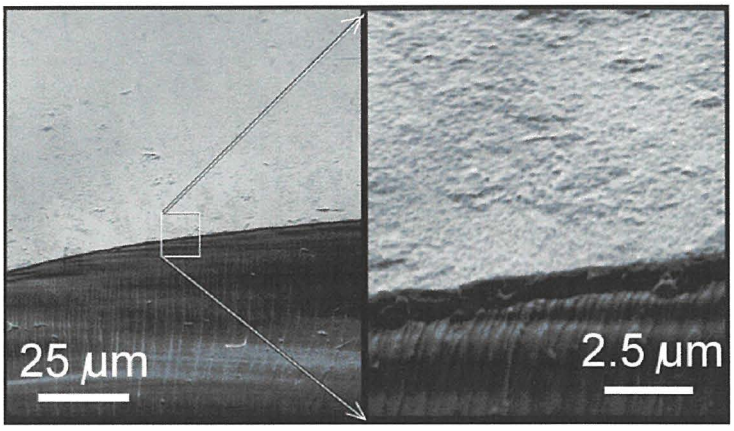

Figure 4.1.9: Scanning electron micrographs of an FTO glass after acid-cleaning at 303 K.

Figure 4.2.0 shows typical micrographs of the film obtained. The image at left shows the surface at the intersection of two scratches made upon the surface with a needle after sputtering with gold and before insertion into the SEM instrument.

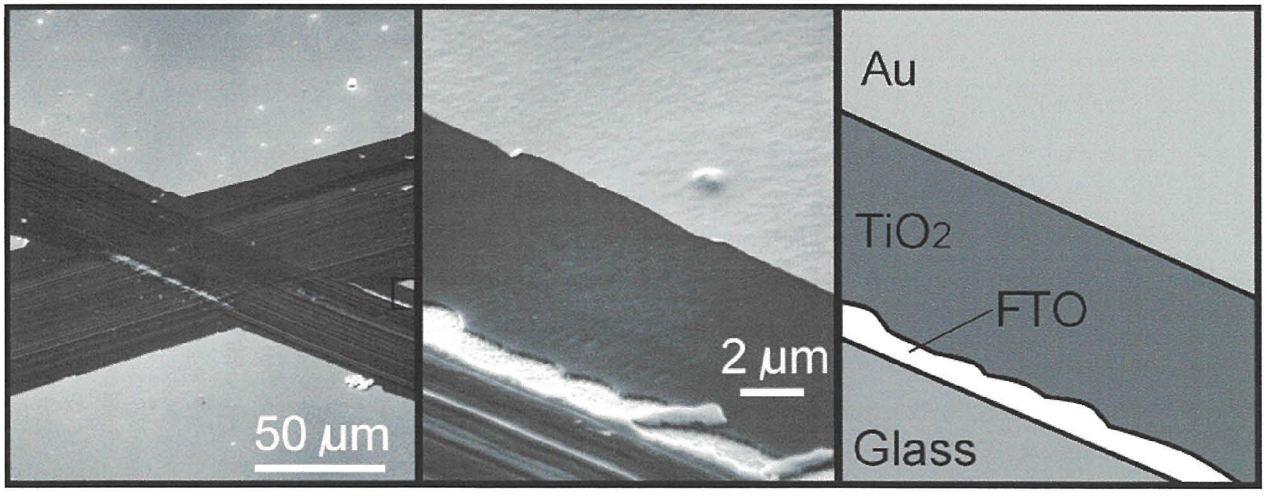

Figure 4.2.0: Scanning electron micrographs of a single layer, titania coating, thermally treated at 723 K, on a FTO glass slide.

Closer inspection of the rectangular region marked in the left image shows (centre) that a good quality film of even thickness has been deposited onto the conducting glass surface. The graphic (right) identifies each component of the film. The presence of titania was confirmed by X-ray photoelectron spectroscopy (XPS). Figure 4.2.1 shows a survey scan of an undoped titania thin film on a fluorine-doped tin oxide (FTO) conducting glass substrate.

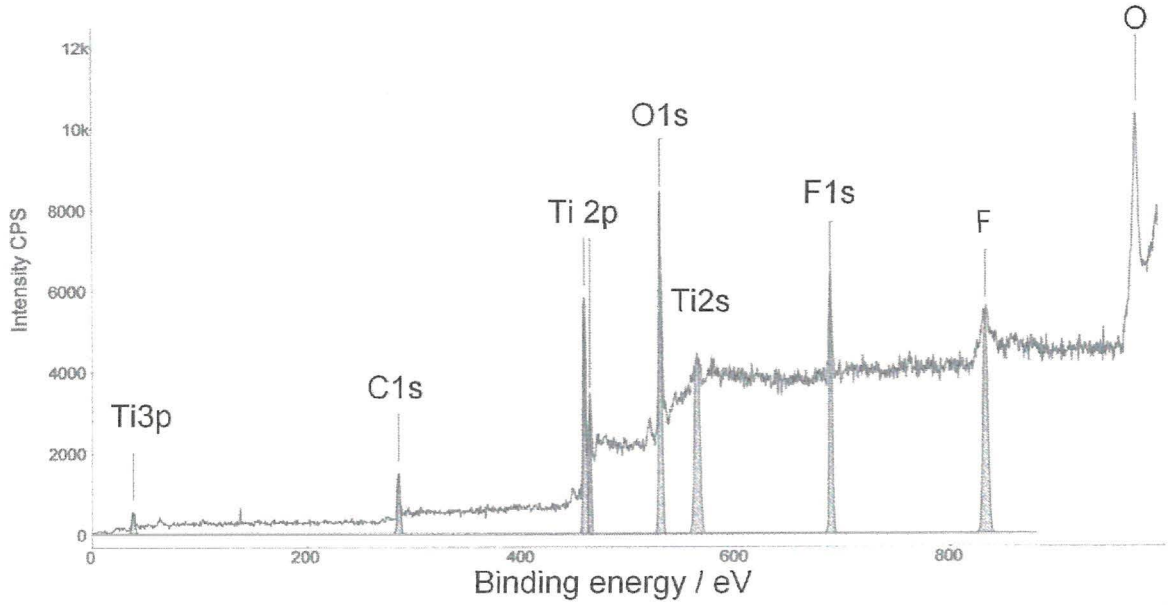

Figure 4.2.1: XPS broad scan of an undoped titania thin film on an FTO conducting glass substrate. The key titanium 2p and oxygen 1s signals are clearly visible as are signals obtained from the FTO substrate and surface contamination.

Peaks due to titania and oxygen are seen, together with signals characteristic of the conducting substrate. High resolution spectra shown in figures 4.2.2 and 4.2.3 (both overleaf) indicate that the film is likely to be titanium (IV) oxide. The Ti $2p_{3/2}$ peak (figure 4.2.2) is seen to occur at around 458 eV which is characteristic of titanium in the +4 oxidation state [48-51,59]. It is not possible to distinguish between the presence of anatase and rutile as both polymorphs show identical binding energies [59]. The O1s peak (figure 4.2.3) lies at around 530 eV which is indicative of oxygen bound to a metal as a divalent oxide [48,49,51]. These two results, taken together, support the hypothesis that titania has been deposited. In addition, iterative peak fitting of the O1s peak suggests that in addition to the oxide peak at 530 eV there may also be a peak due to oxygen bound as hydroxide at 532 eV [48,51].

This is interesting in that it would imply that the films are in the anatase structure which has extensive surface hydroxylation rather than rutile, which does not show this feature.

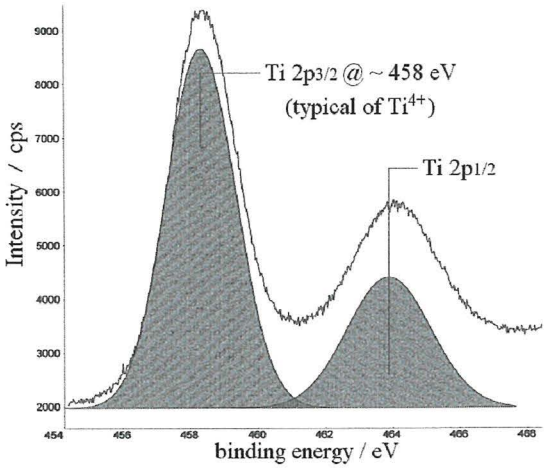

Figure 4.2.2: High resolution XPS scan showing the titania 2p peaks of a thin film on a conducting glass substrate. The $Ti2p_{3/2}$ peak at a binding energy of 458 eV is characteristic of titania in the +4 oxidation state.

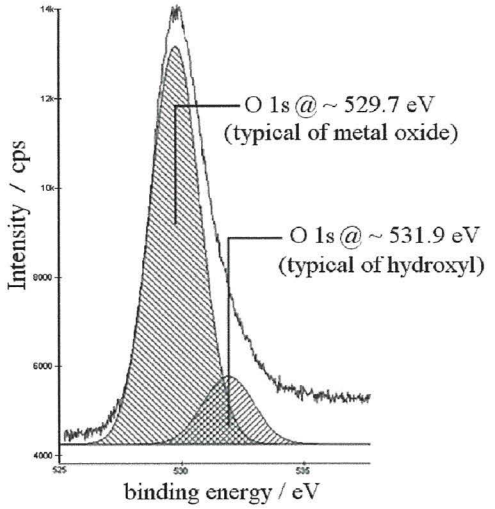

Figure 4.2.3: High resolution XPS scan showing the oxygen 1s peak of a thin film on a conducting glass substrate. The O1s peak at a binding energy of 529.7 eV is characteristic of oxygen bound as a metal oxide. The presence of a side peak at 532.9 eV is suggested by peak fitting and may be indicative of hydroxyl oxygen.

Deposition onto indium-doped tin oxide (ITO) rather than FTO yielded similar results to those shown above. The principle differences observed were the XPS signals of the substrate, where peaks due to indium are seen instead of those for fluorine. The fact that any signals from the substrate materials were seen is somewhat surprising given that the escape depth of photoelectrons in XPS is of the order of 5 nm and film thicknesses are of the order of several hundred nanometres. The presence of the signal is likely due to the lack of complete surface coverage.

Scanning electron micrographs of the coatings were recorded to determine film thickness. Figure 4.2.4 (overleaf) shows an un-calcined sample with three layers of raw gel deposited onto FTO. The sample had been dried under vacuum at 353 K. The graphic at the right of the figure explains the micrograph.

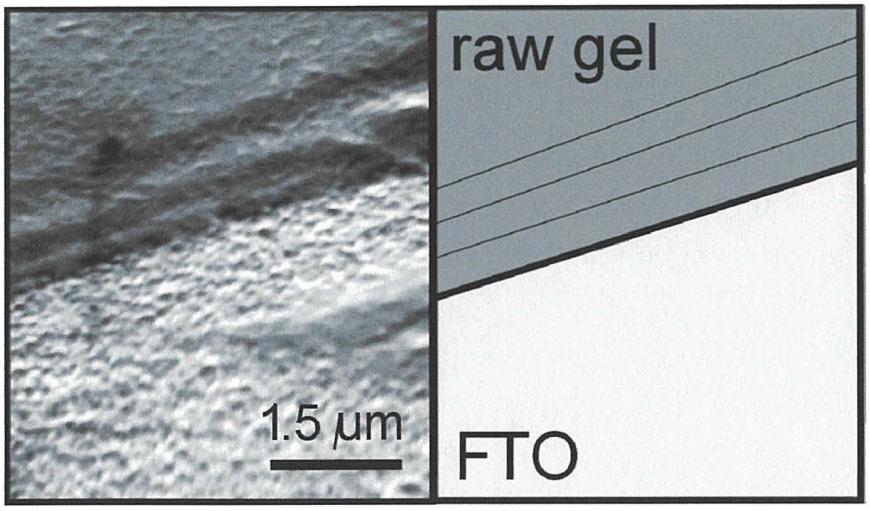

Figure 4.2.4: Scanning electron micrograph of a triple coating of raw gel on FTO glass after drying under vacuum at 353 K.

The three layers are clearly visible as is the surface texture. The gel film with a total thickness of around 1 μm has mimicked the rough pattern of the sputtered FTO substrate. This is similar to an effect reported by Kluson et al [54,55] whereby films applied to substrates adopted the underlying morphology. After thermal treatment of the triple-layered film the layering remains distinct. This is shown in figure 4.2.5, where again the graphic at right explains the micrograph.

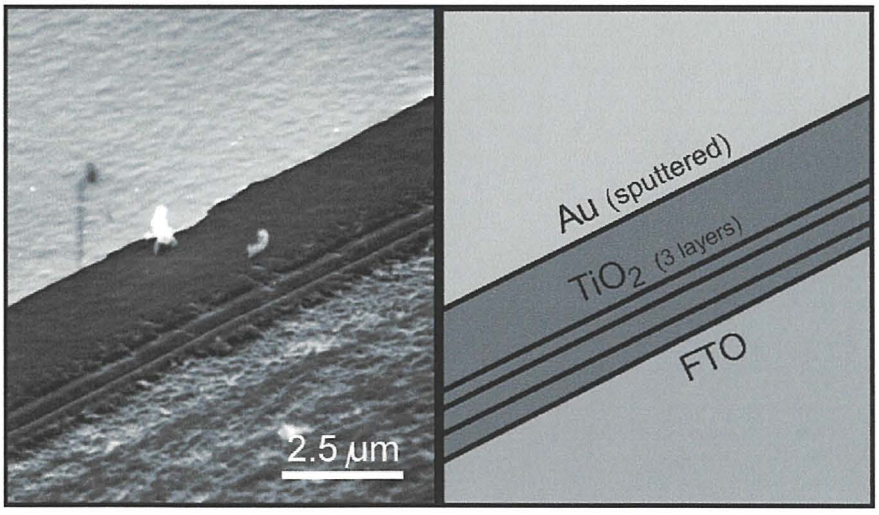

Figure 4.2.5: Scanning electron micrograph of a triple layer coating of titania on FTO glass after thermal treatment at 823 K.

Attempts to determine the crystallinity of the films with X-ray diffractometry were unsuccessful. A typical diffractogram obtained of a blank, uncoated FTO slide is shown in figure 4.2.6.

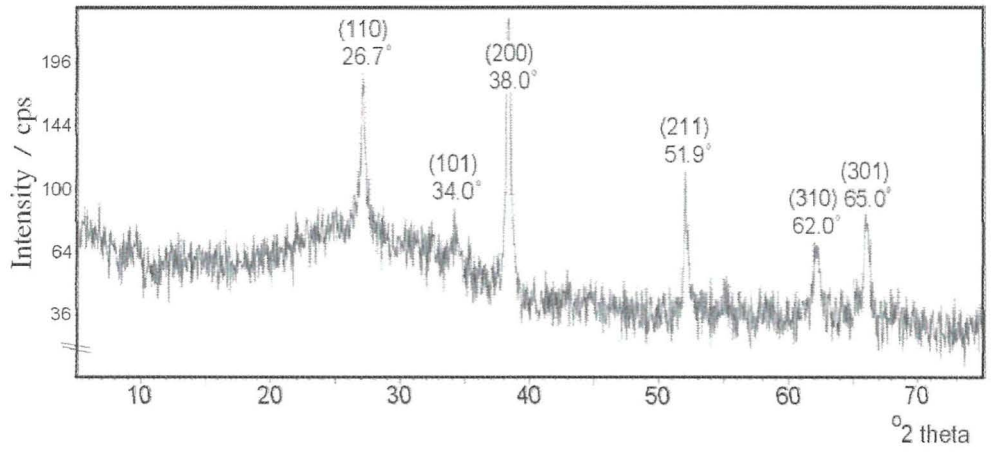

Figure 4.2.6: X-ray diffractogram of a blank, uncoated FTO conducting glass slide. The peaks obtained are in agreement with those quoted in the literature [60]

Comparison of the diffractogram above with that of a calcined titania thin film on FTO (figure 4.2.7) shows that none of the signals characteristic of titania, either anatase [47,50,56,58,61-67] or rutile [47,56,58,61-62,65-67] were seen.

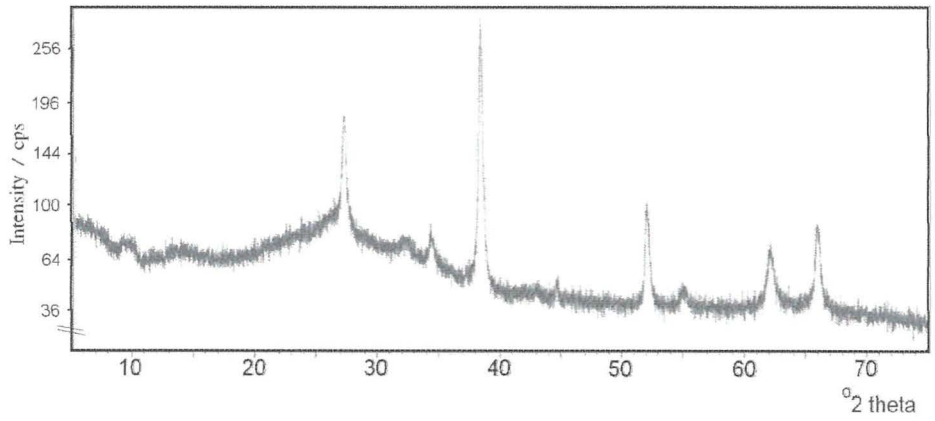

Figure 4.2.7: X-ray diffractogram of a titania coated FTO conducting glass slide. The peaks obtained are only those of the FTO as seen above.

It is thought that this was due to the thin nature of the films. Yu *et al.* [48] reported a similar result and attributed the absence of peaks to film thicknesses being less than 500 nm. They further stated that orientation towards the (101) plane of anatase only began above 500 nm film thickness.

The absence of peaks may of course be due to the fact that the films could be non-crystalline, *i.e.* amorphous, as none of the other results obtained are directly indicative of either an anatase or rutile structure. Given however that we know the film thicknesses rarely exceed 350 nm, it is highly likely that coherent signals are unobtainable due to the thin nature of the films, as described in the literature by Yu *et al.*

UV-visible absorbance spectra were recorded of the thin films on conducting glass substrates. The underlying tin oxide material has its own characteristic absorbance (as shown in figure 4.2.8) and the results obtained were in agreement with those in the literature [68].

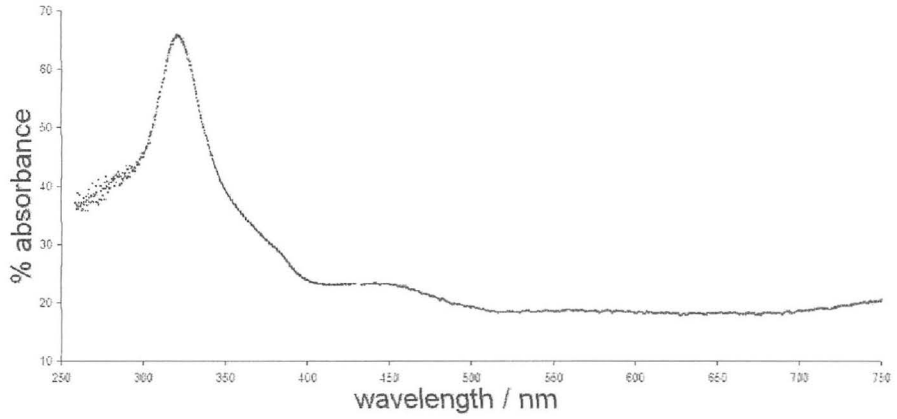

Figure 4.2.8: UV-visible absorbance spectrum of an uncoated FTO coated glass.

Because of this, reference readings were taken of identical uncoated slides prior to measurement of the film spectra and thus the spectra obtained show only the absorbance of the film.

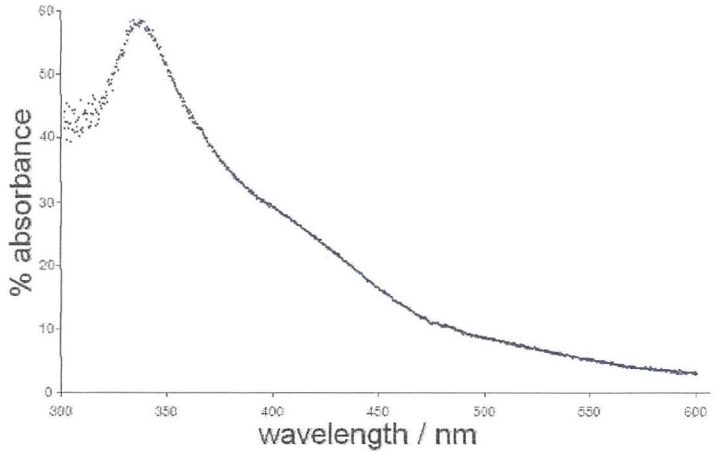

Figure 4.2.9: UV-visible absorbance spectrum of an un-calcined xerogel thin film on a conducting glass substrate.

The spectra obtained from un-calcined films typically lacked a distinct band-edge and showed an appearance such as that illustrated in figure 4.2.9 (above), taken of a xerogel film. After calcining the onset of crystallisation was seen by the appearance of a sharp cut-off region falling consistently between 380 and 400 nm. Figure 4.3.0 shows a spectrum obtained from a thermally treated (calcined) thin film on an FTO slide. This is in agreement with figures quoted by Fretwell [53] and others [48,56,64,68] who report band-edges at around 400 nm for titania thin films deposited by sol-gel methods.

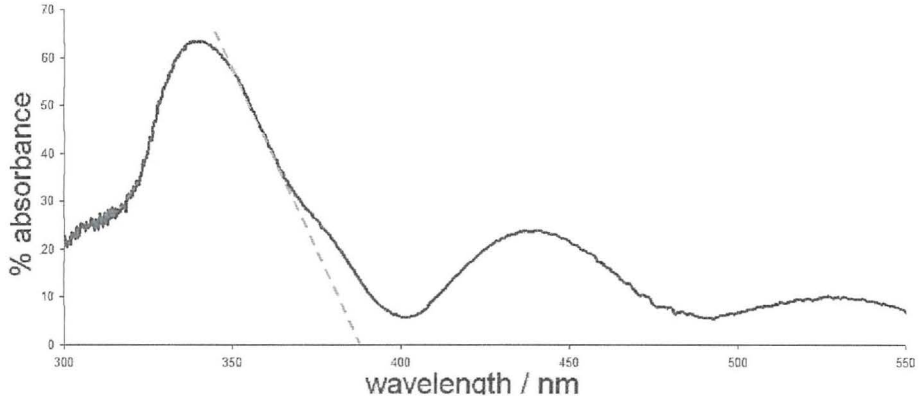

Figure 4.3.0: UV-visible absorbance spectrum of a titania thin film on a conducting glass substrate.

There is some evidence from the spectrum of a shoulder on the main peak at around 380 nm however this may be a continuation of the interference bands observed above 400 nm. Similar interference bands were seen by Yu *et al.* [48] and may be caused in part by scattering [53] and interference due to the film-thickness and incident wavelengths being of comparable dimension.

A crude estimate of the band-edge (which ignores the shoulder) is shown on the figure above. This yields a cut-off wavelength between 380 and 390 nm. This corresponds to a band gap of between 3.17 and 3.26 eV. Anatase titania has a band gap of 3.2 eV [69] whereas rutile has a band gap of only 3.0 eV [69], thus this result may be suggestive of an anatase structure. However, as the band gap of nanoparticles is a size dependent property, if the film were made of discrete particles then this result may not indicate an anatase structure.

If rutile particles were sufficiently small in diameter then a band gap energy of 3.0 eV (equivalent to $\lambda = 413$ nm) could increase. Indeed, Frindell *et al.* [43] reported a band-edge shift of 25 nm (0.2 eV) in doped titania nanocrystals by virtue of their small size.

4.3.2 Doped titania thin films on slides

After successful deposition and generation of undoped titania thin films on slides, attempts were made to deposit cation-doped titania films. Lithium ions are well known to substitute into the titania lattice due to the good match in ionic radii and may induce colourisation properties to the film. Lithium salts were dissolved into water that was subsequently used to hydrolyse the sol. The sols remained stable and good raw-gel films were produced. Figure 4.3.1 shows a smooth raw gel deposited onto a conducting glass slide.

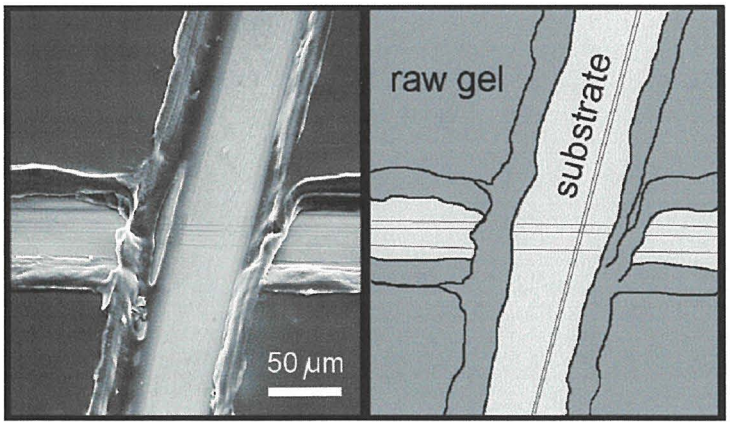

Figure 4.3.1: Scanning electron micrograph of a smooth raw gel deposited onto a conducting glass slide. The cross was made with a needle point to determine film thickness.

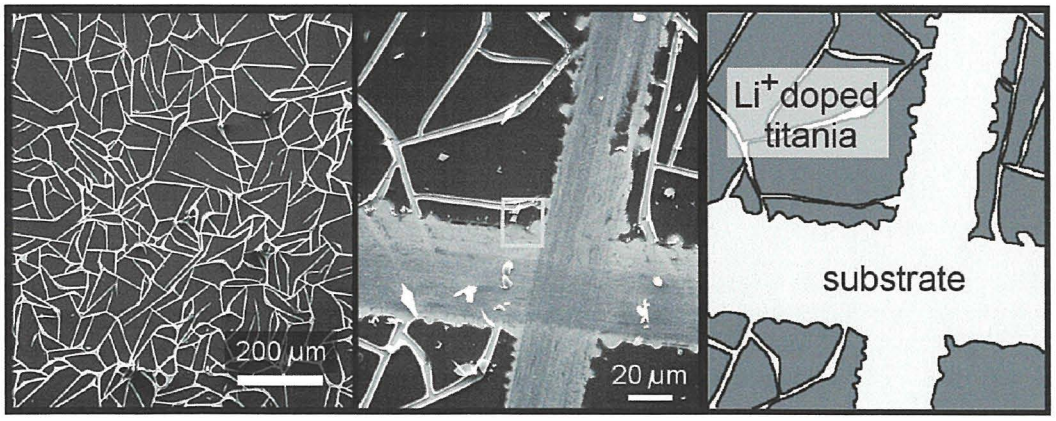

Figure 4.3.2: Scanning electron micrograph of a fractured, calcined film on a conducting glass slide.

Upon calcining the lithium doped films showed a tendency to fracture extensively as can be seen in figure 4.3.2 (above). It is possible that the incorporation of lithium into the titania lattice has resulted in phase separation into Li^+ rich and Li^+ poor regions as suggested by Zachau-Christiansen *et al.*[83].

These two regions would have fundamentally different properties, with the lithium-rich region being characterised by titania with a mean oxidation state nearer +3 and perhaps a rutile phase as suggested by Lopez *et al.* [56]. The lithium-poor region would, on the other hand, be predominantly tetravalent and consist of the anatase phase. These differences in structure could lead to the extensive fracturing seen.

The doped samples were assessed by XPS and the results of a survey scan are shown in figure 4.3.3. Lithium has only a single, weak 1s peak at a binding energy of 54.8 eV [70,71], however this was not seen on the spectra obtained. This is due to the low dopant level used.

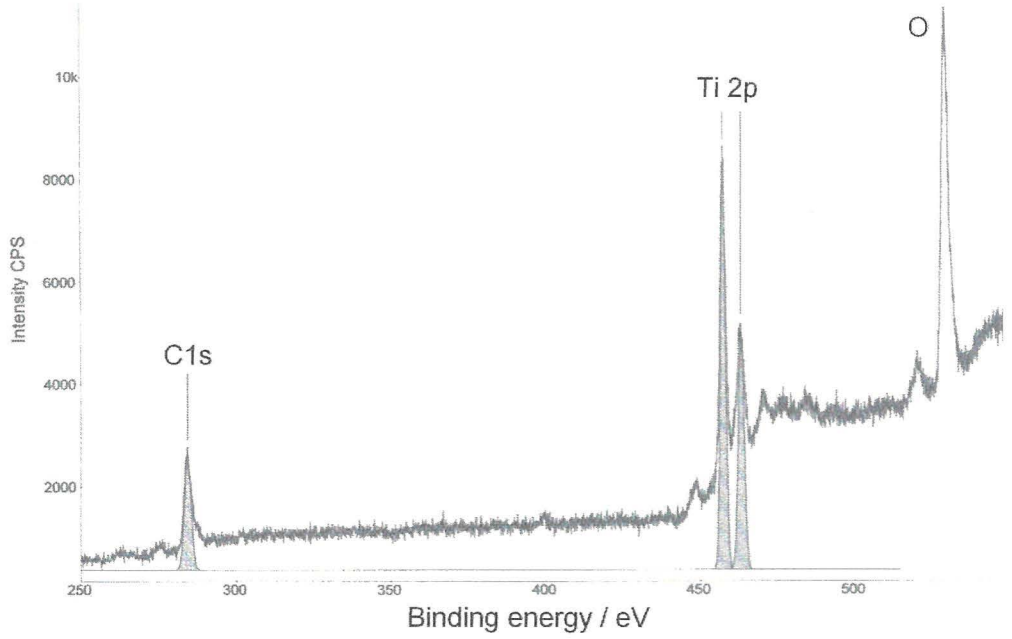

Figure 4.3.3: XPS survey scan of a lithium doped titania thin film on a conducting glass substrate.

Information about the oxidation state of titania in the material can be obtained from a high resolution scan taken of the same sample and shown in figure 4.3.4 (overleaf).

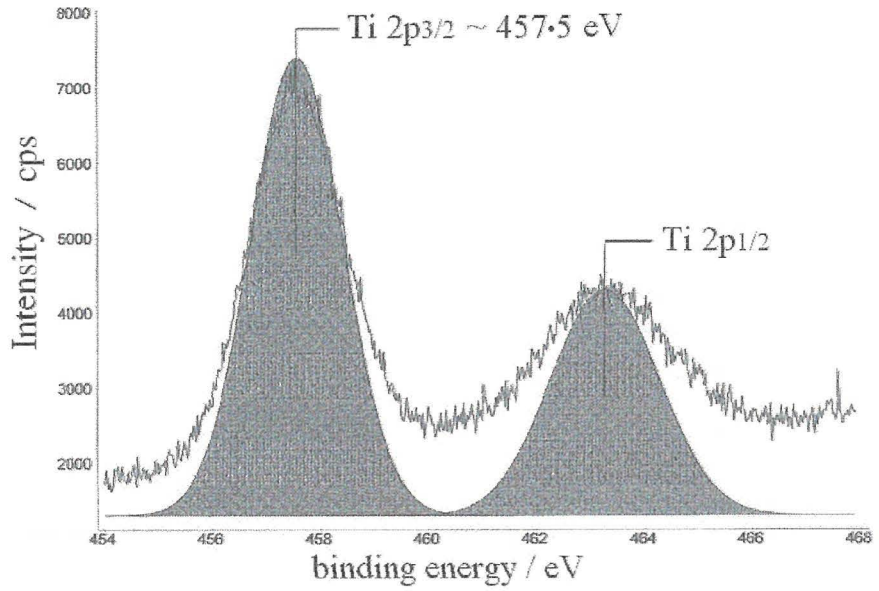

Figure 4.3.4: XPS spectrum of the Ti 2p peak of a lithium doped titania thin film on a conducting glass substrate.

Metallic titania would show a Ti $2p_{3/2}$ peak at a binding energy of 453 to 454 eV [70,72,73]. Titanium (II) shows the same peak in the range 454 eV up to 455 eV [70,73]. Titanium (III) shows the $2p_{3/2}$ peak between 455 and 457.5 eV [73,74,75]. Titanium (IV) generally appears above 458 eV up to about 460 eV although it has been seen around 457.5 eV as seen here [48-51,59,70,72,73,76].

In addition to the formation of a rutile phase, as reported by Lopez [56], the incorporation of Li^+ into the lattice will also induce the reduction of titanium (IV) to titanium (III) in the region of the lattice surrounding the lithium ion. This would be necessary to maintain the charge balance within the lattice.

In addition to direct lithium doping during hydrolysis and polycondensation, simple electrochemical lithium insertion experiments were also performed on undoped films. When an undoped, calcined titania coated electrode was electrochemically reduced in the presence of a lithium containing electrolyte (aqueous lithium perchlorate, 0.1 M) the UV-visible absorption spectrum of the film changed dramatically and a visible darkening (indigo) was seen on the electrode.

Figure 4.3.5 shows the UV-visible absorbance spectra of the oxidised and reduced states of the film, and figure 4.3.6 shows a UV-vis spectrometry time-series of the same sample as the applied potential was cycled with time.

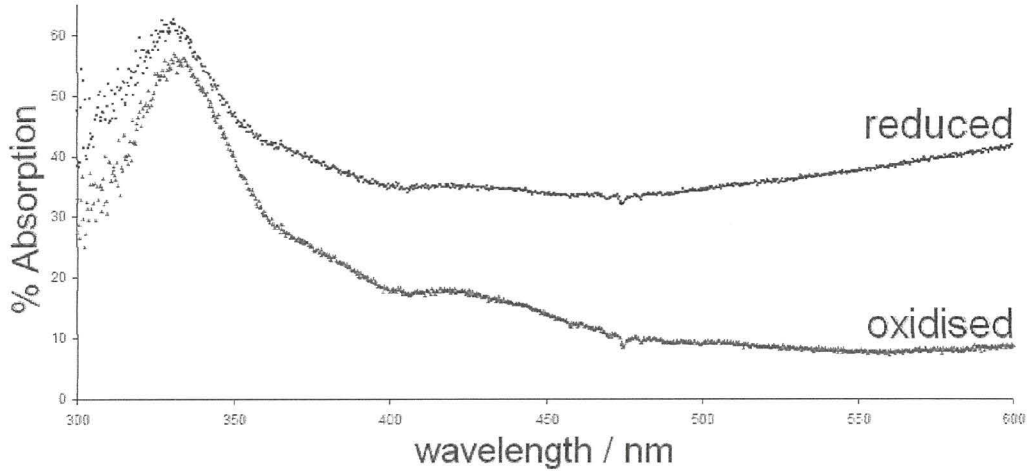

Figure 4.3.5: UV-visible absorbance spectrum of a titania thin film in the oxidised and reduced states during electrochemical lithium insertion.

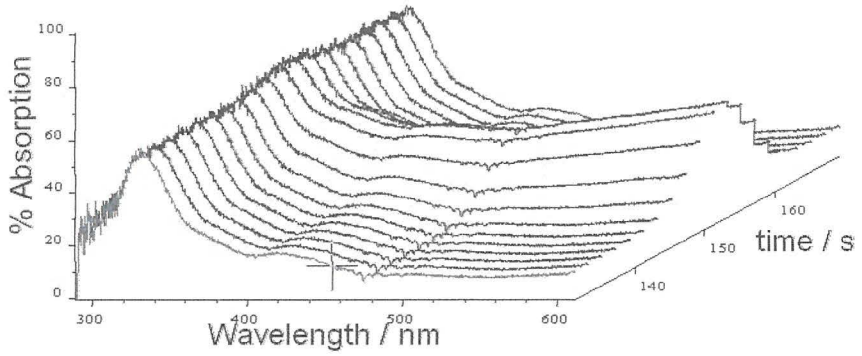

Figure 4.3.6: UV-visible time series showing the fluctuation of film absorbance as the applied potential is cycled with time.

The picture is made clearer by selection of an individual wavelength. The variation in transmittance at 600 nm versus applied potential is plotted in figure 4.3.7 (overleaf). The direction of the scan is indicated with arrows on the plot. The strong optical response of the film indicates that reduction of the film and uptake of lithium ions from the electrolyte is occurring. The film integrity was far superior in the case of electrochemical doping of the film than for chemically doped films.

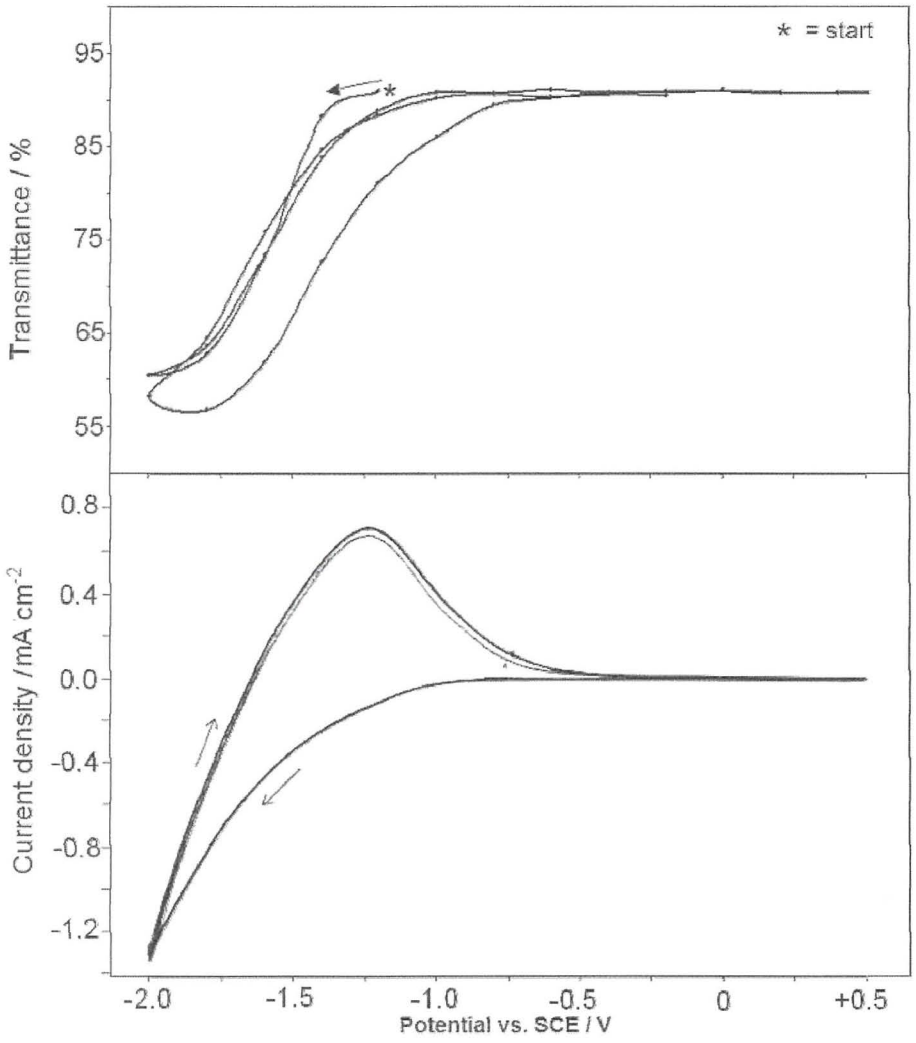

Figure 4.3.7: The change in transmittance of a titania thin film electrode as a function of applied potential at a wavelength of 600 nm is shown plotted together with the corresponding cyclic voltammogram. (Arrow indicates direction of scan at a sweep rate of 100 mVs^{-1}) Optical measurements commenced 15 seconds after the start of the potential cycle which commenced at +0.5 V

The electrode coating did degrade if left at a constant reducing potential due to violent gas evolution at the electrode surface. The indigo colouration of the reduced film faded over several minutes during exposure to air upon removal of the electrode from the cell.

Films doped with 1 ‰ (0.1 %) atomic ratio trivalent europium were also attempted using the same sol-gel process. Film thicknesses slightly thicker than those obtained for undoped films were seen, typically between 500 nm and 1 μm. Good quality thin films were obtained on conducting glass slides.

Only where films were deliberately scratched or at the film edges was it possible to obtain good micrographs which illustrate film thickness, such as that shown in figure 4.3.8.

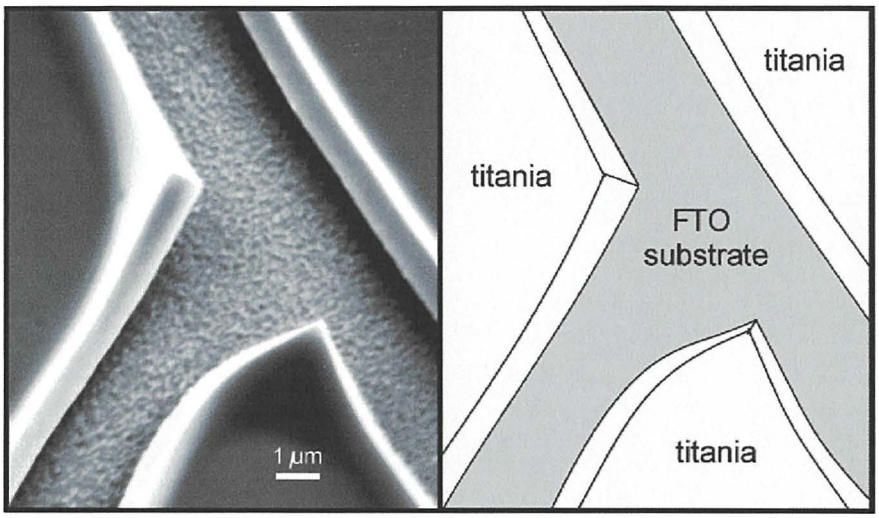

Figure 4.3.8: Scanning electron micrograph showing a single calcined film of titania doped with europium 3+ deposited onto a FTO substrate.

X-ray photoelectron spectroscopy analyses showed some evidence for the presence of europium in the films, with weak signals for europium seen at high binding energy in survey spectra (figure 4.3.9) at binding energies in excess of 1100 eV.

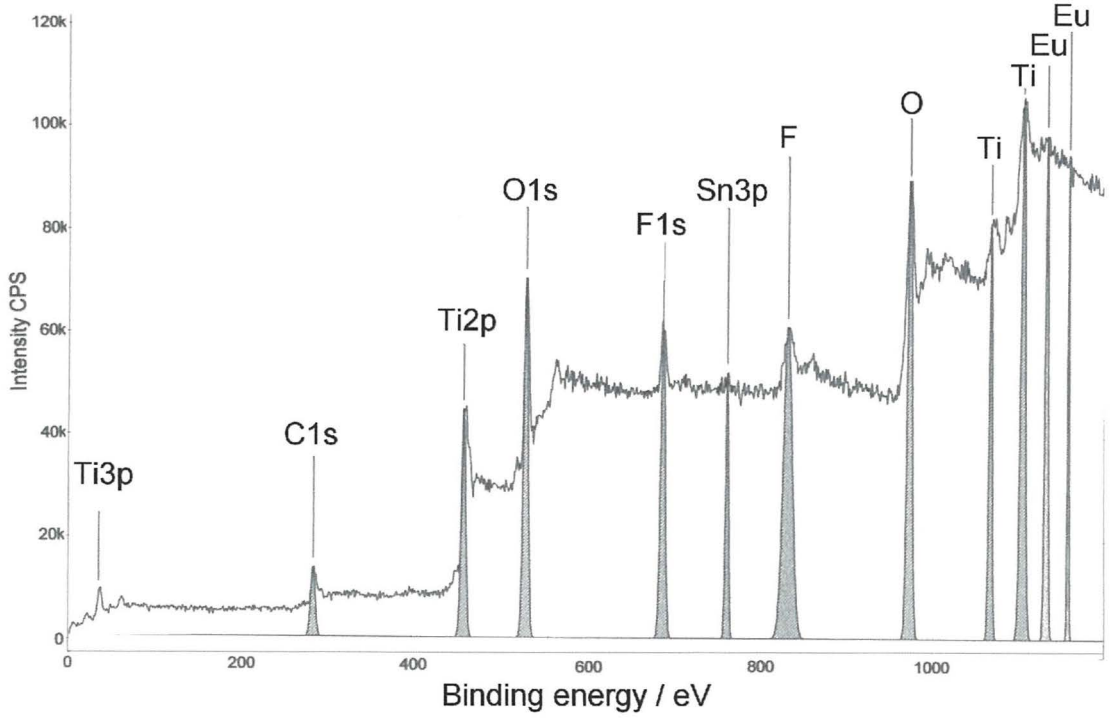

Figure 4.3.9: X-ray photoelectron survey spectrum of a single calcined film of titania, doped with europium 3+ and deposited onto a FTO substrate.

Closer inspection of the regions where the europium signals were expected showed that small amounts of the europium ion have been incorporated. Figure 4.4.0 and figure 4.4.1 show high resolution spectra of the high binding energy region above 1100 eV and the lower energy region around the C1s signal respectively.

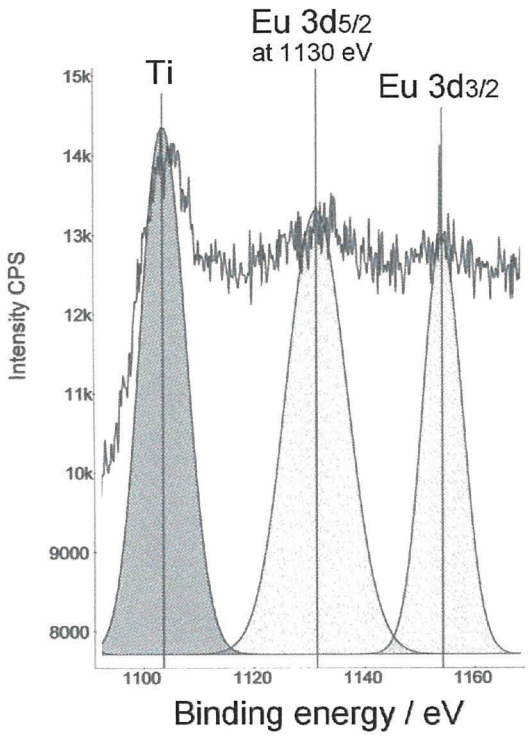

Figure 4.4.0: High binding energy region X-ray photoelectron spectrum of a single calcined film of titania, doped with europium 3+ ions, deposited onto a FTO substrate, showing the weak Eu3d signals at around 1130 and 1155 eV.

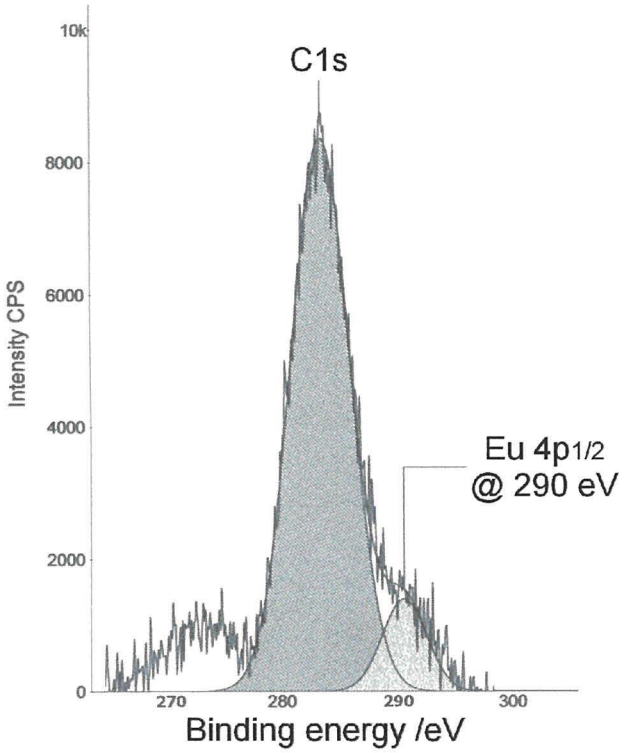

Figure 4.4.1: 270 to 300 eV region of the X-ray photoelectron spectrum of a single calcined film of titania, doped with europium 3+ deposited onto a FTO substrate.

In both instances it is possible to identify weak but characteristic [77] peaks of europium. The 3d signal at 1130 – 1155 eV and the 4p at just below 300 eV as a shoulder on the C1s signal at 285 eV.

Multilayer deposition was demonstrated on single sheets of FTO whereby successive coats were deposited onto calcined earlier layers, figure 4.4.2 (overleaf).

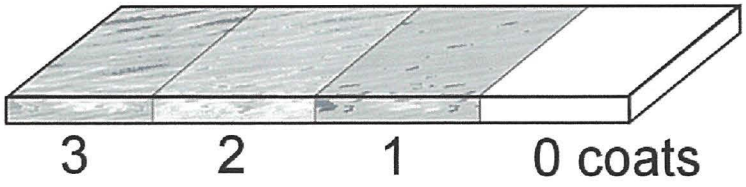

Figure 4.4.2: Illustration of the appearance of multicoated conducting glass slides created by repeated dipping and calcining. Thickness is increased with each additional applied layer.

Film quality, coverage and cohesion was excellent across the bulk of each coated surface except at the steps where successive layers began, at which point film fracture was observed. It was at these fractured regions that scanning electron micrographs were taken to estimate film thickness and layering structure. In the absence of fracturing only smooth, even films were seen with little or no contrast for beam focussing or image capture.

Figure 4.4.3 shows an electron micrograph of the step between the uncoated bare slide and the first doped layer.

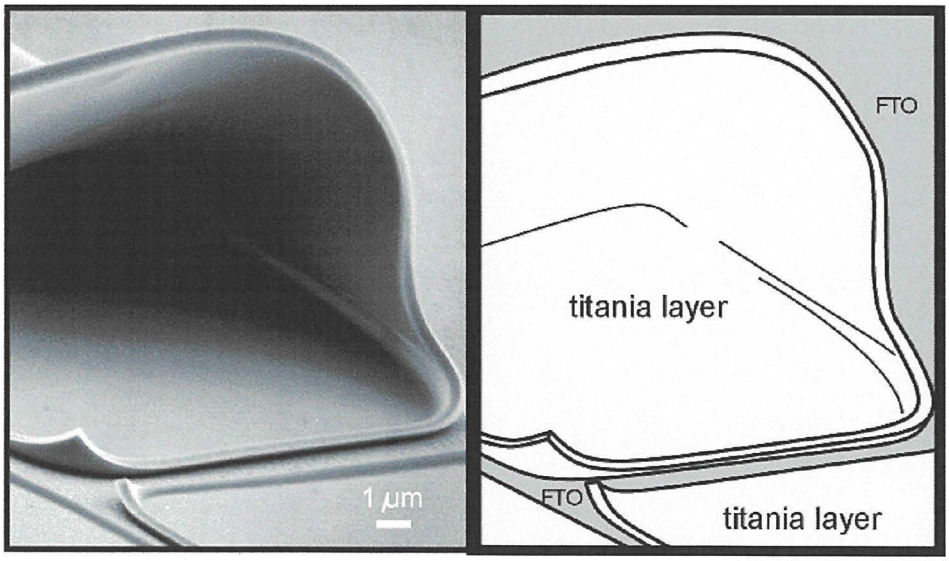

Figure 4.4.3: Scanning electron micrograph showing a single calcined film of titania doped with europium 3+ deposited onto a FTO substrate.

The addition of successive layers is visible in the electron micrographs shown in figures 4.4.4 and 4.4.5 (overleaf). The underlying layers in both images are seen to appear more crystalline in structure with a rougher surface texture, taking on the appearance of the base conducting oxide with each successive layering and repeated calcining.

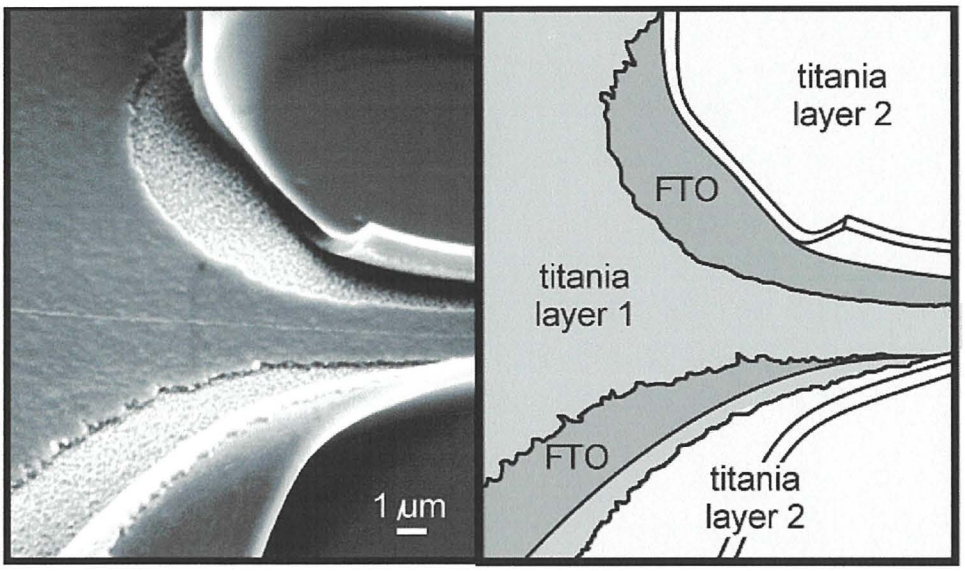

Figure 4.4.4: Scanning electron micrograph showing a FTO substrate coated with two calcined films of titania, both doped with europium 3+.

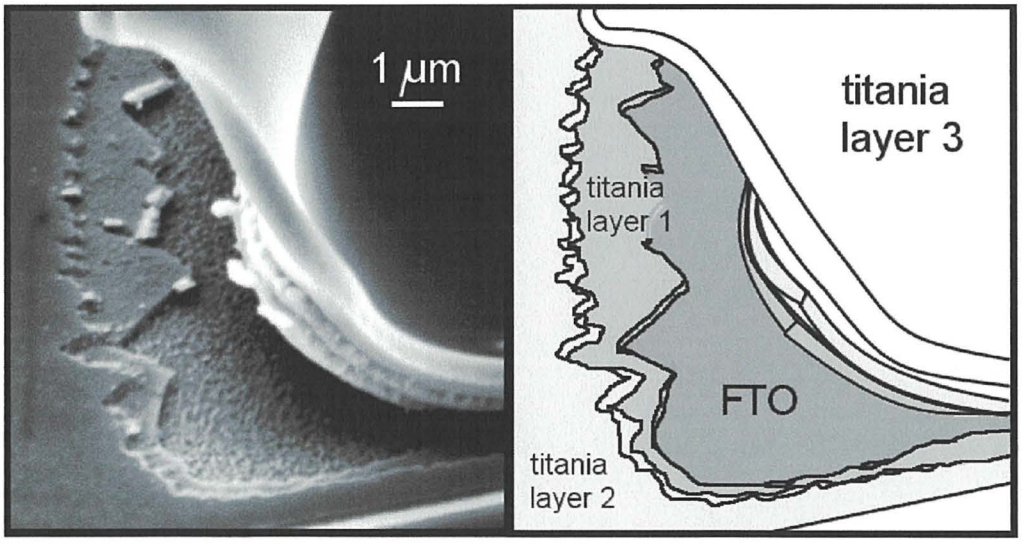

Figure 4.4.5: Scanning electron micrograph showing a FTO substrate coated with three successive calcined films of titania, all doped with europium 3+.

No fluoresence was visible to the naked eye under ultraviolet irradiation. This was not surprising given the low doping concentration used, 1 ‰, which equated to a ratio of 1 Eu:1000 Ti. Higher ratios were not investigated due to the low solubility of the europium (III) salt used. The use of the trinitrate salt would allow higher doping ratios and may thus allow the generation of luminescent films such as the 8 mol % used by Frindell *et al* [43] and others [77-80].

4.3.3 Undoped titania coated optical fibres

Having shown that titania thin films could be deposited onto flat substrates work was carried out to deposit similar films onto optical fibre. The curvature of the fibre surface was likely to cause problems and is illustrated in figure 4.4.6 which shows two electron micrographs (with explanatory diagrams) of an uncoated plastic clad silica (PCS) fibre.

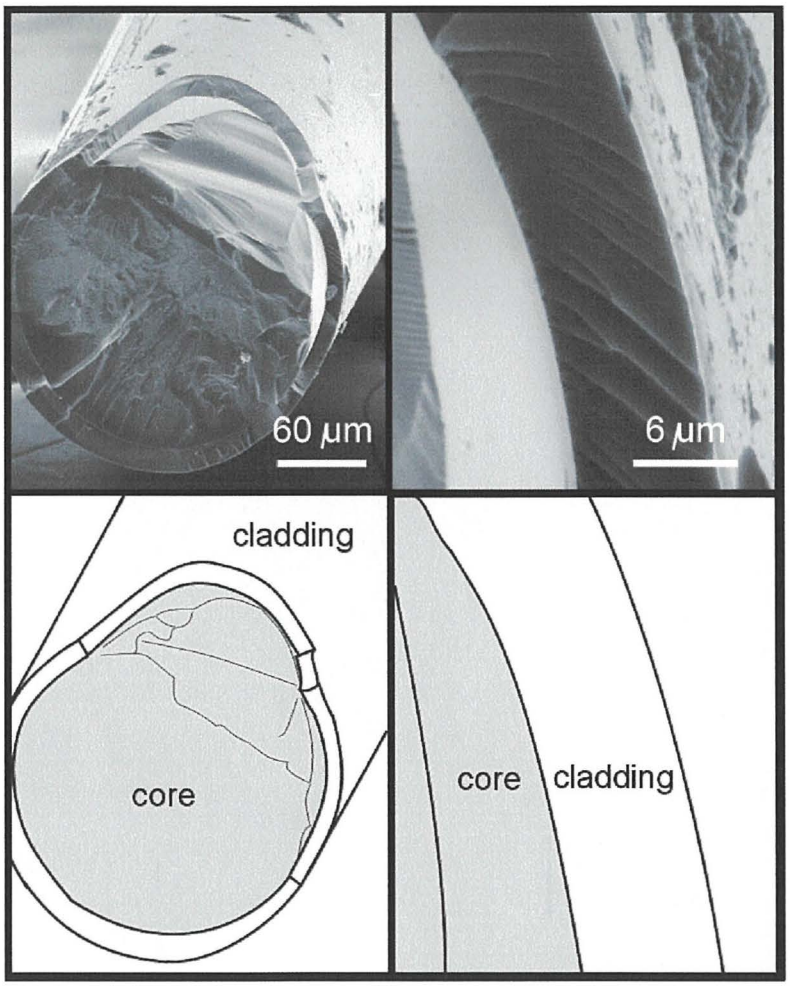

Figure 4.4.6: Scanning electron micrographs of an uncoated, plastic-clad silica fibre.

The silica core and the fibre cladding are clearly visible. The core has a diameter of 200 μm and the cladding is approximately 15 μm thick. Deposition of a single gel coat (without calcining) followed by drying at room temperature in air yielded a uniform film of 1 to 2 μm thickness which showed excellent coverage and even thickness over the entire dipped length. Figure 4.4.7 (overleaf) is a pair of scanning electron micrographs of the cladding and coating.

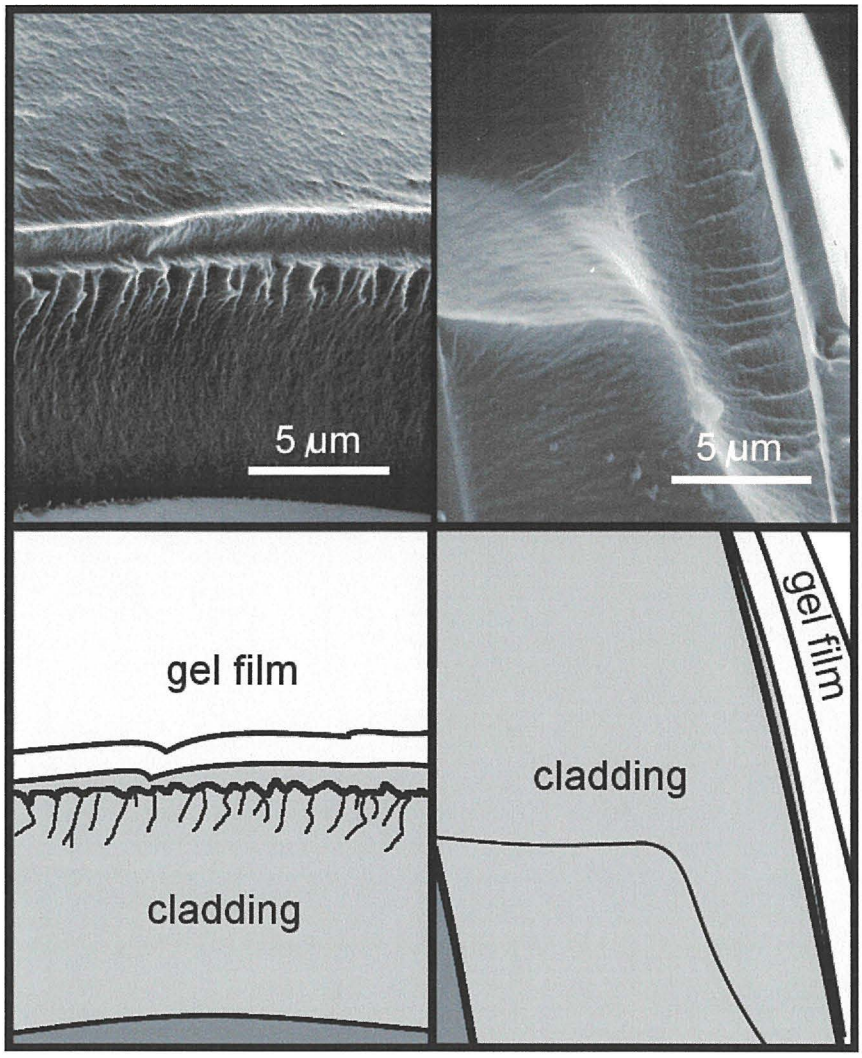

Figure 4.4.7: Scanning electron micrographs of a PCS fibre dip coated with a single layer of un-calcined gel.

Deposition of multiple layers of gel led to thicker and smoother films as shown in figure 4.4.8.

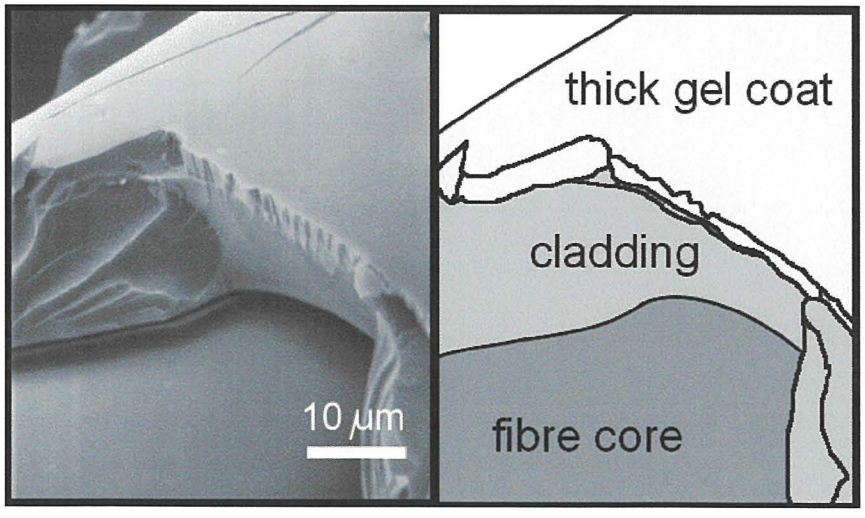

Figure 4.4.8: Scanning electron micrograph of a thick gel coated PCS fibre.

The raw gel coated fibres were analysed using X-ray diffractometry. The results, *e.g.* figure 4.4.9, showed (as expected) an amorphous state.

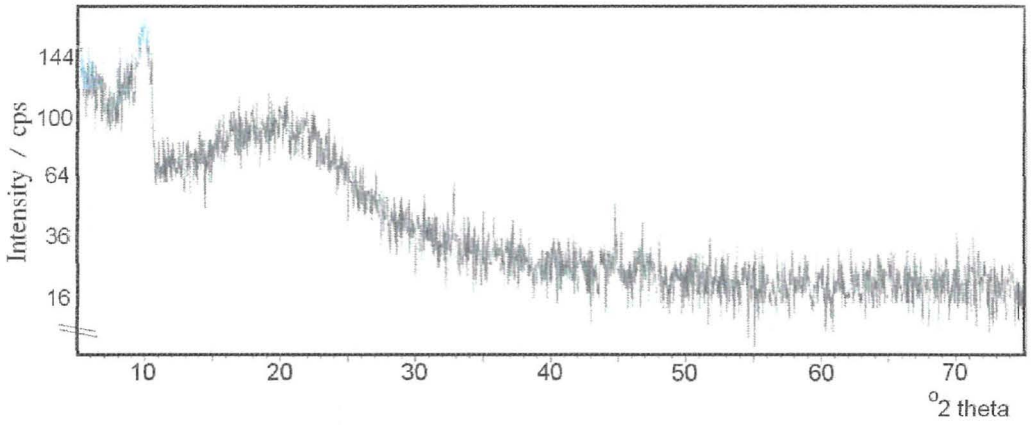

Figure 4.4.9: X-ray diffractogram of PCS fibres coated with raw gel layers showing no crystallinity.

After thermal treatment at temperatures in excess of 350 °C the samples were again subjected to XRD analyses. Results were disappointing as illustrated in figure 4.5.0. No peaks were seen other than a slight sharpening and shifting of the amorphous hump seen around $2\theta = 20$ °.

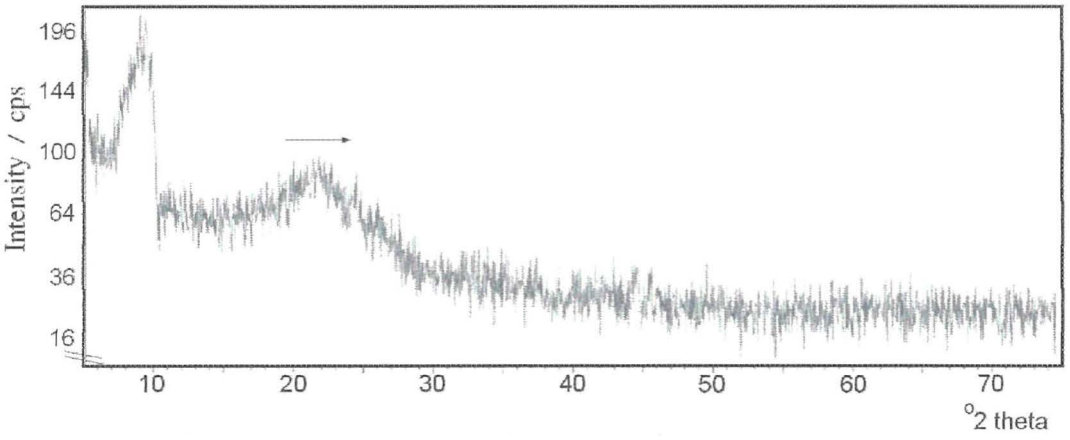

Figure 4.5.0: XRD results for silica optical fibres after thermal treatment (TT) at 420 °C (693 K)

This may be due to experimental difficulties in XRD analysis of the fibres, or, as seen before for coated slides, that insufficient sample was present. As a general rule, samples that were treated at elevated temperature suffered damage due to film shrinkage. Exposure of raw gel coated fibres to temperatures higher than around 150 °C resulted in extensive fracturing of the film. The extent to which fracturing occurred depended upon the applied temperature, the presence or absence of a vacuum and the thickness of the film. Figure 4.5.1 (overleaf) illustrates the fracturing effects seen.

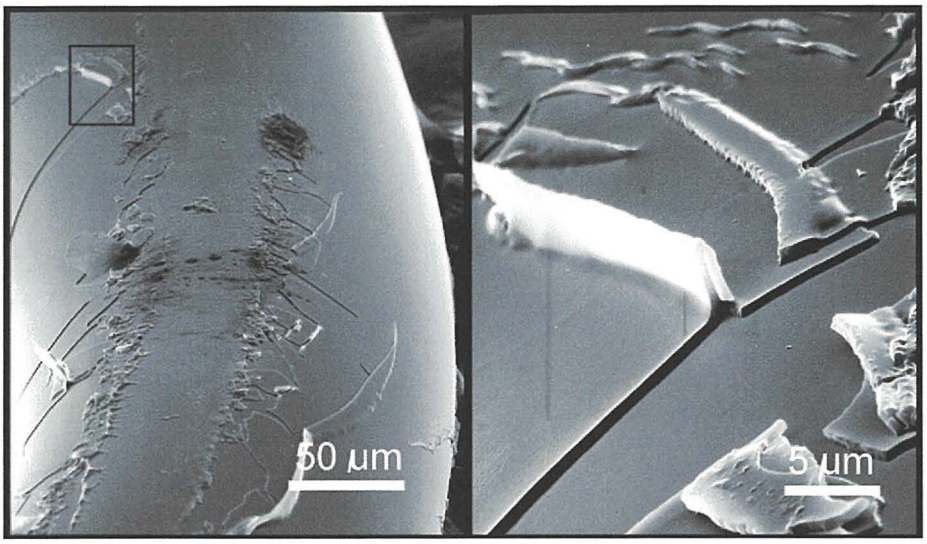

Figure 4.5.1: Scanning electron micrographs of a fibre with a fractured single gel thin film.

As can be seen from the image above, shrinkage of the film leads to failure and subsequently to the formation of extensive networks of cracks. In addition the films receded, exposing the substrate. It was thought likely that the high degree of curvature of the surface would exacerbate the shrinkage problem. Were the cladding to be removed and the coatings applied directly to the core surface, the problem would become more severe.

To address the shrinkage issue, films were applied to larger fibres with a diameter of 1 mm. These fibres (illustrated in figure 4.1.6 in an earlier section, 4.1.3) are made of polymethylmethacrylate and have a significantly less curved surface upon which deposition can occur. Gel films applied to this surface were significantly smoother and thicker as shown in the electron micrograph in figure 4.5.2.

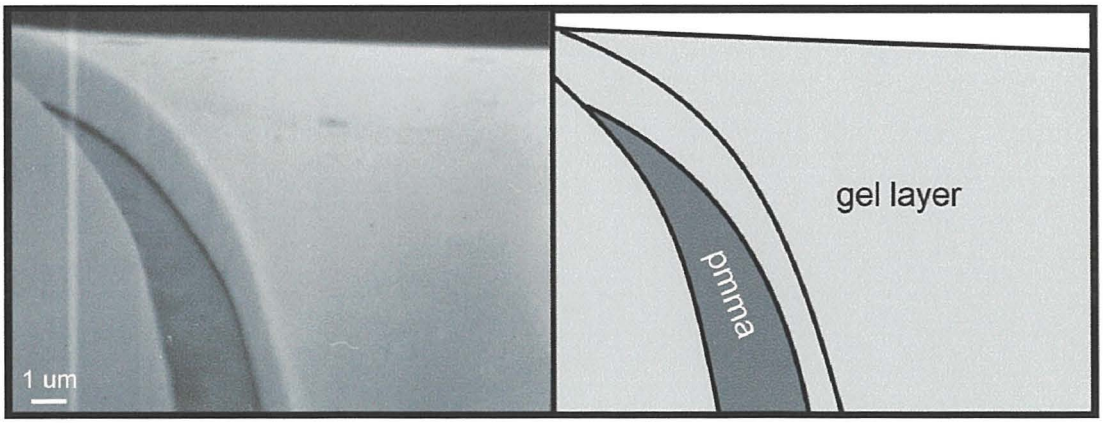

Figure 4.5.2: Electron micrograph of a gel coated, uncalcined PMMA fibre with large (1 mm) diameter.

Despite showing considerably better quality films, the one drawback of the PMMA fibre is its inherent inability to withstand high temperatures. With a melting point below that required for anatase crystallisation another means of calcining the gel and for removing the organic residues was needed. Upon drying of some samples under vacuum at 90 °C (363 K) an interesting phenomena was observed. As shown in figure 4.5.3, the film appeared to undergo rearrangement to form isolated structures. These hexagonal structures were shown to be predominantly titanium using energy dispersive X-Ray (EDX) analysis *in situ.*

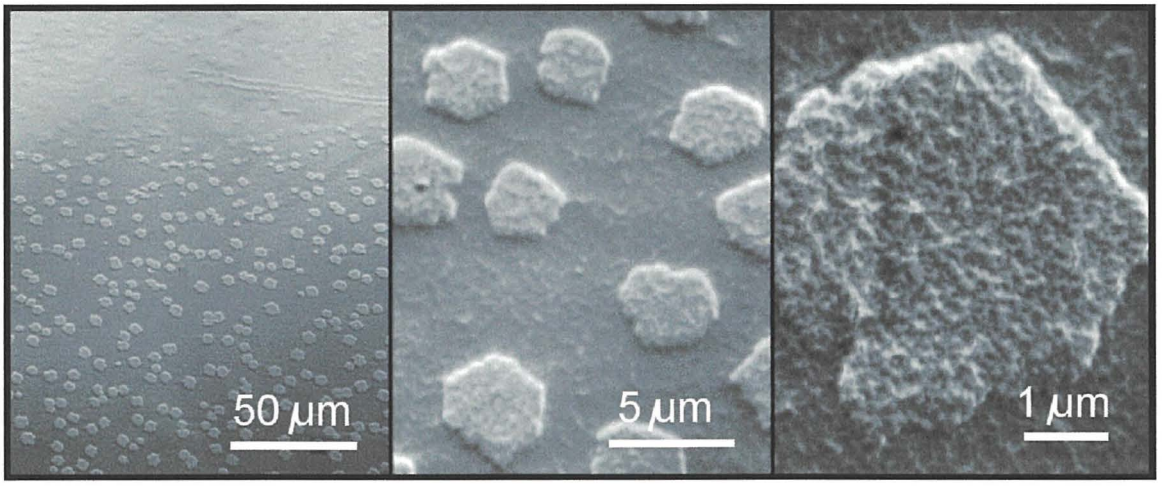

Figure 4.5.3: Scanning electron micrographs showing isolated, hexagonal structures which formed on a gel coated PMMA fibre after vacuum drying.

Fine structure seen in the highest magnification image in figure 4.5.3 (above) is suggestive of a continuation of the hexagonal structuring on a smaller scale. The size of the structures varied between 3 and 5 μm. However, occasional, isolated larger structures with the same general features were observed. One such structure is shown in figure 4.5.4.

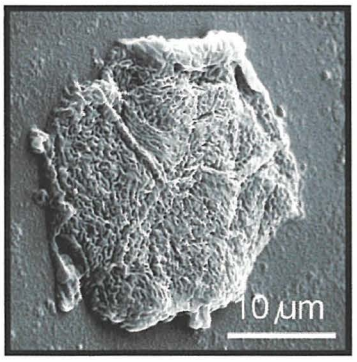

Figure 4.5.4: Micrograph of a large (20 – 30 μm) hexagonal structure observed growing out from the surface of a vacuum dried gel film on PMMA.

Further to the images shown above, after the sample had been aged under vacuum for a further 7 days, additional micrographs were taken and these images are shown in figure 4.5.5.

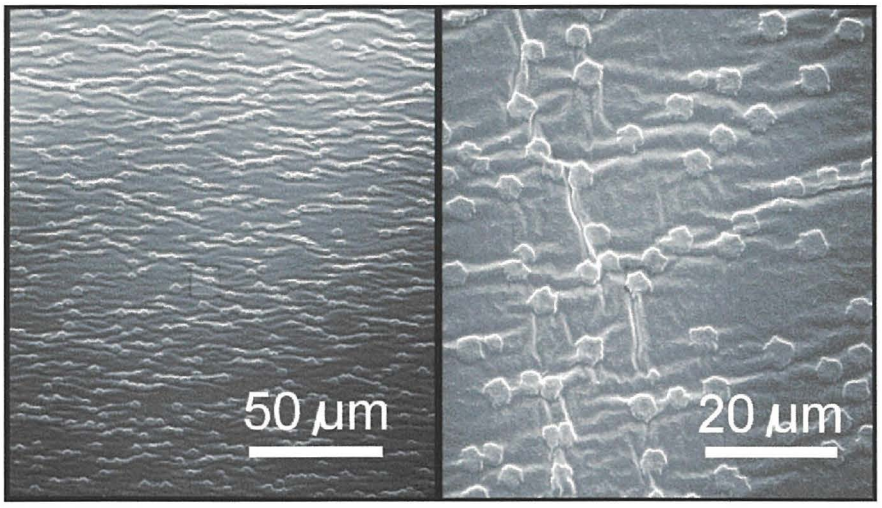

Figure 4.5.5: Micrographs showing network formation between hexagonal structures after 7 days' further growth under vacuum conditions.

The images above clearly show the formation of a branching network connecting the hexagonal features together. No clear explanation for these structures could be found although it is thought that they may indicate the precipitation of a titania salt out of the gel phase under the influence of the vacuum. EDX analysis did not show the presence of any elements other than titanium were present, however this is by no means conclusive as many elements do not show strong signals under EDX spectroscopy. Further work would be required to investigate this phenomenon to determine its precise cause and whether or not the effect was predictable and reproducible. Certainly, in this investigation it was not seen in every sample nor was it possible to identify which treatment if any (other than the vacuum drying) led to its appearance.

Due to the lack of temperature resistance of the coated fibres alternative methods were required to attempt to crystallise the amorphous gels and to remove the Triton-X100 surfactant residues. This work is discussed in the following chapter.

4.4 Conclusions.

The concepts of feasible fibre-optic based point sensors which would incorporate titania thin films have been introduced and their plausible modes of operation outlined. Ideas for novel incorporation of electrochemical sensing using a micro-optical ring electrode (MORE) together with other optical fibre devices have been discussed although no such devices were assembled.

The deposition of thin films of titanium dioxide onto assorted substrates has been shown. Deposition onto conducting glass slides was largely successful, with good robust 300 to 500 nm thin films of nanocrystalline titania being produced. Scanning electron micrographs (SEM) demonstrated that layers of reproducible thickness could be produced as either single or multi-layered films. X-ray diffraction (XRD) investigations into the crystallinity of the films were unsuccessful. Despite this, investigation using X-ray photoelectron spectroscopy (XPS) confirmed that tetravalent titanium dioxide was indeed produced and suggested that a surface-hydroxylated form (anatase) may be present. UV-visible spectra demonstrated that optically transparent films were produced and showed clear differences between raw gel and crystalline films with sharp band-edges indicative of well defined crystal size in samples that were calcined at elevated temperatures.

The deposition of lithium doped thin films on conducting glass slides was less successful. Upon thermal treatment the doped films became extensively fractured which it was surmised may be due to phase separation of the matrix into lithium rich and lithium poor regions. In the absence of secondary ion mass spectrometry imaging or mapping XPS this could not be confirmed. Again, XRD analyses failed to produce spectra of the films, likely due to their very thin (<500 nm) thicknesses. XPS spectra did not show direct evidence of the presence of Li^+ in the films. Given the weak signal expected from the single Li1s electron in XPS generally, this was not surprising. The high resolution spectra of the Ti2p signal showed that the $Ti2p_{3/2}$ peak for lithium doped films was found at the bottom end of the range expected for

tetravalent titanium and lay in the range where Ti^{3+} may be seen. This may be indirect evidence for the presence of Li^{+} in the lattice as this would cause a reduction in the mean oxidation state of titanium within the lattice overall. Electrochemical lithium insertion into both lithium-doped and pure titania thin film electrodes on conducting glasses showed that room temperature intercalation was possible accompanied by a pronounced change in the optical properties of the film. The presence of such intercalation at room temperatures is indicative of an anatase (or brookite) structure. When the film potential was swept in the negative direction a cathodic reduction current was seen, associated with the reduction of Ti (IV) to Ti (III) and the intercalation of lithium and was accompanied by a change from a transparent to a deep blue colour. The film returned to its deintercalated transparent state when the scan direction was reversed and an anodic current peak was recorded. Cyclic plots of transmittance *versus* film potential showed a sigmoidal shape but did not overlay on each repeat cycle, nor was superimposition observed for successive voltammograms where a diminishing current response was observed with cycling. The films were thus not wholly optically reversible and the redox reaction was not fully stable. Over several cycles it was possible to observe film degradation with each charging/de-charging cycle and films deteriorated fully after between 5 and 10 cycles.

Europium doped films were produced successfully, albeit at very low doping ratios. The doping ratios used were of the order of 1 ‰ and were too small for any luminescence to be observed under UV illumination. Nor was the doping of sufficient concentration to produce strong signals in the XPS spectra. Some evidence for the presence of Eu was seen, but no allocation of oxidation state was possible. Stronger doping, between 1 % and 10 % would be required to produce strong signals and visible luminescence. The europium doped films were characterised by excellent adhesion and smooth, unfractured surfaces. Film thicknesses were of the order of 200 to 500 nm and multi-layered structures were produced.

Coating of optical fibre with titania thin films was unsuccessful. Reproducible deposition of raw gel layers and xerogel films was demonstrated, however attempts to calcine these layers to form crystalline films failed. The contraction of films under heating led to catastrophic fracture of the films and in many cases to damage to the underlying fibre support. Use of fibres with considerably larger dimensions to minimise curvature did not solve the problem as these larger core fibres were made of plastics which deformed or melted when exposed to temperatures in excess of 150 to 200 °C. Despite some interesting results with the un-calcined, xerogel films on these PMMA fibres the intention to produce crystalline films on the fibres by standard methods of thermal treatment was scrapped. It then became necessary to determine alternative methods for the production of crystalline films on the fibre surfaces and hence, considerable effort was directed into establishing a series of treatments which would induce crystallisation in the films, remove the organic residues which make up a significant proportion of the un-calcined gels and not exceed the critical thermal criteria imposed by the substrate materials. This is discussed in the next chapter.

4.5 References & bibliography.

1 O.S Wolfbeis, Ed. (1991) *Fibre Optic Chemical Sensors & Biosensors* vol. 1 CRC Press New York

2 R.W. Cattral, (1997) Chemical Sensors, Oxford University Press, Oxford, 74pp

3 T.L. Tipton, B.S. Vogt, *US Patent* 5652810-A 1997

4 L.E. NorenaFranco, F. Kvasnik, *Analyst* **121** (1996) 1115-1118

5 M. Landle, P. Simon, F. Kvasnik, *Sensors and Actuators: B Chem* **51** (1998) 114-120

6 J.E. Alderete, *US Patent* 0535878, 1995

7 E.I. Alatortsev, , V.I. Kabanov, V.N. Larichev, *Russian Patent* RU2078326-C1 1997

8 D.M. Johnson, *US Patent* 5966477-A, 1999

9 B. Culshaw, G. Stewart, F. Dong, C. Tandy, D. Moodie, *Sensors and Actuators* **51** (1998) 25-37

10 W. Fowler, *World Patent* 09709609-A1 1997

11 M.Q. Bai, W.R. Seitz, *Talanta* **41** (1994) 993-999

12 Z. Shakhsher, W.R. Seitz, K.D. Legg, *Anal. Chem.* **66** (1994) 1731-1735

13 M.F. McCurley, W.R. Seitz, *Anal. Chim. Acta.* **249** (1991) 373-380

14 A. Brecht, G. Gauglitz, W. Nahm, *Analusis* **20** (1992) 135-140

15 J. Hopenfield, *US Patent* 5982959-A 1999

16 B. Culshaw, J. Dakin, Eds.(1996) *Optical Fibre Sensors – Components and Subsystems* vol. 3 Artech House, London 237pp

17 L.E. NorenaFranco, F. Kvasnik, *Analyst* **123** (1998) 2185-2189

18 F. Kvasnik, A. McGrath, *US Patent* 5185521 1993

19 B. Culshaw, J. Dakin, Eds.(1997) *Optical Fibre Sensors – Applications, Analysis and Future Trends* vol. 4 Artech House, London 478pp

20 D. Marcuse, *J. Lightwave Technology.* **6** (1988)1273-1279

21 C.M. Davis (1986) *Fiberoptic Sensor Technology Handbook* Optech, Virginia.

22 G. Boisdé, A. Harmer, (1996) *Chemical and Biochemical Sensing with Optical Fibres and Waveguides* Artech House, London 389pp

23 A.D. Kersey, *Optical Fibre Tech.* **2** (1996) 291-317

24 R.A. Potyrailo, S.E. Hobbs, G.M. Heiftje, *Anal Chem.* **70** (1998) 1639-1645

25 C. Malins, A. Doyle, B.D. MacCraith, F. Kvasnik, M. Landl, P. Simon, L. Kalvoda, R. Lukas, K. Pufler, I. Babusik, *J. Environ. Monit.* **1** (1999) 417-422

26 A.R. Lennie, F.Kvasnik, *Anal. Chim. Acta.* **281** (1993) 265-270

27 M. Heinrich, K. Rose, *European Patent* 899244-A2 1999

28 J. Buerck, E. Sensfelder, *Proc SPIE,* **3540** (1998) 98-109

29 G. Stewart, W. Jin, B. Culshaw, *Sens. Actuator* **38** (1997) 42-47

30 W. Jin, G. Stewart, B. Culshaw, *Meas. Sci. Technol.* **6** (1995) 1471-1475

31 R.N. Hamburger, J. Jiang, R. Wang, *US Patent* 5995686-A 1999

32 S.K. Khijwania, B.D. Gupta, *Optics Communications*, **152** (1998) 259-262

33 S.K. Khijwania, B.D. Gupta, *Optics Communications*, **175** (2000) 135-137

34 B.D. Gupta, Ratnanjali, *Sensors & Actuators B*, **80** (2001) 132-135

35 S. Muto, A. Fukasawa, T. Ogawa, M. Morisawa, H. Ito, *Japanese journal of Applied Physics*, **29** (1990) L1023-L1025

36 H.H. Kee, G.P. Lees, T.P. Newson, *Electr. Lett.* **35** (1999) 1869-1871

37 W.W. Morey, J.R. Dunphy, G. Meltz, *Proc. SPIE,* **1586** (1992) 216-220

38 P.R.C. Chan, W. Jin, J.M. Gong, M.S. Demokan, *IEEE Photonics Tech. Lett.* **11** (1999) 1470-1472

39 Y.J. Rao, *Optics and Lasers in Eng.* **31** (1999) 297-324

40 R.J. Maron, *US Patent* 6016702-A 1999

41 G.I. Pennarun, C. Boxall, D. O'Hare, *Analyst*, **121** (1996) 1779-1788

42 J.S. Symanski, S. Bruckenstein, *J. Electrochem. Soc.*, **135** (1988) 1985

43 K.L.Frindell, M.H.Bartl, A. Popitsch, G.D. Stucky, *Angew. Chem. Int. Ed.*, **41** (2002) 960-962

44 N. Casillas, P. James, W.H. Smyrl, *J. Electrochem. Soc.*, **142** (1995) L16-L18

45 P. James, N. Casillas, W.H. Smyrl, *J. Electrochem. Soc.*, **143** (1996) 3853-3865

46 M. Kubeckova, M. Sedlar, V. Matejec, *J, Non. Cryst. Solids*, **147 & 148** (1992) 404-408

47 I.M.Arabatzis, S. Antonaraki, T. Stergiopoulos, A. Hiskia, E. Papaconstantinou, M.C. Bernard, P.Fakras, *J. Photochem. and Photobiol A: Chemistry,* **5929** (2002) 1-9

48 J. Yu, X. Zhao, Q. Zhao, G. Wang, *Materials Chemistry and Physics,* **68** (2001) 253-259

49 K. Baba, R. Hatada, *Surface & coatings technology*, **136** (2001) 241-243

50 Z. Ding, X. Hu, P.L. Yue, G.Q.Lu, P.F.Greenfield, *Catalysis Today*, **68** (2001) 173-182

51 B.C. Kang, S.B. Lee, J.H. Boo, *Surface & Coatings Technology*, **131** (2000) 88-92

52 Q. Fan, B. McQuillan, D.D.C. Bradley, S. Whitelegg, A.B.Seddon, *Chemical Physics Letters,* **347** (2001) 163-166

53 R. Fretwell, P. Douglas, *J. Photochem & Photobiol A: Chem*, **143** (2001) 229-240

54 P. Kluson, P. Kacer, T. Cajthaml, M. Kalaji, *J. Mat. Chem*. **11** (2001) 644-651

55 P. Kluson, P. Kacer, *Chemicke Listy*, **94** (2000) 432 - 436

56 T. Lopez, J.Hernandez-Ventura, R. Gomez, F.Tzompantzi, E. Sanchez, X. Bokshimi, A.Garcia, *J. Molecular Catalysis A: Chemical*, **167** (2001) 101-107

57 S. Yamazaki, N. Fujinaga, K. Araki, *Applied Catalysis A: General*, **210** (2001) 97-102

58 N. Savage, B. Chwieroth, A. Ginwalla, B.R. Patton, S.A. Akbar, P.K.Dutta, *Sensors and Actuators B*, **79** (2001) 17-27

59 G.S. Hermann, Y. Gao, T.T. Tran, J.O. Osterwalder, *Surface Science*, **447** (2000) 201-211

60 F.M. Amanullah, K.J. Pratap, V. Hari Babu, *Materials Science and Engineering*, **B52** (1998) 93-98

61 M. Zheng, M. Gu, Y. Jin, H. Wang, P. Zu, P. Tao, J. He, *J. Mat. Sci. & Eng.*, **B87** (2001) 197-201

62 P.P. Ahonen, U. Tapper, E.I. Kauppinen, J.C. Joubert, J.-L. Deschanvres, *Materials Science & Engineering*, **A315** (2001) 113-121

63 T. Dittrich, J. Weidmann, V.Y. Timashemko, A.A Petrov, F. Koch, M.G. Lisachenko, E. Lebeder, *Mat. Sci & Eng.*, **B69** (2000) 489-493

64 S.V. Manorama, K.M. Reddy, C.V.G. Reddy, S. Narayanam, P.R. Raja, P.R. Chatterji, *J. Phys. Chem. Solids* **63** (2002) 135-143

65 S. Yamazaki, N. Fujinaga, K. Araki, *Applied Catalysis A: General*, **210** (2001) 97-102

66 G.R. Bamwenda, T. Vesigi. Y. Abe, K. Sayama, H. Arakawa, *Applied Catalysis A: General*, **205** (2001) 117-128

67 N. Bonini, M.C. Carotta, A. Chiorino, V. Guidi, C. Malagi, G. Martinelli, L.Paglialonga, M. Sacerdoti, *Sensors & Actuators*, **B68** (2000) 274-280

68 M.J. Alam, D.C. Cameron, *Surface & Coatings Technology*, **142-144** (2002) 776-780

69 H. Lin, S. Kumon, H. Kozuka, T.Yoko, *Thin Solid Films*, **315** (1998) 266-272

70 D. Briggs, M.P.Seah, (1996) *Practical Surface Analysis*, Wiley & Sons, Vol. 1, 2nd edition

71 C.D. Wagner, W.M. Riggs, L.E. Davis, J.F. Moulder, *Handbook of X-ray Photoelectron Spectroscopy*, Perkin Elmer Corporation, Physical Electronics Division.

72 K. Hamrin, G. Johansson, A. Fahlman, C. Nordling, *J. Phys. Chem. Solid.*, **30** (1969) 1835-1847

73 M.V. Kuznetsov, J.F. Huravlev, V.A. Gubanov, *J. Electron Spectroscopy and Related Phenomena*, **38** (1992) 169-176

74 R. Bertoncello, A. Casagrande, M.Casarin, A. Glisenti, E. Lanzow, L. Mirenghi, E. Tondello, *Surface and Interface Analysis*, **18** (1992) 525-531

75 Y. Ozazaki, T. Tateishi, Y. Ito, *Materials Transactions JIM*, **38** (1997) 78-84

76 G. Hopfengartner, D. Borgmann, I. Rademacher, G. Wedler, E. Hums, G.W. Spitznagel, *J. Electron Spectroscopy and Related Phenomena*, **63** (1993) 91-116

77 R. Vercaemst, D. Poelman, L. Fiermans, R.L.Van Meirhaeghe, W.H. Laflere, F. Cardon, *J.Photoelectron Spectroscopy and Related Phenomena*, **74** (1995) 45-56

78 J. Ovenstone, P.J. Titler, R. Withnall, J. Silver, *J. Phys. Chem. B*, **105** (2001) 7170-7177

79 N.P. Gaponenko, I.S. Molchan, G.E. Thompson, P. Skeldon, A. Pakes, R. Kudrawiec, L. Bryja, J. Misiewicz, *Sensors and Actuators A*, **99** (2002) 71-73

80 R. Palomino-Merino, A. Conde-Gallardo, M. Garcia-Rocha, I. Hernandez-Calderon, V. Castano, R. Rodriguez, *Thin Solid Films*, **401** (2001) 118-123

81 B. Zachau-Christiansen, K. West, T. Jacobsen, S. Atlung, *Solid State Ionics*, **28-30** (1988) 1176-1182

82 P. Krtil, D. Fattakhova, L. Kavan, S. Burnside, M. Gratzel, *Solid State Ionics*, **135** (2000) 101-106

83 M.V. Koudriachova, N.M Harrison, S.W. de Leeuw, *Physics Review Letters*, **86** (2001) 1275-1278

84 P. Swift, *Surface Interface Analysis*, **4** (1982) 47-49

85 F. Le Kien, A. Koreeda, K. Kuroda, M. Suzuki, K. Hakuta, *Jpn. J. Appl. Phys.*, **42** (2003) 3483-3489

86 W.S. Li, Z.X. Shen, Z.C. Feng, S.J. Chua, *J. Appl. Phys.*, **87** (2000) 3332-3337

87 H.H. Burke, I.P Herman, *Physical Review B*, **48** (1993) 15016-15024

CHAPTER 5

Investigation into the development of alternative methods for the post-coating treatment of titania gel-coated optical fibres.

5.1 Introduction

It is a further aim of this work to develop a low temperature annealing process so that optical fibres that would not otherwise survive the high temperature calcination regime can be coated with well crystallised thin films of anatase titania. It has been established that the room temperature reverse sol-gel methods discussed in earlier chapters will yield amorphous films and therefore some means of densification and crystallisation must be found.

Work has been conducted into calcining sol-gel films by treatment with supercritical fluids, UV irradiation, hydrothermal treatment, steaming or a combination of these. Crystalline products may be obtained *in situ*, without any thermal treatment, although only if direct micelle methods, *i.e.* those in aqueous media, are used. Guan *et al* [1] for example reported that titania nanocrystals were anatase as prepared by a photoassisted sol-gel process in acidic aqueous media. The removal of the extensive organic residues found with the reverse micellar microemulsion method discussed in earlier chapters is paramount and, it is hoped, may be achieved by the use of a combination of the above treatment methods. This will also hopefully lead to crystallisation of the anatase form of titania at low temperatures. In addition, if metamorphosis from the amorphous to the anatase phase occurs before complete removal of organic residues it may be possible to photocatalytically degrade the organic material *in situ* by irradiation with appropriate (near UV) light sources.

5.1.1 Supercritical fluid extraction (SFE) treatment of sol-gel coatings

Supercritical fluid extraction (SFE) with carbon dioxide has been reported [2,3] as a means of removing organic residues. The supercritical carbon dioxide process used is performed above the critical point of carbon dioxide, at low temperature, *i.e.* 304 K, and high pressures, *i.e.* 7.4 MPa. Supercritical fluids have the useful property of total miscibility with gases, and diffusion coefficients similar to those of gases, yet they retain the ability to solubilise quantities of

solute equivalent to that of liquids [2,3]. Furthermore above the critical point it is possible to modify solvent properties such as viscosity, diffusivity and dielectric constant by varying the temperature and pressure. By way of example, the dielectric constant of supercritical water is so low that it is capable of dehydrating hydrous metal oxides and as such has been recently reported as a novel method for the synthesis of mesoporous titania nanopowders [4].

Supercritical carbon dioxide has been shown to substantially reduce the carbon content of gels and gel coatings. For example, a decrease from 59 wt% down to 9.8 wt% carbon content after SFE was reported by Kluson *et al.*[2]. This shows that it is possible to remove a substantial proportion of the organic residues by treatment with supercritical CO_2. However, after SFE the gels remain in the amorphous state and hence, samples still require a high-temperature annealing step after this treatment. Ayral *et al.* [3] reported that supercritical treatment of silica can increase skeletal density slightly; it will be important to assess whether the same phenomenon is observed in titania gels and if so what impact this will have on porosity. Ayral *et al.* [3] also reported that treatment with supercritical methanol will result in the generation of a hydrophobic methylated surface by removal of the surface hydroxylation. Thus, SFE represents a powerful method for the removal of labile components and for modification of the surface chemistry of the gel matrix.

5.1.2 Hydrothermal treatment

Hot water, humidity and steam treatments have been quoted as effective in removal of organics, rearrangement of films and subsequent crystallisation of titania. Such processes are attractive for the treatment of titania on low heat resistant substrates as the treatment temperature rarely exceeds the melting points of the materials being treated.

Hayashi and Torii [4] reported the production of high specific surface area, mesoporous titania nanopowders *via* a novel process combining aqueous hydrolysis of titanium (IV) isopropoxide

followed by hydrothermal treatment with both sub- and supercritical water regimes. Imai *et al.*[5] emphasised that steaming of films in an autoclave led to measurable increases in their refractive index and showed in an earlier paper [6] that titania films were converted to anatase by exposure to water vapour in the 60 to 180 °C range. Kotani *et al.* [7] have successfully prepared transparent and porous anatase nanocrystals in the presence of polyethyleneglycol by treatment of gel films with hot water at atmospheric pressure. Burgos and Langlet [8] coated organic substrates with titania gels and found that after treatment with water the flexibility and hardness of coatings became more compatible with the polymeric substrate and thus improved adhesion. Surfactant mediated deposition of nanoscale anatase at temperatures between 40 and 70 °C from aqueous solutions of titanium tetrafluoride was reported by Shimizu *et al.* [9] and post-depositional treatment of thin films with a mixture of ammonia and water vapour is reported to improve scratch resistance in silica films [10]. Hydrothermal treatment at higher temperatures, by Aruna *et al.* [11], led to the production of pure rutile nanocrystals by addition of an isopropanol solution of titanium isopropoxide to nitric acid followed by autoclaving at 250 °C. Acidic media may be used in combination with hydrothermal methods to produce selected phase-pure titania products by variation of temperature, pressure and concentration as reported by Wu *et al.* [12]. In an earlier work [13], Wu *et al.* synthesised both anatase and rutile powders by a microemulsion-mediated hydrothermal method using a Triton X-100/water/hexanol/cyclohexane microemulsion in an autoclave in which crystalline powders were achieved without the need for further calcination. Thus, it is hoped in this work that similar hydrothermal treatments of amorphous, raw gel films deposited on optical fibres may aid in gel rearrangements leading to crystallisation and the removal of surfactant residues and reaction by-products.

5.1.3 Ultraviolet irradiation

In addition to SFE and hydrothermal treatments, there is evidence in the body of literature to suggest that it may be possible to aid in the development of the anatase crystal structure by irradiation of films with UV radiation *in situ*, during the dip-coating step.

Guan *et al.* [1] reported the generation of anatase nanocrystals *in-situ* by photoassisted sol-gel methods. After hydrolysis of titanium (IV) butoxide in acidic medium under UV radiation, well crystallised, highly photocatalytic anatase was obtained and confirmed by XRD. Crystallisation of titania in xerogel films is also possible [5,14] by bombardment with an ultraviolet laser. Imai *et al.* [5] observed densification and crystallisation of titania thin films by film irradiation with a 4.7 eV (264 nm) UV laser. They stated that rather than using IR or visible laser photons for the direct heating of coatings as used by Taylor and Fabes [15], UV photons will directly promote dehydration and bond cleavage through electronic processes and thus will directly promote the densification and crystallisation of thin films. Further, it was stressed by Scherer [16] that fast heating of sol-gel films, such as that seen with IR or visible laser irradiation, favours densification over crystallisation, thus the use of UV photons will improve crystallinity without directly promoting densification which could limit the specific surface area obtainable. Vandeleest [17] reported that thin films made by alkoxide hydrolysis can be annealed at low temperature, *i.e.* less than 373 K, by irradiation with UV light of less than 200 nm (> 6.2 eV). Liu *et al.* [18] reported on the production of titanium dioxide nanoparticles *via* a photoassisted sol-gel process using a 500 W Hg lamp with an estimated intensity of 20 $mWcm^{-2}$ at the cell surface. This process led to a reduction in the phase transition temperature of anatase to as low as 100 °C, at which temperature, grain sizes of 3.6 nm were reported. In an earlier paper [19] Liu *et al.* explained the decrease in the anatase phase transition observed with UV irradiation. They found a shift in the Raman spectra indicative of a non-stoichiometry in the anatase samples and found that the samples were oxygen deficient.

The oxygen vacancy defects, which were confirmed by electron diffraction and X-ray photoelectron spectroscopy, were generated by the ultraviolet light and these vacancies acted as nucleation sites for the transition from amorphous to anatase phases. They also pointed out that as the transition to anatase involves a rearrangement of the oxygen framework (hence the volume shrinkage) that the production of the oxygen vacancies in the lattice may serve to accelerate these rearrangements.

In general, the sources of ultraviolet radiation quoted range from high intensity UV lasers to discharge lamps and fluorescent tubes, with varying degrees of success. The work described in this chapter aims to determine whether the use of UV irradiation in isolation or in combination with hydrothermal or supercritical fluid treatments would be successful in overcoming the restrictions imposed by the choice of optical fibre materials.

5.2 Experimental

5.2.1 Supercritical fluid extraction

Optical fibres and conducting glass slides were coated with thin films of sol-gel titania by the method reported in earlier chapters. Film thicknesses varied with differing numbers of dipcoats. Optical fibres with both thin (2 to 3 coats, <500 nm total) and thick (10 to 15 coats, >5 μm total) were prepared. Coated samples were dried as before at 70 °C (343 K) and atmospheric pressure and then at the same temperature under vacuum for 24 hours. Samples were shipped to Dr. Petr Kluson at the Chemical Institute in Prague for extraction with supercritical carbon dioxide. SFE was performed in a two stage process. Firstly, pressurised fluid extraction (PFE) was performed (at 14.2 MPa, 373 K for 60 minutes) with methanol at a flow rate of 1 cm^3min^{-1}. Secondly, pressurisation of the reaction cell with a 90 % CO_2 / 10 % methanol mixture at 373 K and 45.6MPa and a flow rate of $1cm^3$ min^{-1} was followed by extraction with carbon dioxide (SFE grade) under the same conditions. Samples destined for SFE analyses were first subjected to elemental analysis to determine carbon content using a Perkin-Elmer, CHN-240C. This assessment was repeated on samples after SFE to determine the proportion of organic extracted.

After SFE was completed, samples were examined with electron microscopy either in Prague or Bangor to determine the integrity of the film. X-ray diffractograms and adsorption isotherms were recorded to determine the crystallinity, porosity and structure of the films. Volumetric nitrogen and argon adsorption measurements were performed at 77 K after samples were placed into high vacuum (10^{-5} Torr, 423 K, 6h). Experiments with carbon dioxide were performed at 298 K. These measurements were made in Prague by Dr. Petr Kluson and results sent to Bangor. The surface area of the films was estimated by BET analysis [20-22] of the adsorption data and pore size diameter (PSD) estimates [22-24] were also determined by BJH methods.

5.2.2 Hydrothermal treatment of gels

Bulk gels in both raw and dried states were subjected to steaming with distilled water, both at atmospheric and elevated pressures using open and closed vessels respectively (illustrated in figure 5.0.1). Thin gel films were treated in the same manner both on conducting glass slides and on optical fibres. Steaming was performed for 1 hour in all cases after which all samples were dried under vacuum at 343 K for 24 hours.

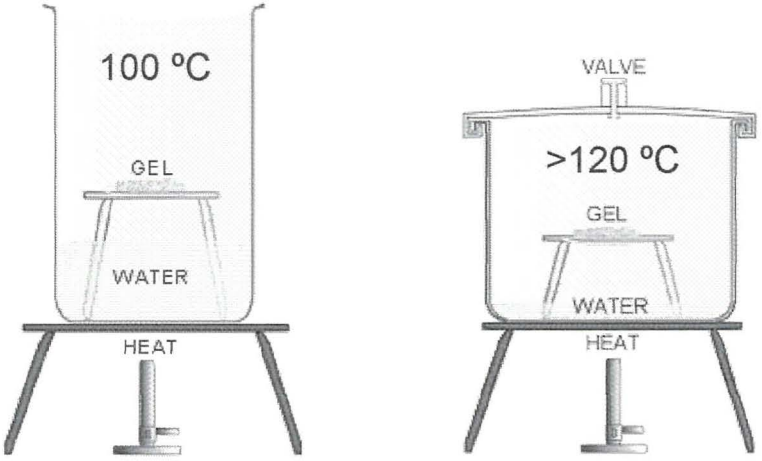

Figure 5.0.1: Diagram to illustrate the two steaming systems used during hydrothermal treatment of gel samples and thin gel films. The two systems were OPEN, ATMOSPHERIC PRESSURE (left) and CLOSED, ELEVATED PRESSURE (right).

After drying the resulting bulk gel samples and any leached exudate were subjected to FTIR spectroscopy and elemental analysis by combustion. Electron microscopy was also used to determine any morphological change in the specimens, both bulk gel and thin films.

5.2.3 UV treatment of gels

Samples of raw whole gel, and raw gel coated fibres were exposed, after gelling completion, to UV radiation from a series of sources. The sources used were a mercury vapour discharge lamp, a xenon arc lamp (Oriel Research Lamp, λ = 190 nm – 1100 nm broad spectrum) and an UV discharge lamp (λ = 254 nm).

Masks (figure 5.0.2) with circular apertures (Φ = 5 mm) were used to block out sections of sample so as to only expose a controlled region to the incident radiation.

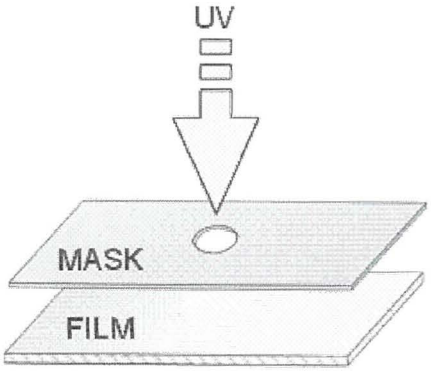

Figure 5.0.2: Diagram to illustrate the use of masks during UV illumination of samples.

Samples were irradiated for between 12 and 24 hours. Electron micrographs were recorded to observe the quality of films and to discern any morphological changes in the film surface after irradiation.

5.2.4 Production and deposition of pre-calcined nanoparticles

Gels were calcined in the presence of air at temperatures varying from 350 °C (623 K) up to 550 °C (823 K) in a muffle furnace. The resulting powdered samples were stored in glass vials prior to use for coating. The nanocrystalline particles were resuspended in volatile solvents. Ultrasonic agitation was applied for 10 minutes to break up larger agglomerates. Samples of optical fibre were dipped and withdrawn from the suspensions at a constant rate of 10 cm per second. The coated fibres were then dried at 70 °C (343 K) for 2 hours prior to storage and characterisation. Both straight and coiled optical fibres were used. Coiled fibres were prepared by heating of the fibre using a bunsen flame (for silica fibres) or oven (plastic fibres) and then coiling/bending around a suitably curved surface as described in the next section. Coated samples were characterised by electron microscopy.

5.2.5 Substrate preparation – fibre coiling

In order to increase the evanescent field of the optical fibres, a method was developed to produce permanent coils of fibre which could then be coated with thin films. Various methods of support and adhesives for the fibre coil were tested. Heat treatment as a possible means of setting the fibres into a coiled orientation was assessed with varying temperature regimes and coiling dimensions. Lengths of plastic fibre (1 m) were cut and coiled around glass tubes of varying diameter and fixed in place with wire. The glass tubes were then heated in a furnace and removed and allowed to cool before removal from the support. Coils heated at 523 - 623 K for between 5 and 10 minutes maintained a tightly coiled geometry upon cooling to room temperature. Fibres heated at greater temperatures showed a tendency to melt uncontrollably whereas those heated to lower temperatures failed to maintain a helical geometry after cooling. Coils with diameters of 20 mm and 32 mm were produced. The coils of plastic fibre were coated using the same procedure as for the straight optical fibres.

Silica optical fibres required a simpler approach whereby brief heating of the exposed silica fibre to a bunsen flame caused sufficient softening of the core to allow manual bending of the fibre into U-bends or coils as shown in figure 5.0.3 below. Again, excess or insufficient heating led to uncontrollable melting or fracture respectively.

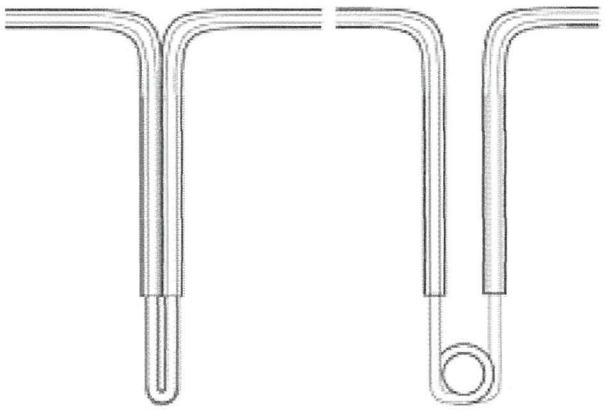

Figure 5.0.3: Diagram to illustrate the geometry of fibres after bending/coiling.

5.3 Results & Discussion

5.3.1 Supercritical fluid extraction

Electron micrographs obtained of the thin films after SFE show (figure 5.0.4) the emergence of granularity on the nanoscale, with a grain size between 30 and 50 nm. The images also show that the films are severely damaged by the supercritical process which leads to a highly fractured surface with individual flakes of dislodged films overlying each other. In fact, it may be inferred from the images that this damage occurred in an early stage of the process and that the crystallization and densification of the films occurred, efficiently, after the damage was incurred. It is possible that the initial PFE (pressurized fluid extraction) with methanol may be responsible. Further work, beyond the scope of this research, may reveal the explanation.

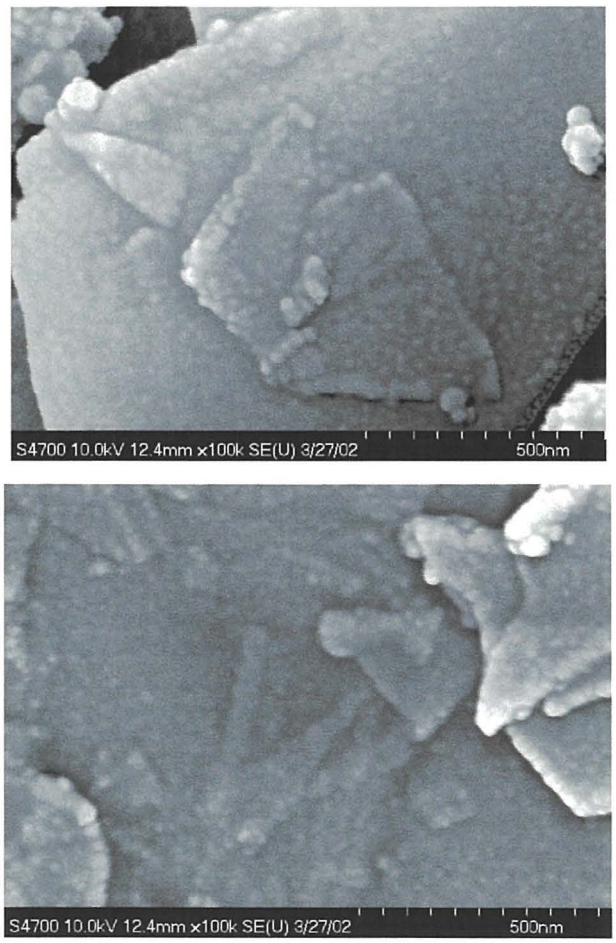

Figure 5.0.4: Scanning electron micrographs showing two different views of thin gel films after SFE at a magnification of 10^5 times. The grain size is shown to be approximately 30 to 50 nm. These images were taken by Dr. Kluson, in Prague.

The SFE process also led to the successful removal of a large proportion of the surfactant residues from the film. This can be seen with FTIR spectroscopy as is shown in figure 5.0.5 below. It is interesting that the hydroxyl peak at 3500 wavenumbers sharpens after SFE. As anatase titania has a hydroxylated surface it is possible that a small amount of the anatase polymorph has been formed however this is not shown in XRD results.

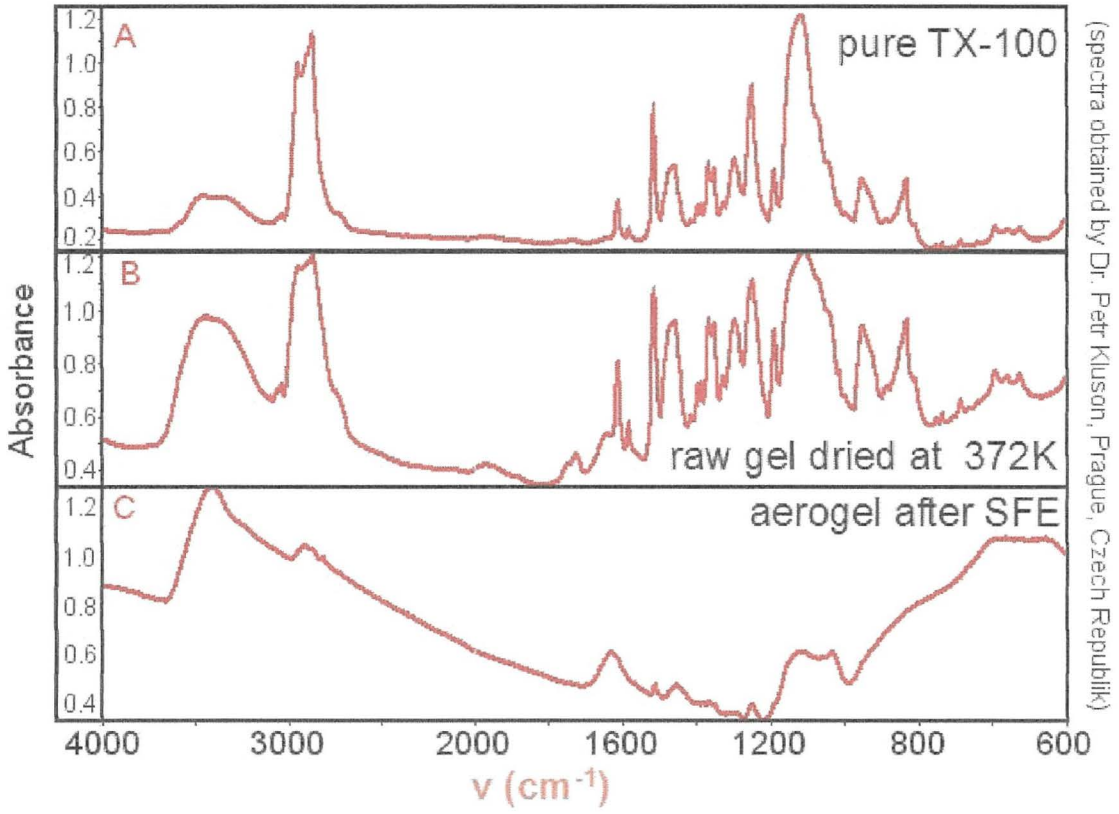

Figure 5.0.5: Infrared spectra of thin film before (B) and after (C) SFE together with the spectrum of pure Triton X-100 (A). The characteristic trace of TX-100 is clearly visible in the spectrum of the raw film but has disappeared after SFE treatment.

XRD spectra that were obtained of thin films demonstrated the same problems that were seen in thin gels on conducting slides, discussed in an earlier chapter. No clear peaks of titania were obtained, again perhaps due to the lack of a sufficiently thick film. As seen in previous diffractograms, a broad, positive deviation in the trace was always found between 20° and 40° 2θ and no peaks of either anatase or rutile were seen. It was only after additional thermal treatment was performed that any peaks were observed.

As shown in the example XRD trace in figure 5.0.6, thermal treatment at temperatures in excess of 650 °C (723 K) led to the emergence of a single sharp peak at 29 °2θ that does not correspond to any of the characteristic peaks of titania.

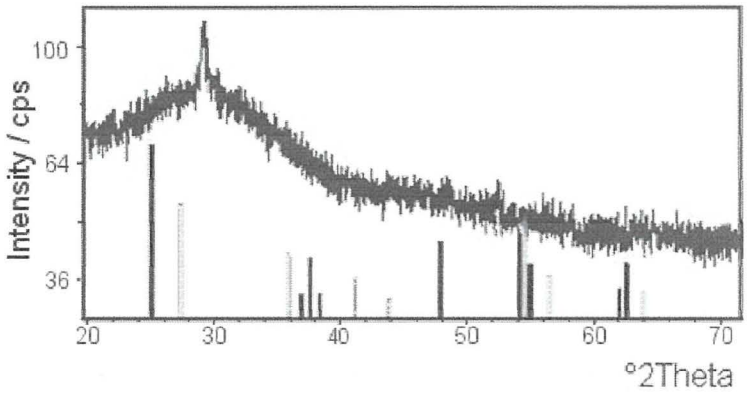

Figure 5.0.6: X-Ray diffractogram of a thin film after SFE and thermal treatment at 723 K. A distinct peak is observed *circa* 29 ° 2θ which does not correspond to any of the expected peaks characteristic of anatase or rutile (shown as black and grey bars respectively for comparison). A diffractogram taken of a sample treated at a higher temperature (773 K) showed no difference from the above trace.

Volumetric gas adsorption studies demonstrated that the film develops a mesoporous structure after SFE without further thermal treatment. Figure 5.0.7 shows a BET plot of the adsorption data for a thin film after drying (as described earlier; 343 K, 24 hours) and SFE, without further thermal treatment, together with the original isotherm obtained.

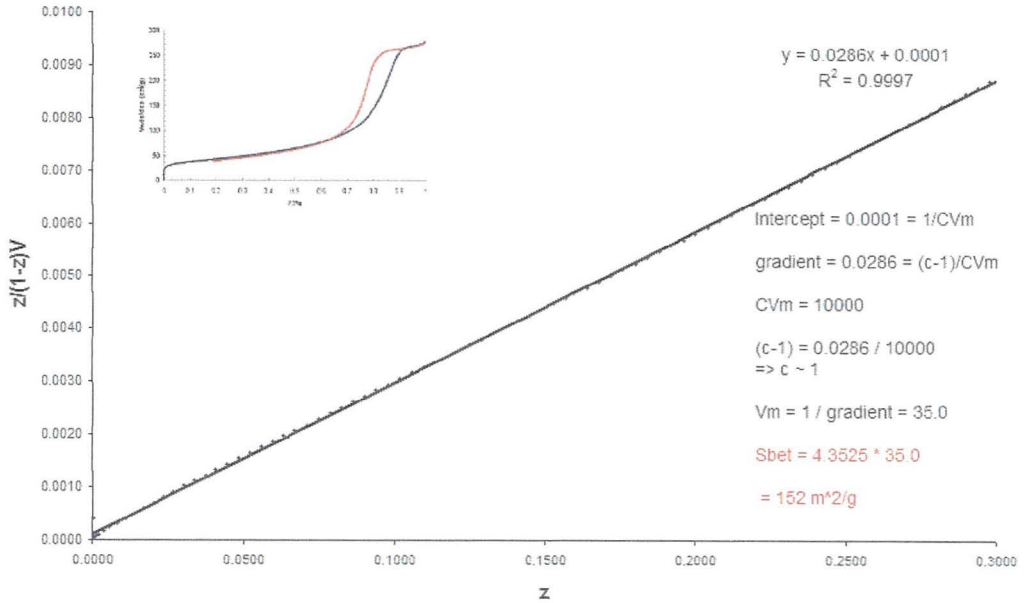

Figure 5.0.7: Figure showing BET plot of data for TiO_2 thin film (after drying @ 343K and SFE) SBET = 152 m^2/g (Data obtained by Dr. Petr Kluson, Prague) Inset shows the type IV isotherm[20] obtained; typical of mesoporous materials. ($z = p/p_0$)

The shape of the isotherm obtained is of type IV, and is thus indicative of a mesoporous structure[20]. Five isotherm shapes were defined by Brunauer *et al.*[20]. Type I is the well-known Langmuir isotherm describing monolayer formation [20,23] and has become characteristic of microporous materials as the plateau is indicative of the completion of pore filling processes [22]. The second isotherm, type II, is known as the sigmoid or S-shaped isotherm and shows a positive deviation from the type I curve with the adsorbed volume rising as the vapour pressure, p_0, is approached. Type II & III isotherms are closely related to types IV and V, where the key difference is a positive deviation from the corresponding type II or III and a plateau region before the adsorbed gas vapour pressure is reached. In the case of a type IV isotherm, characteristic of mesoporous materials [22], this deviation is caused by the onset of capillary condensation below the expected condensation pressure of the adsorbate [23]. It is generally only possible to differentiate between types II & IV if the adsorption isotherm is measured to sufficiently high partial pressures, *i.e.* close to $p/p_0 = 1$.

BET treatment of the linear region of the isotherm shown in figure 5.0.7 gave an estimate of the surface area of 152 m^2g^{-1}. BET treatment allows the estimate of surface area by treatment of the adsorption isotherm at low pressures, *i.e.* between $p/p_0 = 0.05$ and 0.3. Below this region, BET treatment underestimates adsorption and overestimates adsorption above it.

As shown in the equation below, the BET treatment relates the ratio of the adsorbed volume, V to the volume of monolayer coverage, V_m, with the ratio of the partial pressure, p, to the vapour pressure above the adsorbate layer, p_0:

$$\frac{V}{V_m} = \frac{cz}{(1-z)\{1-(1-c)z\}} \qquad where \quad z = \frac{p}{p_0} \qquad \& \qquad c = e^{(\Delta_{des}H^{\ominus} - \Delta_{vap}H^{\ominus})/RT}$$

Rearranging gives:

$$\frac{z}{(1-z)V} = \frac{1}{cV_m} + \frac{(c-1)z}{cV_m}$$

Thus it is possible to plot $\frac{z}{(1-z)V}$ on the y-axis and z on the x-axis to give a linear plot.

The y-intercept will be equal $\frac{1}{cV_m}$ and the gradient will equal to $\frac{(c-1)}{cV_m}$.

By combination of these two quantities V_m may be obtained and thus the surface area estimated. In addition to the S_{BET} measurements, porosity measurements were made from the adsorption/desorption curves of the above film.

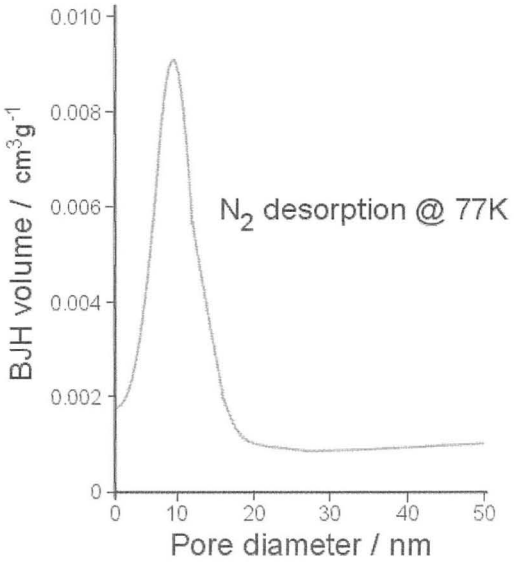

Figure 5.0.8: Differential mesopore data obtained from the nitrogen desorption curve of a film that had been dried at 343 K and treated with SFE. The mesopore diameter is estimated at 10 nm.

Figure 5.0.8 above shows the mesopore diameter as calculated by the BJH method [22-24], whereby an estimate of the mesopore diameter of 10 nm is obtained. These results show that the SFE process is successful at the removal of the pore-filling surfactant residues without further thermal treatment and that the development of porosity is promoted.

Further thermal treatment of the thin films at temperatures in excess of 350 °C (623 K) led to the development of a greater surface area, as expected. Figure 5.0.9 (overleaf) is a BET plot, showing a similar treatment of results as that above, but for a film that has been calcined at 400 °C (673 K) after completion of the SFE process. The BET surface area obtained has increased, by more than a factor of 4, up to 631 m^2g^{-1}, as a result of the calcining process.

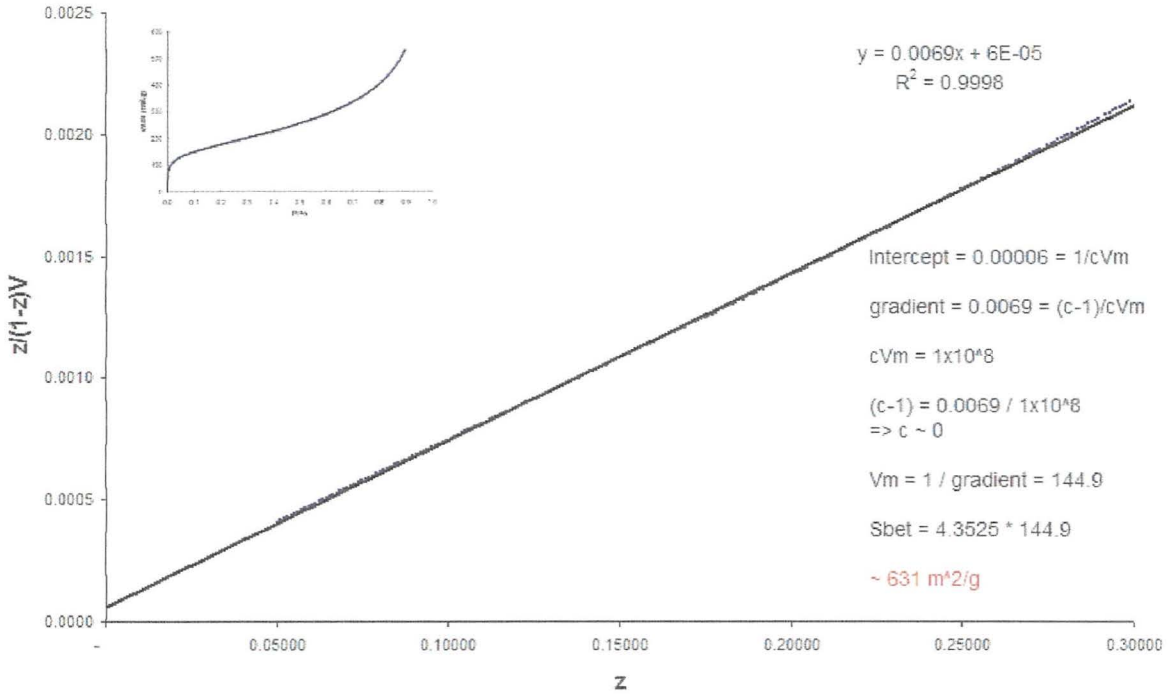

Figure 5.0.9: Figure showing BET plot of data for TiO_2 thin film (after thermal treatment @ 673K and SFE) SBET = 631 m^2/g (Data obtained by Dr. Petr Kluson, Prague) Inset shows the type II isotherm shape obtained.

This large value is in agreement with those obtained during earlier work in this area by Kluson *et al.* [2] It can be seen that the isotherm obtained is ostensibly of type II, however the isotherm was only obtained up z = 0.9 and thus it is not clear whether it may be type IV. Certainly, the onset of the plateau in the isotherm shown in figure 5.0.7 occurs at around 0.9. From close inspection of the latter portion of the type II isotherm there is a slight upwards curvature (with respect to the x-axis) which would indicate that it is indeed a type II isotherm (figure 5.1.0). This would imply that thermal treatment of the films after SFE leads to significant densification and the possible loss of mesostructure. This will be determined by future work on similar thin films.

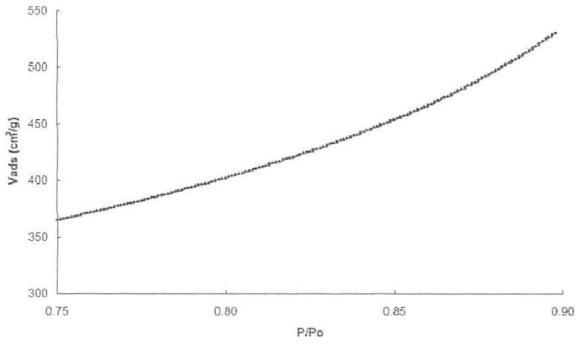

Figure 5.1.0 Figure showing magnification of the adsorption isotherm from figure 5.0.9.

Application of the supercritical fluid extraction process to gel coated optical fibres was largely unsuccessful. In all samples, SFE treatment led to catastrophic film fracture and peeling. This can be seen in figure 5.1.1 and 5.1.2 below which show the surface of several coated fibres after SFE.

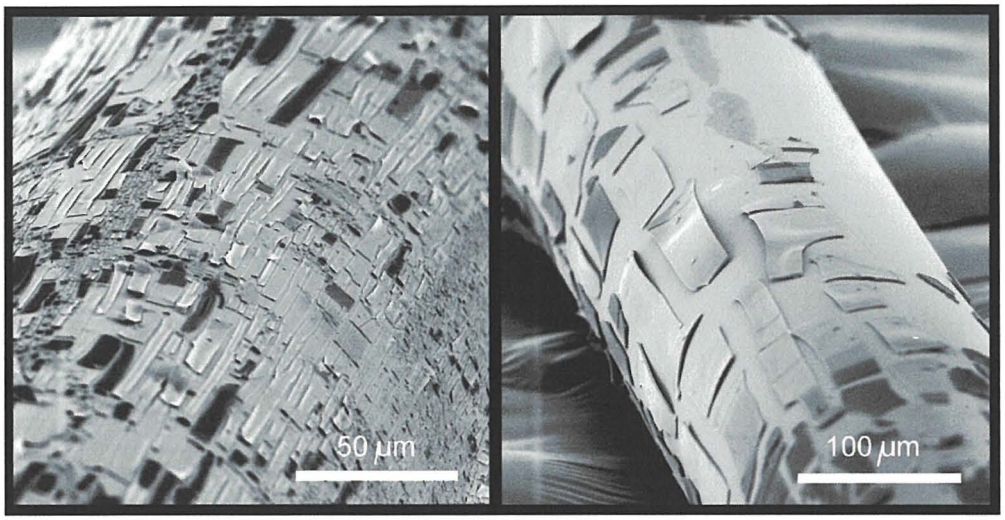

Figure 5.1.1: Scanning electron micrographs illustrating the catastrophic fracturing of films routinely observed for fibres that had been subjected to SFE treatments. In addition to the fracturing of the films it is possible to see that the remaining flakes/plates have lifted off the fibre surface.

It is not clear from the micrographs obtained whether the observed flakes represent the entire film after contraction or whether film loss has occurred.

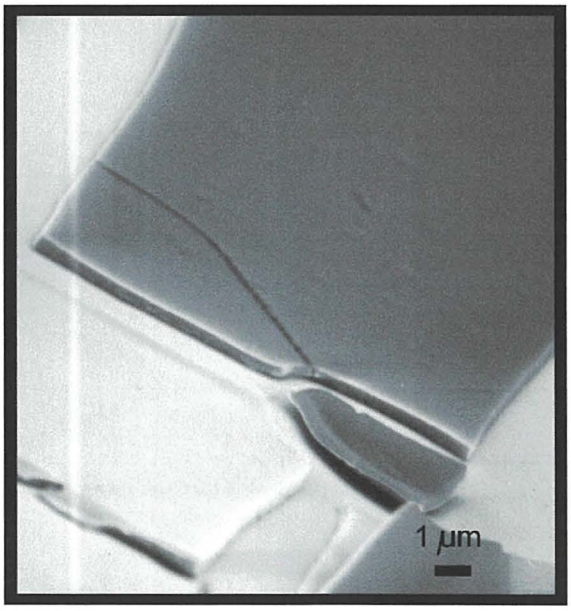

Figure 5.1.2: Higher magnification scanning electron micrograph to illustrating the appearance of the flakes/plates remaining on the fibre surface. The surface of each flake is seen to remain remarkably smooth and the film thickness appears constant. In addition, the colour of flakes can vary from white, to black, under the electron beam.

It is thought that as the extraction of surfactant residues proceeds, the film contracts to a large degree. This is feasible as the organic residues have been shown to make up for some 50 % of the film. Thus, its removal is likely to cause a large decrease in volume (in addition to the ~ 10 % shrinkage expected [19] from lattice rearrangements), which in the case of a thin film will cause lateral contraction and especially in the presence of a significantly curved substrate this contraction will inevitably be accompanied by fracturing as axial strains are induced in the receding films. A secondary phenomenon that is visible in most electron micrographs obtained and seen in both figures above is that of the 'colour' of the flakes under the electron beam. It can be seen that while some flakes are black, others are white or a shade of grey in between. Each flake maintains a constant appearance within itself yet neighbouring plates may be completely different. It is possible that this is simply a result of surface charging within the microscope chamber however this is thought to be unlikely as the samples were sputtered with gold prior to examination such that any surface charge would be dissipated. Due to the failure of fibre coatings to survive the SFE process, no XRD or adsorption data were obtained.

5.3.2 Hydrothermal treatment of gels

Bulk raw gel samples were subjected to steaming both at atmospheric and elevated pressures. After steaming the gels changed in appearance from a straw coloured gel to a dark orange-brown material with a friable consistency as can be seen in the photograph, figure 5.1.3.

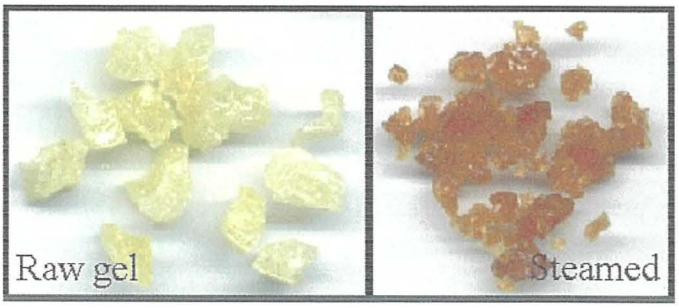

Figure 5.1.3: Photographs showing the appearance of gels prior to and after steam treatment.

The dark gel was to be found immersed in a clear, transparent, viscous fluid, similar in appearance and texture to fresh Triton X-100. This can be seen in the photograph in figure 5.1.4 below.

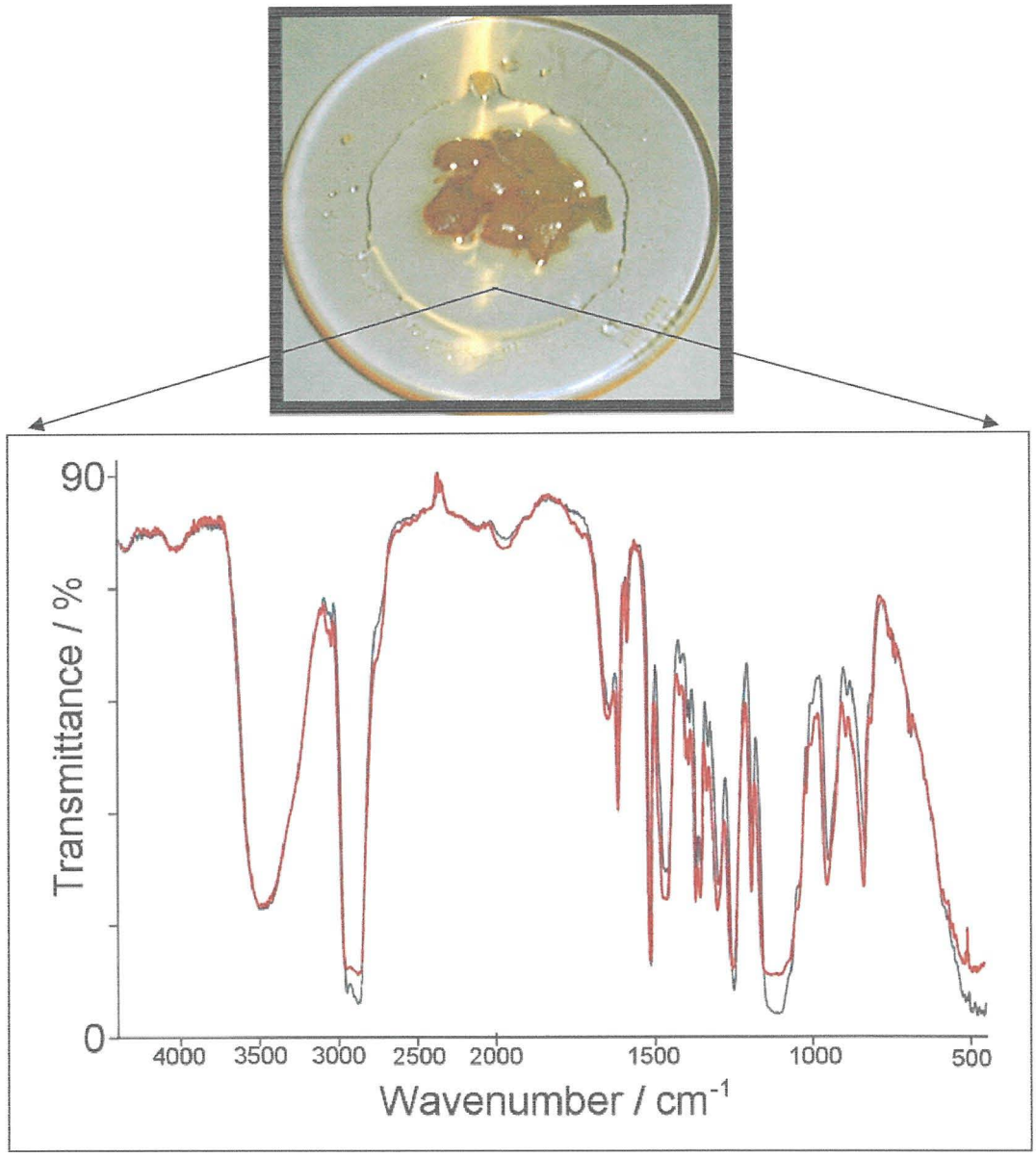

Figure 5.1.4: Photograph of the steamed gel immersed in the clear exudate, together with overlaid infrared spectra of the exudate (black) and steamed TX100 (red) confirming the identity of the exudate as liberated surfactant residues.

The identity of the exudate was confirmed as liberated surfactant after comparison of the FTIR spectra of the exudate with that of steam-treated TX100. As can be seen in the previous figure the match is conclusive. Attempts to determine if the exudate was a single compound or a

mixture using gas chromatography were unsuccessful due to the viscous, non-volatile nature of the fluid.

The gel samples were removed from the exudate and rinsed in dry cyclohexane to remove all traces of the surfactant residues. The gels were then dried and submitted for combustion analysis. The results of the combustion analyses were compared to those obtained (and discussed in chapter 3) for raw gel samples dried/calcined at varying temperatures. The results of this comparison are shown in the plot in figure 5.1.5 whereby it can be seen that steaming at atmospheric pressure reduced the % carbon (by mass) to a little over 30 %, and steaming at elevated pressures reduced the % carbon to between 20 and 30 %. This is equivalent to the reduction obtained by a calcination temperature of between 350 and 375 °C (623 and 648 K) and in the case of the high pressure steaming represents a halving of the organic content.

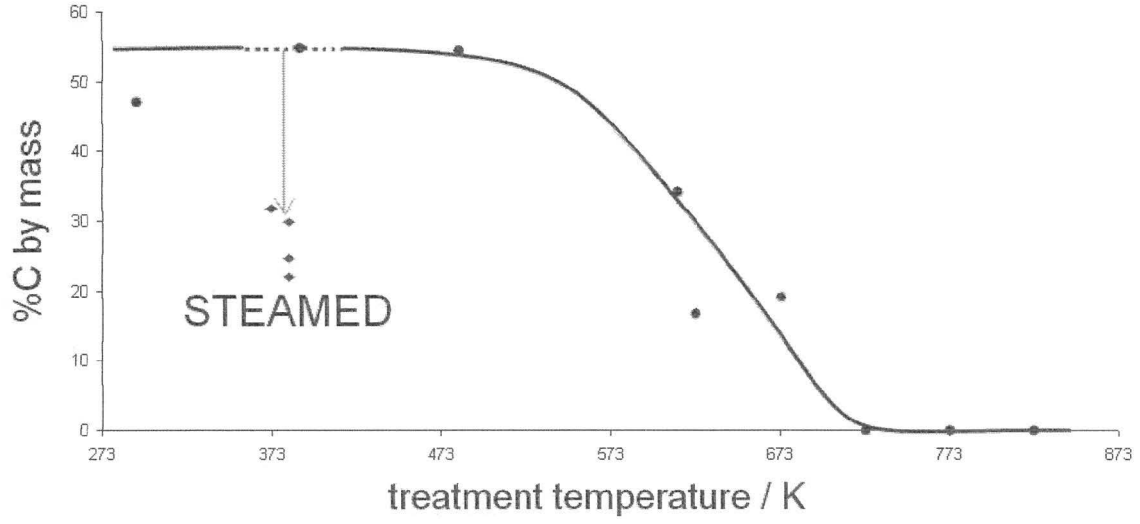

Figure 5.1.5: Graph illustrating the effect of hydrothermal treatment of gels on the residual carbon content (as %C by mass) superimposed onto the trace seen earlier in Chapter 3, Figure 3.2.0

Thus, steaming of bulk gels was shown as an effective means of removing surfactant residues. It is not known whether the increased extraction observed with increasing temperature was as a result of the increased temperature of the steam or the increased pressure within the vessel. It is likely that the penetration of the steam into the gel matrix and its interstices was greater with increasing pressure and thus greater extraction was observed. Steam treatment led not only to

a decrease in carbon content but also to the onset of anatase crystallisation. This was observed with X-ray diffraction measurements.

Despite the temperature of treatment being some 250 to 300 ° cooler than the usual anatase phase transition temperature, distinct anatase signatures were observed by XRD measurements. The diffractograms shown in figure 5.1.6 demonstrate the onset of crystallisation with hydrothermal treatment.

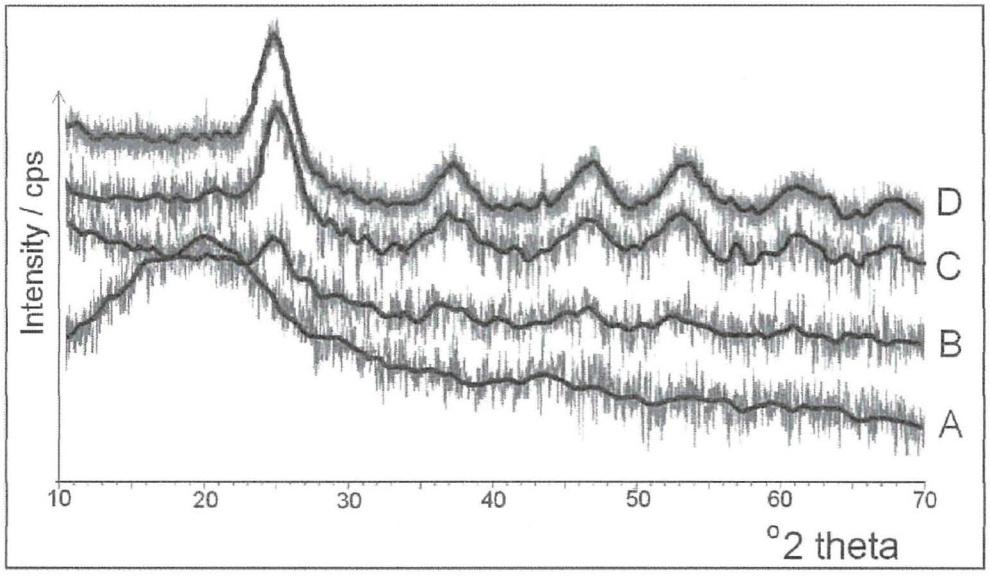

Figure 5.1.6: X-ray diffractograms illustrating the effect of hydrothermal treatment on the crystallinity of gel samples. **A**: Raw, amorphous gel; **B**:Gel steamed at 373 K (1 atm. pressure) for 1 hour; **C**: Gel steamed at 383-393 K (elevated pressure) for 1 hour; **D**: Gel steamed at 383-393 K (elevated pressure) for 2 hours.

After steaming at atmospheric pressure the amorphous hump at 20 °2θ disappears and weak peaks of anatase can be seen to emerge from the noise at 25.4 °2θ and at greater angles. With increasing temperature (and pressure) of treatment the intensity of the anatase signal grows considerably and shows a slight further sharpening after an increased time in the treatment chamber.

Assessment of the gel samples with electron microscopy revealed little visible change in the gel structure after steaming. Comparison of the electron micrographs in figure 5.1.7 overleaf illustrates that unlike the difference between raw gels and calcined gels shown in figure 5.1.8 (also overleaf) the physical changes induced by steaming are more subtle and involve a

softening of the gel edges. Were a field emission source electron microscope available and thus inspection at higher magnification possible then differences between the two samples may be discernible.

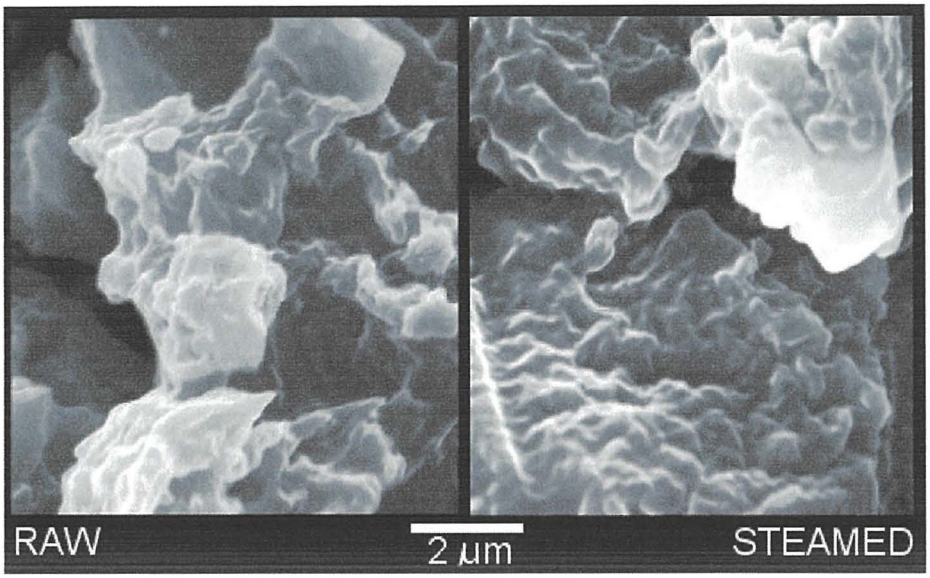

Figure 5.1.7: Scanning electron micrographs showing a comparison between the morphologies of a raw gel sample and a steamed gel sample.

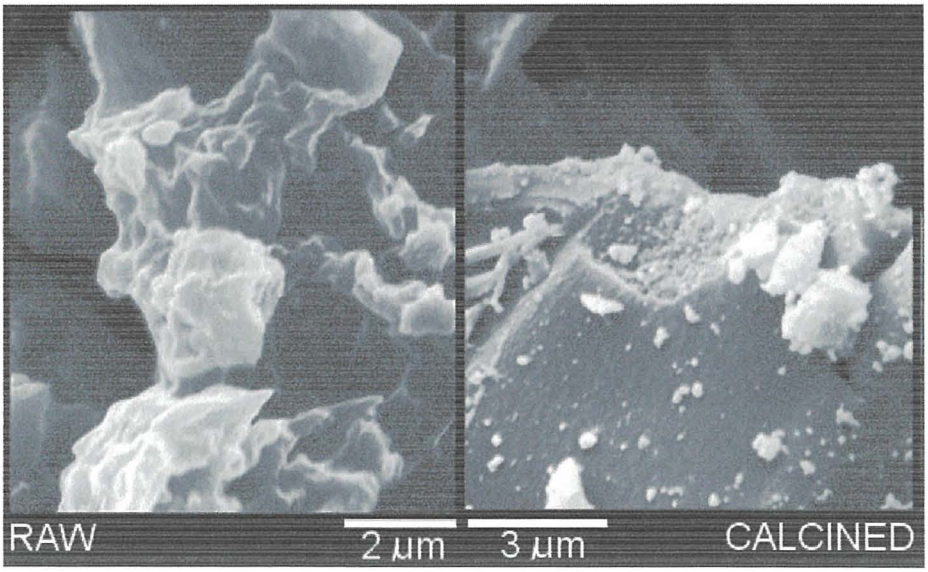

Figure 5.1.8: Scanning electron micrographs showing a comparison between the morphologies of a raw gel sample and a calcined gel sample.

Nevertheless, the onset of crystallinity in bulk gels was confirmed by XRD and the decrease in organic content by combustion analyses. For thin films on conducting glass slides it was hoped a similar trend would be observed with a noticeable decrease in surfactant content and

anatase phase transition temperature. Steaming of gel films on conducting slides, both glass and polyester (PET), gave mixed success. Steaming of flat thin films on slides led to reasonably intact films.

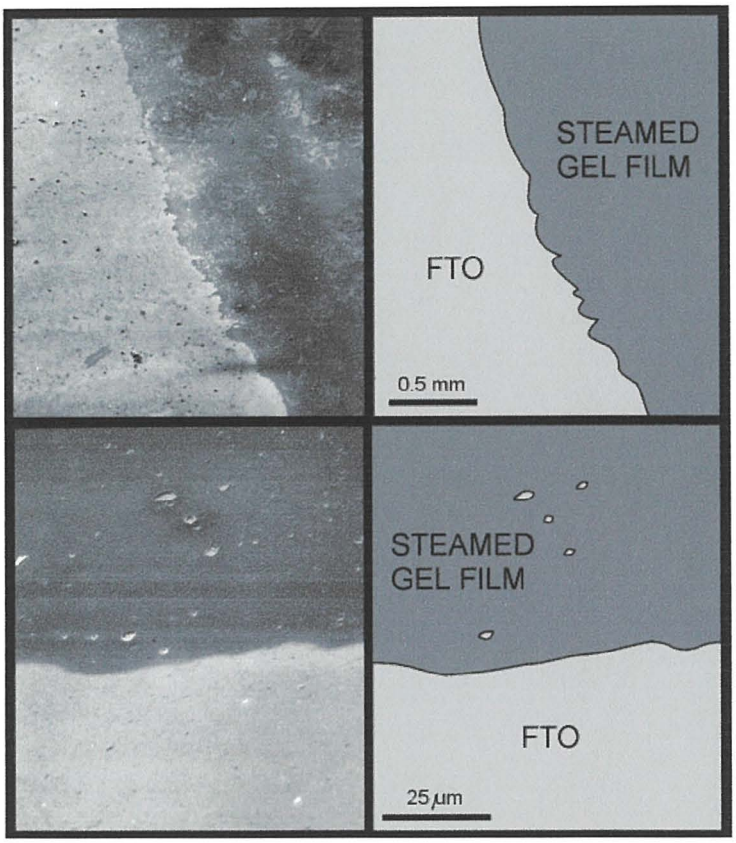

Figure 5.1.9: Pair of electron micrographs at low and higher magnifications, showing the patchiness of thin gel films after steaming. The figures at right are graphics to illustrate the different regions of the left hand micrographs.

In most instances as demonstrated in figure 5.1.9 above, the resultant films were of a patchy nature with numerous localised defects including cracking and blistering.

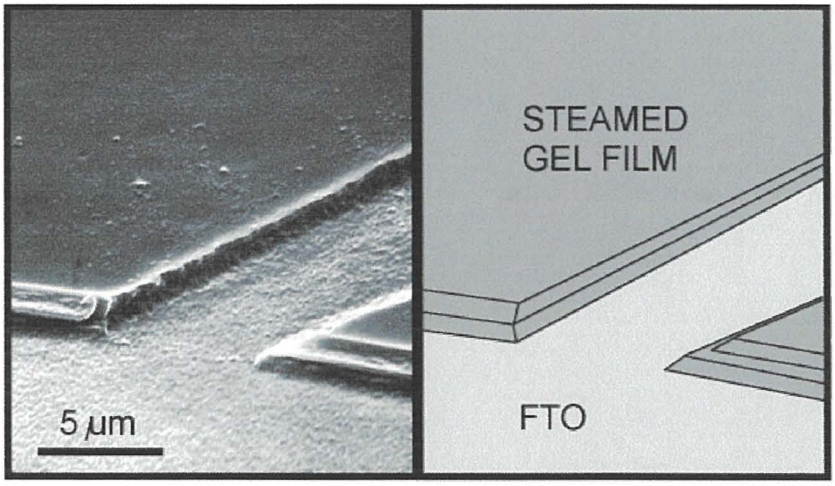

Figure 5.2.0: Electron micrograph showing the surface texture of a thin gel film after steaming. The right figure is a graphic to illustrate the different regions of the left hand micrograph.

Thin films, those less than 10 μm, showed the best survival with a noticeable surface texture present after steaming, figure 5.2.0 above. Where gel films were substantially thicker, in the order of 50 μm, films showed extensive fracturing (figure 5.2.1) similar to that observed for SFE treated samples, as predicted by Ayral *et al.* [25] who also saw cracks in thick sol-gel films and reported that only films less than 1 μm thick will remain crack-free during drying.

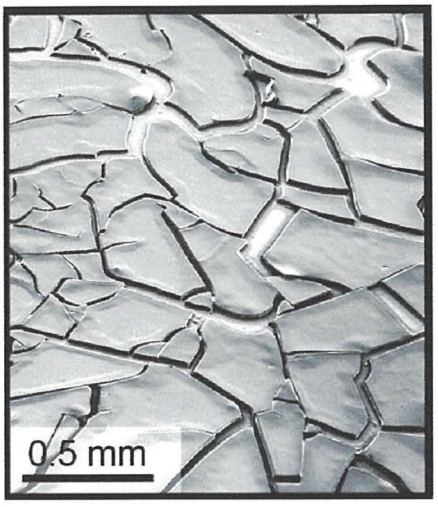

Figure 5.2.1: Electron micrograph showing the fracturing of a thick gel film after steaming.

In all cases, the edges of the defects showed a characteristic spreading. This is thought to be indicative of partial gel dissolution and redeposition at the gel boundaries. This can be seen in the figure above and is further illustrated in figure 5.2.2 which shows an un-steamed, thick raw gel edge for comparison.

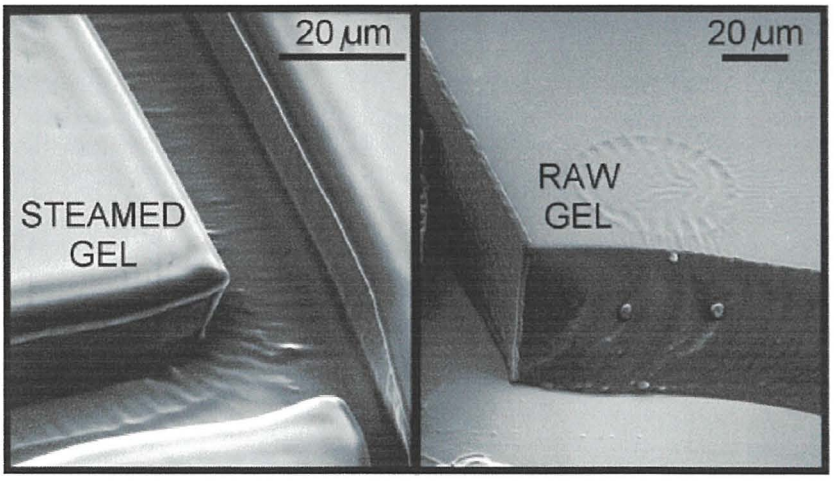

Figure 5.2.2: Pair of electron micrographs showing the edge features of a thick gel films after steaming and in the raw state.

Figure 5.2.3 shows the boundary spreading of a film that had been steamed at elevated temperature and in addition, shows the presence of anomalous protrusions at the surface of the film. The mechanism of formation of these structures is unknown, but again is thought to be due to eruption of partially dissolved gels out from the gel matrix.

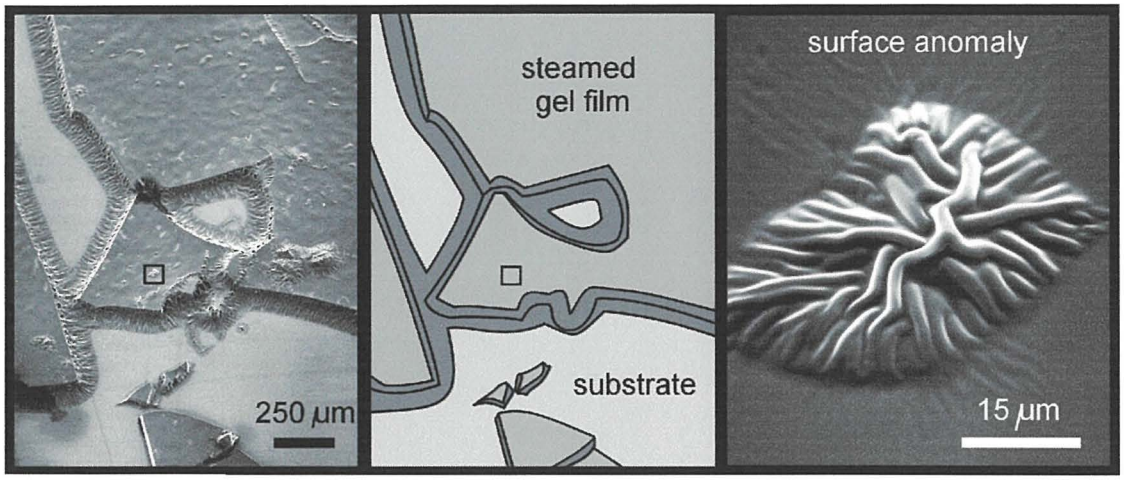

Figure 5.2.3: Series of electron micrographs showing the surface features of a thin gel film after steaming. The centre figure is a graphic to illustrate the different regions of the left hand micrograph.

In films which were steamed under pressure for 1 hour the phenomena were seen to extend 200 μm or more from the film edges resulting in the appearance of 'staining' of the substrate (figure 5.2.4) with no visible thickness at higher magnifications, (not shown).

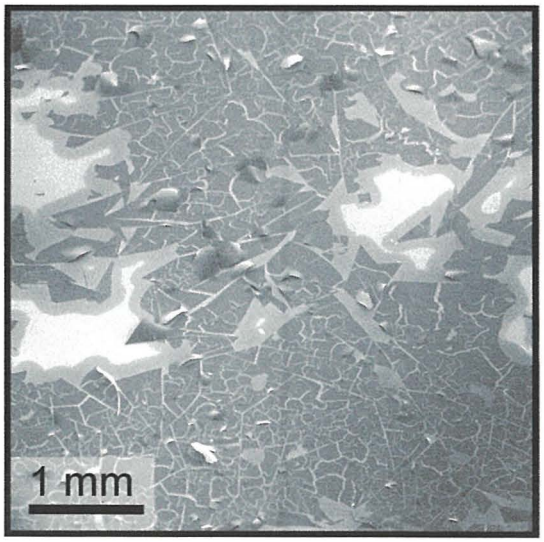

Figure 5.2.4: Electron micrograph showing considerable fracturing of a thin gel film after steaming for 1 hour at elevated pressure. The extensive edge staining surrounding the film is clearly visible.

Finally, hot water (non-boiling, ~85 °C) treatments were attempted whereby coated slides were immersed in heated liquid water. These treatments led to catastrophic film failure as can be seen in figure 5.2.5.

Figure 5.2.5: Electron micrograph showing the destruction observed after immersion of a thin gel film into hot liquid water. Only a few (dark) pieces of film remain adhered to the (light) substrate.

Thus, hydrothermal treatments were shown to give mixed results. Certainly, fracturing was seen in the large majority of cases. The lines of fracture seen for thin films on slides were randomly oriented in marked contrast with the fractures seen in the case of SFE treated fibres which tended to align with either the axial or longitudinal axes of the coated fibres. In the case of the slides, the contraction stresses have no dominant alignment. There is some evidence, (figures 5.2.1 and 5.2.4) for primary and secondary fracturing occurring. In many cases it is possible to observe a network of predominantly straight fractures intersecting at individual points which outline a series of larger gel plates. These large plates are then internally fractured by curved, random cracks forming still smaller plates. It is possible that the larger, linear cracks appear first during early stages of treatment and that the smaller curved cracks appear at a later time as contraction of the film progresses during later stages of steaming or more likely during the drying phase after removal from the steambath.

Hydrothermal treatment of coated fibres failed completely, with none of the applied films surviving the process. Again, as seen in the case of supercritical fluid extraction, the forces generated during the considerable contraction of the films were sufficient to first fracture the films and then to completely detach them from the underlying curved substrates. Post-coating treatments to remove the surfactant residues, both hydrothermal and supercritical, have thus been shown to be unsuccessful due to the high organic content of the films and the associated degree of film contraction upon organic removal. It is possible that reducing the organic component of the film prior to or during coating would seem a better prospect for the deposition of intact, well adhered films.

5.3.3 Ultraviolet irradiation

Irradiation of the films during or after coating with high intensity ultraviolet light may be sufficient to stimulate the onset of crystallinity by direct bond cleavage and rearrangement. Irradiation of a monolithic gel cast in a watchglass through a mask led to a profound deepening of the yellow colouration in the exposed region (figure 5.2.6).

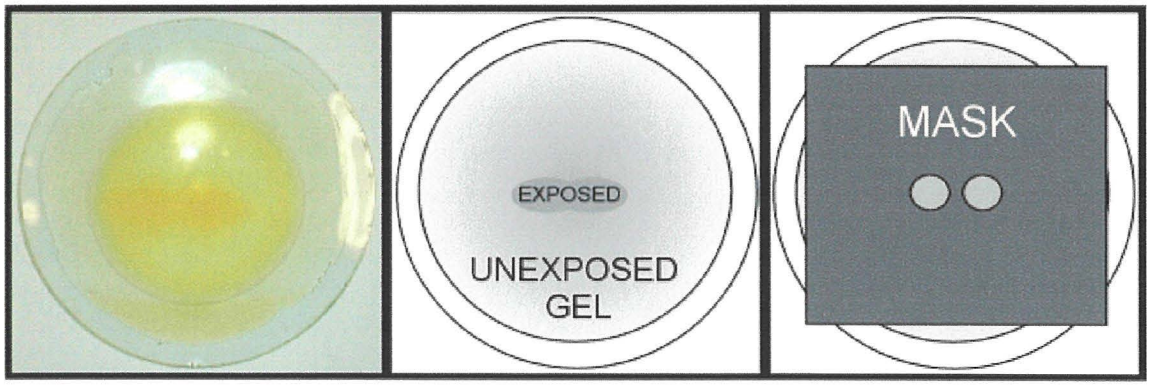

Figure 5.2.6: Diagram illustrating the change in colour observed in a gel monolith after exposure to ultraviolet light at 254 nm for 1 hour, through a mask with two 5mm holes (illustrated at right).

This gel was ground up and the exposed portion of gel compared under an electron microscope with an unexposed gel sample.

The micrographs obtained, at several magnifications, are shown in figure 5.2.7. It is clear by comparison with the micrographs of a raw gel in the figure below (5.2.8) that the gel has undergone a fundamental change in structure.

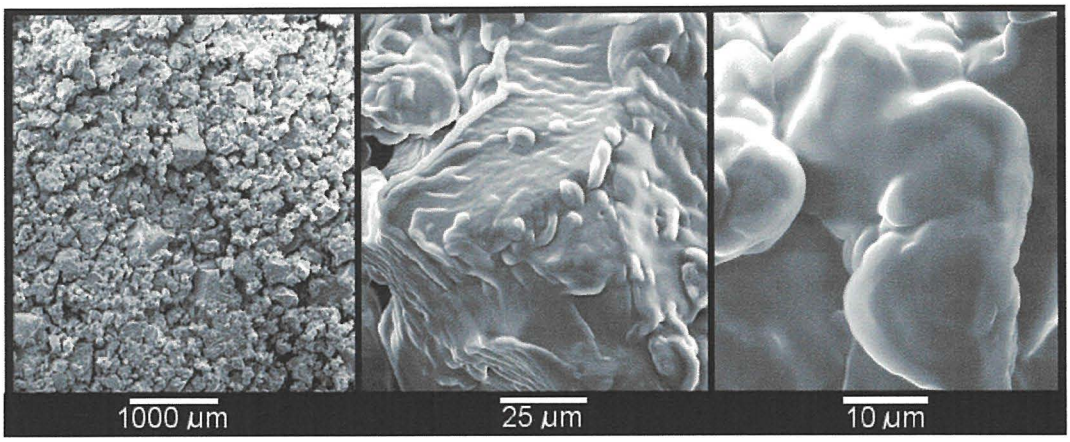

Figure 5.2.7: Series of scanning electron micrographs showing the morphology of a raw gel sample after it has been exposed to UV radiation.

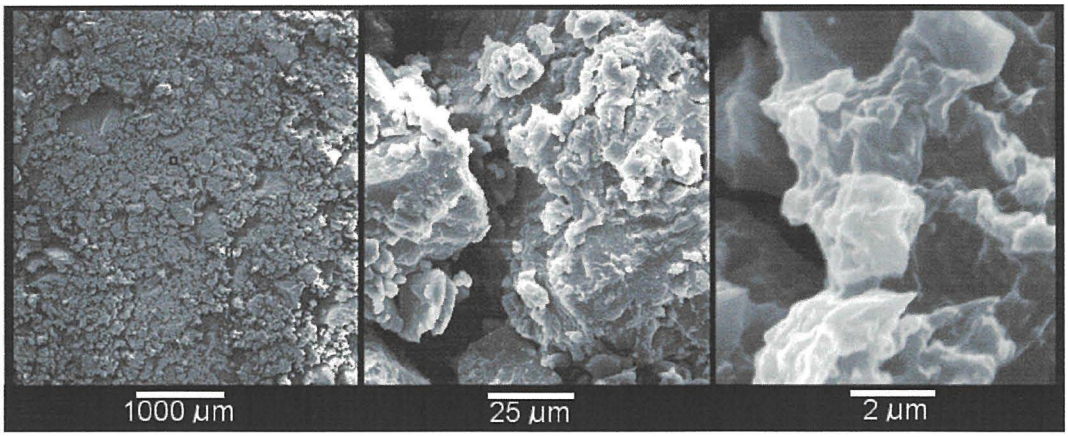

Figure 5.2.8: Series of scanning electron micrographs showing the morphology of a raw gel sample.

No change was seen in the XRD traces for UV irradiated gels, and gels retained their amorphous character. Infrared spectra showed no difference between UV treated and raw gels in the bulk state, however a clear change in the visible and near-UV regions was observable. Figure 5.2.9 (overleaf) shows the transmittance spectra of two gels, one after gelling and the second after 24 hours of exposure to UV light from a discharge tube at 254 nm.

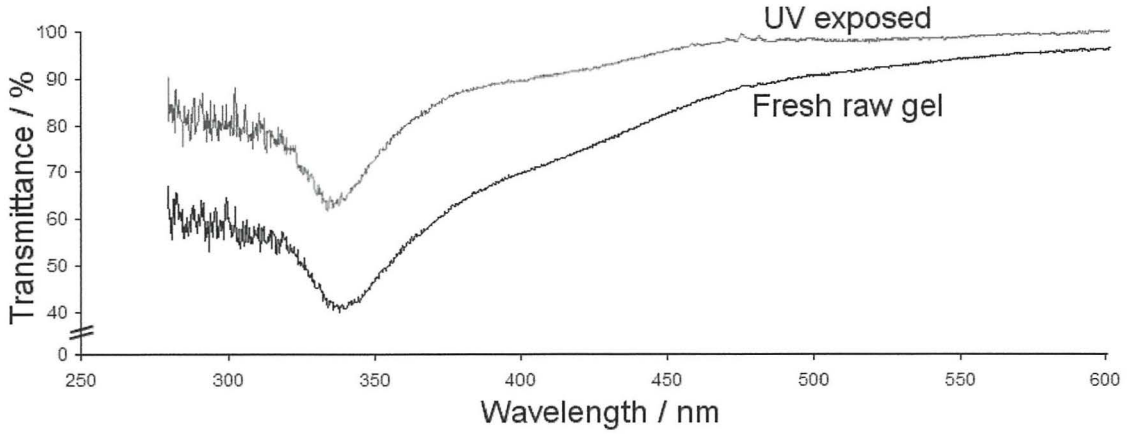

Figure 5.2.9: UV-visible transmittance spectra of a raw gel sample and a gel that has been exposed to UV radiation at a wavelength of 254 nm (after gelling) for 24 hours.

The increased absorbance (decreased transmittance) of the film illustrates the appearance of a pronounced yellow colouration upon irradiation, seen with the naked eye. It is probable that the yellow colour is due to the formation of titanium complexes within the gel matrix. These hydroxy or peroxo complexes can act as precursors for titanium dioxide formation upon calcining.

The irradiation of thin films led, as before, to the formation of cracks and fissures in the film. However, in this instance, unlike for hydrothermal or supercritical methods, there were far fewer fractures formed and the fractures themselves were narrower. Film adhesion was maintained despite a small degree of lateral contraction.

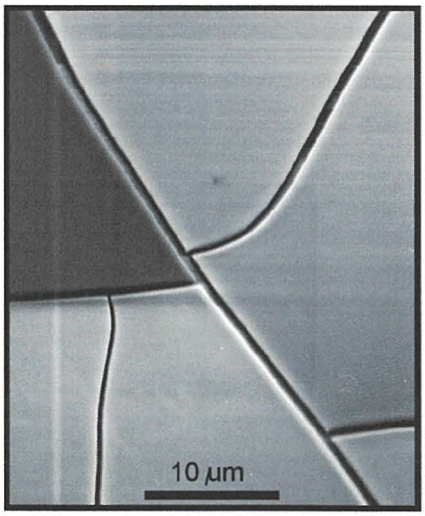

Figure 5.3.0: Scanning electron micrograph of a raw gel film on a flat slide that had been exposed to UV radiation from a mercury lamp for 24 hours.

Figure 5.3.0 (above) is an electron micrograph of an irradiated film on a conducting glass slide showing the appearance of the fissures formed. When thin films were applied to fibres and irradiated well adhered films were the result. No doubt the organic composition remains high and it is this lack of organic removal that prevents significant damage to the film. Figure 5.3.1 is an electron micrograph at low magnification that shows the largely intact film on the fibre surface with only a few narrow fractures extending across the film surface.

Figure 5.3.1: Scanning electron micrograph of a raw gel film on an optical fibre that had been exposed to UV radiation from a mercury lamp for 1 hour.

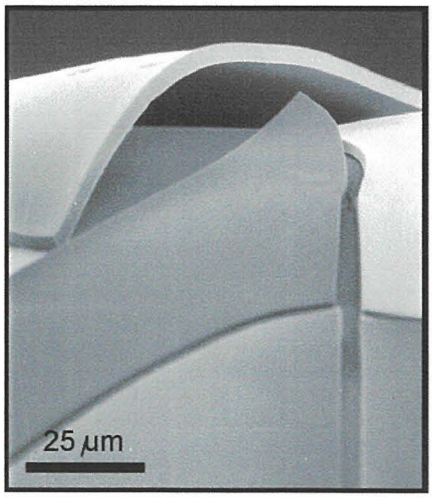

Figure 5.3.2: Scanning electron micrograph of a raw gel film on an optical fibre that had been exposed to UV radiation from a mercury lamp for 24 hours.

After prolonged irradiation the film integrity and adhesion deteriorated. The quantity of fissures increased and the film lifted off the fibre substrate as can be seen in the micrograph in figure 5.3.2.

Attempts to determine the crystallinity of these thin films failed as before, again likely due to insufficient film thickness and material quantity. Figure 5.3.3 illustrates a typical XRD trace obtained. Again, the amorphous hump at 30 °2θ is visible and no titania peaks are seen.

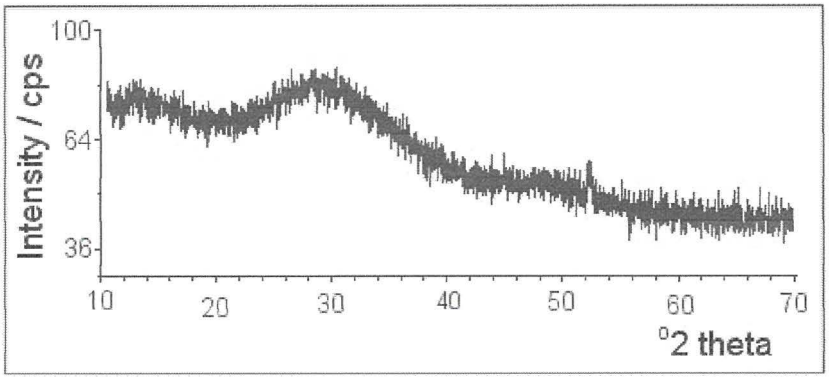

Figure 5.3.3: XRD spectrum of a raw gel film on an optical fibre that had been exposed to UV radiation from a 500 W mercury lamp for 24 hours.

Irradiation with ultraviolet light certainly causes rearrangements within the films. Given the lack of evidence of change in the X-ray and infrared spectra it is unlikely that the use of ultraviolet radiation was sufficient in this instance to induce crystallisation. It is probable that higher intensity sources such as UV lasers would be more appropriate as recommended by Asakuma [14] and Imai [5,6]. It is also probable that radiation of higher energy would be more effective than the near UV sources used in this study. Vandeleest [17] recommends a maximum incident wavelength of 200 nm, equivalent to an energy of 6.2 eV. Continuing on what is becoming a recurring theme, the presence of such high organic content in these films, as an unavoidable consequence of the reverse micelle procedure, seems to be responsible for the lack of success. Were the organic component of the films less, then the use of ultraviolet radiation, hydrothermal treatment and supercritical fluids may be more effective.

The inevitable contraction of the films as organic constituents are removed is highly detrimental to film integrity and leads in most instances to catastrophic film failure. It is seen in the case of UV irradiation, that even where little or no organic residues are removed there is still a degree of film densification and contraction due to bond rearrangements. It is thought that were the films less organic in the first instance then the associated contraction would be less and it may be feasible to use the above treatments either in combination or individually to induce crystallisation and remove the organic residues at temperatures low enough to be compatible with the optical fibres used. A further complication is that the thicker a film is the more likely it is to crack. This was seen in this work repeatedly as films cast onto slides were thinner and showed better integrity whereas films deposited onto fibres were invariably thicker for given sol conditions and demonstrated a tendency to fracture catastrophically. It has been suggested in the literature [25] that only sol-gel films less than 1 μm thick can dry without cracking and this is likely to be considerably more significant where some 50 % of the film volume has to be removed by post coating treatments.

5.3.4 Direct particle deposition

Removal of the organic component completely prior to coating was attempted by calcination of the bulk gels to produce nanocrystalline powders of titania. These powders were then deposited onto optical fibres using a novel technique of partial dissolution of the fibre cladding using volatile solvents. Acetone suspensions of precalcined titania particles were dispersed using ultrasound for 10 minutes after which time glass slides were dipped and withdrawn. Scanning electron micrographs of the slides after deposition are shown in figure 5.3.4 (overleaf). Likewise, silica optical fibres were similarly coated and assessed by SEM. In both cases, little or no deposition was seen. Trials to determine if the deposition could be

improved by varying the solvent showed that deposition was not improved in any of the common laboratory solvents.

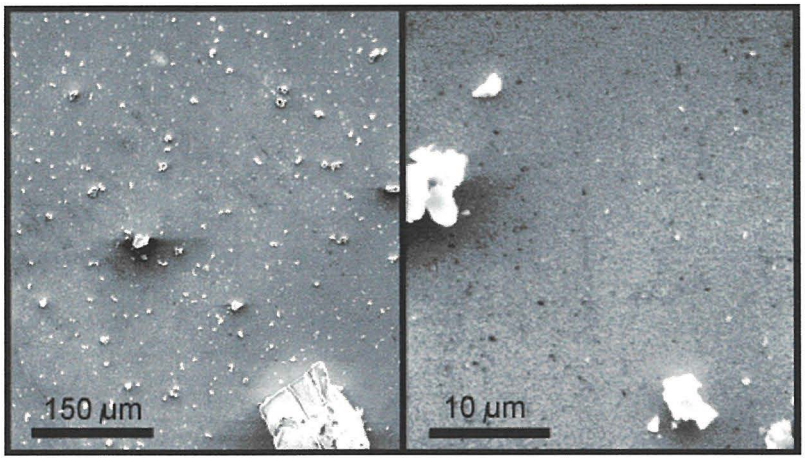

Figure 5.3.4: Scanning electron micrograph showing precalcined titania particles deposited onto a conducting glass slide from suspension. The particles size can be seen to vary from 150 µm down to sub-micrometer sized.

Those few particles that were seen to adhere were large, random shaped agglomerates such as those seen in figure 5.3.4. Thus the ultrasonic agitation had failed to break down micron-sized aggregates and a particle size distribution ranging from sub-micrometer dimensions up to hundreds of microns was observed. Attempts to deposit precalcined titania particles from acetone appeared to be immediately successful in the case of plastic (PMMA) fibres. After dipping in the opaque white suspension, the fibres showed a white coating on their surface, visible to the naked eye. Examination of this coating with SEM suggested that the particles were dispersed and reformed to produce a fine net or mesh on the surface of the fibre. Figure 5.3.5 (overleaf) is a micrograph showing this mesh on the surface of a PMMA fibre. The appearance of this high surface area mesh coating and its porous nature is further illustrated at higher magnification in figure 5.3.6 (overleaf), which shows enlargements of the two boxes in figure 5.3.5. As can be seen the mesh consisted of interconnecting pores with the suggestion of deeper layers of porosity beneath. It was hypothesised that these networks were formed during evaporation of the solvent after dipping as the suspended particulates migrated to the edges of solvent bubbles or droplets and reaggregated.

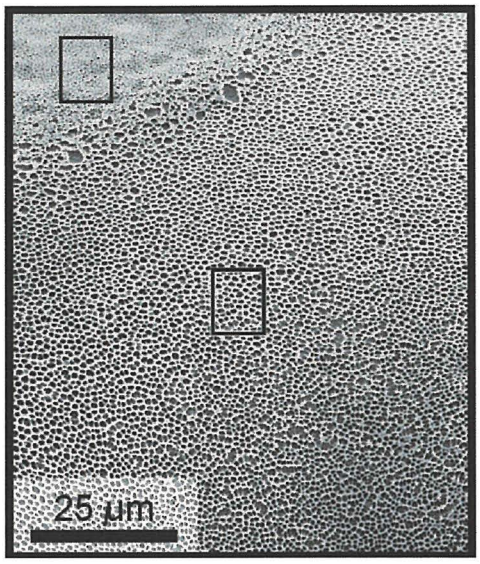

Figure 5.3.5: Scanning electron micrograph showing the extensive mesh covering the surface of a PMMA fibre after dipping in the titania suspension. The boxes mark regions that are magnified in the next figure.

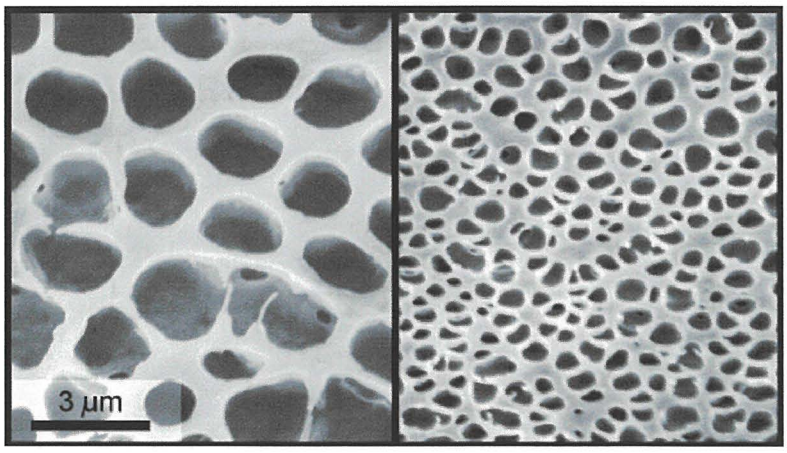

Figure 5.3.6: Scanning electron micrographs showing the extensive mesh covering the surface of a PMMA fibre after dipping in the titania suspension. Both images are at the same magnification.

The presence of titania could not be confirmed by EDX as the facility was in repair. To determine whether or not the mesh was titania, a control sample of PMMA fibre was treated in a similar fashion in pure acetone. In this instance, the white coating was again seen, thus demonstrating that the mesh was not made of titania. Figure 5.3.7 compares two micrographs; one of a fibre dipped in a titania suspension and the second in pure acetone.

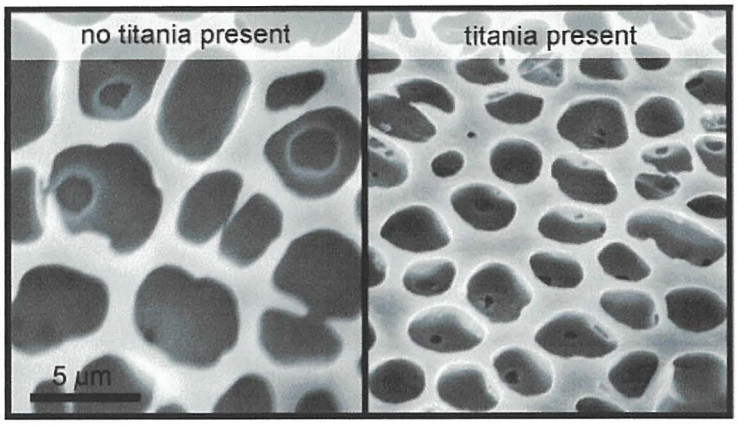

Figure 5.3.7: Scanning electron micrographs showing that the mesh formed is not titania and is caused by partial dissolution of the fibre surface. Both images are at the same scale.

As can be seen, the two mesh structures are near-identical. The discovery of this mesh structure is serendipitous as it would represent a fascinating means of entrapping a coating to the fibre wall or of allowing solution ingress into the region where the evanescent field will be at its strongest. Further examination of samples showed that it was indeed possible to trap the precalcined titania particles within the matrix of the mesh (figure 5.3.8).

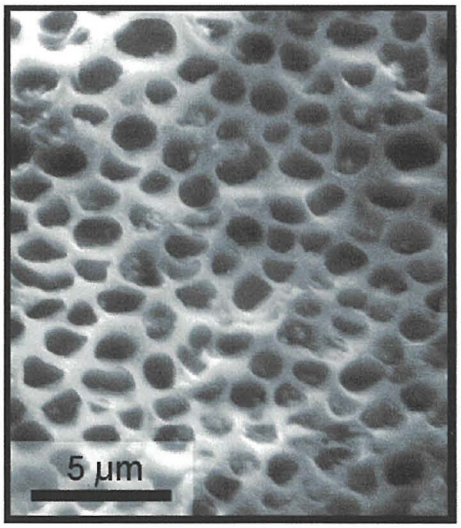

Figure 5.3.8: Scanning electron micrograph showing fine, sub-micron sized embedded particles of titania within the PMMA mesh.

By first exposing the fibre to pure acetone in order to produce a surface mesh, and then dipping the mesh-covered fibre into an acetone suspension of titania nanocrystallites it was possible to trap small crystals within the pores of the net as can be seen in the figure above;

furthermore this would in theory protect the fibres from mechanical removal from the fibre surface and bring them into greater interaction with the evanescent field.

Attempts were made to increase the particle loading of the fibre coating by increasing the volume fraction of titania in the suspension, by increasing the dipping exposure time and by applying multiple coats. This was performed on a PMMA fibre to produce a thick coating onto the cut end of a straight fibre. Thus, it was possible to manufacture a device with a remote tip that would be in the direct path of the incident beam as it struck the endface of the fibre core. Figure 5.3.9 shows a series of micrographs at increasing magnification of the coated fibre tip.

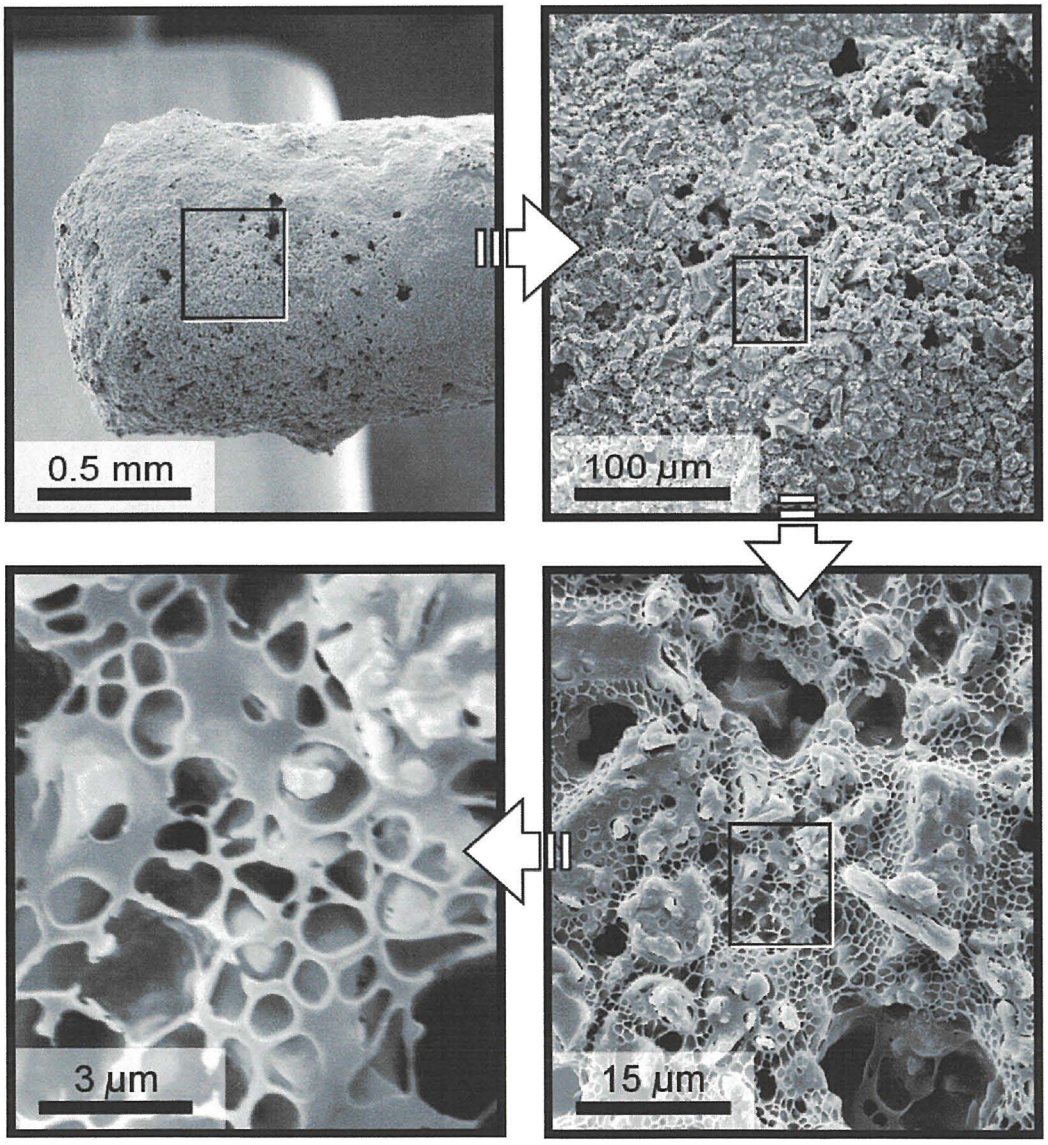

Figure 5.3.9: Series of scanning electron micrographs showing that it is possible to trap titania crystallites within the mesh with multiple dip-coatings in the titania suspension. Image magnification increases clockwise from the top-left.

Given the porous nature of the coating it is feasible that such a device could show great potential if incorporated into a fibre sensor or photocatalytic device. Such a coating could be applied to an optical absorption probe of the type shown in figure 5.4.0 below.

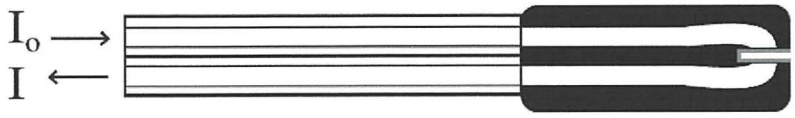

Figure 5.4.0: Diagram of an absorption probe with a notched head which could be filled with the porous titania mesh if using a PMMA fibre.

This would enable the use of absorption, fluorescence or scattering spectroscopy to identify compounds that permeated into the porous mesh and could remotely monitor their photodegradation at the photoactivated anatase surface.

The porosity and surface area of the mesh and embedded particles were not known but the embedded particles were much greater than micron sized. This was likely due to a lack of complete deaggregation of the secondary particles. Further work was carried out to disperse the particles in n-methyl pyrollidone (nmp) which shows greater solubilising power for many materials [26-28]. Nmp was used in the place of acetone and tests were performed to determine if a similar mesh would be obtained. Coiled fibres were immersed in pure nmp and scanning electron micrographs recorded. Figure 5.4.1 is an example of the results obtained and includes a descriptive graphic.

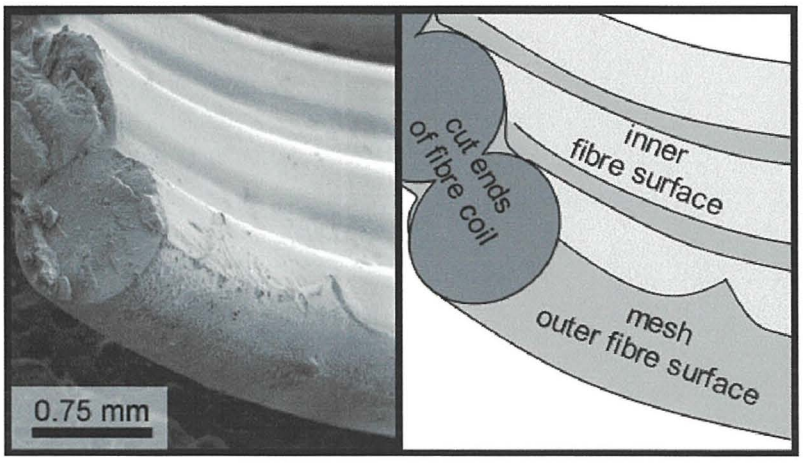

Figure 5.4.1: Scanning electron micrograph showing a cut section of a fibre coil. The coil, which contained 3 turns of PMMA fibre was dipped into nmp, dried and then a section of the coil of 10 mm length was removed and mounted for SEM analysis. The inner surface showed no mesh, which was only observed on the outside of the coil and on the material between the fibres.

In contrast to the meshes obtained with acetone the meshes observed with nmp were only found on the outer surface of the coil and the material between individual fibre strands. This is a feature not of the nmp but of the mechanism of fibre coiling. The fibres are coiled and then heated briefly to fuse the fibres together prior to removal from their support. This fusing process serves to melt the thin outer cladding layer on the PMMA fibres and use it as a 'glue' upon cooling to hold the fibre coil in its required form.

It is this material that is responsible for mesh formation. As it migrates to the outer faces of the coil and between the individual fibre strands during melting it is only at these regions that meshes are found.

Figure 5.4.2 shows a further micrograph which more clearly illustrates the binding material between the fibre strands.

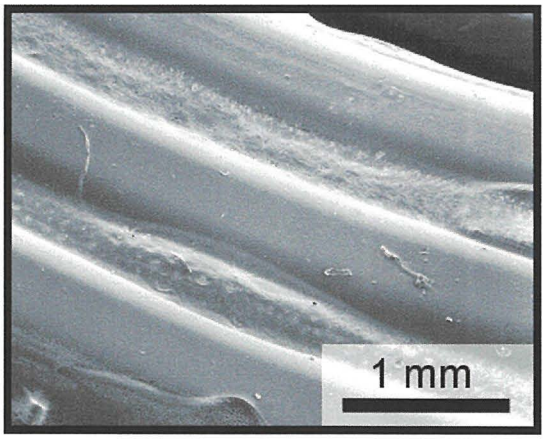

Figure 5.4.2: Scanning electron micrograph showing the material between the fibre sections in a cut fibre coil after immersion into nmp.

One clear difference with nmp was that the morphology of the mesh was rougher and suggested the presence of a more complicated wall structure. This again was likely to be due to the heat-setting process.

Figures 5.4.3 and 5.4.4 overleaf illustrate the granularity of the mesh when nmp was used.

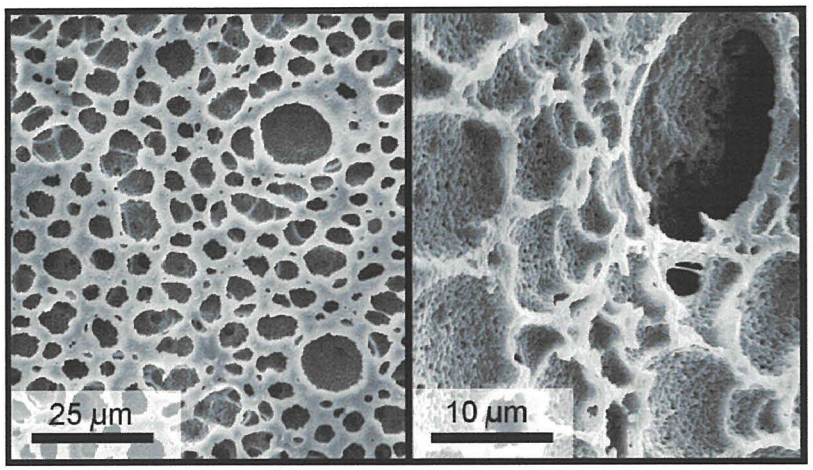

Figure 5.4.3: Pair of scanning electron micrographs showing the mesh obtained on the fibre coils after immersion into nmp. It is interesting that in the case of nmp, a much rougher mesh surface is obtained.

As the plastic fibre was briefly heated in excess of its glass transition temperature the resulting material upon cooling would be somewhat harder and more brittle and would therefore behave differently in the presence of the solvent. The precise mechanism of the mesh formation remains unexplained and would be addressed in any continuation of this work.

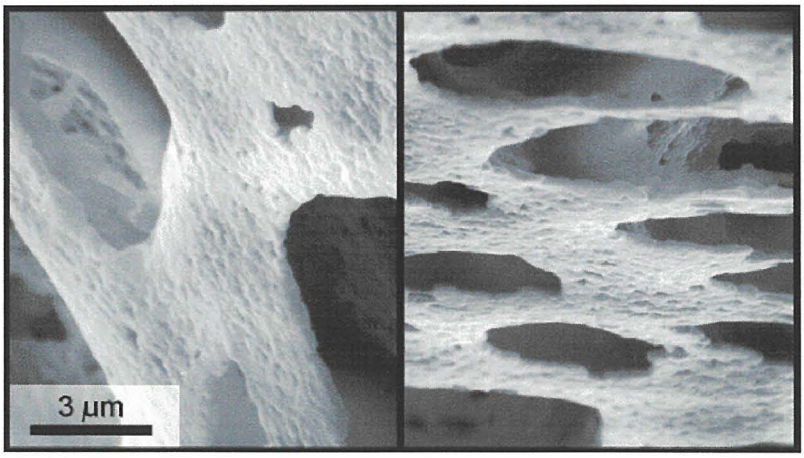

Figure 5.4.4: Pair of scanning electron micrographs showing the mesh obtained on the fibre coils after immersion into nmp. It is possible to see that the mesh is composed of smaller grains joined together to form sheets.

The key result in the favour of the use of nmp came when the titania particles were suspended within it. As predicted the use of nmp as the solvent enabled better dispersion of the titania particles. Analysis with SEM after coating showed that the large titania particles had been broken down into spherical aggregates which in turn were partially broken down into smaller

aggregates and some primary particles. Figure 5.4.5 is a series of micrographs at varying magnification showing the distribution of the spheres over the mesh surface between the fibre strands and the appearance of the aggregates.

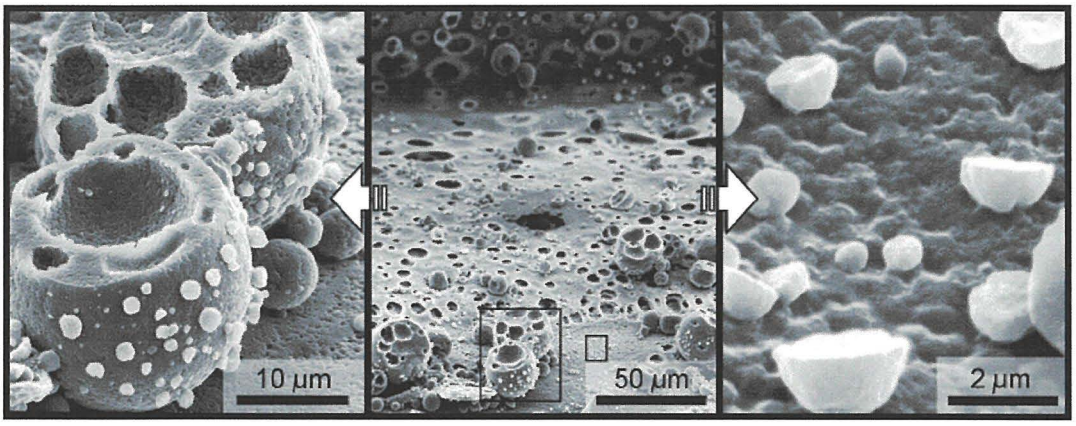

Figure 5.4.5: Scanning electron micrographs showing detail of the structure of the spherical aggregates deposited from an nmp suspension of titania particles onto a PMMA fibre. The two outermost images are enlargements of the centre image and show the polydisperse nature of the aggregates.

These images give clues as to their formation. Each sphere is composed of a collection of smaller spheres which are in turn composed of smaller particles again. This implies that the primary driving force behind agglomeration is direct coalescence of small particles followed by growth of fresh titania between the aggregated particles, perhaps by an Ostwald ripening process. Ostwald ripening may be defined [29] as a very general phenomena that may occur in liquids, solids or on solid surfaces and which involves the growth of larger particles at the expense of smaller particles [29-31]. Although the factors controlling growth in the solid state are still not fully elucidated [29], two key processes have been described for grain coarsening in porous nanocrystalline materials. The first is the growth of particles by an evaporation /condensation route [29-32] and the second involves surface diffusion across terraces and reattachment to larger particles [31,33,34].

Observed particle size was highly polydisperse with particles varying in size from 10 µm spheres to primary particles less than 500 nm in size. This is partly illustrated in figure 5.4.6 overleaf.

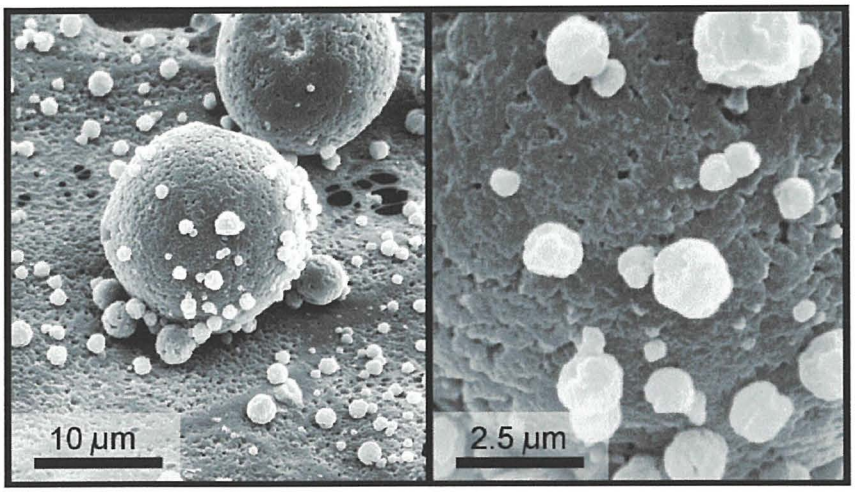

Figure 5.4.6: Scanning electron micrographs showing detail of the structure of the spherical aggregates and the polydisperse nature of the particles, varying from sub-micron to 10s of microns in diameter.

Coils of PMMA fibre which had been coated with these spherical particles were immersed in aqueous solutions of methanol and illuminated with a broad spectrum white light from a Xe arc lamp source. The coiling of the fibres was shown to be highly effective at increasing the light penetration through the coating surfaces.

Measurement of the increasing UV-visible absorption with coiling showed (figure 5.4.7 overleaf) that a loss of near-UV light (at a wavelength of 350 nm) of 10 % absorption with a single coil (relative to an uncoiled fibre) was obtained and that with additional coiling it was possible to further increase this loss to 35 % for a fibre with 10 coils. This light energy is lost directly through the cladding walls around the coils and will penetrate the coating on the fibre surface.

Figure 5.4.8 (also overleaf) shows two photographs of the coated fibre coils immersed in methanolic solutions. Bubbles were seen to form on the surface of the fibres (as can be seen in the figure). Tests were performed on the solutions using gas chromatography to determine the concentration of methanol in the solutions both prior to and after the fibre immersions. These tests were inconclusive as changes observed (less than 10 %) could be attributable to experimental error.

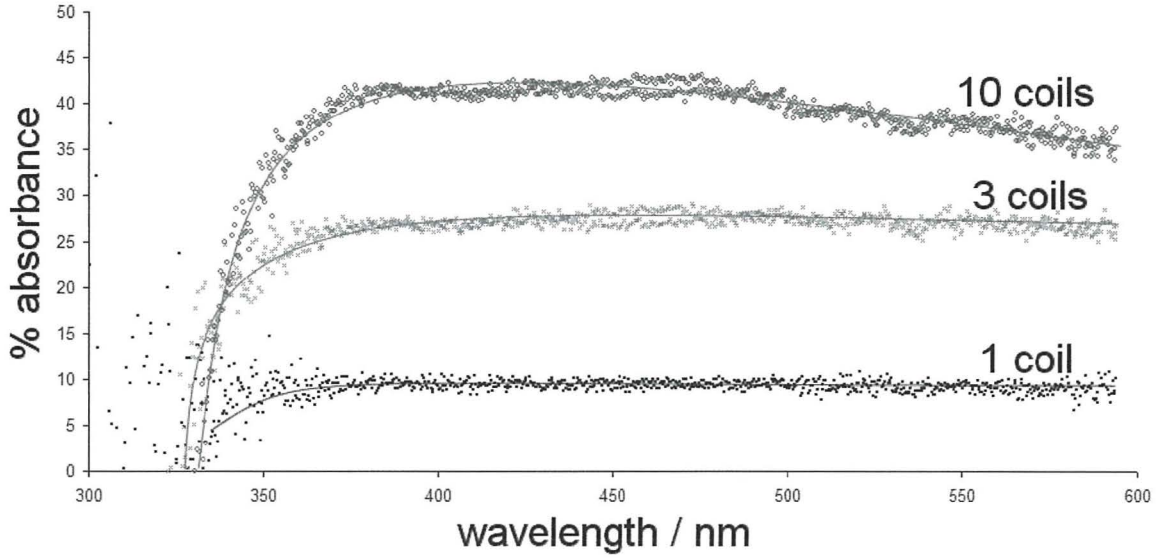

Figure 5.4.7: UV-visible spectrum showing absorption (light loss) increase with coiling of fibre.

Figure 5.4.8: Photographs of bubbles formed on coiled, titania coated PMMA fibres.

5.4 Conclusions

Supercritical fluid extraction of films deposited onto glass slides was shown to produce films of exceedingly large specific surface area with estimates of the BET surface area in excess of 150 m^2 per gram for films that had not been calcined, increasing up to values in excess of 600 m^2 per gram for films that were calcined. Unfortunately, SFE treatment often led to catastrophic fracturing of films and in the case of films on optical fibre the technique as it stands would not be feasible. Where SFE treatment did not lead to film failure, gas adsorption measurements demonstrated that high surface area, mesoporous films could be produced by this technique. Further work is advised (and ongoing) to determine whether modification of the extraction regimes may lead to improved film integrity and adhesion.

Hydrothermal treatment after gelation was shown to successfully induce the crystallisation of the anatase phase in bulk gels. Steaming at atmospheric pressure was sufficient to lower the carbon content by 40 % and when steamed at elevated pressures this reduction was increased to greater than 50 % of the starting composition. The steam treatment led to the liberation of surfactant as a viscous exudate that was easily washed from the steamed gels with isopropanol or cyclohexane. In the case of thin films, as was seen for SFE methods, extensive fracturing was observed after hydrothermal treatment, with partial removal of the film. Complete removal of the film from slides was seen after immersion in heated liquid water. For thin films on optical fibres hydrothermal treatment led to the complete destruction of films and their removal from the fibre surface.

No work was carried out to investigate the effect of ambient humidity upon gelling rates in thin films and all depositions were performed in open conditions. A series of experiments in a glovebox environment would allow the influence of environmental conditions on the deposition process to be characterised. It is thought that increasing the ambient humidity would increase the rate of gelling of films as they are dipped.

Porosity and surface area measurements on hydrothermally treated samples would be useful in any future work to fully determine the effects of treatment on the films.

Ultraviolet irradiation of films did not cause any measurable change in phase, however significant shrinkage was observed which is attributed to condensation reactions between neighbouring hydroxyl groups within the oxide skeleton of the gel. Evidence for these condensation processes was seen by the intensification of the yellow colouration of the films, due to the formation of coloured titanium complexes with the liberated species.

Despite the poor performance of the thin films deposited and their extensive fracturing it would be beneficial to pursue these processes in an attempt to produce films on optical fibre that show the unusually high specific surface area seen for the thin films on conducting glass slides, in excess of 600 m^2 per gram. The inherent problem with the reverse micelle microemulsions used in this work is the high organic content of the resulting films. The removal of some 50 % of the film volume after deposition will inevitably cause massive film shrinkage and thus likely failure. Extreme fracturing of films was observed for all post-coating treatments and this is an issue that needs resolving for coatings onto the optical fibres. Better results for fibres would almost certainly be obtained using direct micelle techniques in aqueous media, e.g. with nitric acid and ethanol. Such techniques are by the far the most commonly reported in the literature. However, the best surface area estimates reported are only 150 to 250 m^2 per gram. No work was performed with different surfactants, and this work concentrated solely on the use of the non-ionic octylphenylpolyoxyethylene ether Triton X-100, although there are other common surfactants within the Triton range in which the polyoxyethylene chain is shorter. There are also saturated analogues of Triton X100 in which the octyl phenyl moiety is replaced with a substituted cyclohexane ring. In addition of course there is a vast range of non-ionic surfactants that could be used in this system. Furthermore,

water was the only hydrolysing agent considered whereas it would be possible to use hydrogen peroxide or to look at an acid catalysed process.

The lack of XRD traces for thin films caused great difficulty in discerning any phase change in the films after treatments. A series of measurements using Raman spectroscopy or ellipsometry would enable phase information and changes in physical properties to be detected. The use of ellipsometry as a tool for monitoring fluctuations in the refractive indices of films would have been invaluable.

The production of a mesh structure was formed during dip-coating of PMMA fibres in acetone or n-methylpyrrolidone suspensions of titania. This mesh phenomenon was at first attributed to deposition of titania but was subsequently confirmed to be a phenomenon related to the dissolution and redeposition of the fibre cladding material. The mesh was shown to be capable of entrapping titania particles and a rudimentary device was assembled by immobilisation of titania crystallites onto the tip of an optical fibre. The serendipitous discovery of this mesh phenomena could be harnessed in future work to produce novel fibre devices by immobilisation of dyes or sensing materials within the mesh matrix. In addition it would be interesting to use a mesh covered optical fibre as a support for sol-gel deposition of the titania material. Subsequent SFE or hydrothermal treatments may produce highly porous, high surface area structures without the concerns of fracturing seen in the case of thin films.

5.5 References

1 Z.S. Guan, X.T. Zhang, Y. Ma, Y.A. Cao, J.N. Yao, *J. Mat Res*, **16** (2001) 907-909

2 P. Kluson, P. Kacer, T. Cajthaml, M. Kalaji, *J. Mat. Chem.*, **11** (2001) 644-651

3 A. Ayral, J. Phalippou,T. Woignier, *J. Mat Sci*, **27** (1992) 1166-1170

4 H. Hayashi, K. Torii, *J. Mat. Chem.*, **12** (2002) 3671-3676

5 H. Imai, H. Hirashima, K. Awazu, *Thin Solid Films*, **351** (1999) 91-94

6 H. Imai, H. Morimoto, A. Tominaga, H. Hirashima, *J. Sol-Gel Sci Tech,* **10** (1997) 45-54

7 Y. Kotani, A. Matsuda, M. Tatsumisago, T. Minami, T. Umezawa, T. Kogure, *J. Sol-Gel Sci Tech,* **19** (2000) 585-588

8 M. Burgos, M. Langlet, *J. Sol-Gel Sci Tech*, **16** (1999) 267-276

9 K. Shimizu, H. Imai, H. Hirashima, K. Tsukuma, *Thin Solid Films,* **351** (1999) 220-224

10 J. Wang, G.M. Wu, J. Shen, T.H. Yang, Q.Y. Zhang, B. Zhou, Z.S. Deng, B. Fan, D.P. Zhou, E.S.Zhang, *J. Sol-Gel Sci. Tech*, **18** (2000) 219-224

11 S.T. Aruna, S. Tirosh, A. Zaban, *J. Mat. Chem.,* **10** (2000) 2388-2391

12 M. Wu, G. Lin, D. Chen, G. Wang, D. He, S. Feng, R.Xu, *Chem. Mater.* **14** (2002) 1974-1980

13 M. Wu, J.B. Long, A.H. Huang, Y.J. Luo, S.H. Feng, R.R. Xu, *Langmuir* **15** (1999) 8822-8825

14 N.Asakuma, T. Fukui, M. Aizawa, M. Toki, H. Imai, H. Hirashima, *J. Sol-Gel Sci Tech,* **19** (2000) 333-336

15 D.J. Taylor, B.D. Fabes, *J. Non Crystalline Solids*, **147** (1992) 457-462

16 G.W. Scherer, *J. Sol-gel Sci. Tech.*, **8** (1997) 353-363

17 R.E. Vandeleest, *Applied Surface Science*, **86** (1995) 278-285

18 H. Liu, W. Yang, Y. Ma, Y. Cao, J. Yao, J. Zhang, T. Hu, *Langmuir*, **19** (2003) 3001-3005

19 H. Liu, W. Yang, Y. Ma, Y. Cao, J. Yao, *New J. Chem.*, **26** (2002) 975-977

20 S. Brunauer, L.S. Deming, W. Edwards Deming, E. Teller, *J. Am. Chem. Soc.*, **62** (1940) 1723-1732

21 D. Dollimore, P. Spooner, A. Turner, *Surf. Technol.*, **4** (1976) 121-160

22 K. Sing, *Colloids & Surfaces A*, **187-188** (2001) 3-9

23 S. Storck, H. Bretinger, W.F. Maier, *Applied Catalysis A: General*, **174** (1998) 137-146

24 P.N.J. Henrion, M.J. Put, *Powder Tech.*, **23** (1979) 21-30

25 A. Ayral, A. El Mansouri, M.P. Vieira, C. Pilon, *J. Mater. Sci. Lett.*, **17** (1998) 883-885

26 B. Niemczewski, *Transactions of the Institute of Metal Finishing*, **79** (2001) 68-72

27 R. Eustaquio-Rincon, A. Romero-Martinez, A. Trejo, *Fluid Phase Equilibria*, **91** (1993) 187-201

28 R. Eustaquio-Rincon, R. Molnar, A. Trejo, *Fluid Phase Equilibria*, **68** (1991) 187-195

29 V.P. Zhdanov, B.Kasemo, *Surface Science*, **437** (1999) 307-316

30 A. Martino, A.G. Sault, J.S. Kawola, E. Boespflug, M.L.F. Phillips, *J. Catalysis*, **187** (1999) 30-38

31 A. Howard, C.E.J. Mitchell, R.G.Egdell, *Surface Science*, **515** (2002) L504-L508

32 D. Fan, L.Q. Chen, *J. Am. Ceram. Soc.*, **80** (1997) 1773-1780

33 J. Zhu, L.Q. Chen, J. Shen, V. Tikare, *Computational Materials Science*, **20** (2001) 37-47

34 P.Heitjans, S. Indris, *J. Phys. Condens. Matter.*, **15** (2003) R1257-R1289

CHAPTER 6

Conclusions and final comments

An operating sensor cable incorporating a proprietary polysiloxane coating was produced which showed a response to low molecular weight, low viscosity liquids and solvents (such as petrols) in less than 30 seconds. Responses to high volatility solvents, such as chloroform, were almost immediate. Successful operation of the sensor system at ranges between 500 m and 2 km was reproducibly demonstrated and some success was shown at lengths greater than 2 km. Occasionally it was observed that a response higher than expected was seen. This was attributed to the synergistic effects of microbending and macrobending losses, where the periodic stress applied to the core-cladding interface lay at a critical harmonic spacing. The sensors were found to work virtually irrespective of the applied period and it was seen that responses were around 0.07 dB per metre wetted for all the harmonics of the binding. On occasions where the periodicity of the binder matched one of the theoretical harmonics, an enhanced response was observed.

Considerable scope remains for the further development of the DISH sensor. It was concluded that tuning of the sensor for aviation fuel would open up a huge potential range of applications, on the ground and in the air. Development of a sensor for crude oil and common petrochemical or other industrial feedstocks, products and wastes would be similarly rewarded. The sensor cable could be adapted to monitor other analytes of interest by prediction of polymer/solvent compatibility from solubility parameters, followed by experimental assessment of the swelling responses of the identified polymer/fluid pairs.

The use of an aramid material for the binder led to problems with attenuation and tension damage at elevated or lowered temperatures. This would be solved by the use of an alternative binder material with a positive coefficient of expansion.

Stable sols were prepared from Triton X-100 in dry cyclohexane that remained stable and transparent after the addition of water and liquid alkoxide. Viscometry confirmed the presence of a short induction period. Viscometry and aging behaviour showed that the sols would remain stable for an indefinite period, in excess of several months, where solvent evaporation and water ingress was prevented. Where evaporation was unrestricted, densification and extensive polymerisation occurred leading to the formation of solid monolithic gels after between 24 and 48 hours. Further aging led to gel fracture and the development of a characteristic, intense yellow colouration that gradually became more amber as aging continued over several days. Aging also led to the liberation of surfactant residues (together with a small quantity of excess water from polycondensation reactions) in the form of a viscous, oily exudate. X-ray diffractometry confirmed that the as-produced gels were amorphous and retained their amorphous state until thermal treatment induced crystallisation of the anatase phase. Thermal treatment enabled the consistent production of nanocrystalline titania powders as either single-phase anatase or a mixed-phase (anatase & rutile) dependent upon the temperature regime employed. Crystal grain sizes, calculated from the Scherrer relationship, were shown to vary from approximately 5 nm for anatase phase at 623 K to almost 25 nm for mixed phase at temperatures in excess of 823 K. Carbon content was shown to decrease with increasing temperature of thermal treatment, requiring a temperature of greater than 723 K to remove all residual organic content.

Conceptual fibre-optic based point sensors incorporating titania thin films were introduced and their modes of operation outlined. Ideas for novel incorporation of electrochemical sensing using a micro-optical ring electrode together with other optical fibre devices were discussed although the assembly of any such devices was not possible within the timeframe of this project.

The deposition of thin films of titanium dioxide onto assorted substrates was shown. Deposition onto conducting glass slides was largely successful, where 300 to 500 nm thin films of nanocrystalline titania were produced. Scanning electron micrographs demonstrated that layers of reproducible thickness could be produced as either single or multi-layered films. X-ray diffraction investigations into the crystallinity of the films were unsuccessful. Despite this, investigation using X-ray photoelectron spectroscopy confirmed that tetravalent titanium dioxide was indeed produced and suggested that a surface-hydroxylated form (anatase) may be present. UV-visible spectra demonstrated that optically transparent films were produced and showed clear differences between raw gel and crystalline films with sharp

band-edges indicative of well-defined crystal size in samples that were calcined at elevated temperatures.

The deposition of lithium doped thin films on conducting glass slides was less successful. Upon thermal treatment, the doped films became extensively fractured which was attributed to phase separation of the matrix into dopant-rich and dopant-poor regions. In the absence of secondary ion mass spectrometry imaging or mapping XPS, this could not be confirmed. Again, XRD analyses failed to produce spectra of the films, likely due to their very thin (<500 nm) thicknesses. XPS spectra did not show direct evidence of the presence of Li^+ in the films. Given the weak signal expected from the single Li1s electron in XPS generally, this was not surprising. The high resolution spectra of the Ti2p signal showed that the $Ti2p_{3/2}$ peak for lithium doped films was found at the bottom end of the range expected for tetravalent titanium and lay in the range where Ti^{3+} may be seen. This may be indirect evidence for the presence of Li^+ in the lattice as this would cause a reduction in the mean oxidation state of titanium within the lattice overall. Electrochemical lithium insertion into both lithium-doped and pure titania thin film electrodes on conducting glasses showed that room temperature intercalation was possible accompanied by a pronounced change in the optical properties of the film. The presence of such intercalation at room temperatures is indicative of an anatase (or brookite) structure. When the film potential was swept in the negative direction a cathodic reduction current was seen, associated with the reduction of Ti (IV) to Ti (III) and the intercalation of lithium. This was accompanied by a change from a transparent to a deep indigo colour. The film returned to its deintercalated transparent state when the scan direction was reversed and an anodic current peak was recorded. Cyclic plots of transmittance *versus* film potential showed a sigmoidal shape but did not overlay on each repeat cycle, nor was superimposition observed for successive voltammograms where a diminishing current response was observed with cycling. The films were thus not wholly optically reversible and the redox reaction was not fully stable. Over several cycles, it was possible to observe film degradation with each charging/de-charging cycle, and films deteriorated fully after between 5 and 10 cycles.

Europium doped films were produced successfully, albeit at very low doping ratios. The doping ratios used were of the order of 1 ‰ and were too small for any luminescence to be observed under UV illumination. Nor was the doping of sufficient concentration to produce strong signals in the XPS spectra. Some evidence for the presence of Eu was seen, but no allocation of oxidation state was possible. Stronger doping, between 1 % and 10 % would be required to produce strong signals and visible luminescence. The europium-doped films were

characterised by excellent adhesion and smooth, unfractured surfaces. Film thicknesses were of the order of 200 to 500 nm and multi-layered structures were produced.

Coating of optical fibre with titania thin films was unsuccessful. Reproducible deposition of raw gel layers and xerogel films was demonstrated, however attempts to calcine these layers to form crystalline films failed. The contraction of films under heating led to catastrophic fracture of the films. Use of fibres with considerably larger dimensions to minimise curvature did not solve the problem as these larger core fibres were made of plastics that deformed or melted when exposed to temperatures in excess of 150 to 200 °C. Despite some interesting results with the un-calcined, xerogel films on these PMMA fibres, the intention to produce crystalline films on the fibres by standard methods of thermal treatment was scrapped. It then became necessary to determine alternative methods for the production of crystalline films on the fibre surfaces. Hence, considerable effort was directed into establishing a series of treatments that would induce film crystallisation and remove the organic residues that make up a significant proportion of the un-calcined gels.

Supercritical fluid extraction of films deposited onto glass slides was shown to produce films of exceedingly large specific surface area with estimates of the BET surface area in excess of 150 m^2 per gram for films that had not been calcined, increasing up to values in excess of 600 m^2 per gram for films that were calcined. Unfortunately, SFE treatment often led to catastrophic fracturing of films. In the case of films on optical fibre, it was concluded that the technique as it stands would not be feasible. Where SFE treatment did not lead to film failure, gas adsorption measurements demonstrated that high surface area mesoporous films could be produced by this technique. Further work is advised (and ongoing) to determine whether modification of the extraction regimes may lead to improved film integrity and adhesion.

Hydrothermal treatment after gelation was shown to successfully induce the crystallisation of the anatase phase in bulk gels. Steaming at atmospheric pressure was sufficient to lower the carbon content by 40 % and when steamed at elevated pressures this reduction was increased to greater than 50 % of the starting composition. The steam treatment led to the liberation of surfactant as a viscous exudate that was easily washed from the steamed gels with isopropanol or cyclohexane. In the case of thin films, as was seen for SFE methods, extensive fracturing was observed after hydrothermal treatment, with partial removal of the film. Complete removal of the film from slides was seen after immersion in heated liquid water.

For thin films on optical fibres hydrothermal treatment led to the complete destruction of films and their removal from the fibre surface.

No work was carried out to investigate the effect of ambient humidity upon gelling rates in thin films and all depositions were performed in open conditions. A series of experiments in a glovebox environment would allow the influence of environmental conditions on the deposition process to be characterised. It is thought that increasing the ambient humidity would increase the rate of gelling of films as they are dipped.

Porosity and surface area measurements on hydrothermally treated samples would be useful in any future work to fully determine the effects of treatment on the films.

Ultraviolet irradiation of films did not cause any measurable change in phase, however significant shrinkage was observed which was attributed to condensation reactions between neighbouring hydroxyl groups within the oxide skeleton of the gel. Evidence for these condensation processes was seen by the intensification of the yellow colouration of the films, due to the formation of coloured titanium complexes with the liberated species.

Despite the poor performance of the thin films deposited and their extensive fracturing it would be beneficial to pursue these processes in an attempt to produce films on optical fibre that show the unusually high specific surface area seen for the thin films on conducting glass slides, in excess of 600 m^2 per gram.

The inherent problem with the reverse micelle microemulsions used in this work is the high organic content of the resulting films. The removal of some 50 % of the film volume after deposition will inevitably cause massive film shrinkage and thus likely failure. Extreme fracturing of films was observed for all post-coating treatments, which is problematic for coatings onto optical fibre. Better results for fibres would almost certainly be obtained using direct micelle techniques in aqueous media, e.g. with nitric acid and ethanol. Such techniques are by the far the most commonly reported in the literature. However, the best surface area estimates reported are only 150 to 250 m^2 per gram. No work was performed with different surfactants, and this work concentrated solely on the use of the non-ionic octylphenylpolyoxyethylene ether Triton X-100, although there are other common surfactants within the Triton range in which the polyoxyethylene chain is shorter. There are also saturated analogues of Triton X-100 in which the octylphenyl moiety is replaced with a substituted cyclohexane ring.

In addition, there is a vast range of non-ionic surfactants that could be used in this system. Furthermore, water was the only hydrolysing agent considered whereas it would be possible to use hydrogen peroxide or to look at an acid catalysed process.

The lack of XRD traces for thin films caused great difficulty in discerning any phase change in the films after treatments. A series of measurements using Raman spectroscopy or ellipsometry would enable phase information and changes in physical properties to be detected. The use of ellipsometry as a tool for monitoring fluctuations in the refractive indices of films would be invaluable in any continuation of this work.

The production of a mesh structure was formed during dip coating of PMMA fibres in acetone or n-methylpyrrolidone suspensions of titania. This mesh phenomenon was at first attributed to deposition of titania but was subsequently confirmed to be a phenomenon related to the dissolution and redeposition of the fibre cladding material. The mesh was shown to be capable of entrapping titania particles and a rudimentary device was assembled by immobilisation of titania crystallites onto the tip of an optical fibre. The serendipitous discovery of these mesh phenomena could be harnessed in future work to produce novel fibre devices by immobilisation of dyes or sensing materials within the mesh matrix. In addition, it would be interesting to use a mesh covered optical fibre as a support for sol-gel deposition of the titania material. Subsequent SFE or hydrothermal treatments may produce highly porous, high surface area structures without the concerns of fracturing seen in the case of thin films.

If this work were continued it is thus recommended that alternative surfactants be explored possibly including ionic surfactants and that a means of reducing organic content of the gel prior to coating be found. It is also recommended that the use of other titanium alkoxides or tetrahalides be considered together with the use of other hydrolysing agents, specifically hydrogen peroxide and dilute acids.